THE FORMATION OF RINGS AND GAPS IN MAGNETIZED WIND-LAUNCHING DISKS

Scott Stephen Suriano
Altamont, NY

B.S. Physics, State University of New York College at Oneonta, 2012
B.A. Mathematics, State University of New York College at Oneonta, 2012

M.S. Astronomy, University of Virginia, 2014

A Dissertation Presented to the Graduate
Faculty of the University of Virginia
in Candidacy for the Degree of
Doctor of Philosophy

Department of Astronomy

University of Virginia
August 2018

Committee Members:

Zhi-Yun Li
Philip L. Arras
Shane W. Davis
Kento Yagi

Abstract

Radial substructures in disks around young stellar objects are now routinely detected by state-of-the-art observational facilities. There is also growing evidence that large-scale magnetic fields threading the disks are responsible for launching wide-angle outflows. The magnetic fields that launch disk winds play a crucial role in the dynamics of protoplanetary disks. In this thesis we investigate theoretically the formation of radial structures, i.e., rings and gaps, in magnetized disks through three numerical simulation projects of increasing complexity.

We start with two-dimensional (2D) disk simulations under the assumption of axisymmetry, and we include the simplest of the non-ideal magnetohydrodynamic (MHD) effects, Ohmic dissipation. We find two distinct modes of disk accretion depending on the Ohmic resistivity and magnetic field strength. A small resistivity or high field strength promotes the development of rapidly infalling "avalanche accretion streams" in a vertically extended disk envelope that dominates the dynamics of the system, especially the mass accretion. These streams are suppressed in simulations with larger resistivities or lower field strengths, where most of the accretion instead occurs through a laminar disk. In these simulations, the disk accretion is driven mainly by a slow wind that is typically accelerated by the pressure gradient from a predominantly toroidal magnetic field; however, there are lightly mass-loaded regions that are accelerated magnetocentrifugally to speeds exceeding 100 km s^{-1}. Both the wind-dominated and stream-dominated modes of accretion create prominent features in the surface density distribution of the disk, with a strong spatial variation of the (poloidal) magnetic flux relative to the mass. Regions with low mass-to-flux ratios accrete quickly and lead to the development of gaps, whereas regions with higher mass-to-flux ratios accrete more slowly, allowing matter to accumulate and

form dense rings. In some cases, avalanche accretion streams produce dense rings directly through continuous feeding.

In the second project, we retain the simplifying assumption of axisymmetry but focus on ambipolar diffusion (AD), the dominant non-ideal MHD effect at disk radii of tens of au or larger (scales that are observationally accessible using current facilities). We find that rings and gaps naturally develop in the AD-dominated disks as well. In particular, we find that disks which are moderately well-coupled to the magnetic field remain relatively laminar, with a radial electric current that is steepened by AD into a thin layer near the midplane. The toroidal magnetic field sharply reverses polarity in this layer, generating a large magnetic torque that drives fast accretion. The poloidal magnetic field is dragged inward through this accretion layer into a highly pinched radial configuration. The reconnection of this pinched field creates magnetic loops where the net poloidal magnetic flux (and thus the accretion rate) is reduced, yielding dense rings. Neighboring regions with stronger poloidal magnetic fields accrete faster, forming gaps. In better magnetically coupled simulations, the accretion streams develop continuously near the disk surface as before, rendering the disk-wind system more chaotic. Nevertheless, prominent rings and gaps are still produced by reconnection, which again enables the segregation of the poloidal field and the disk material. However, the reconnection is now driven by the non-linear growth of MRI channel flows.

In the last part of the thesis, we present ongoing work that extends the 2D (axisymmetric) simulations of AD-dominated disks to three dimensions (3D). We find that rings and gaps develop naturally in 3D from the same basic mechanism that was identified in 2D: namely, the redistribution of poloidal magnetic flux (relative to disk material) from the reconnection of sharply pinched poloidal magnetic field lines.

There is still a clear anti-correlation between the mass surface density and the vertical magnetic flux through the disk midplane. The formation of rings and gaps proceeds in an axisymmetric fashion at early simulation times; non-axisymmetric variations arise spontaneously at later times, but they do not grow to such an extent as to disrupt the rings and gaps. These radial disk substructures persist through the full duration of the simulations, which run for thousands of orbital periods at the innermost edge of the simulated disks. The longevity of the azimuthally coherent rings make them attractive sites for trapping large grains that would otherwise rapidly migrate inward due to gas drag. We find that rings and gaps are formed over a range of ambipolar diffusivities and magnetic field strengths in 3D. They are more prominent in disks that are better coupled to the magnetic field and disks that are more strongly magnetized.

Acknowledgements

First, I would like to thank my advisor Zhi-Yun Li. Without his guidance and patience throughout my studies at UVA, I wouldn't have been able to complete the work in this dissertation. I will be forever grateful for the time he invested in my career. Thank you to Phil Arras, Shane Davis, and Kent Yagi for reading through my thesis and being a part of my committee. I want to thank my past teachers and professors from all phases of my education: Guilderland, SUNY Oneonta, and UVA. A special thank you to my undergraduate advisor, Hugh Gallagher, and the professors of my graduate program at UVA. Thanks to my fellow graduate student classmates, especially those that I matriculated with in 2012. Without their help, I wouldn't have been able to survive the grueling workload of our first two years of coursework. I would like to thank my mom, dad, and brother for their love and encouragement throughout the entirety of my life. Also, thanks to my extended family and friends for their continued inspiration and amusement. Finally, I would like to thank my wife, Jenni, for her unwavering love and support, especially in the first few years of graduate school when I was never around. You are the best part of my life and nothing makes me happier than spending time with you. And thanks to Maya "Noodle," Fira, Moose, and the late, great Mr. Bibster Magoo for being happy to see me when I get home.

Table of contents

List of Figures

Chapter 1

Introduction

Giant molecular clouds are stellar nurseries that contain enough gas and dust to form tens of thousands of stars. When dense regions within these giant molecular clouds, called prestellar cores, accumulate enough mass they begin a runaway collapse under their own gravity. The process of core collapse does not happen symmetrically, because any initial rotation in the core is amplified as the core shrinks due to the conservation of angular momentum. The rotating material close to the central star will be supported from further collapse perpendicular to the axis of rotation, with the end result being the formation of a flattened, rotating disk having a radial extent on the scale of 100 au. The formation of circumstellar disks around young protostars is inevitable as long as the star-forming cores are rotating; likely most stars, if not all, have had a disk around them at one point in their past. The disk material can now evolve in one of three ways over the course of its $\sim 1 - 10$ Myr lifetime: (1) slowly accrete onto the protostar, (2) escape the system via a wind/outflow, or (3) form a planetary system. In general, we expect all three to happen simultaneously. The interplay between these end results is of great interest to researchers, as it provides the link between the evolution of protoplanetary disks, the formation of planetary

systems, and the possible development of life on habitable planets.

To understand the evolution of protoplanetary disks, we must first understand their dynamics. Magnetic fields are widely believed to be the primary driver of disk dynamics, either through internal angular momentum redistribution via magnetic stresses or through external angular momentum removal via a disk wind. Magnetic fields have been difficult to study theoretically because they are only partially coupled to the lightly ionized disk material, which necessitates the inclusion of the so-called "non-ideal MHD (magnetohydrodynamic) effects" in any simulation that seeks to incorporate them. The goal of this thesis is to improve our understanding of the dynamics of wind-driving magnetized disks through non-ideal MHD simulations. We find that simulated disks spontaneously develop the intricate radial substructures, such as rings and gaps, that are now routinely observed in real sources. Such substructures likely have important implications for the dynamics and growth of dust grains, the crucial first step towards the formation of planetesimals and, ultimately, planets.

In the rest of Chapter 1 we provide background information on observations of protoplanetary disks, some theory of disks and their associated outflows, non-ideal MHD effects, and the numerical code used for our simulations. Chapter 2 lays the groundwork for the formation of rings and gaps through MHD processes. We explore these processes using two-dimensional (2D) axisymmetric simulations that include the simplest of non-ideal MHD effects, Ohmic resistivity, which dominates the innermost regions of the disk. Chapter 3 focuses on the outer, ambipolar diffusion-dominated disk regions, where our 2D simulations reveal a novel mechanism for the development of a radially varying vertical magnetic flux that leads to the formation of rings and gaps. Chapter 4 shows that disk substructures are still formed through these MHD

processes in three-dimensional simulations. Finally, Chapter 5 summarizes the main results of this thesis and offers perspectives on future directions.

1.1 Disk observations

1.1.1 YSO classification

Young, pre-main sequence stars are classified according to their mass. Low-mass ($0.08 \lesssim M_*/\mathrm{M}_\odot \lesssim 2$) pre-main sequence stars of spectral types F through M are called "T Tauri stars" (or TTSs for short) and intermediate-mass ($2 \lesssim M_*/\mathrm{M}_\odot \lesssim 8$) pre-main sequence stars are called Herbig Ae/Be stars[1]. The term "young stellar object" (YSO) is used as a catch-all to describe young stars of all masses and all evolutionary stages whose physical nature/observational appearance may be obfuscated by the circumstellar environment (Strom 1972). YSOs have long been classified by the shape of their infrared spectrum, usually from 2 to 25 μm (Williams & Cieza 2011). The infrared spectral index is defined as (Wilking & Lada 1983; Lada 1987)

$$\alpha_{\mathrm{IR}} \equiv \frac{d\log(\nu S_\nu)}{d\log\nu} = \frac{d\log(\lambda S_\lambda)}{d\log\lambda}, \tag{1.1}$$

where ν and λ are the frequency and wavelength of the light, respectively, and S_ν and S_λ are the observed flux density per unit frequency or wavelength. YSOs are classified as follows (Lada 1987; Greene et al. 1994):

- Class 0: α_{IR} is not defined – typically no observable infrared emission
- Class I: $\alpha_{\mathrm{IR}} > 0.3$ – optically obscured by infalling envelope

[1]It is more difficult to quantify the early evolutionary stages of pre-main sequence A and B stars because they evolve more quickly onto the zero-age main sequence than their lower-mass counterparts.

- Flat-spectrum sources: $-0.3 < \alpha_{\rm IR} < 0.3$ – intermediate between Class I and II
- Class II: $-1.6 < \alpha_{\rm IR} < -0.3$ – infrared excess from accreting disk
- Class III: $\alpha_{\rm IR} < -1.6$ – SED resembles pre-main sequence stellar photosphere

The evolutionary progression of this infrared classification scheme was recognized by Adams et al. (1987) and is illustrated in Fig. 1.1. Class 0 sources are completely enshrouded by the envelope from which they are forming, and most of their mass is still contained in that envelope. Class I sources still retain an envelope, but a disk has formed and the star has a mass comparable to, or larger than, what remains in the envelope. By Class II the envelope is gone and the disk is actively accreting onto the star. Class III objects have passive (i.e., non-accreting) disks. Low-mass YSOs that are not optically obscured are further classified by the strength of their Hα emission. Classical T Tauri stars (CTTSs) have large Hα equivalent widths and strong UV emission; weak-lined T Tauri stars (WTTSs) show no signs of active accretion onto the stellar photosphere. As such, CTTSs and WTTSs closely correspond to Class II and III, respectively (Williams & Cieza 2011).

1.1.2 Winds, jets, and outflows

In the 1950s, George Herbig (1951) and Guillermo Haro (1952, 1953) independently observed two large nebulous patches in the Orion A Molecular Cloud. These structures had broad continuum emission as well as very bright Hα emission and many forbidden transitions. It was initially assumed that the emission from these regions, now called HH objects, were reflection nebulae associated with young stars. Although this assumption proved to be correct in some sense, it was not until the 1980s that HH objects were confirmed to be outflows fueled by the parent star and its disk in

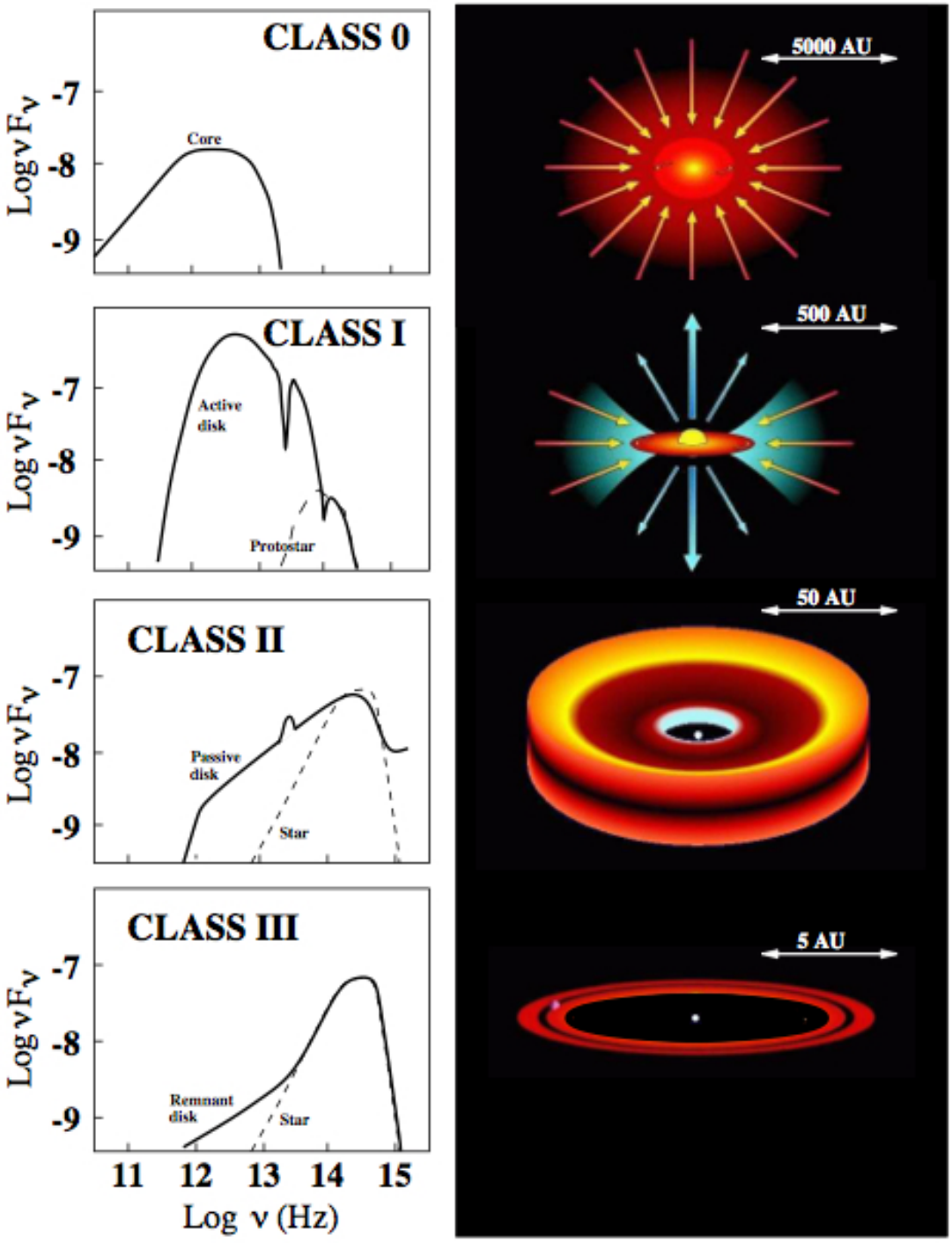

Fig. 1.1.— Illustration of YSO classification. Note that jets are still observed to be launched from Class 0 sources despite the top right illustration. Image credit: Isella (2006) and https://ay201b.wordpress.com/tag/sed-modeling/.

the form of collimated bipolar jets (Bally et al. 2007). Over the next decade, the *Hubble Space Telescope* (HST) provided wide-field optical/NIR imaging for many HH objects, revealing their full (up to pc-sized) extent oriented perpendicular to the YSO disks (e.g., Burrows et al. 1996; Reipurth et al. 2000).

The outflows from young stars can be separated into two categories: (1) fast ($v \gtrsim 100$ km s^{-1}) collimated jets launched from the inner disk or (2) slow ($v \sim 1 - 30$ km s^{-1}) wide-angle outflows launched over a range of disk radii. The collision of the supersonic jets with the ambient cloud material produces the bright shocks observed as HH objects at distances up to several parsecs away from the protostar where they were launched. The physical nature of how fast jets are launched from the inner disk or star is still not well determined (see Section 1.2.2). The slow molecular outflows are thought to be the remnant dense core material that has yet to fall into the protostar and that is swept up by a wide-angle wind launched from the disk. The wind carves out bipolar cavities with opening angles that increase as a function of the YSO lifetime, eventually clearing away all the remnant core material. Both types of outflows could be important for controlling the star formation efficiency, either by removing the core material in which individual stars form or stripping away the core material of other (neighboring) YSOs, especially in clustered environments.

Optical forbidden lines such as [OI] and [SII] are a hallmark of classical T Tauri star spectra. These broad blueshifted lines[2] show two distinct velocity components, a high-velocity component (HVC) and a low-velocity component (LVC). The HVC ranges from approximately $50 - 150$ km s^{-1} while the LVC is closer to ~ 5 km s^{-1}. The origin of the low velocity component is thought to be either a photoevaporative (thermal) wind[3] or a slow MHD disk wind. The HVC is believed to be the jet

[2]It is usually assumed that the flows are bipolar; however, the redshifted line is obscured at optical wavelengths by the dusty disk.

[3]The photoevaporative wind will be launched where the thermal energy of the disk material

component, produced from either the inner part of the disk, from the interaction of the stellar magnetosphere with the disk (the so-called "x-wind," see Section 1.2.1.1), or from a confined stellar wind. Figure 1.2 shows the spectra of the 6300 and 5577 Å [OI] forbidden line for T Tauri stars observed with Keck/HIRES by Simon et al. (2016) (see their figure 10). The LVC can be further separated into a broad and narrow kinematic component. Both broad and narrow components have line widths that correlate with disk inclination, consistent with line broadening from Keplerian rotation at $0.05 - 0.5$ au and $0.5 - 5$ au, respectively. The broad component (BC), indicated by the red line in Fig. 1.2, is likely due to an MHD disk wind as the velocity offset is largest for face-on disks. The origin of the narrow component (NC) is less clear.

The optical and UV excess of T Tauri stars is attributed to the magnetospheric accretion of disk material onto the stellar photosphere (Lynden-Bell & Pringle 1974; Koenigl 1991; Hartmann et al. 1994). The mass outflow rates can be estimated from the strengths of the optical emission lines. The luminosity of the Hα line, for example, is converted to an accretion luminosity (Gullbring et al. 1998; Hartmann et al. 1998; Alcalá et al. 2014; Simon et al. 2016). The accretion luminosity is then related to the mass accretion rate as

$$L_{\rm acc} = \frac{GM_*\dot{M}_{\rm acc}}{2R_*}. \tag{1.2}$$

Using this technique, the measured accretion rates found from classical T Tauri stars are approximately $10^{-10} - 10^{-7}$ $M_\odot$ yr^{-1}, with median mass accretion rates near 10^{-8} $M_\odot$ yr^{-1} (Hartmann et al. 2016). Hartmann et al. (1998) estimate that an

exceeds the gravitational binding energy. Equating these two energies leads to a critical disk radius beyond which the thermal wind is launched as high-energy stellar UV and X-ray photons heat the upper disk layers. This "gravitational radius" is thus approximately $R_g \simeq GM_*/c_s^2$. Although these winds are important for the dispersal of protoplanetary disks (see Alexander et al. 2014 for a review), they are not likely to be important for driving disk accretion.

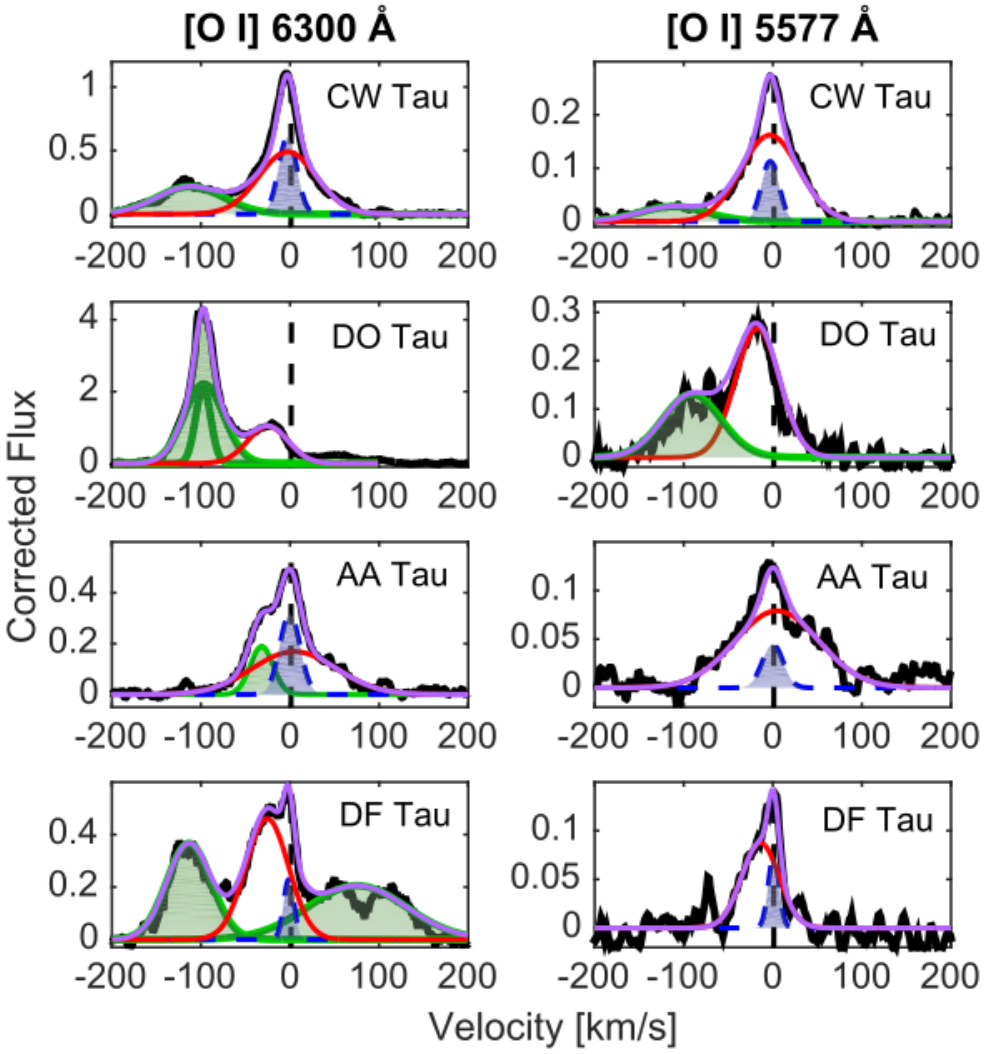

Fig. 1.2.— T Tauri star [OI] spectra. When both [OI] lines are present, the LVC components for 6300 Å (*left*) and 5577 Å (*right*) are very similar. The NC of the LVC is shaded in blue, and the BC is outlined in red. Areas shaded in green meet the criteria for HVC and the purple line shows the sum of all fits. Figure 10 from Simon et al. (2016).

accretion rate of 10^{-8} $M_\odot$ yr^{-1} corresponds to an effective alpha parameter of $\alpha = 10^{-2}$ (see Section 1.2 for the definition of the α parameter). However, recent molecular line observations from ALMA have found $\alpha \lesssim 3 \times 10^{-3}$ in some disks (Hughes et al. 2011; Flaherty et al. 2017).

1.1.3 Evidence for disk winds

There is growing observational evidence that wide-angle outflows launched from circumstellar disks are in fact MHD disk winds (Matthews et al. 2010; Pontoppidan et al. 2011; Greenhill et al. 2013; Banzatti & Pontoppidan 2015; Simon et al. 2016; Bjerkeli et al. 2016; Hirota et al. 2017; Tabone et al. 2017; Lee et al. 2018; see Section 1.2.1.1 for more on magnetic disk wind mechanisms). Perhaps the most clear-cut example of a disk wind is seen from the high-mass protostar Orion Source I (located in the Orion BN/KL region), where SiO maser emission in a rotating outflow has been observed for a decade. Figure 1.3 shows the proper motion (over a nine year span) and line-of-sight velocities of SiO and H_2O masers in the disk wind around Source I observed with the Very Large Array (Greenhill et al. 2013). As for disk winds from low mass protostars, ALMA observations of the Class I protostar TMC1A shows a rotating CO outflow from the disk (see Fig. 1.4; Bjerkeli et al. 2016). This slow CO outflow emanates directly from the disk over radii of $2 - 20$ au, and it is estimated that the wind has a specific angular momentum of ~ 100 au km s^{-1}. The removal of a significant amount of angular momentum over an extended region of a disk around a young ($t \lesssim$ a few $\times 10^5$ yr) protostar lends credence to the notion that magnetic disk winds play an important role in protoplanetary disk evolution.

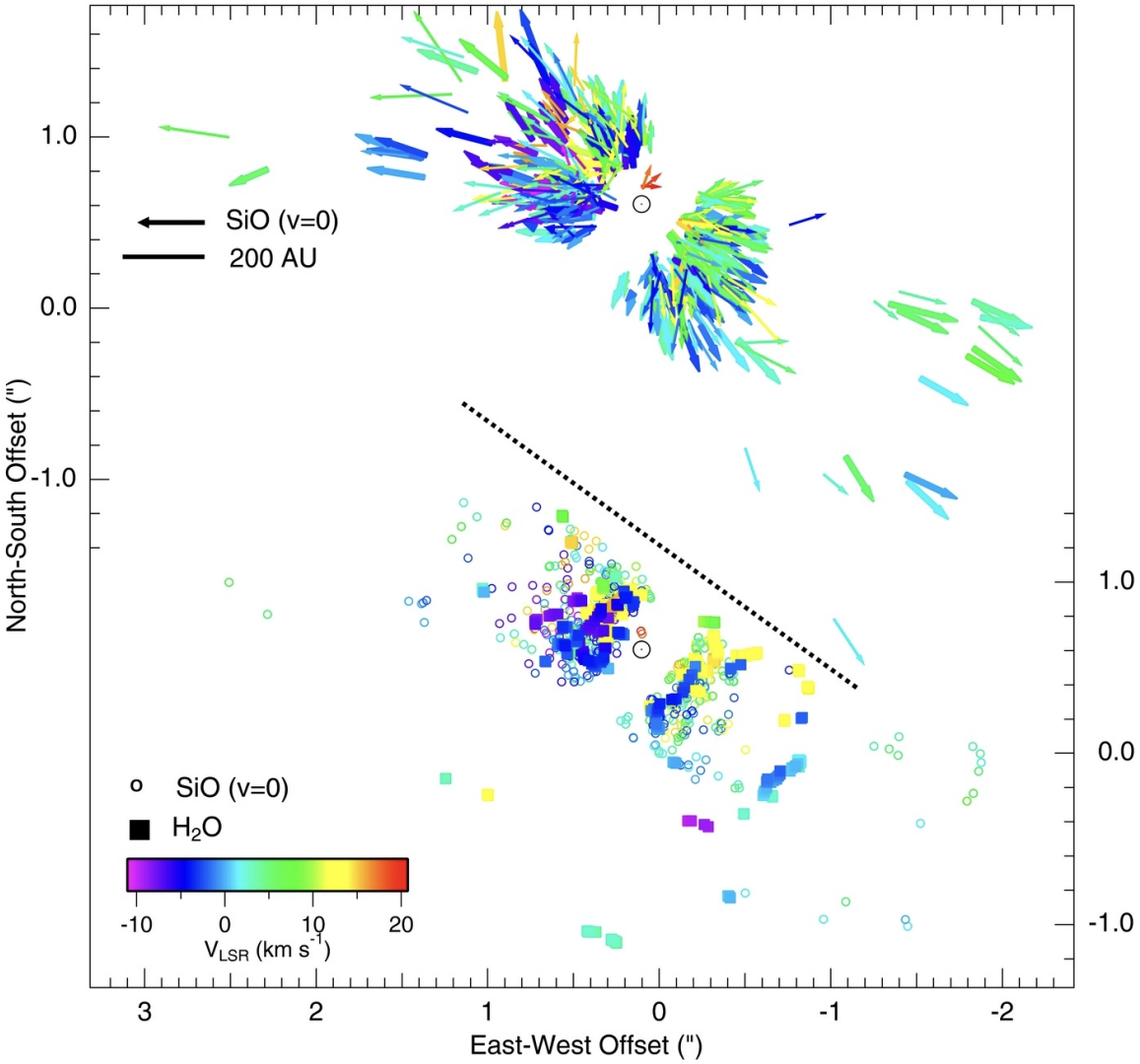

Fig. 1.3.— Figure 2 from Greenhill et al. (2013) shows the line-of-sight (below the dashed line) and proper motion (above) of the SiO and H_2O masers from Orion Source I. For more on the possible MHD disk wind from Orion Source I, see Matthews et al. (2010); Hirota et al. (2017).

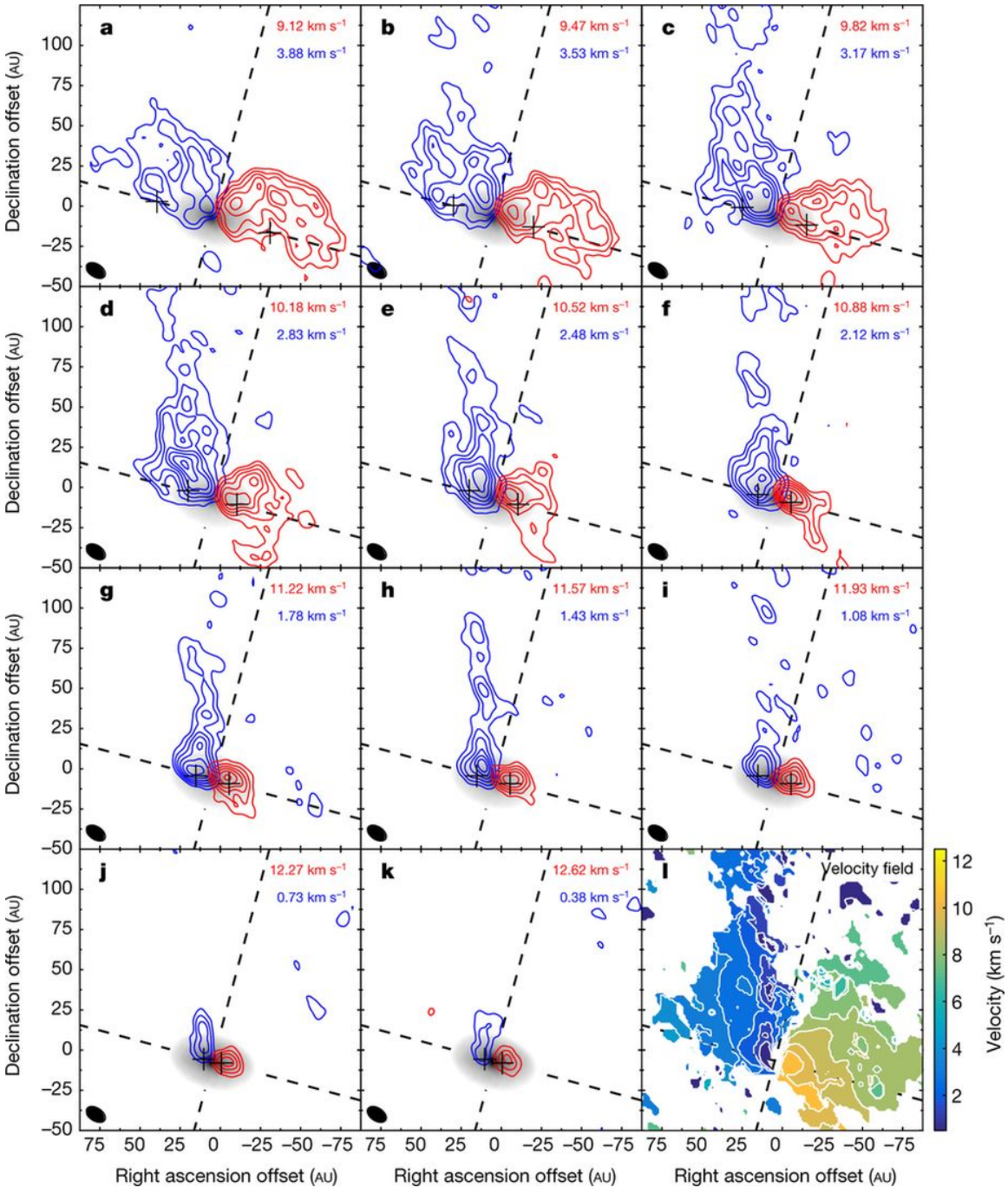

Fig. 1.4.— ALMA observations of the blue and redshifted ^{12}CO emission from the Class I protostar TMC1A ($v_{\rm sys} = 6.4$ km s^{-1}). The dashed lines show the disk plane (nearly horizontal) and the perpendicular outflow axis. The greyscale shows the dust continuum emission. Figure 1 from Bjerkeli et al. (2016).

1.1.4 Disk imaging and substructure

Far-infrared observations from the Infrared Astronomical Satellite (IRAS) in the 1980s all but confirmed that the excess infrared emission seen from T Tauri stars must be from dusty circumstellar disks (Hartmann 1998). The first high-resolution images of circumstellar disks were taken by HST towards sources in the the Orion Nebula. These disks were either illuminated by or seen in absorption against the bright HII regions surrounding high-mass stars (O'dell et al. 1993; O'dell & Wen 1994; McCaughrean & O'dell 1996; O'dell 1998; Stapelfeldt et al. 1998). Figure 1.5 shows the well-known HST image of the nearly edge-on disk HH 30 in the nearby star-forming Taurus molecular clouds (Burrows et al. 1996). The dark dust lane of the disk midplane is seen in contrast to the bright upper layers of the disk (produced when the light from the central source scatters off dust grains) and the bright emission of the fast inner (atomic) jet.

Our knowledge of circumstellar disks has come a long way since the first resolved disk images were taken by HST in the early 1990s. In just the past few years, the field was once again transformed by the advent of the Atacama Large Millimeter/submillimeter Array (ALMA). The high-resolution images from ALMA have revealed that many protoplanetary disks show intricate substructures in their dust continuum images, the first example being the disk around HL Tau (ALMA Partnership et al. 2015). This image is shown in Fig. 1.6, where the appearance of concentric bright rings and dark gaps stand out. Also shown in Fig. 1.6 is the image of the $\sim$10 Myr-old disk around TW Hya, the closest gas-bearing protoplanetary disk to the Sun (Andrews et al. 2016). Because TW Hya is at a distance of only $\sim$54 pc, ALMA can resolve substructure in its disk down to $\sim$1 au. The list of circumstellar disks observed to have dust substructure continues to grow (e.g., Zhang et al. 2016;

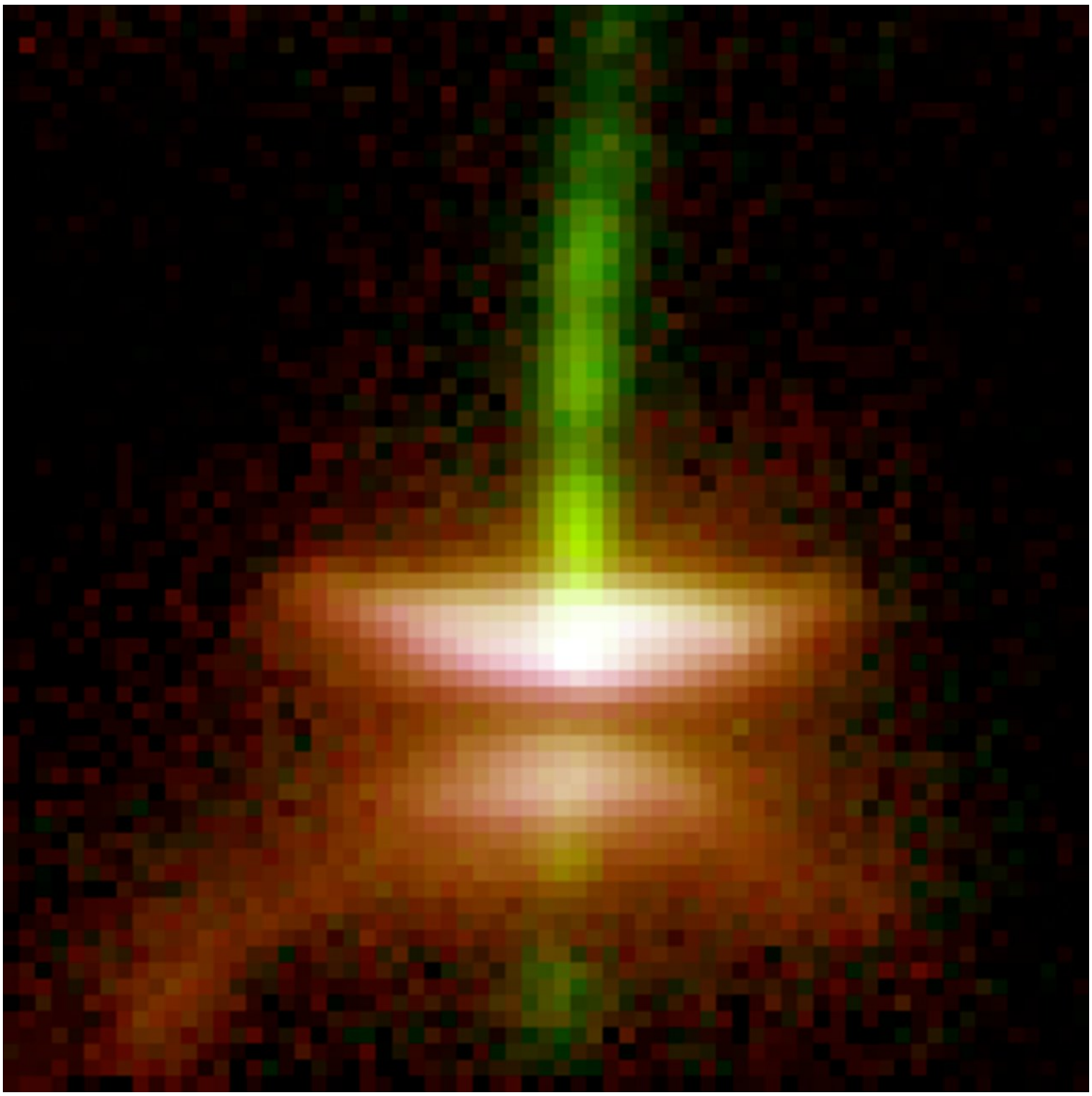

Fig. 1.5.— HST observations of the HH 30 disk. Image credit: Chris Burrows (STScI), the WFPC2 Science Team and NASA/ESA (Burrows et al. 1996). Also, see Lee et al. (2017) for the similar appearance of a dark dust lane in HH 212 at submillimeter wavelengths.

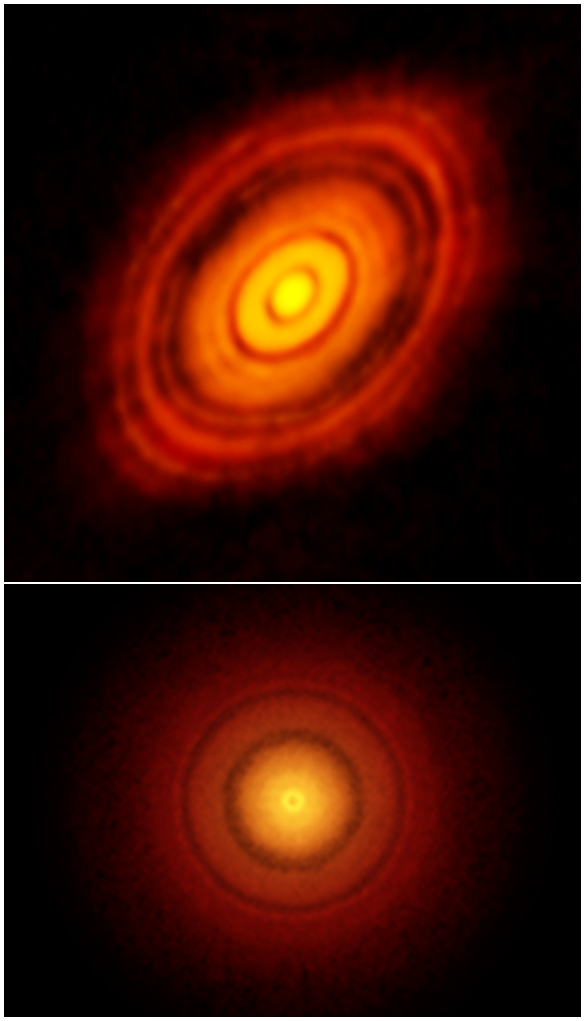

Fig. 1.6.— *Top:* ALMA observation of HL Tau (C. Brogan, B. Saxton, ALMA; see also ALMA Partnership et al. 2015). *Bottom:* ALMA observation of TW Hya at 870 μm(S. Andrews, B. Saxton, ALMA; see also Andrews et al. 2016).

Nomura et al. 2016; Pérez et al. 2016; Isella et al. 2016; Cieza et al. 2016; van der Plas et al. 2017; Loomis et al. 2017; Fedele et al. 2017, 2018; Dipierro et al. 2018; Sheehan & Eisner 2018). These disk structures, or the shadows they cast on the outer disk, are also seen in optical and near-infrared scattered light images from instruments like the SPHERE on the Very Large Telescope, HiCIAO and SCExAO on the Subaru Telescope, and the Gemini Planet Imager (e.g., Momose et al. 2015; Ginski et al. 2016; Stolker et al. 2016; Benisty et al. 2017; van Boekel et al. 2017; Monnier et al. 2017; Pohl et al. 2017; Avenhaus et al. 2018).

1.2 Disk theory

The basic theory of thin accretion disks was originally developed in the 1970s by Shakura & Sunyaev (1973) and Lynden-Bell & Pringle (1974). Lynden-Bell & Pringle (1974) describe the time evolution of a viscous accretion disk (where the specific angular momentum increases outward), whereby frictional torques between adjacent differential rotating disk rings lead to the outward transfer of angular momentum and the inward transfer of mass (as energy is dissipated in the process). The classic diffusion-like equation for the evolution of the disk surface density, $\Sigma \equiv \int_{-\infty}^{+\infty} \rho dz$, is

$$\frac{\partial \Sigma}{\partial t} = \frac{3}{R} \frac{\partial}{\partial R} \left[R^{1/2} \frac{\partial}{\partial R} \left(\nu \Sigma R^{1/2} \right) \right], \tag{1.3}$$

with a radial velocity profile given by

$$v_R = -\frac{3}{\Sigma R^{1/2}} \frac{\partial}{\partial R} \left(\nu \Sigma R^{1/2} \right), \tag{1.4}$$

where ν is the kinematic viscosity with units of $\mathrm{cm}^2\ \mathrm{s}^{-1}$. The presence of viscosity drives the spread of disk material such that all of the disk angular momentum eventually goes to infinity and all of the disk mass is accreted onto the central source (see also Pringle 1981). For a disk with a constant viscosity, the mass accretion rate will be $\dot{M}_{\rm acc} = 2\pi R \Sigma v_R$.

A main problem in such a theory was that there was no explanation for the physical nature of the viscous processes. It was known that the microscopic molecular viscosity would yield an accretion time that would be too long to be astrophysically interesting (Shu 1992). For example, a molecular viscosity of the order $\nu \sim v_{\rm th}\lambda_{\rm mfp} \sim 10^6\ \mathrm{cm}^2\ \mathrm{s}^{-1}$, would give an viscous accretion timescale at 1 au of $t_{\rm acc} \sim R^2/\nu \sim 10^{14}$ yr, which is at least 10^7 times larger than inferred disk lifetimes of $1 - 10$ Myr. Since the source of the viscosity was uncertain, it was initially characterized by the now famous "α parameter" defined as (Shakura & Sunyaev 1973)

$$\nu \equiv \alpha c_s h, \tag{1.5}$$

where h is the disk scale height[4]. Following this definition, the accretion velocity from Eq. 1.4 is of the order (Melia 2009)

$$\frac{v_R}{c_s} \sim \alpha \left(\frac{h}{R}\right). \tag{1.6}$$

In the next section, we will discuss the most likely processes that could supply this viscosity. In doing so, we will encounter a more physically relevant parametrization

[4]The disk scale height is defined as $h \equiv c_s/\Omega_K$ from vertical hydrostatic equilibrium. It is the characteristic height over which the density drops off by half an e-folding, i.e., $\rho(z) = \rho_{\rm mid} \exp\left(-z^2/2h^2\right)$. For thin disks, $h/r = c_s/v_K \ll 1$.

of the α parameter (Shakura & Sunyaev 1973; Balbus & Hawley 1998),

$$T_{i\phi} \equiv \alpha P_{\rm gas}. \tag{1.7}$$

$T_{i\phi}$ is the $i\phi$ component of the total stress tensor, including both the Reynolds (hydrodynamic) and Maxwell (magnetic) stresses,

$$T_{i\phi} = \rho v_i \delta v_\phi - \frac{B_i B_\phi}{4\pi}, \tag{1.8}$$

where $i = R, z$ (i.e., the radial or vertical component in a cylindrical coordinate system) and δv_ϕ is deviation of the azimuthal velocity from the Keplerian velocity, $\delta v_\phi = v_\phi - v_K$.

1.2.1 Angular momentum transport

In the viscous disk model angular momentum is radially redistributed, allowing mass to accrete. However, angular momentum can also be removed from the disk vertically. The two most likely physical mechanisms for angular momentum transport in circumstellar accretion disks are the magnetorotational instability (MRI) and the magnetocentrifugal wind (MCW), or disk wind for short. The MRI redistributes angular momentum in the disk radially, while disk winds extract angular momentum from the disk vertically. Both mechanisms rely on the presence of magnetic fields in the disks and are more efficient if the disk has a net vertical magnetic flux (Turner et al. 2014b).

1.2.1.1 Magnetic disk winds

Blandford & Payne (1982) showed through analytic self-similar solutions that gas from an infinitely thin, cold disk can be centrifugally accelerated along large-scale open magnetic field lines if they tilt away from the disk normal by 30° or greater. This so-called "magnetocentrifugal wind" extracts angular momentum from the disk via the magnetic braking torque, allowing mass to be accreted. This process removes angular momentum without the need for disk viscosity, although the strength of the accretion can still be characterized by an effective α parameter as defined in Eq. 1.7, where the magnetic wind stress is $T_{z\phi} = -B_z B_\phi / 4\pi$.

The physical picture behind the launching of the MCW is illustrated in Fig. 1.7. The magnetic energy in the disk is less dynamically important than the gas pressure. Moving vertically upward from the disk midplane the density falls off exponentially, and eventually the magnetic pressure will come to dominate the total energy in the disk "corona." Near the transition between theses two regimes, where the magnetic field and gas are in equipartition (plasma-β=1), the magnetic field becomes rigid. Thus, any material lifted off the disk surface and loaded onto the rigid magnetic field lines will be centrifugally accelerated along field lines as though they were "beads on a wire." The acceleration ceases when the dynamical energy of the flow, ρv^2, exceeds the magnetic energy. At this location, called the Alfvén surface (or radius) because it is where $v_{\rm w} = v_A$, the magnetic field is no longer rigid and will begin to wind up. This leads to the collimation of the wind by the magnetic hoop stress (Heyvaerts & Norman 1989).

In the regime where the magnetic field is rigid, it rotates with the angular velocity of its footpoint in the disk. As the disk material moves along the field line, its angular momentum will increase until it reaches the Alfvén radius, R_A. Therefore, the angular

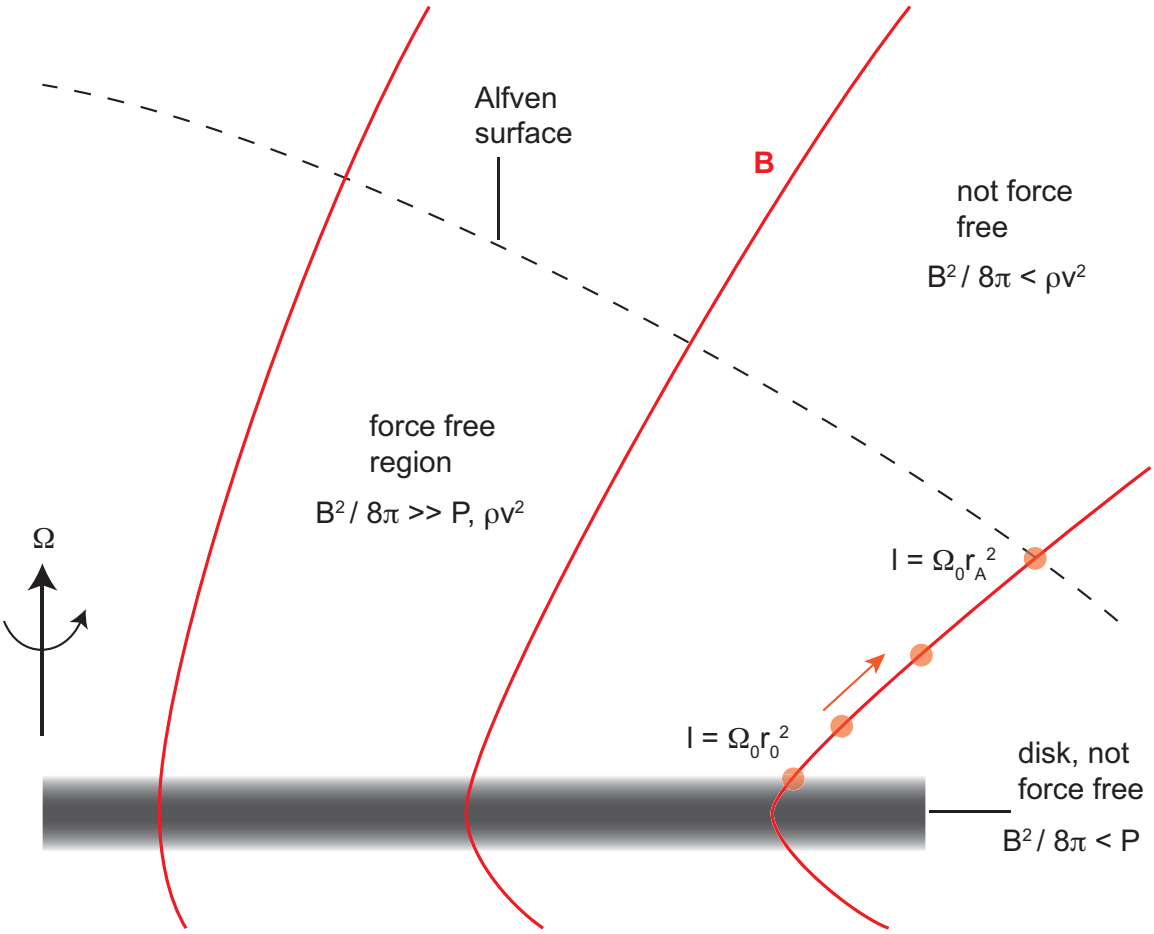

Fig. 1.7.— Illustration of the magnetocentrifugal disk wind. Figure 13 from Armitage (2015), adapted from Spruit (1996).

momentum that is extracted from the disk by the magnetic braking torque will be equal to the angular momentum of the wind at the Alfvén radius, or $\dot{L}_{\rm w} = \dot{M}_{\rm w} R_A^2 \Omega_0$, where Ω_0 is the angular velocity of the magnetic field footpoint at R_0. Since the angular momentum lost from the disk is equal to that lost in the wind, the mass accretion rate through the disk must be $\dot{M}_{\rm acc} = 2\dot{L}_{\rm w}/(R_0^2\Omega_0)$. Therefore, the ratio of the mass loss rate of the MCW to the mass accretion rate in the disk is

$$\frac{\dot{M}_{\rm w}}{\dot{M}_{\rm acc}} = \frac{1}{2}\left(\frac{R_0}{R_A}\right)^2. \tag{1.9}$$

The ratio R_A/R_0 depends on many factors, including the magnetic field strength and mass loading of the wind. A value of approximately $R_A/R_0 = 3$ is required to match with observations where the outflow rate is often estimated to be 10% of the accretion rate (Konigl & Pudritz 2000). The mass accretion rate can also be estimated directly from the magnetic torque exerted on the disk, which is approximately (Bai & Goodman 2009)

$$\dot{M}_{\rm acc}(R) \approx \frac{R B_z B_\phi}{\Omega_K}. \tag{1.10}$$

In addition to the MCW, another type of magnetic disk wind – called the "magnetic tower" (Lynden-Bell 1996, 2003) – is driven by the toroidal magnetic pressure gradient from a highly wound cylinder of toroidal magnetic field loops (the height of the cylinder increases for every turn of the field). This type of launching mechanism would become more important when the magnetic field is dynamically less important, so instead of having a rigid magnetic field to launch gas centrifugally the weak magnetic field is instead wound up by the rotating disk. In this scenario the Alfvén radius will be much closer to the disk surface, increasing the expected mass outflow rate in the wind.

Finally, it is thought that disk material can be accelerated along open magnetic field lines emanating from the disk corotation radius (where the Keplerian angular velocity of the disk is equal to the angular velocity of the star, which is close to the radius where the inner disk is truncated by the stellar magnetosphere). This type of outflow is called the "x-wind" (Shu et al. 1994, 2000). Although the x-wind model is not exclusive of other disk wind models that are launched over a range of disk radii, it has been invoked to explain the fast and narrow jets that are launched close to the central source. Current observational evidence suggests that disk winds are likely launched from disk radii larger than the corotation radius, as the conserved quantities of MCW winds can be used to link the toroidal and poloidal velocities of the outflow at large distances back to the launching radius at the disk surface (Anderson et al. 2003).

1.2.1.2 Magnetorotational instability

As described in the previous section, the molecular viscosity is too small to provide adequate angular momentum transport in circumstellar disks. Alternative viscosities are needed. One possibility is the effective viscosity associated with turbulence, which is in principle possible given the large disk Reynolds numbers, Re $\sim hc_s/\nu \sim 10^{10}$. However, there is no obvious source for generating turbulence in the absence of a magnetic field. Keplerian disks are known to be hydrodynamically stable according to the Rayleigh criterion for stability, because their angular momentum increases radially outward,

$$\frac{\partial\left(R^2\Omega\right)}{\partial R} > 0. \tag{1.11}$$

The situation is drastically different in the presence of a weak vertical magnetic field. Originally realized by Velikhov (1959) and Chandrasekhar (1960, 1961), but later

reinterpreted for its importance in accretion disks by Balbus & Hawley (1991), the magnetorotational instability develops when

$$\frac{d\Omega^2}{dR} < 0. \tag{1.12}$$

This criterion is satisfied in astrophysical disks where $\Omega = \Omega_K$ increases with decreasing radius. Remarkably, this criterion does not depend on the strength of the magnetic field. The maximum growth rate of the instability is $\frac{3}{4}\Omega$, with the wavelength of the fastest growing mode being

$$\lambda_{\rm MRI} = \frac{4}{\sqrt{15}}\frac{2\pi v_A}{\Omega}. \tag{1.13}$$

The instability is shut off when the vertical magnetic field is strong, i.e., when the magnetic field strength is large enough to be dynamically important ($\beta \geq 1$). In other words, the disk is stable to the MRI if the magnetic field is large enough that even the shortest unstable wavelength $\lambda_{\rm crit}$ (perturbations with shorter wavelengths are stablized by magnetic tension) exceeds the vertical thickness of the disk, i.e., $\lambda_{\rm crit} > 2h$ (Hawley et al. 2015).

The physical nature of the MRI can be visualized by considering two rotating masses along a single vertical magnetic field line. The masses are separated by half a wavelength of the perturbed MRI mode in the vertical direction at radius r_0 (see the first box of Fig. 1.8). The upper mass is now displaced inward towards the $-r$ direction and the lower mass in the $+r$ direction. The inner (outer) mass will now be rotating faster (slower) than the Keplerian rotation speed at r_0 (second box of Fig. 1.8) and the two masses will drift relative to each other in the azimuthal ϕ direction (the direction of rotation). The magnetic tension force associated with the now-distorted vertical magnetic field points in the $-\phi$ direction for the inner mass

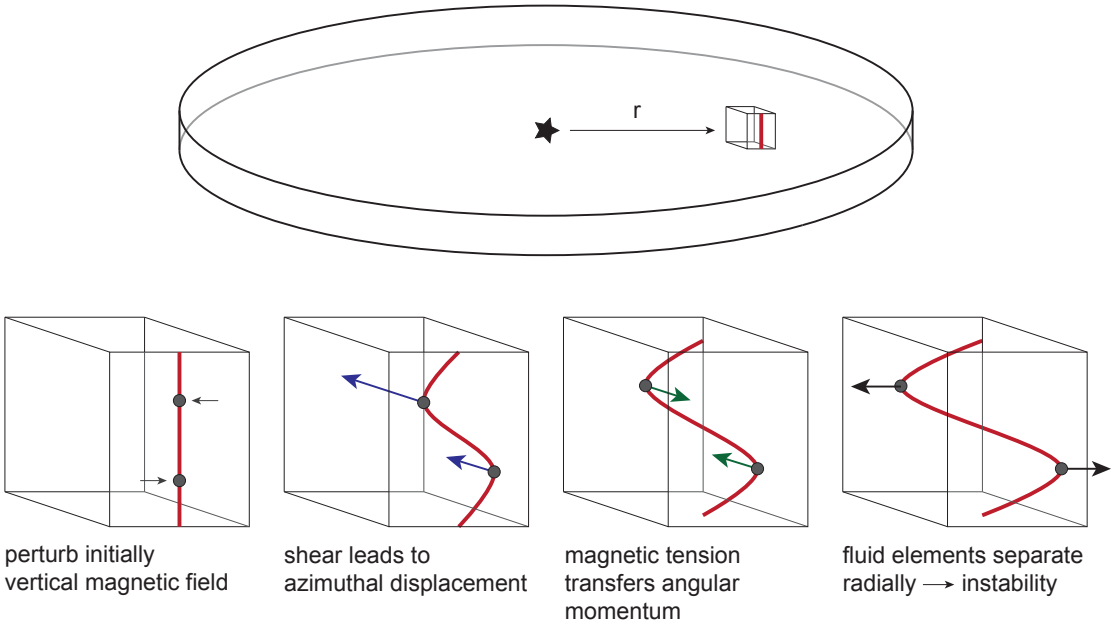

Fig. 1.8.— Illustration of the magnetorotational instability. Figure 18 from Armitage (2015).

and the $+\phi$ direction for the outer mass (third box of Fig. 1.8). Thus, the magnetic tension force will remove angular momentum from the inner mass, forcing it to move further inward to a smaller radius consistent with its new angular momentum. The angular momentum extracted from the inner mass is transferred to the outer mass, which will move further outward (final box of Fig. 1.8). The process repeats itself in a runaway fashion until it is saturated by non-linear effects (Balbus & Hawley 1998; Hawley et al. 2015).

1.2.2 Substructure formation

A number of mechanisms have been proposed to explain the presence of rings and gaps in protoplanetary disks. The mechanism that has received most attention to date invokes planet-disk interactions. Such interactions were studied well before protoplanetary disks were imaged or exoplanets were observed (Goldreich & Tremaine 1980). Planets in disks drive spiral density waves at both the inner and outer Lindblad resonances. The inner (outer) density wave leads (trails) the planet inward (outward) of its orbital radius. The gravitational attraction of the planet to the inner (outer) spiral density waves exerts a positive (negative) torque on the planet. The non-zero net torque causes the planet to drift or *migrate* relative to the disk material at a rate and direction that largely depend on the physical properties of the disk. If the planet is massive enough, however, the angular momentum imparted to the spiral density waves is deposited locally in the disk, leading to the clearing of a gap as the disk material is moved away from the planet's orbital radius. The size and depth of the gap depends on the planet's mass and the disk model parameters, and the planet will migrate inward on the viscous accretion timescale (type II migration; Lin & Papaloizou 1986; see also Kley & Nelson 2012 for a review). It is thus natural to

postulate that the concentric rings and gaps in disks observed by ALMA are formed in the presence of planets (e.g., for the case of HL Tau, see Dong et al. 2015; Dipierro et al. 2015). It has now been shown that multiple concentric disk gaps can be opened by the presence of one single super-Earth of mass ~ 10 $M_\oplus$ (Dong et al. 2017; Bae et al. 2017).

There are non-planet mechanisms for gap opening as well. One involves the condensation of abundant volatile species, especially H_2O, which increases the mass of solids near the condensation front or snow line (Zhang et al. 2015). Just outside the snow line, the higher surface density of the icy grains speeds up the growth of the grains to larger "pebble" sizes. Such pebbles do not radiate efficiently, making the condensation front relatively dark, and thus gap-like. Indeed, the prominent innermost gap at 13 au of the HL Tau disk (see Fig. 1.6) appears to coincide with the condensation front of the most abundant volatile species, H_2O, lending support to this mechanism. However, this mechanism cannot explain all of the gaps that have now been identified in many sources. For example, Sheehan & Eisner (2018) found three gaps in the disk of the Class I protostar GY 91 in the nearby rho Ophiuchus L1688 molecular cloud. Only the outermost gap roughly matches the freeze out region of N_2. There are no condensation fronts identified for the inner two gaps.

A related mechanism for forming rings (instead of gaps) was proposed by Okuzumi et al. (2016), who showed that the process of dust grain "sintering" just below the sublimation temperature (just outside the snow line) produces brittle grains that fragment more readily[5]. The sintered grains therefore have smaller sizes, which enable them to be better coupled to the gas and have a slower radial drift compared to the larger grains; the slower radial drift leads to a pile up of the grains outside the

[5]Sintering is the processes by which dust grains are fused together at thick "necks" even at temperatures that are lower than the sublimation temperatures of the grains or their icy mantles. It is one of the most important processes in making ceramics.

condensation front (or snow line), yielding a bright ring. This mechanism appears consistent with the rings observed in the HL Tau disk. However, it cannot explain all observed rings since not all of them are located right outside condensation fronts of major volatile species.

The mechanisms most relevant to this thesis are those relying on the magnetic fields in the disk to form substructure. These include abrupt changes in the effective viscosity in magnetized disks at the boundaries between the well-ionized MRI-active zones and "dead zones" where the ionization level is too low for the MRI to be active (Flock et al. 2015; Ruge et al. 2016), and the so-called "zonal flows" formed from magnetic self-organization (Béthune et al. 2016, 2017). These mechanisms will be described in more detail later in Sections 2.5.1 and 3.5.1, where we will contrast them with the MHD mechanisms of ring and gap formation proposed in this thesis.

1.3 Magnetohydrodynamics

1.3.1 Ideal MHD

As the name suggests, magnetohydrodynamics (MHD) describes the dynamics of magnetized fluids. Thus, the equations are the combination of the conservation laws of fluid dynamics with Maxwell's equations. The fluid equations are applicable to systems where we can define physical quantities over some length scale that is much larger than the mean free path of any one particle, yet still smaller than the typical macroscopic scales of the entire system. Many astrophysical fluids of interest are sufficiently ionized and, therefore, highly conductive. The ideal MHD approximation is that the fluid is a perfect conductor and that the fluid flow velocities are much less than the speed of light. These assumptions imply that the electric field vanishes in a

frame comoving with the fluid, $\boldsymbol{E}' = 0$. Therefore, upon Lorentz transformation, the electric field as measured by an observer is

$$\boldsymbol{E} = -\frac{1}{c}\boldsymbol{v} \times \boldsymbol{B}, \tag{1.14}$$

while the magnetic field is equivalent in both the comoving and the inertial frame, $\boldsymbol{B'} = \boldsymbol{B}$. Substituting Eq. 1.14 into Maxwell's equation (the modified Faraday's law of induction) yields the induction equation of ideal MHD,

$$\frac{\partial \boldsymbol{B}}{\partial t} = \nabla \times (\boldsymbol{v} \times \boldsymbol{B}) \,. \tag{1.15}$$

Since the displacement current, $\partial \boldsymbol{E}/\partial t$, of Maxwell's modified Ampère's law is of order $(v/c)^2$ compared to the curl of the magnetic field, we get that the electric current density is

$$\boldsymbol{J} = \frac{c}{4\pi} \nabla \times \boldsymbol{B}. \tag{1.16}$$

This is to say that the only "source" for magnetic fields in ideal MHD are the currents. Taking the divergence of Eq. 1.16 yields $\nabla \cdot \boldsymbol{J} = 0$, i.e., currents in MHD have no sources or sinks. Finally, the Lorentz force per unit volume is

$$\boldsymbol{F}_L = \frac{1}{c}\boldsymbol{J} \times \boldsymbol{B} = \frac{1}{4\pi} (\nabla \times \boldsymbol{B}) \times \boldsymbol{B}. \tag{1.17}$$

Note that this can be rewritten using the triple vector product as

$$\boldsymbol{F}_L = \frac{1}{4\pi} (\boldsymbol{B} \cdot \nabla) \boldsymbol{B} - \frac{1}{8\pi} \nabla \left(|\boldsymbol{B}|^2 \right), \tag{1.18}$$

where the first term on the right hand side is the magnetic tension force and the second term is the force from the gradient of the magnetic pressure, $P_B = B^2/8\pi$.

Combing the above equations with the mass and momentum conservation equations of fluid mechanics gives the fundamental equations of ideal MHD: the mass continuity equation

$$\frac{\partial \rho}{\partial t} + \nabla \cdot (\rho \boldsymbol{v}) = 0; \tag{1.19}$$

the equation of motion

$$\rho \frac{\partial \boldsymbol{v}}{\partial t} + \rho \left(\boldsymbol{v} \cdot \nabla \right) \boldsymbol{v} = -\nabla P + \frac{1}{c} \, \boldsymbol{J} \times \boldsymbol{B} - \rho \nabla \Phi_g, \tag{1.20}$$

where Φ_g is the gravitational potential; and the magnetic induction equation

$$\frac{\partial \boldsymbol{B}}{\partial t} = \nabla \times \left(\boldsymbol{v} \times \boldsymbol{B} \right). \tag{1.21}$$

The electric current density, $\boldsymbol{J}$, is defined in Eq. 1.16. We also introduce the energy equation,

$$\frac{\partial e}{\partial t} + \nabla \cdot (e \boldsymbol{v}) = -P \nabla \cdot \boldsymbol{v}, \tag{1.22}$$

with internal energy $e = P/(\gamma - 1)$ and adiabatic index γ.

1.3.2 Non-ideal MHD

As mentioned in the previous section, many astrophysical systems are well ionized, such that they are nearly perfect conductors. However, the gas in circumstellar disks is only lightly ionized, and thus the assumptions of ideal MHD are not always valid. There are three specific non-ideal MHD effects that are important in protoplanetary disks: Ohmic resistivity, ambipolar diffusion, and the Hall effect. They are discussed

individually in the sections below.

1.3.2.1 Ohmic resistivity

First, we will discuss Ohmic resistivity or dissipation. If we assume that the fluid has a finite electrical conductivity, σ, then in the fluid frame the electric field is non-zero and will follow a linear Ohm's law, $\boldsymbol{J}' = \sigma \boldsymbol{E}'$. Just as the magnetic field is the same in both the comoving and inertial frames, so is the electric current density, $\boldsymbol{J}' = \boldsymbol{J}$. Therefore,

$$\frac{\boldsymbol{J}}{\sigma} = \boldsymbol{E}' = \boldsymbol{E} + \frac{1}{c}\boldsymbol{v} \times \boldsymbol{B}. \tag{1.23}$$

With the definition of the current (Eq. 1.16), the induction equation will now become

$$\frac{\partial \boldsymbol{B}}{\partial t} = \nabla \times \left[\boldsymbol{v} \times \boldsymbol{B} - \eta_O \nabla \times \boldsymbol{B}\right], \tag{1.24}$$

where we define the magnetic or Ohmic diffusivity as $\eta_O \equiv \frac{c^2}{4\pi\sigma}$ with units of cm^2 s^{-1}. The name "magnetic diffusion" is appropriate because if η_O is constant in space, the second term on the right takes the form of the diffusion equation, where $\partial B/\partial t \propto \eta_O \nabla^2 B$. The introduction of this term in the magnetic induction equation means that the idea of "magnetic flux-freezing" no longer applies, i.e., the magnetic field is not directly tied to the fluid elements and the gas can diffuse through the magnetic field. The magnetic diffusivity can be estimated numerically as (Blaes & Balbus 1994)

$$\eta_O = 230 \text{ cm}^2 \text{ s}^{-1} \left(\frac{n_e}{n}\right)^{-1} \left(\frac{T}{\text{K}}\right)^{1/2} \tag{1.25}$$

where $x_e \equiv n_e/n$ is the ionization fraction. Ohmic dissipation dominates when neither ions nor electrons are well tied to the magnetic field.

1.3.2.2 Ambipolar diffusion

In the opposite limit where both ions and electrons are well tied to the magnetic field, the magnetic field can still slip through the bulk neutral material through the so-called "ambipolar diffusion." This is because the magnetic forces act directly only on charged particles, and these forces are transmitted to the bulk neutral material through a frictional (or drag) force between the charged particles and the neutrals. In particular, the drag force exerted by the ions on the neutrals is

$$\boldsymbol{F}_d = \gamma \rho \rho_i (\boldsymbol{v_i} - \boldsymbol{v}), \tag{1.26}$$

where the subscript i denotes the ion species and $\gamma = \langle \sigma v \rangle_i / (m + m_i)$ is the frictional drag coefficient with units of cm^3 g^{-1} s^{-1}. The difference $\boldsymbol{v_i} - \boldsymbol{v}$ is the drift velocity between the ions (and the magnetic field tied to them) and the neutrals. This drag force is equal to the Lorentz force, $\boldsymbol{F}_L$, that is transmitted to the neutrals through the ion-neutral collisions (Shu 1992). The ideal induction equation can now be written with the neutral velocity replaced by the ion velocity.

$$\frac{\partial \boldsymbol{B}}{\partial t} = \nabla \times (\boldsymbol{v_i} \times \boldsymbol{B}) \,. \tag{1.27}$$

Replacing $\boldsymbol{v_i}$ with the drag in Eq. 1.26 set equal to the Lorentz force gives

$$\frac{\partial \boldsymbol{B}}{\partial t} = \nabla \times \left[\boldsymbol{v} \times \boldsymbol{B} + \frac{(\boldsymbol{J} \times \boldsymbol{B}) \times \boldsymbol{B}}{c \gamma \rho \rho_i} \right]. \tag{1.28}$$

It is common to rewrite this in terms of an equivalent ambipolar diffusion coefficient,

$$\eta_A = \frac{B^2}{4\pi \gamma \rho \rho_i}, \tag{1.29}$$

such that the induction equation can be written, including the Ohmic term, as

$$\frac{\partial \boldsymbol{B}}{\partial t} = \nabla \times (\boldsymbol{v} \times \boldsymbol{B}) - \frac{4\pi}{c} \nabla \times (\eta_O \boldsymbol{J} + \eta_A \boldsymbol{J}_\perp), \tag{1.30}$$

where $\boldsymbol{J}_\perp = -(\boldsymbol{J} \times \boldsymbol{B}) \times \boldsymbol{B}/B^2$ is the component of the current that is perpendicular to the magnetic field.

In accretion disks, the magnitude of the ion density, and therefore the ion-neutral drag force $\boldsymbol{F_d}$, can be quantified through the dimensionless ambipolar Elsasser number[6] (Chiang & Murray-Clay 2007; Perez-Becker & Chiang 2011b; Bai & Stone 2011),

$$\Lambda = \frac{\gamma \rho_i}{\Omega} = \frac{v_A^2}{\eta_A \Omega}, \tag{1.31}$$

where $v_A = B/\sqrt{4\pi\rho}$ is the Alfvén velocity and Ω is the angular frequency of the disk rotation. Physically, the Elsasser number is the collision frequency (normalized to the Keplerian orbital frequency) of a neutral particle in a sea of ions having density ρ_i. For example, the Elsasser number will be unity when the neutral particle collides with ions 2π times in one orbital period. As the neutral-ion collision frequency increases to infinity, so does the Elsasser number, and the bulk neutral medium becomes perfectly coupled to the ions/magnetic field (i.e., the ideal MHD limit). Similarly, as the Elsasser number drops to zero, the neutrals and ions no longer collide; the neutrals are entirely decoupled from the magnetic field.

[6]The Ohmic Elsasser number would be $\Lambda_O = v_A^2/(\eta_O \Omega)$.

1.3.2.3 The Hall effect

When electrons are well tied to the magnetic field but ions are not[7], the Hall effect becomes important. Although the Hall effect is not included in the simulations in this thesis, we will briefly describe it here for completeness. For magnetic fields well tied to the electrons, the induction equation in Eq. 1.21 can be written with the neutral velocity replaced by the electron velocity, $\boldsymbol{v_e}$, so that

$$\frac{\partial \boldsymbol{B}}{\partial t} = \nabla \times (\boldsymbol{v_e} \times \boldsymbol{B}) \,. \tag{1.32}$$

The electron velocity can be decomposed into the combination of the neutral velocity and the Hall and ambipolar drift velocities, $\boldsymbol{v_e} = \boldsymbol{v} + (\boldsymbol{v_e} - \boldsymbol{v_i}) + (\boldsymbol{v_i} - \boldsymbol{v})$ (Bai & Stone 2017), where the Hall drift velocity is

$$\boldsymbol{v_e} - \boldsymbol{v_i} = -\frac{\boldsymbol{J}}{en_e}, \tag{1.33}$$

and the ambipolar drift velocity $(\boldsymbol{v_i} - \boldsymbol{v})$ is given by eq. 1.26. Replacing the electron velocity with the combination involving two drift velocities gives the induction equation in the form (including the Ohmic term)

$$\frac{\partial \boldsymbol{B}}{\partial t} = \nabla \times (\boldsymbol{v} \times \boldsymbol{B}) - \frac{4\pi}{c} \nabla \times (\eta_O \boldsymbol{J} + \eta_H \boldsymbol{J} \times \boldsymbol{B} + \eta_A \boldsymbol{J}_\perp) \,, \tag{1.34}$$

where the Hall diffusivity is

$$\eta_H = \frac{cB}{4\pi e n_e}. \tag{1.35}$$

[7]Electrons are much lighter than ions and can gyrate around the field lines at a higher frequency, making them harder to knock off the field lines by collisions.

In summary, the induction equation of non-ideal MHD is derived from Maxwell's equation, $\partial_t \boldsymbol{B} = -c\nabla \times \boldsymbol{E}$, using a generalized Ohm's law, (Armitage 2015)

$$\boldsymbol{E} = -\frac{\boldsymbol{v} \times \boldsymbol{B}}{c} + \frac{4\pi\eta_O \boldsymbol{J}}{c} + \frac{\boldsymbol{J} \times \boldsymbol{B}}{en_e c} - \frac{(\boldsymbol{J} \times \boldsymbol{B}) \times \boldsymbol{B}}{c^2 \gamma \rho \rho_i}. \tag{1.36}$$

1.3.3 The Zeus code

In their simplest form, the equations of ideal MHD (Eq. 1.19-1.22) are a set of coupled partial differential equations. They can be solved numerically using the finite difference method. The equations are discretized on an Eulerian grid and evolved in time. The source terms are calculated at every grid cell and the transport terms are advected through the faces of the cell for all cells (in two or three dimensions). The numerical MHD code used in this thesis is from the ZEUS family of codes originally developed by Stone & Norman (1992a,b) and Stone et al. (1992). The MHD algorithm uses the method of constrained transport (CT, Evans & Hawley 1988), whereby the magnetic field transport is calculated using the loop integral of the electromotive force (EMF), defined as $\boldsymbol{\mathcal{E}} \equiv \boldsymbol{v} \times \boldsymbol{B}$, around the edges of the cell face.[8] As long as the "no magnetic monopole" condition is satisfied initially at $t = 0$, the CT method will ensure that $\nabla \cdot \boldsymbol{B} = 0$ for all later times. Although the algorithms of the ZEUS code are relatively simple compared to higher-order Godunov schemes, the ZEUS code is known throughout the computational astrophysics community for its speed, flexibility, and availability since its inception. It is certainly one of the most used and well-tested MHD codes in the field today (Clarke 2010).

Specifically, we use the ZeusTW code developed by Krasnopolsky et al. (2010), in spherical polar coordinates (r, θ, ϕ). The ZeusTW code is based on the ideal MHD

[8] Using Stokes' theorem, the induction equation, Eq. 1.21, can be rewritten in integral form as $\partial\Phi_B/\partial t = \oint_{\delta S} (\boldsymbol{v} \times \boldsymbol{B}) \cdot d\boldsymbol{\ell}$, where Φ_B is the magnetic flux through surface S.

code, ZEUS-3D (version 3.4; Clarke 1996, 2010). The ZeusTW code can treat all the non-ideal MHD effects. Of the three, only Ohmic resistivity and ambipolar diffusion are explored in this thesis. Ohmic resistivity is treated using the algorithm described in Fleming et al. (2000) and AD is implemented using the fully explicit method of Mac Low et al. (1995). This non-ideal MHD code has been used extensively for studies of disk formation out of lightly ionized, magnetized dense cores of molecular clouds with good success (e.g., Krasnopolsky et al. 2011; Li et al. 2011; Zhao et al. 2018).

Chapter 2

Axisymmetric resistive MHD simulations

This Chapter is adapted from Suriano et al. 2017, MNRAS, 468, 3850, with minimal modifications.

Abstract

Rings and gaps are being observed in an increasing number of disks around young stellar objects. We illustrate the formation of such radial structures through idealized, 2D (axisymmetric) resistive MHD simulations of coupled disk-wind systems threaded by a relatively weak poloidal magnetic field (plasma-$\beta \sim 10^3$). We find two distinct modes of accretion depending on the resistivity and field strength. A small resistivity or high field strength promotes the development of rapidly infalling 'avalanche accretion streams' in a vertically extended disk envelope that dominates the dynamics of the system, especially the mass accretion. The streams are suppressed in simulations with larger resistivities or lower field strengths, where most of the accretion instead

occurs through a laminar disk. In these simulations, the disk accretion is driven mainly by a slow wind that is typically accelerated by the pressure gradient from a predominantly toroidal magnetic field. Both wind-dominated and stream-dominated modes of accretion create prominent features in the surface density distribution of the disk, including rings and gaps, with a strong spatial variation of the magnetic flux relative to the mass. Regions with low mass-to-flux ratios accrete quickly, leading to the development of gaps, whereas regions with higher mass-to-flux ratios tend to accrete more slowly, allowing matter to accumulate and form dense rings. In some cases, avalanche accretion streams are observed to produce dense rings directly through continuous feeding. We discuss the implications of ring and gap formation driven by winds and streams on grain growth and planet formation.

2.1 Introduction

Disks around young stellar objects (YSOs) are the birthplaces of planets. Planet formation and evolution thus depend critically on the properties of these disks. Given the large number of super-Earths and mini-Neptunes discovered by *Kepler* at distances between ~ 0.1 and ~ 1 au from their host stars (Winn & Fabrycky 2015), there is strong motivation for studying the structure and evolution of the inner ($\lesssim 1$ au) parts of protostellar disks. This will be the focus of our investigation.

The inner circumstellar disk plays an important role in launching outflows. Jets and winds are ubiquitously observed in YSOs and have a long history of observational and theoretical study (see Frank et al. 2014 for a review and references therein). It is thought that such outflows are driven by rapidly rotating magnetic field lines, although where the outflow-driving field lines are anchored remains unclear. One school of thought posits that the field lines are trapped at the inner edge of the disk,

giving rise to so-called 'X-winds' (Shu et al. 2000). Another suggests that they are distributed over a more extended region of the inner disk, driving a 'disk wind' (Konigl & Pudritz 2000). Part of the outflow may also be attributed to an accretion-enhanced stellar wind (e.g., Matt & Pudritz 2008). Some evidence favoring disk winds comes from the observed gradients in the line-of-sight velocity measured across optical jets (e.g., Bacciotti et al. 2000) and molecular outflows (e.g., Launhardt et al. 2009). If such gradients arise from rotation in a magnetocentrifugal wind (Blandford & Payne 1982), the implied outflow launching region would extend to au scales or larger (e.g., Anderson et al. 2003; Ray et al. 2007; Bjerkeli et al. 2016; however, see Lee et al., *submitted*, for SiO observations of HH 212 that provide evidence for X-winds). The outflow would carry angular momentum away from the disk in a launching region that is directly relevant to the formation of the terrestrial planets in the Solar system and a considerable fraction of the exoplanets discovered by *Kepler*.

The idea of magnetic wind-driven disk evolution has been discussed in the literature for a long time (e.g., Pudritz & Norman 1983; Wardle & Koenigl 1993; Combet & Ferreira 2008; Königl et al. 2010; Bai 2016; Suzuki et al. 2016, and references therein). One way to quantify the effects that winds have on disks is to construct global, coupled wind-disk solutions to the MHD equations. Many of the early investigations along this line adopted simplifying self-similarity assumptions (e.g., Wardle & Koenigl 1993; Li 1995; Ferreira 1997; Salmeron et al. 2011). These semi-analytic treatments have been important for illuminating the basic mechanics of the coupled system, including how a small fraction of the accreting material is peeled off of the disk surface and ejected along the rapidly rotating field lines as a wind, how the wind removes angular momentum from the disk and drives it to accrete, and how the accretion and ejection processes depend on the non-ideal MHD effects (Ohmic dissipation,

ambipolar diffusion, and the Hall effect) that are expected to occur in the lightly ionized YSO disks. Self-similar solutions require that all physical quantities, such as the density, magnetic field strength, and the coefficients for non-ideal MHD effects, must scale with the radius as power-laws with specific indices. This requirement limits the applicability of the self-similar solutions to realistic systems. We seek to relax the self-similarity ansatz through a series of MHD simulations that incorporate non-ideal effects.

Simulations of coupled wind-disk systems have been carried out by several groups (e.g., Kato et al. 2002; Casse & Keppens 2002, 2004; Zanni et al. 2007; Murphy et al. 2010; Lii et al. 2012; Sheikhnezami et al. 2012; Čemeljić et al. 2013; Stepanovs & Fendt 2014, 2016). These simulations confirmed and extended the earlier semi-analytic results, finding self-consistent wind-disk solutions for a wide range of disk masses and magnetic field distributions. However, the focus of such simulations has typically been on the launching of outflows from the disk and on their propagation to large distances. We are thus motivated to start a long-term program to investigate the wind-disk system that will eventually include all three non-ideal MHD effects using the ZeusTW MHD code (Krasnopolsky et al. 2011; Li et al. 2011), focusing in particular the structure of the disk in such a system. As a first step, we start with the simplest case of a resistive wind-disk system under the assumptions of axisymmetry (2D) and reflection symmetry across the disk midplane.

Resistive disk winds under such an idealized geometry have been studied by several groups, especially Stepanovs & Fendt (2016), who were able to determine wind properties (such as its mass loss rate, energy, and angular momentum) for disks with a wide range of magnetic field strengths. The emphasis of such work has been on quasi-steady state wind-disk solutions, which enable the computation of several well-

known conserved quantities along each magnetic flux surface (e.g., Spruit 2010) that can be checked against the semi-analytic solutions. However, a steady state can only be obtained when outward diffusion of the magnetic field in the disk is balanced by inward advection of the field, which occurs only under rather restrictive conditions for the prescribed magnetic diffusivity. Under more general conditions, the magnetic winds remain highly variable, driving non-steady disk accretion even for 2D (axisymmetric) systems; they are likely to be exacerbated in 3D simulations. Such non-steady state phenomena are the focus of this investigation. We find that the disk structure can be completely reshaped from its initial state by even a weak initial magnetic field, often with rapidly accreting streams developing near the disk surface and rings and gaps developing near the disk midplane.

The accretion streams are a form of the magnetorotational instability (MRI) channel flows (Balbus & Hawley 1991; Goodman & Xu 1994). They are the result of the runaway magnetic braking of an infalling stream, which is linked to more slowly rotating material at larger radii. We term them 'avalanche accretion streams', motivated by the work of Kudoh et al. (1998) who find similar structures in ideal MHD simulations of thick AGN disks (see also Stone & Norman 1994; Matsumoto et al. 1996; Kudoh et al. 2002; Beckwith et al. 2009). We find that the accretion streams become more numerous and more important dynamically as the disk material becomes better coupled to the magnetic field. Their rapid formation and disruption forms a thick envelope of chaotic infall and outflow motions above the disk, which is intimately related to the so-called 'coronal accretion' found recently by Zhu & Stone (2018) in global (3D) ideal MHD simulations of thin disks with net vertical magnetic flux (see also Beckwith et al. 2009). These investigations highlight the possible importance of vigorous accretion in a vertically extended structure outside the dense disk on disk

evolution.

The formation of rings and gaps on sub-au scales strongly influences how dust grains are trapped and thus affects how the grains grow into planetesimals and ultimately planets. Although our simulations are limited to the inner ($\sim 0.01 - 1$ au scale) disk, the same mechanism of ring and gap formation through variable disk winds and avalanche accretion streams should operate at larger radii as well, where rings and gaps have now been observed in a number of disks (ALMA Partnership et al. 2015; Andrews et al. 2016; Zhang et al. 2016; Isella et al. 2016). The 2D simulations presented in this study serve as an illustration of these generic mechanisms, although they are likely to generate rings and gaps more easily than 3D simulations, because of the assumed axisymmetry. Nevertheless, they provide a starting point for future explorations that will include more detailed disk microphysics and less restrictive geometry.

The rest of the Chapter is organized as follows. In Section 2.2, we describe the simulation setup. In Section 2.3, we present the results of a reference simulation. In Section 2.4, we analyze how the simulation outcome depends on three key dimensionless parameters that control the disk magnetic field strength, resistivity and disk thickness. In Section 2.5, we discuss this work in the context of previous studies and examine its implications. The results are summarized in Section 2.6.

2.2 Problem setup

2.2.1 MHD equations

We use the ZeusTW code (Krasnopolsky et al. 2010) to solve the time-dependent, resistive magnetohydrodynamic (MHD) equations in axisymmetric spherical coordi-

nates (r, θ, ϕ). The equations solved are as follows:

$$\frac{\partial \rho}{\partial t} + \nabla \cdot (\rho \boldsymbol{v}) = 0, \tag{2.1}$$

$$\rho \frac{\partial \boldsymbol{v}}{\partial t} + \rho \left(\boldsymbol{v} \cdot \nabla \right) \boldsymbol{v} = -\nabla p + \boldsymbol{j} \times \boldsymbol{B}/c - \rho \nabla \Phi_g, \tag{2.2}$$

$$\frac{\partial \boldsymbol{B}}{\partial t} = \nabla \times \left(\boldsymbol{v} \times \boldsymbol{B} - \eta \nabla \times \boldsymbol{B} \right), \tag{2.3}$$

$$\frac{\partial e}{\partial t} + \nabla \cdot (e \boldsymbol{v}) = -p \nabla \cdot \boldsymbol{v}. \tag{2.4}$$

The current density is $\boldsymbol{j} = (c/4\pi) \nabla \times \boldsymbol{B}$, the internal energy is $e = p/(\gamma - 1)$, and η is the resistivity. The remaining parameters have their usual definitions. When referring to cylindrical coordinates, we will use the notation (R, ϕ, z) such that $R = r \sin\theta$ and $z = r \cos\theta$.

2.2.2 Initial conditions

The simulation domain is separated into two regions: a thin, cold, rotating disk orbiting a 1 $M_\odot$ central source at the grid origin and a stationary, hot corona above the disk. We choose $\gamma = 1.01$ so that the disk and corona regions are locally isothermal.

2.2.2.1 Disk

The geometrically thin disk is characterized by the dimensionless parameter $\epsilon = h/r = c_s/v_K \ll 1$, where h is the disk scale height, c_s is the sound speed, and v_K is the Keplerian speed. The disk is limited to the equatorial region where the polar

angle $\theta \in [\pi/2 - \theta_0, \pi/2]$, with disk (half) opening angle set to $\theta_0 = \arctan(2\epsilon)$. The disk density takes the form of a radial power law multiplied by a Gaussian function of $z/r = \cos\theta$,

$$\rho_d(r,\theta) = \rho_0 \left(\frac{r}{r_0}\right)^{-\alpha} \exp\left(-\frac{\cos^2\theta}{2\epsilon^2}\right), \tag{2.5}$$

as dictated by hydrostatic balance. The subscript '0' refers to values on the disk midplane at the inner radial boundary. For all simulations shown this paper, we use $\alpha = 3/2$. The choice of power-law exponent is consistent with sub-millimeter observations of Class II sources that find surface density power-law exponents of $0.4 - 1.1$ (Andrews et al. 2010). The disk pressure is set as

$$p_d(r,\theta) = \rho_d c_s^2, \tag{2.6}$$

with $c_s = \epsilon v_K$. The radial pressure gradient causes the equilibrium rotational velocity v_ϕ to be slightly sub-Keplerian as

$$v_\phi = v_K \sqrt{1 - (1+\alpha)\epsilon^2}. \tag{2.7}$$

2.2.2.2 Corona

We require that the hydrostatic corona is initially in pressure balance with the disk surface. This constraint sets the density drop from the disk surface to the corona as $(1+\alpha)\epsilon^2$. Therefore, the coronal density and pressure are

$$\rho_c(r) = \rho_0 \epsilon^2 (1+\alpha) \exp\left[-\frac{\cos^2\theta_0}{2\epsilon^2}\right] \left(\frac{r}{r_0}\right)^{-\alpha} = \rho_{c,0} \left(\frac{r}{r_0}\right)^{-\alpha}, \tag{2.8}$$

$$p_c(r) = \rho_c v_K^2/(1+\alpha). \tag{2.9}$$

2.2.2.3 Magnetic field

To ensure that the magnetic field is divergence-free initially, we set the magnetic field components using the magnetic flux function Ψ as in Zanni et al. (2007),

$$\Psi(r,\theta) = \frac{4}{3} r_0^2 B_{\rm p,0} \left(\frac{r\sin\theta}{r_0}\right)^{3/4} \frac{m^{5/4}}{\left(m^2+\cot^2\theta\right)^{5/8}}, \tag{2.10}$$

where the $B_{\rm p,0}$ is the poloidal field strength on the midplane at r_0, and the parameter m controls the bending of the field. Since varying m from 0.1 to 1 has little effect on the long-term disk or wind magnetic field structure (Stepanovs & Fendt 2014), we use $m = 0.5$ for all simulations presented in this work. The initial magnetic field components are then calculated as

$$B_r = \frac{1}{r^2\sin\theta}\frac{\partial\Psi}{\partial\theta}, \tag{2.11}$$

$$B_\theta = -\frac{1}{r\sin\theta}\frac{\partial\Psi}{\partial r}. \tag{2.12}$$

2.2.2.4 Resistivity

For illustrative purposes in this initial study, we adopt a spatially and temporally constant resistivity $\eta(\boldsymbol{r},t) = \eta$; more refined treatments, including one based on detailed ionization calculation, are postponed to future investigations. To quantify the relative importance of the prescribed resistivity, we define a dimensionless magnetic diffusivity parameter $D \equiv \eta/(hc_s)$ (where h is the disk scale height and c_s is the disk sound speed) as in Li (1995), similar to the well-known α-parameter of Shakura & Sunyaev (1973). This diffusivity parameter is initially proportional to $r^{-1/2}$ with $D_0 = 0.16$ at the inner edge of the disk in the reference simulation. This implementation differs from the resistivity profile prescribed in other disk wind simulations where

$\eta \propto h v_A$ (v_A is the Alfvén speed) inside the disk and $\eta = 0$ outside (e.g., Stepanovs & Fendt 2014).

2.2.3 Grid

The equations are solved for $r \in [0.02, 10]$ au and $\theta \in [0, \pi/2]$, where $\theta = 0$ corresponds to the polar axis and $\theta = \pi/2$ to the disk midplane. We choose $r_0 = 0.02$ au ~ 4 $R_\odot$ as the inner radius because it is approximately the inner radius of a protostellar disk truncated by the magnetosphere of a classical T Tauri star (Hartmann et al. 2016). It yields an inner orbital period $t_0 \approx 1$ d. For this initial study, we focus on only one hemisphere and assume that the system has reflection symmetry across the disk midplane. This assumption will be relaxed in future investigations. In the radial direction, a 'ratioed' grid is used, such that dr_{i+1}/dr_i is constant and $r_{i+1} = r_i + dr_i$. The grid spacing at the inner edge is set such that $dr_0 = 2.3 r_0 d\theta$. The grid is uniform in the θ-coordinate for most simulations presented in the work, with a resolution of $n_r \times n_\theta = 400 \times 360$. This results in 32 grid cells from the disk midplane to surface (at two disk scale heights) in the reference run.

In the simulation called x2-grid, the θ-grid is separated into two regions: a uniform grid in the disk region ($\theta \in [\pi/3, \pi/2]$), and a ratioed grid in the corona ($\theta \in [0, \pi/3]$), with $d\theta$ matched at the boundary and increasing towards the polar axis. The uniform region contains 240 cells, thereby decreasing $d\theta$ by a factor of two compared to the reference run. The non-uniform grid section has 120 cells, so the total number of cells in the θ-direction remains 360. We decrease the value of dr_0 in order to have the ratio of $\frac{dr_0}{r_0 d\theta}$ be the same in all runs. The value of $d\theta$ increases to 1.3° at the polar axis for this ratioed grid.

2.2.4 Boundary conditions

The inner radial boundary is separated into two regions. For $\theta \in [0, \pi/2 - \arctan(4\epsilon)]$, mass is injected into the simulation domain with $\rho = \rho_{c,0}$ and $v = 10$ km s^{-1} (Krasnopolsky et al. 1999). The injection boundary is used to lower the Alfv́en speed in polar region close to the inner boundary and thereby increase the simulation time step, as the region would quickly be evacuated by gravitational infall if the standard outflow boundary was used. The total mass that enters the simulation domain through the inner boundary is small compared to both the initial mass in the simulation and the mass that is eventually carried through the outer boundary via the disk wind. It thus has little influence on the dynamics of the simulation. The remaining section of the inner radial boundary, $\theta > \pi/2 - \arctan(4\epsilon)$, and the outer radial boundary both use the standard outflow condition, as usual in Zeus codes.

The reflection boundary condition is used on the polar axis ($\theta = 0$) and the equatorial plane ($\theta = \pi/2$). The ϕ-component of the magnetic field is set to zero on the polar axis. The assumed reflection symmetry across the midplane ($\theta = \pi/2$) demands that $B_\phi = 0$ at this boundary. We also set B_ϕ to vanish on the inner radial boundary because it is not rotating.

2.3 Reference model

We start by discussing the result of a 'reference' simulation. It is used to highlight the salient features of the coupled wind-disk system, and serves as a benchmark against which other simulations with different parameters will be compared in Section 2.4. Of the parameters that will be changed in Section 2.4, the reference model has $\epsilon = 0.05$, an initial magnetic field strength characterized by plasma-β of 10^3 on the disk

midplane (corresponding to 0.27 G at 1 au), and a dimensionless magnetic diffusivity parameter of $D_0 = 0.16$. This simulation runs for 1820 inner orbital periods ($\sim$ 5 yr). Fig. 2.1 shows the initial conditions for the system and snapshots at three representative times.

2.3.1 Global evolution

The initially weak poloidal magnetic field is wound up by differential rotation between the (nearly) Keplerian disk and the static corona, which inflates a bubble of strong toroidal magnetic field that expands outward against the coronal material. This winding operates fastest near the inner edge of the disk, where the orbital period is the shortest. As a result, the outflow propagates with the highest speed near the polar axis. By $t = 150t_0$ (Fig. 2.1(b)), the outflow has reached the outer edge of the computation domain along the axis, but remains confined by the initial coronal material away from the polar region. By $t = 1200t_0$ (Fig. 2.1(c)), most of the initial coronal material has been completely swept out of the computational domain. Beyond this time, the effects of the initial corona on the coupled wind-disk system should be relatively small, and for the inner part of the system (where much of our analysis is focused; see Section 2.3.3.3 below), the initial corona ceases to be important at an even earlier time. The wind-disk system shows large spatial and temporal variability throughout the simulation. This variability is reflected in Fig. 2.1(d) at $t = 1800t_0$; its appearance is broadly similar to that in panel (c), but there are important differences such as the appearance of low-density wind 'channels' that are more prominent in the outflow of the former than the latter. The variability of the outflow is intimately tied to the structures that develop in the disk.

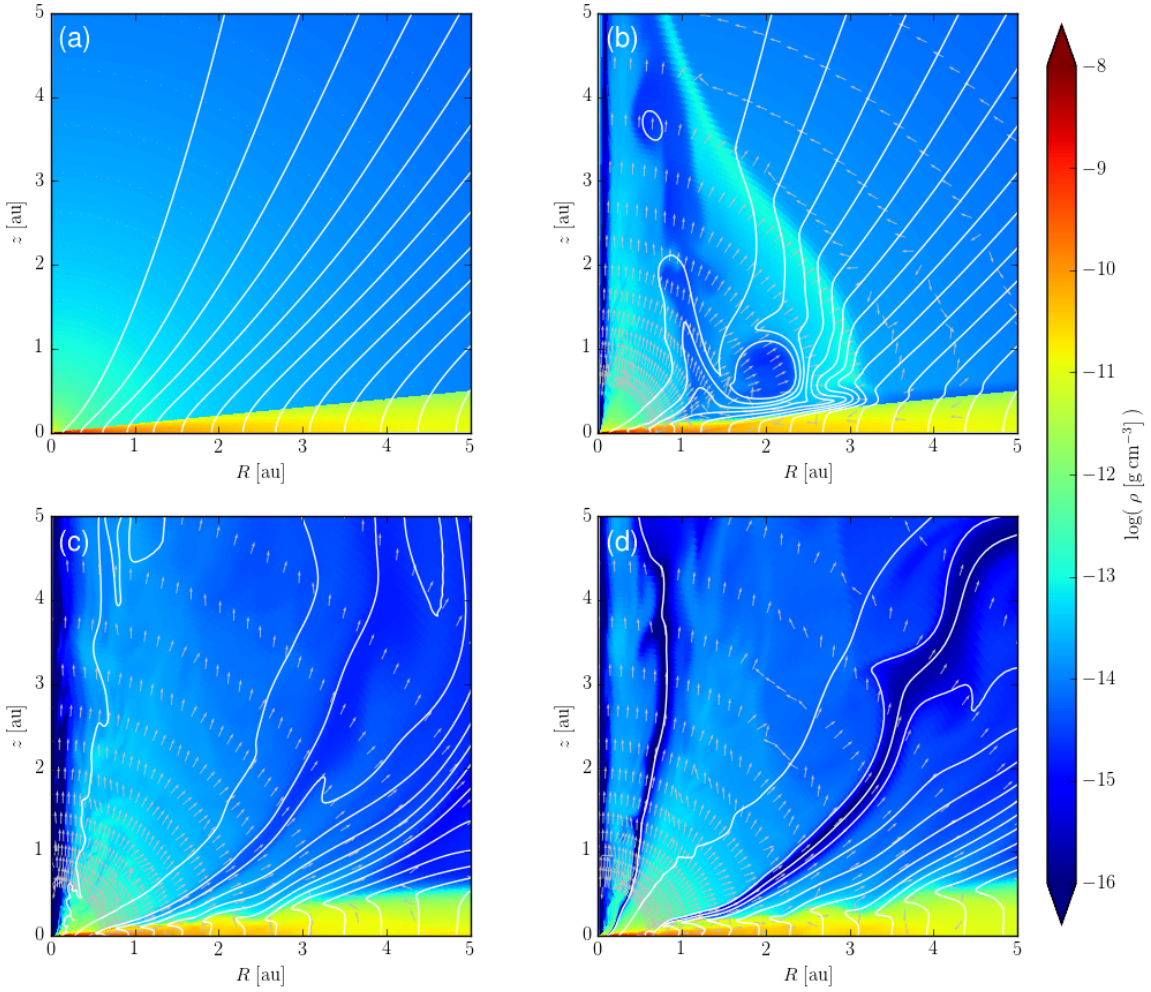

Fig. 2.1.— A representative ('reference') axisymmetric simulation of a coupled disk-wind system. Shown is the mass volume density (logarithmically spaced color contours in units of g cm^{-3}), the poloidal magnetic field lines (white), and the poloidal velocity unit vectors (gray). Panels (a)-(d) corresponding to simulation times of 0, 150, 1200, and 1800 inner orbital periods, respectively. (See the supplementary material of Suriano et al. 2017 in the online journal for an animated version of this figure.)

2.3.2 Outflow

Even though the initial magnetic field at the disk midplane is rather weak ($\beta = 10^3$), it is still able to drive a powerful outflow. Unlike in the disk, the pressure in the outflow is dominated by the magnetic field rather than the thermal gas, as illustrated in Fig. 2.2(a). This dominant magnetic pressure is provided mostly by the toroidal component B_ϕ, as shown in panel (b) where the ratio of the toroidal and poloidal components $|B_\phi/B_p|$ is plotted. This ratio is spatially inhomogeneous, with a filamentary appearance. The dominance of the toroidal field component suggests that the outflow is driven mostly by the magnetic pressure gradient, as is expected for a relatively weak initial magnetic field (e.g., Stepanovs & Fendt (2016)) or a heavy mass loading (e.g., Anderson et al. 2005). The exceptions are a narrow region near the polar axis and two filaments at roughly $\theta = 10^\circ$ and 80°. The magnetic field lines that run through the polar axis region are connected to the inner radial boundary, which is assumed to be non-rotating; the lack of a toroidal field component here is therefore expected. The other two filaments are physically meaningful and correspond to the two low-density 'channels' that are prominent in the density map of Fig. 2.1(d). In these channels, the thermal pressure is completely dominated by the magnetic pressure, with a plasma β less than 10^{-3} (see Fig. 2.2(a)). In other words, their field lines are much more lightly mass-loaded than in the rest of the outflow. As a result, the magnetic field is able to accelerate the mass to a much higher speed than in the denser surrounding regions (see Fig. 2.2(c)).

The distribution of the poloidal velocity is plotted in panel (c) of Fig. 2.2. The outflow in the outer low-density channel reaches a speed of ~ 50 km s^{-1}, whereas that in the inner channel is much faster, reaching up to 200 km s^{-1}. The outflow close to the axis can also reach a relatively high speed of $\sim 50 - 100$ km s^{-1}. However,

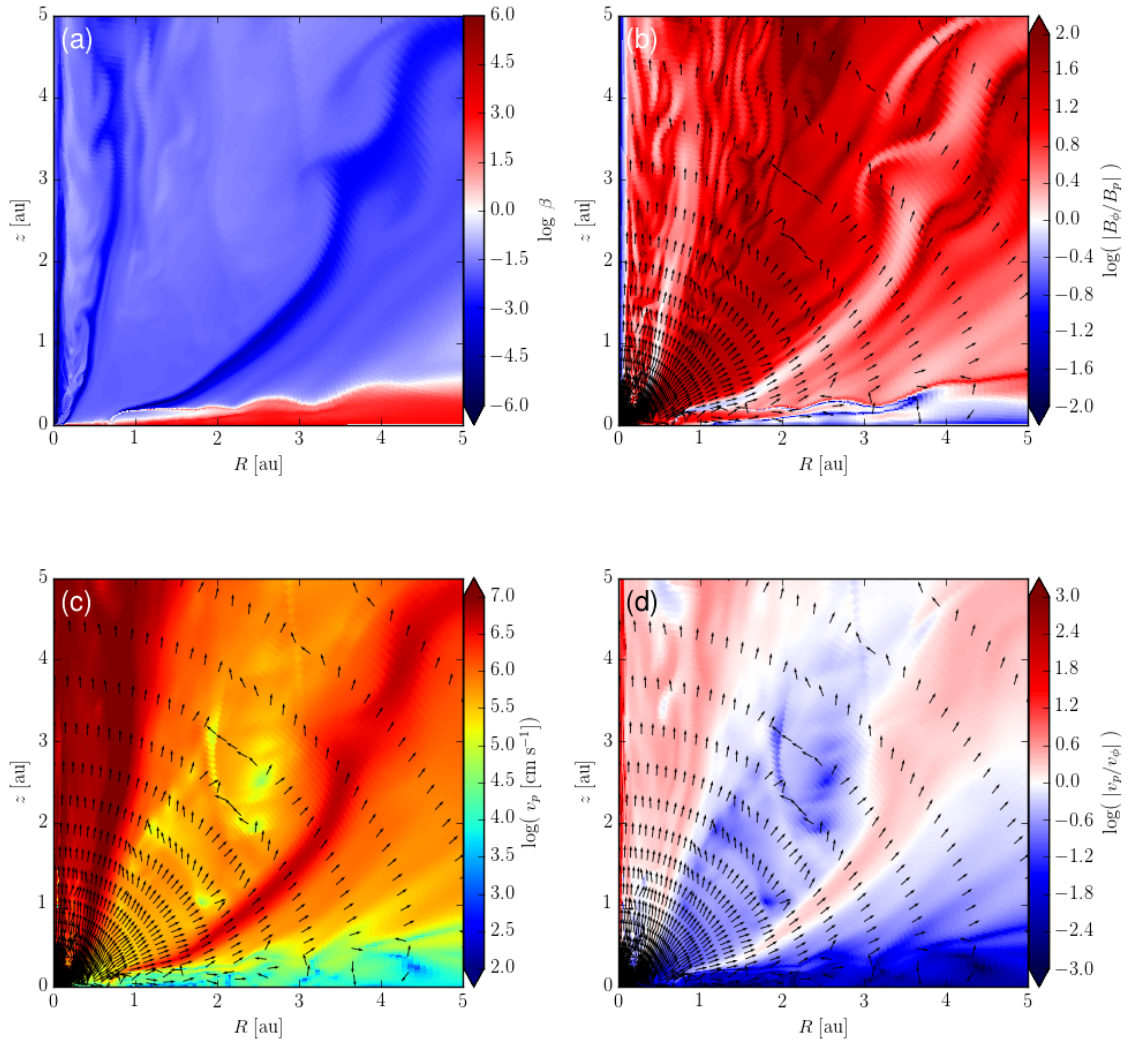

Fig. 2.2.— The reference simulation at time $t = 1800\ t_0$. The logarithmically spaced color contours show (a) the plasma-β, (b) the ratio of the toroidal to the poloidal magnetic field components, $|B_\phi/B_p|$, (c) the poloidal velocity (cm s^{-1}), and (d) the ratio of poloidal to the toroidal velocity components, $|v_p/v_\phi|$. Panels (b)-(d) show poloidal velocity unit vectors (black).

over most of the simulation volume, especially to the right of the inner channel, the poloidal outflow speed is rather low, typically a factor of two or more smaller than the the rotation speed and well below the local free-fall speed (see Fig. 2.2(d)). Except for the channels and polar axis region, the magnetic and velocity fields of the slowly-expanding, low plasma-β outflow are dominated by their toroidal components.

Even though the outflow is slow in general, there is disk material that gets accelerated to a high speed. In Fig. 2.3, we plot the mass flux of the outflowing material with a radial velocity greater than 100 km s^{-1} as a function of time through a hemisphere of radius of $r = 1$ au. It is clear that the fastest component of the outflow is highly variable in time. The mass outflow rate routinely changes by an order of magnitude on timescales of $t \lesssim 100t_0$, and can sometimes drop by four orders of magnitude on similar timescales. This variability may be essential for generating internal shocks that are required to keep the outflow heated to a relatively high temperature and visible through, e.g, optical forbidden lines (e.g., Shang et al. 2002). The average mass loss rate of this fast component is approximately 5×10^{-8} M$_\odot$ yr^{-1}, which is at the high end of the mass loss rate inferred in the classical T Tauri jets (e.g., Frank et al. 2014). This fast, massive outflow component is remarkable in light of the fact that the disk is only weakly magnetized, at least initially with a midplane plasma-β of 10^3.

The fast component is only a relatively minor component of the outflow produced in the reference simulation. This is illustrated in Fig. 2.3, where the mass loss rate is plotted as a function of time for the slow (1 km s^{-1}< v_r < 10 km s^{-1}) and intermediate-speed (10 km s^{-1}< v_r < 100 km s^{-1}) components of the outflow. Both components have mass loss rates of order 10^{-6} M$_\odot$ yr^{-1}, which is at least an order of magnitude higher than the mass flux of the fast component. Such a massive outflow is

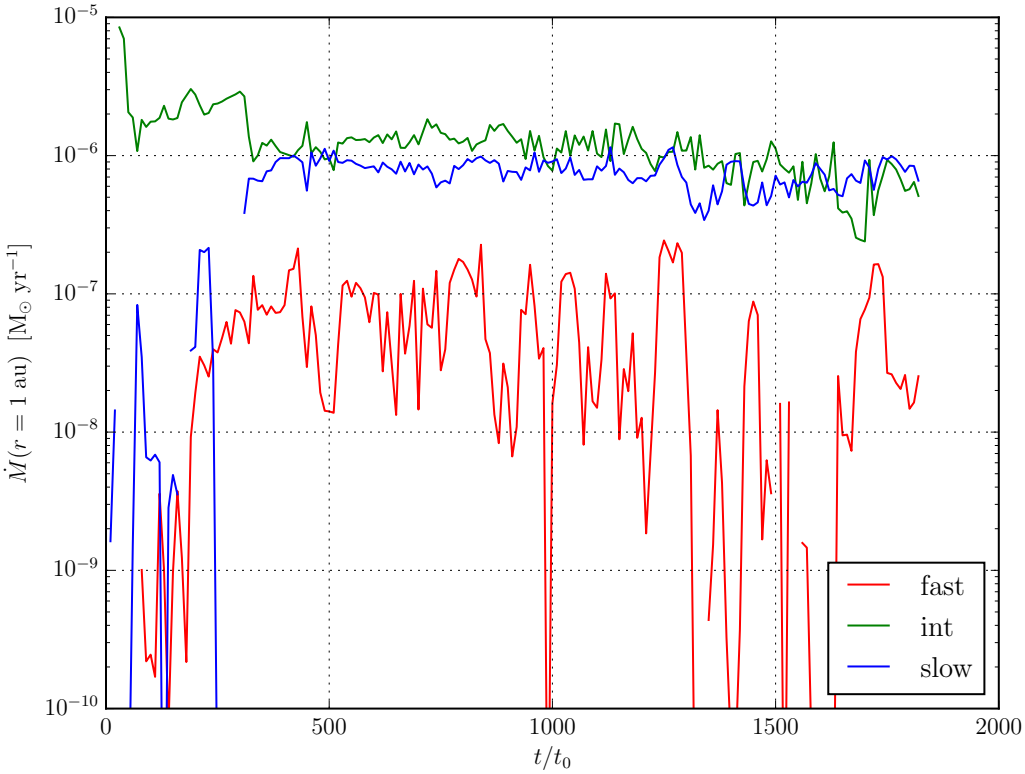

Fig. 2.3.— Mass outflow rate ($\mathrm{M}_\odot$ yr^{-1}) through hemisphere of $r = 1$ au as a function of time in the reference simulation. The mass loss rate is separated into three velocity components. The fast velocity component ($v_r > 100$ km s^{-1}) is shown in red, the intermediate velocity component (10 km $\mathrm{s}^{-1} < v_r < 100$ km s^{-1}) in green, and the slow velocity component (1 km $\mathrm{s}^{-1} < v_r < 10$ km s^{-1}) in blue.

expected to strongly affect – indeed, control – the disk dynamics, as we demonstrate in Section 2.3.3.1.

2.3.3 Disk-wind connection

Fig. 2.4 shows the density distribution and magnetic field lines for the final time frame of the reference simulation, as in panel (d) of Fig. 2.1 and 2.2, but now zoomed in on the inner part of disk where the disk structure is most strongly affected by the outflow. As expected, the modification of disk structure starts near the inner edge, where the rotation period is the shortest. By $t = 1800\ t_0$ (Fig. 2.4), three distinct regions have been established: (1) an inner region ($r < 0.1$ au) with a highly variable mass distribution that contains prominent dense rings and gaps, (2) an intermediate radius region (0.1 au $< r <$ 0.5 au) with a much smoother mass density distribution, and (3) an outer region ($r > 0.5$ au) where the disk 'puffs up' due to the presence of a dense surface layer – the 'avalanche accretion stream.' We label these regions Zone I, II, and III, respectively, and discuss each in detail below. We save the discussion of the most variable region, Zone I, until Section 2.3.3.3.

2.3.3.1 Zone II: Steady wind-driven accretion

We start our discussion with the most laminar, intermediate radius region, Zone II. The location of this region drifts radially outward as the simulation progresses. By $t = 1800 t_0$ (Fig. 2.4), it is located roughly between 0.1 and 0.5 au. The magnetic field line intersecting the midplane at a radius of 0.3 au is marked by a dashed line in Fig. 2.4 (left panel). Fig. 2.5(a) plots the density distribution along that field line, with the location of the sonic point marked. For comparison, we also plot the density profile expected for an isothermal (thin) disk with the temperature set to

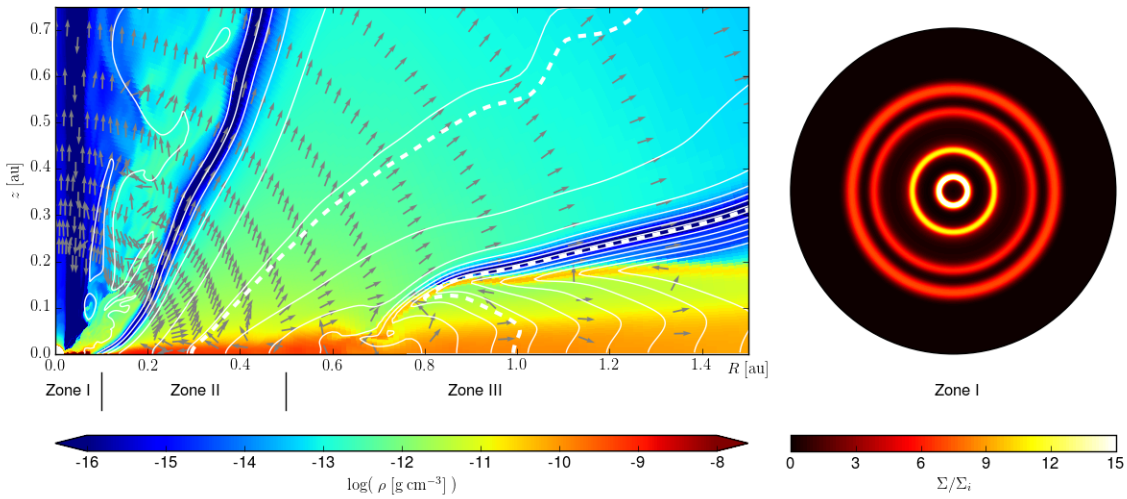

Fig. 2.4.— The reference simulation at $t = 1800t_0$. Left: The mass volume density (g cm^{-3}) is shown in logarithmically spaced color contours. Magnetic field lines are shown in white and the two dashed lines show the field lines with midplane footpoints of 0.3 and 1.0 au (along which the quantities in Fig. 2.5 and 2.6 are plotted). The gray arrows denote the velocity field and show that the bulk of the disk material is expanding under the surface accretion stream beyond a radius of ~ 0.7 au. Right: The 'face-on' axisymmetric surface density normalized to its initial distribution is shown in color contours for Zone I ($r \leq 0.1$ au).

that at the midplane. Clearly, the presence of the magnetic field and the launching of a magnetized wind have significantly changed the vertical density profile of not only the disk itself, but also the region surrounding the disk. Specifically, the vertical density gradient is steeper near the disk surface compared to an isothermal (non-magnetic) profile. This difference is explained by a decreasing temperature along the path and by an increasing toroidal component of the magnetic field, B_ϕ, which reaches a maximum near 0.02 au before decreasing again (Fig. 2.5(b)). Indeed, the toroidal field becomes so strong near the disk surface that it dominates the thermal pressure (see Fig. 2.5(f) and discussion below), and generates a downward magnetic pressure force that compresses the disk significantly. Above the disk surface, the magnetic pressure force has a positive radial component conducive to launching a wind.

The transition from disk to wind can be seen most clearly in the distribution of the radial component of the velocity v_r along the field line (Fig. 2.5(c)). The transition occurs approximately ~ 0.03 au above the disk midplane. Material below this point moves radially inward with a speed of $\sim$0.2 km s^{-1}, while material above this point is gradually accelerated outward. Beyond the sonic point the flow speed becomes more variable, because the wind has yet to reach a steady state. Even though the wind speed becomes supersonic at large distances, it remains well below the rotational speed except toward the edge of the simulation domain (see Fig. 2.5(d)). In fact, v_ϕ is close to the speed needed to be rotationally supported against the gravitational pull from the central star in the cylindrical radial (R) direction (also shown in Fig. 2.5(d) for comparison). The implication is that, just like the disk, the slowly expanding wind is almost entirely supported in the R-direction by rotation. The difference lies in the vertical direction; whereas the disk is supported against gravity (and magnetic compression) mostly by the thermal pressure gradient, the wind is supported mostly

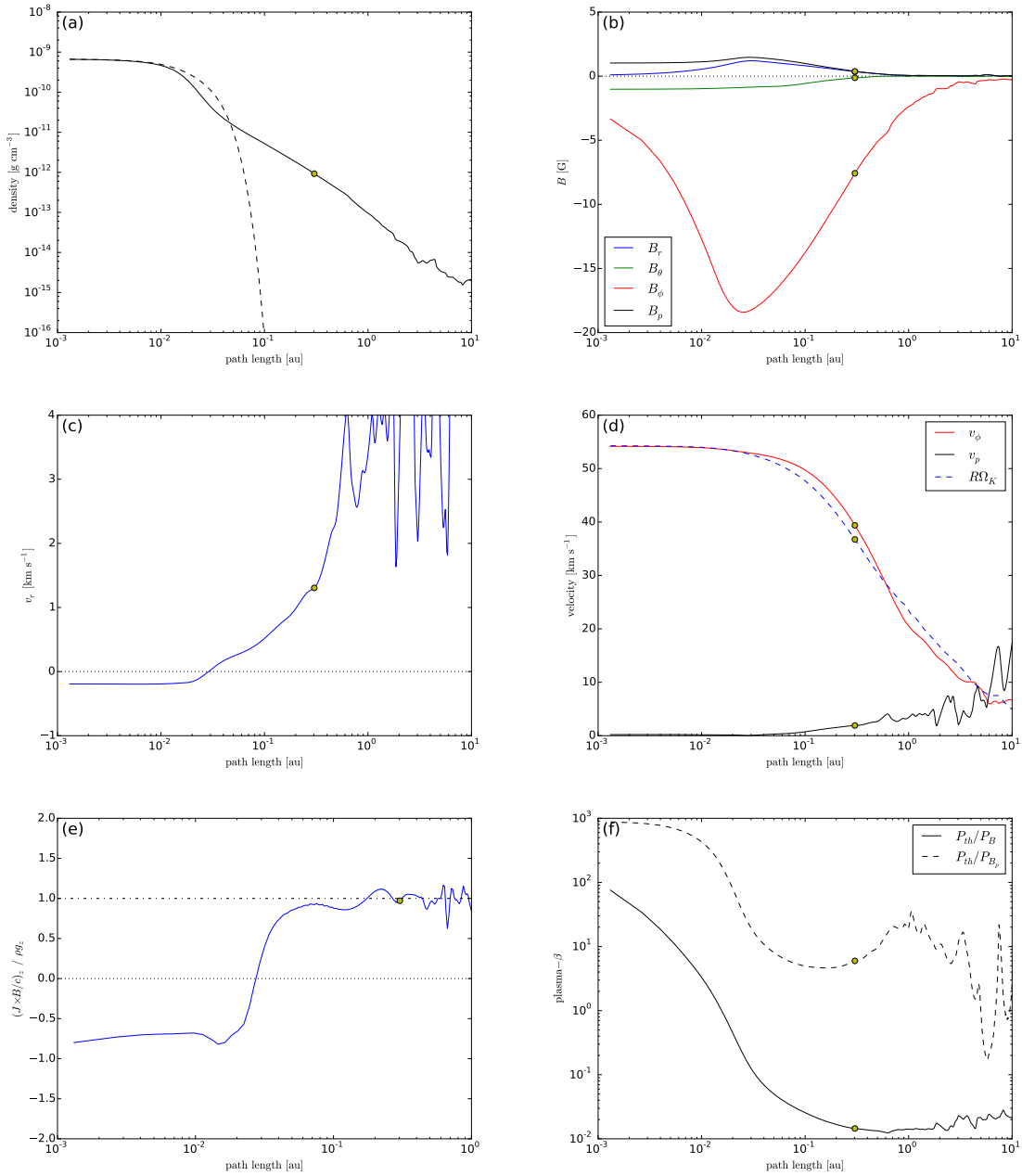

Fig. 2.5.— Physical quantities plotted along a poloidal magnetic field line as a function of the distance along the line. The representative field line has a footpoint at $r = 0.3$ au (Zone II) and can be seen in Fig. 2.4 (white dashed line). Yellow circles show the sonic point ($v_p = c_s$). The panels show (a) the density distribution (solid) and the distribution expected based on the mid-plane temperature (dashed), (b) the magnetic field components, (c) the radial velocity, (d) the poloidal (black) and toroidal (red) velocities with the corresponding Keplerian velocity ($R\Omega_K$; dashed blue line), (e) the vertical component of the Lorentz force relative to the gravitational force, and (f) plasma-β for the total magnetic field strength (solid) and for the poloidal magnetic field strength (dashed).

by the magnetic pressure gradient. This difference is highlighted in Fig. 2.5(e), which shows that the ratio of the vertical component of the Lorentz force to the gravitational force changes sign at the disk surface/wind base and reaches unity just before the sonic point. The available evidence points to a magnetically dominated wind (Fig. 2.5(f)) that is slowly lifted out of the (deep) gravitational well near the disk surface by the magnetic pressure gradient, consistent with the 'magnetic tower' picture of Lynden-Bell (1996).

Despite being much slower than the Keplerian speed at its footpoint, the wind launched from 0.3 au strongly affects the disk structure and dynamics. First, it rapidly depletes the disk material. To estimate a local disk mass depletion time, we define a magnetic flux tube containing an infinitesimally small magnetic flux $\Delta\Psi$ around the field line. The cross-sectional area of the flux tube is $\Delta A = \Delta\Psi/B_p$, where B_p is the poloidal magnetic field. The rate of wind mass flux along the magnetic flux tube is

$$\Delta\dot{M} = \rho\Delta A\left(\frac{\boldsymbol{v}_p\cdot\boldsymbol{B}_p}{B_p}\right) = \rho\Delta\Psi\left(\frac{\boldsymbol{v}_p\cdot\boldsymbol{B}_p}{B_p^2}\right). \tag{2.13}$$

This is to be compared with the amount of mass contained inside the flux tube

$$\Delta M = \int \rho\Delta A ds = \Delta\Psi\int(\rho/B_p)ds, \tag{2.14}$$

where the integration is along the field line, and is dominated by the mass inside the disk. The local disk mass depletion time due to wind mass loss is then

$$t_{dep} = \frac{\Delta M}{\Delta\dot{M}} = \int(\rho/B_p)ds\left(\frac{\rho\boldsymbol{v}_p\cdot\boldsymbol{B}_p}{B_p^2}\right)^{-1}. \tag{2.15}$$

In a steady state, the quantity $\Delta\dot{M}$ should be constant along a field line. However,

the wind does not reach a strict steady-state, and the non-steadiness introduces some variation to that combination, especially at large distances. We obtain a depletion time of $t_{dep} \approx 9.6$ yr, which is 58 times the local orbital period at the footpoint. This time scale is to be compared with the accretion time scale for the disk material, which is roughly

$$t_{acc} = r/v_r. \tag{2.16}$$

For an average accretion speed of ~ 0.2 km s^{-1} at 0.3 au, the accretion timescale is $t_{acc} \approx 8.6$ yr, or 52 times the local orbital period. The fact that the accretion time is comparable to the depletion time means that a significant fraction of the disk will be ejected in the wind.

One way to quantify the disk accretion rate is through an effective α parameter, defined as

$$\alpha_{eff} = -v_r v_K / c_s^2, \tag{2.17}$$

which, for $v_r \approx 0.2$ km s^{-1}, $v_K = 54$ km s^{-1}, and $c_s = 2.3$ km s^{-1}at 0.3 au, yields $\alpha_{eff} \approx 2$. This is much larger than the effective α typically obtained from turbulent MRI simulations ($\alpha \sim 1/\beta$, Hawley et al. 2015), which highlights the dynamical importance of the slow disk wind launched even by a relatively weak initial poloidal magnetic field, in that it can still drive rapid disk accretion.

2.3.3.2 Zone III: Avalanche accretion stream and slow midplane decretion

For the outer disk region ($r > 0.5$ au), we plot the physical properties of the gas and magnetic field along a representative field line that starts from a radius of ~ 1 au on the disk midplane (Fig. 2.6). Panel (a) of Fig. 2.6 shows the density distribution as a function of the distance along the field line. We can see that near the midplane, the density profile is close to that expected for a (non-magnetic) isothermal disk

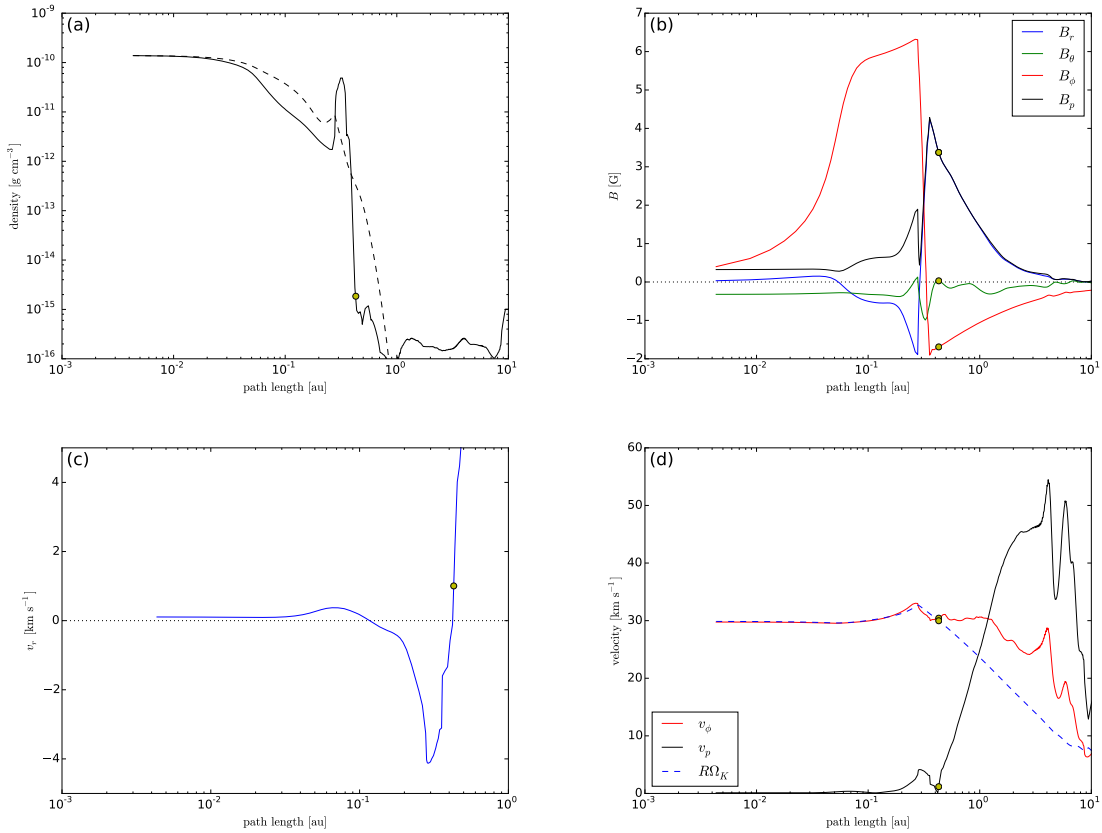

Fig. 2.6.— Physical quantities plotted along a poloidal magnetic field line as a function of the distance along the line. The representative field line has a footpoint at $r = 1$ au (Zone II) and can be seen in Fig. 2.4 (white dashed line). Yellow circles show the sonic point in the outflowing wind ($v_p = c_s$). The panels show (a) the density (solid) and equilibrium density (dashed) distributions, (b) the magnetic field components, (c) the radial velocity, and (d) the poloidal (black) and toroidal (red) velocities with the corresponding Keplerian velocity ($R\Omega_K$; dashed blue line).

(dashed line), indicating that the magnetic field is not important in the vertical force balance. Moving closer to the disk surface (where the magnetic pressure dominates the thermal pressure), magnetic compression causes the density to drop significantly below the isothermal value, as in Zone II. The difference is that the density in Zone III increases sharply again before dropping off precipitously. This density spike marks the 'avalanche accretion stream' that is prominent in Fig. 2.4. It is the defining characteristic of Zone III, not only in the density structure but also in the magnetic field structure.

From Fig. 2.4, it is clear that the dense stream occurs where the magnetic field line pinches severely, with a sharp reversal of the radial field component across it. This reversal shows up clearly in Fig. 2.6(b), where all components of the magnetic field are plotted. The poloidal magnetic field line near the midplane first bows outward, with a small but positive radial component, as in Zone II (see Fig. 2.6(b)). However, it is forced to bend sharply inward (see Fig. 2.4) by the rapidly infalling stream, producing a large (negative) value for B_r. The toroidal field component increases from the midplane towards the stream, dominating the other two field components before reversing direction across the stream (Fig. 2.6(b)).

As the material in the stream falls radially inward, it is orbiting faster relative to material both above and below it, as shown in Fig. 2.6(d), where we plot v_ϕ along the representative field line. Simple geometric considerations show that the faster rotation at the tip of the sharply pinched field line will twist the inward-directing field into a toroidal field of positive sign and the outward-directing field into a toroidal field of the opposite sign, as shown in Fig. 2.6(b). The twisted magnetic field geometry efficiently brakes the stream as it loses angular momentum to both the wind and the disk material that is magnetically linked to the stream at larger radii. Both B_r

and B_ϕ are amplified as the fast-rotating stream accretes, which leads to a stronger magnetic braking torque. The end result is a run-away collapse of the stream similar to the MRI, and hence the name 'accretion avalanche' (Kudoh et al. 1998). At the time shown in Fig. 2.6, the infall speed of the stream is supersonic and reaches about 2 km s^{-1} (only the sonic point in the wind above the the stream is shown in the figure). The bulk of the disk material below the stream moves much more slowly and in the opposite direction, as shown in Fig. 2.4 (left panel). The contrast between the fast accreting stream and slowly expanding disk is quantified in the radial velocity profile plotted in Fig. 2.6(c). This 'decretion' is caused by the disk material receiving angular momentum from the infalling stream and is opposite of the disk motion in Zone II (compare to Fig. 2.5(c)).

Although the stream infalls supersonically, its infall speed is still much smaller than the rotation speed v_ϕ (Fig. 2.6(d)). Indeed, the rotation speed is close to the value needed for the centrifugal force to balance the gravity in the cylindrically radial direction inside both the disk and the stream, indicating that both are close to being rotationally supported. A supersonic wind is launched above the stream, reaching speeds of $\sim$50 km s^{-1}, which is higher than that reached along the field line originating from 0.3 au (see Fig. 2.5(d)). This speed difference is mainly due to lower mass loading, which allows the wind to experience greater acceleration despite rotating more slowly near the footpoint. Nevertheless, both the velocity and magnetic field are still dominated by the toroidal component over a large fraction of the wind, which is broadly similar to the wind driven from Zone II. The thermal pressure of the wind here is also completely dominated by the magnetic pressure, again similar to the wind from Zone II. Therefore, the formation of the stream appears to modify, but not completely disrupt, the wind launching and acceleration.

2.3.3.3 Zone I: Rings and gaps in inner disk

The innermost disk region ($r < 0.1$ au) is most strongly modified from its initial state during the simulation because it has the shortest rotation period and is located where the (poloidal) magnetic flux tends to accumulate through disk accretion. It is also the most variable region of the disk-wind system. The spatial variation of mass distribution is evident in Fig. 2.4, where the right panel shows a 'face-on' view of the axisymmetric (one hemisphere) surface density normalized by the initial surface density distribution, $\Sigma_i = 810$ g cm^{-2} $(r/r_0)^{-1/2}$, to highlight features at large radii. There is a striking contrast between the dense inner rings and their surrounding gaps; in fact, most of the mass of the inner disk is concentrated in these rings. Through the course of the simulation up to five rings are formed in Zone I. The first is formed just outside of the inner boundary and is quickly accreted after 200 inner orbital periods. The remaining rings all form in an inside-out manner; once one ring and gap are formed (with the gap located at a larger radius than the ring), another ring develops at a slightly larger radius than the first gap. Once formed, the multiple rings and gaps drift slowly inward maintaining their relative order.

Although the magnetic field topology near the rings and gaps is irregular, winds are still launched from Zone I. The winds that are launched from the gaps accelerate material to very high velocities ($v_r > 100$ km s^{-1}), both because very little mass gets loaded onto the field lines anchored in the low-density gaps and because the vertical magnetic field strength peaks in the gaps (allowing for rigid rotation of the field lines out to a larger radius). This is quantified in Fig.2.7(a), where the column density as a function of radius at a representative time ($t = 1250\ t_0$) is plotted. One might naively expect the vertical component of the magnetic field ($-B_{\theta,\mathrm{mid}} = |B_{\theta,\mathrm{mid}}|$ at the midplane, since $B_{\theta,\mathrm{mid}}$ is negative because the initial magnetic field points upward) to

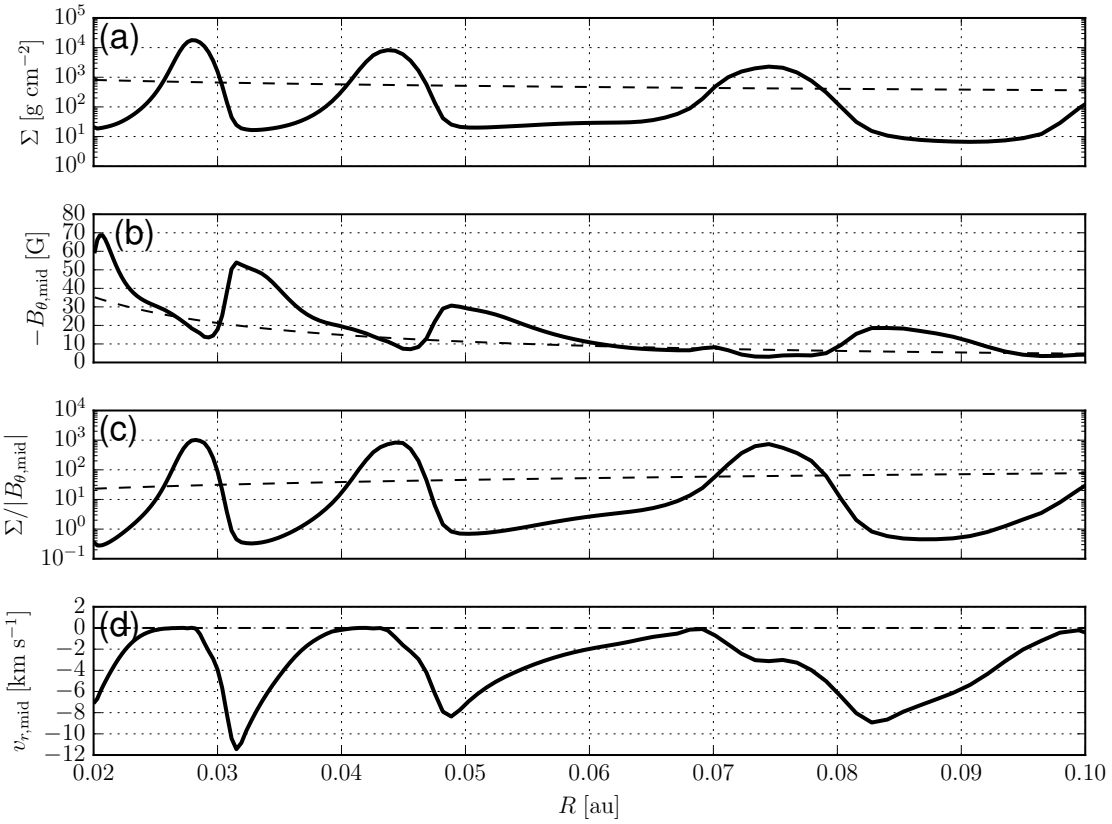

Fig. 2.7.— Ring and gap formation in Zone I of the reference simulation at $t = 1250t_0$. (a) The surface density, (b) the vertical magnetic field strength at the midplane ($-B_{\theta,\mathrm{mid}}$), (c) the mass-to-flux ratio $\Sigma/|B_{\theta,\mathrm{mid}}|$ in units of g cm^{-2} G^{-1}, and (d) the radial velocity (negative means accretion towards the central source). The initial distribution of these quantities are shown for comparison (dashed lines).

be concentrated in the high density rings, because the mass-to-flux ratio, $\Sigma/|B_{\theta,\mathrm{mid}}|$, would be conserved in the strict ideal MHD limit. However, there is a tendency for the vertical field to be *weaker* in the dense rings than in the gaps. This anti-correlation is shown in Fig. 2.7(b), where $-B_{\theta,\mathrm{mid}}$ is plotted versus radius. It is clear that the dense rings are less magnetized relative to both the initial disk value and the neighboring gaps. The contrast between the rings and gaps is particularly striking for the distribution of the mass-to-flux ratio shown in Fig. 2.7(c).

Since the innermost rings are always observed to form first, it is natural to relate their formation to the inside-out development of the disk wind (i.e., at any given time, the disk wind is further developed at smaller disk radii because of their shorter dynamical times). The wind drains angular momentum from the disk, forcing the disk material to accrete and drag magnetic flux along with it. In the ideal MHD limit, the accumulation of mass at a given location would lead to a corresponding pile-up of magnetic flux at the same location. But in the resistive MHD of this simulation, the field lines diffuse away from the region of magnetic flux concentration. This leads to two key steps in the formation of a ring and gap. First, the magnetic flux begins to drop in the region where surface density starts to spike. The decreasing dynamical importance of the magnetic field in this region increases the accretion timescale of the dense ring, effectively creating a trap for mass accretion from larger radii. Second, the magnetic flux begins to accumulate just outside the growing overdensity. Now the low mass-to-flux region can efficiently drain disk material of angular momentum, quickly moving any remaining mass to smaller radii where it is added to the ring. The fast accretion of the material in the gaps onto the nearly stationary rings is shown in Fig. 2.7(d), where the radial component of the velocity at the disk mid-plane is plotted. This interplay of magnetic flux redistribution, angular momentum removal

through magnetic wind, and disk accretion naturally leads to a configuration of a high mass-to-flux region (ring) just inside of a low mass-to-flux region (gap; Fig. 2.7(c)). Once an over-dense region is formed, its survival allows for the development of similar patterns at larger radii.

2.3.4 Magnetic diffusivity and the disk-wind structure

To summarize, there are three distinct zones that develop in the reference simulation. The dimensionless diffusivity parameter $D = \eta/(hc_s)$ decreases with radius as $D \propto r^{-1/2}$. Zone I is thus the most magnetically diffusive region initially, as measured by D. It is also the region where the most prominent rings and gaps form, because magnetic diffusion is needed for the redistribution of magnetic flux relative to the matter. In Zone II the magnetic diffusion is such that the outward diffusion balances the inward advection of the magnetic field, thereby establishing a laminar, quasi-steady disk-wind system. The least magnetically diffusive region, Zone III, develops a dense surface accretion stream that dominates the mass accretion in that region and drives the disk material below it to expand. These results suggest that the level of magnetic diffusion is a key factor in controlling the structure and dynamics of the coupled disk-wind system.

2.4 Parameter study

In order to determine how robust the basic features of the reference simulation are, especially the formation of rings, gaps and avalanche accretion streams, we performed several additional simulations in which we varied three dimensionless model parameters: D_0, β, and ϵ. These characterize the disk magnetic diffusivity, field strength, and disk thickness (or temperature), respectively (see Table 2.1).

We find that all simulations show characteristics of at least one of the three Zones described in the reference simulation and all simulations develop variable winds (see Fig. 2.9). Almost all simulations show enough spatial variation in the surface density that rings and gaps are readily apparent, and many of the simulations show dense avalanche accretion streams developing near the disk surface. In some cases the inner disks appear to be entirely dominated by rapid formation and break-up of short-lived accretion streams, forming a vertically extended 'envelope' above the disk characterized by chaotic infall and outflow motions. In the following subsections we discuss the effects of each of the three dimensionless parameters in turn, focusing in particular on the lower diffusivity (D_4), stronger field (model beta_3), and higher temperature (t4, or thicker disk) cases (illustrated in Fig. 2.8 and Fig. 2.9).

2.4.1 Resistivity

We start with model D_4, where all parameters are the same as in the reference case except for the (constant) resistivity η, which is reduced by a factor of four (thereby reducing D_0 by the same amount). The reduction in η makes the magnetic field lines better coupled to the material in the disk. We expect this to facilitate the formation of avalanche accretion streams, as in Zone III of the reference simulation, and this is indeed the case. Movies of simulation D_4 (see the supplementary material of Suriano et al. 2017 in the online journal for animated versions of Fig. 2.8) show that avalanche accretion streams form continuously, starting as early as ~ 10 inner orbital periods. Many of the streams are pushed up high into the disk corona by the growing toroidal magnetic fields beneath them (as in the case of the stream in Zone III of the reference simulation, see Fig. 2.6(b)). They are eventually disrupted as they fall radially inward and towards the midplane. The constant formation and disruption

of the (often elevated) avalanche accretion streams leads to a thick, clumpy envelope above the disk that is highly inhomogeneous in density, velocity, and magnetic field. This stream-produced envelope can be seen clearly in Fig. 2.8(a), where its maximum vertical extent is comparable to the cylindrical radius and is positioned between the denser equatorial disk and the more tenuous polar wind region. While the (poloidal) field lines in the polar wind region are well organized, those in the envelope are disordered with severe bunching of field lines in some places and looping (due to reconnection) in others. The disordered field is a reflection of the chaotic motions inside the envelope characterized by simultaneous infall and outflow. The motion of the envelope is best seen in Fig. 2.8(b), where the spatial distribution of mass flux per unit polar angle, $d\dot{M}/d\theta = 2\pi r^2 \rho v_r \sin\theta$, is plotted. The mass accretion in the envelope is dominated by the fragments of disrupted avalanche accretion streams (blue in middle row of Fig. 2.8). They are mixed together with packets of outflow (red) that sometimes extend to the disk midplane. The picture is reminiscent of the MRI-driven channel flows that are seen, e.g., in the thick disk simulations of Kudoh et al. (2002), and they share the same physical origin – the exchange of angular momentum between magnetically connected material located at different radii. In our thin-disk case, the difference is that the alternating pattern of inflow and outflow occurs mostly in the envelope above the disk rather than inside the disk. This dynamic envelope is a new feature that formally does not exist in the reference simulation, although it is intimately related to the avalanche accreting stream of Zone III.

In addition to the envelope, a wind is also launched in the low-resistivity case (model D_4). The wind can be seen in Fig. 2.8(a), especially in (but not limited to) the polar region. The wind is highly variable, as illustrated in Fig. 2.9 (blue line), where the mass loss rate for the fastest wind component ($v_r > 100$ km/s)

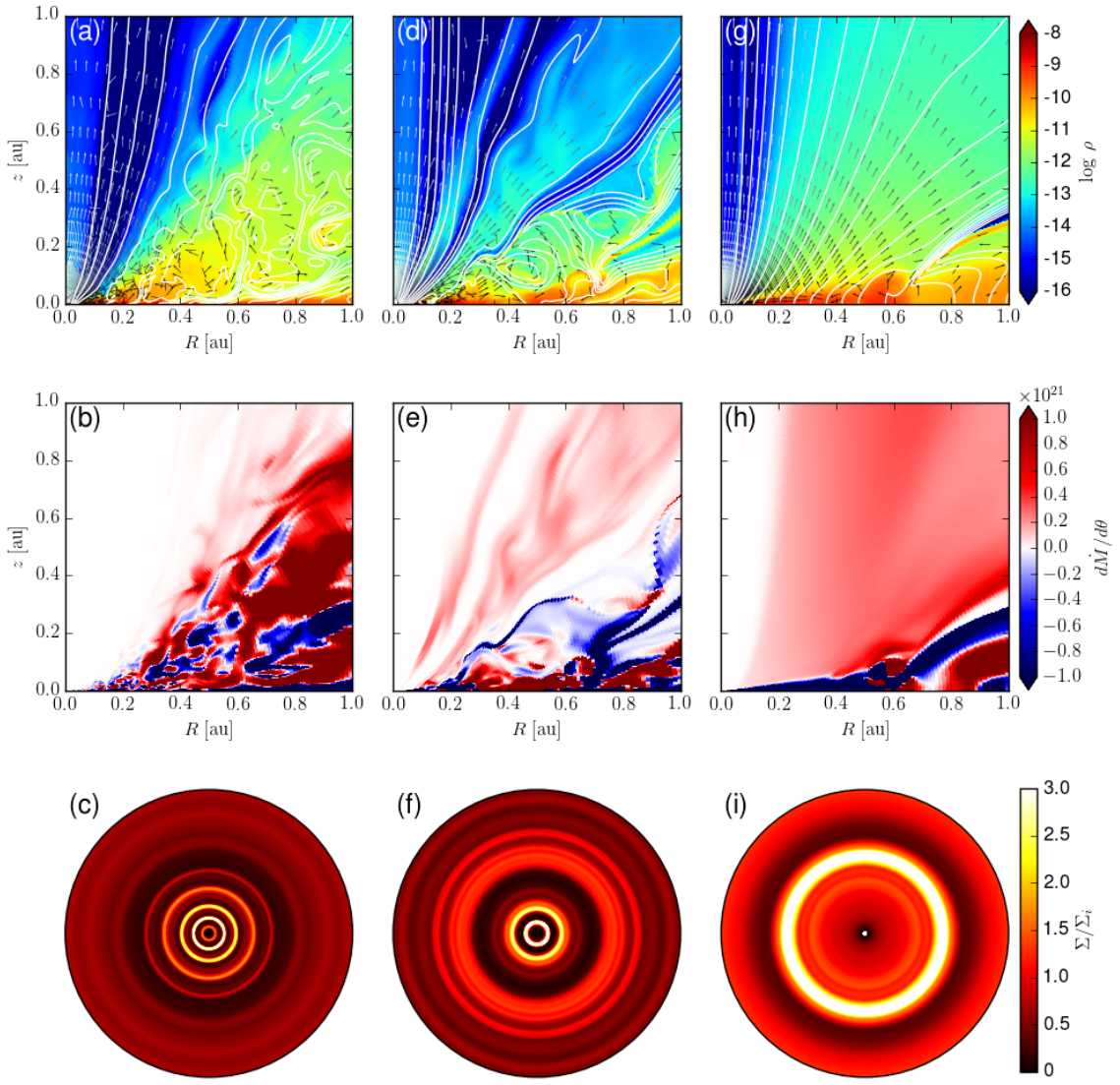

Fig. 2.8.— Snapshots of three simulations at $t = 1650t_0$. The left, middle, and right columns correspond to simulations D_4, beta_3, and t4, respectively. The top row shows the mass density (g cm^{-3}) in logarithmically spaced color contours with magnetic field lines in white and velocity (unit) vectors in grayscale. The middle row shows the radial mass flux per unit polar angle $d\dot{M}/d\theta = 2\pi r^2 \rho v_r \sin\theta$ where negative (blue) values correspond to infall and positive (red) to outflow. The bottom row shows the 'face-on' view of the axisymmetric surface density normalized to its initial distribution for $r \leq 1$ au. (See the supplementary material of Suriano et al. 2017 in the online journal for animated versions of this figure, including the reference simulation.)

is plotted as a function of time. The mass loss rate is comparable to that in the reference case, especially in the second half of the simulation. The highly variable wind and the chaotic envelope create radial structures in the disk. Fig. 2.8(c) shows a face-on view of the surface density normalized by its initial distribution. Several rings and gaps are clearly visible, and they are quantified in Fig. 2.10(b), where the surface density is plotted as a function of radius. The development of rings and gaps starts at small radii, and gradually spreads to large radii, because the dynamical time increases with radius. Some of the rings appear to change quickly, while others are more stationary. These features are present throughout the simulation, suggesting that they are a robust characteristic of the coupled disk-envelope-wind system. We find that the surface density anti-correlates with the poloidal field strength on the disk, with the dense rings typically less magnetized than the gaps, as in Zone I of the reference simulation. This indicates that magnetic flux redistribution through either the relatively small resistivity or turbulent reconnection, is playing a role in creating the rings and gaps. Since the disk is tightly connected to the stream-dominated envelope, the streams are also expected to play an important role in gap and ring formation. This role is difficult to quantify precisely, however, because of the chaotic flow pattern in the disk and envelope. A cleaner case of stream-induced ring formation will be presented in the higher-temperature case below (see Section 2.4.3). We have also carried out an ideal MHD simulation with the same parameters except for $\eta = 0$, and found results broadly similar to this low-resistivity case.

In contrast to D_4, the more resistive model D4 is much more laminar. A wind is launched steadily throughout the run over most of the disk radii that have had time for at least one orbit to take place, as in the smooth Zone II of the reference run. There are no avalanche accretion streams in the simulation. A new feature of model

Table 2.1: Model parameters for all simulation runs. Note: the diffusivity parameters D_0 and $D_{m,0}$ are measured at the inner edge of the disk, and the simulation ref-x2grid has a higher resolution in the disk region (see Section 2.2.3).

	ϵ	β	η [cm^2 s^{-1}]	D_0	$D_{m,0}$
reference	0.05	10^3	2.5×10^{15}	0.16	3.6
D_4	0.05	10^3	6.25×10^{14}	0.04	0.89
D4	0.05	10^3	10^{16}	0.64	14
beta_3	0.05	3.33×10^2	2.5×10^{15}	0.16	2.1
beta3	0.05	3.0×10^3	2.5×10^{15}	0.16	6.2
beta100	0.05	10^5	2.5×10^{15}	0.16	36
t4	0.1	10^3	10^{16}	0.16	3.6
ref-x2grid	0.05	10^3	2.5×10^{15}	0.16	3.6

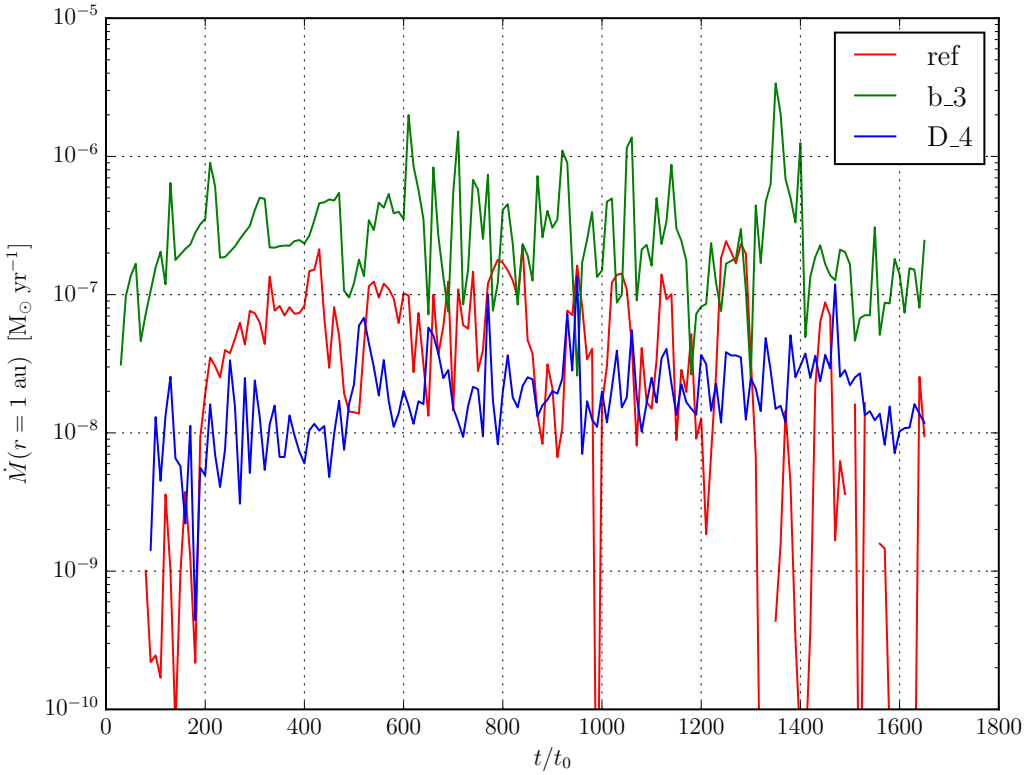

Fig. 2.9.— Mass outflow rate ($\mathrm{M}_\odot\ \mathrm{yr}^{-1}$) through a hemisphere of $r = 1$ au as a function of time for three simulations (reference, beta_3, and D_4). Only the mass outflow rate of the fast velocity component ($v_r > 100$ km s^{-1}) is shown.

D4 is that, because of its high resistivity, the wind from the innermost part of the disk becomes weaker with time as the magnetic flux in the region diffuses to larger radii. By $t = 1800t_0$, the region of weakened wind launching extends to a radius ~ 0.2 au (Fig. 2.10(e)). In this region, the rate of angular momentum removal by the wind is significantly reduced, allowing mass to accumulate there. This results in a large plateau in the surface density profile followed immediately by a gap at 0.2 au, with a drop in surface density of one order of magnitude. Model D4 therefore provides another example of gap formation through a wind of varying strength at different radii, in addition to Zone I of the reference simulation. At 2200 inner orbital periods, the mass in the disk within $r < 0.2$ au has doubled, and the magnetic flux has dropped well below its initial value. The magnetic field remaining in the dense plateau is too weak to break the surface density into rings and gaps, unlike Zone I of the reference case. The drastically different behaviors of models D_4, D4, and the reference model underscores the key role of the magnetic diffusivity in determining the structure and dynamics of the coupled disk-wind system.

2.4.2 Magnetic field strength

We will focus first on model beta_3, where the (vertical) magnetic field is $\sqrt{3}$ times stronger than that of the reference case at the disk midplane (i.e., β is decreased by a factor of three). One expects a stronger magnetic field to drive a more powerful disk wind, and this is indeed the case. Fig. 2.9 shows that the wind mass loss rate is typically well above that of the reference case. It is also clear from Fig. 2.9 that the disk wind in this case is just as variable as, if not more variable than, that in the reference case.

The flow pattern in and around the disk in model beta_3 is more similar to that in

the least resistive model D_4 than to the reference case. Specifically, it is dominated by the constant formation and disruption of dense avalanche accretion streams (like that seen in Zone III of the reference case); the quasi-laminar region (Zone II) has all but disappeared. These changes are expected because the magnetic torque exerted by a stronger field removes angular momentum from the disk more efficiently, allowing the accreting streams to develop earlier and at smaller radii. The first prominent stream develops within 150 inner orbital periods (earlier than the reference run but later than model D_4) and terminates near $r = 0.2$ au. By 500 inner orbital periods the inner disk is almost completely restructured by the interaction of multiple avalanche streams, as in model D_4, again leading to the formation of a thick envelope where matter moves rather chaotically both inward and outward (see Fig. 2.8(d)). Compared with model D_4 at similar times, the number of avalanche streams is smaller, the stream-dominated envelope is thinner (typically reaching only $z \sim 0.5R$ compared to $\sim R$), and the wind above the envelope is more massive (compare Fig. 2.8(e) and (b)). In addition, the expansion of disk material near the midplane is more clearly visible in model beta_3; for example, about half of the disk inside 0.6 au is decreting at the time shown in Fig. 2.8(e). Nevertheless, the flow patterns in the two cases are fundamentally similar: both are dominated by the avalanche accretion streams, as they are not suppressed by a large enough magnetic diffusivity. We will return to this important point toward the end of the subsection.

The strong, highly variable wind and the stream-dominated envelope create structures in the disk surface density distribution, which can be seen in Fig. 2.8(f) and Fig. 2.10(c). There are numerous rings and gaps at the time shown ($t = 1650t_0$). Their development starts near the inner boundary and spreads outward with time, as the disk material at an increasingly larger radius becomes affected by the magnetic

wind launching and the formation of streams. We find an anti-correlation between the surface density and vertical magnetic field strength in the midplane (as in model D_4 and Zone I of the reference case), although the interpretation of the anti-correlation is again complicated by the chaotic motions in the disk and envelope.

The weaker field model, beta3, is dominated by a quasi-laminar region beyond 0.1 au (similar to Zone II of the reference run), and lacks a region with avalanche streams. In fact, not a single stream is formed throughout the duration of the simulation. Within a radius of 0.1 au, a wind appears only intermittently and is less efficient in carrying away angular momentum compared to the wind launched beyond this radius. This allows mass accumulation at small radii, forming the high surface density plateau, as in model D4 (Fig. 2.10(f)). This plateau is adjacent to a prominent gap at $r = 0.1$ au, which separates the variable inner and steady outer wind launching region, similar to the boundary between Zone I and Zone II in the reference case. This difference is further illustrated by the weakest magnetic field model, beta100. In this case, an outflow is still launched, but is unable to escape the simulation domain; instead, it inflates a bubble up to $z \sim 1$ au that is dominated by the toroidal magnetic field with $\beta \approx 5 \times 10^{-2}$. The disk remains laminar and mostly unchanged from its initial state.

Taken together, the four models with different field strengths but the same resistivity (beta100, beta3, reference, and beta_3) show a clear trend: as the field becomes stronger, the disk-wind system becomes less laminar, with the avalanche accretion streams becoming increasingly more important. This is the same trend that we see in Section 2.4.1, where the importance of the avalanche accretion streams increases as the resistivity decreases for a given field strength. The similarity indicates a deep connection between the effects of a stronger magnetic field and a lower resistivity.

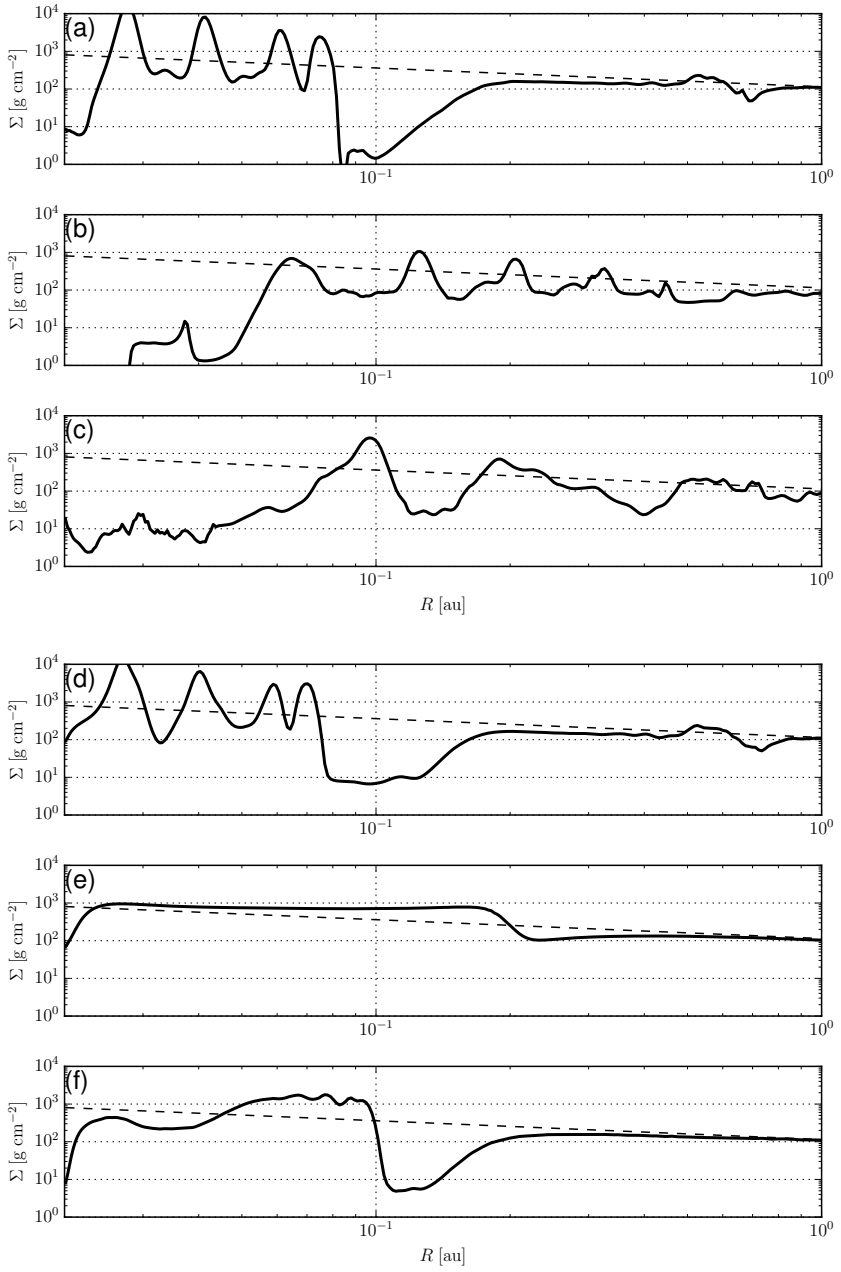

Fig. 2.10.— Surface density profiles. Both columns compare the reference simulation (top row) to two simulations below it at a given simulation time. The initial surface density profile is shown for comparison (dashed). (a) reference, (b) D_4, and (c) beta_3 at $t = 1650t_0$, and (d) reference, (e) D4, and (f) beta3 at $t = 1800t_0$.

The connection can be understood with the help of a second diffusivity parameter $D_m \equiv \eta/(hv_A)$, where v_A is the Alfvén speed; it is the inverse of the standard Lundquist number in plasma physics, $S \equiv hv_A/\eta$, and is related to the first diffusivity parameter as $D_m = \sqrt{\beta/2}\ D$. It measures the importance of the resistive magnetic diffusion on magnetically induced motions. Obviously, a lower resistivity would lead to a better coupling between the magnetic field and the matter. Perhaps less obvious is that a stronger magnetic field would also lead to a better field-matter coupling. This is because a stronger field induces a faster motion over a given length-scale, which leaves less time for the field lines to diffuse resistively relative to the matter. In this sense, the diffusivity parameter D_m provides a better indicator for how the coupled disk-wind system behaves: the smaller D_m is, the more important the avalanche accretion streams would become. Conversely, the streams are suppressed by a large enough D_m (analogous to the suppression of the MRI). This explanation applies not only to models with different parameters, but also across different regions of the reference model. For example, it naturally explains why an avalanche accretion stream develops only at the largest radius (Zone III) of the reference simulation, where the parameter D_m is the lowest because it initially decreases with radius as $r^{-1/2}$.

2.4.3 Disk thickness/temperature

In the simulation t4, the disk aspect ratio ϵ is increased by a factor of two, thereby increasing the initial disk temperature by a factor of four (see Table 2.1). To keep β and D_0 (and $D_{m,0}$) the same as the reference run, we increase the initial poloidal field strength $B_{p,0}$ by a factor of two and the resistivity η by a factor of four. In this simulation, there is an extended period of time where a stable disk wind is launched within a radius of $r < 0.5$ au. Immediately outside of this is an avalanche accretion

stream that terminates at $r \approx 0.5$ au. The mass deposited by the stream grows fast enough to form a ring (see Fig. 2.8(g) and (i)), while the disk region beneath the stream moves radially outward (Fig. 2.8(h)). This provides the cleanest evidence that a ring can be formed directly from a stream. This ring formation process was also present in the reference model, where it increased the surface density at $r = 0.5$ au by a factor of five relative to its neighboring gap (at a slightly larger radius). The effect is even more noticeable in model t4, with the surface density contrast between the ring and gap increased to a factor of 40. We again see an anti-correlation between the surface density and magnetic flux for the rings and gaps created via an avalanche accretion stream. Naturally, material being deposited at the end of the accretion stream will increase the disk mass locally, but the magnetic flux will not increase here because the mass accretion through the stream is nearly parallel to the field that confines the flow. The magnetic flux is reduced in the region under the stream that has been moving radially outward.

2.4.4 Resolution

In order to study the effects of the grid resolution on the simulations, we increase the disk resolution by a factor of two in the θ-coordinate direction in model ref-x2grid. The grid now contains 240 uniformly-spaced cells from $\theta = \pi/3$ to $\pi/2$ and 120 non-uniform cells from $\theta = \pi/3$ to the polar axis ($\theta = 0$) with a constant ratio for the widths of adjacent cells (see Section 2.2.3). In order to match the cell aspect ratio with all previous simulations, we also decrease the value of dr_0 by two (dr_0 is the width of the first cell on the r-grid). This simulation has the same qualitative evolution as the reference run, and we can separate the disk evolution into three zones with radial delineations matching those described for the reference run. The primary

difference seen between the reference run and the high resolution run is in the number of rings/gaps formed in Zone I. There are up to three rings at any one time in the high resolution run, but by $t = 1650t_0$ they have accreted to form one large ring outside the inner boundary at $r = 0.03$ au. The remaining zones follow similar behavior to the reference run, indicating that the qualitative behavior of the disk-wind system – especially the disk-wind variability and the ring, gap, and stream formation – are independent of the simulation resolution.

2.5 Discussion

2.5.1 Comparison with other work

2.5.1.1 Steady disk-wind

Although one of the focuses of this work is on the variability of winds and their impact on forming radial structures in disks, previous studies have focused largely on steady winds such as those seen in Zone II of the reference simulation. Many authors aim to explore the parameter space of disk properties in an effort to connect them to properties of the wind (e.g., Tzeferacos et al. 2009; Murphy et al. 2010; Sheikhnezami et al. 2012; Stepanovs & Fendt 2014; Stepanovs & Fendt (2016)). In these works, the resistivity often takes the form $\eta \propto hv_A$ inside the disk and zero outside. The scaling of this expression is chosen such that the inward accretion and outward diffusion of magnetic flux are able to reach a quasi-steady state, with a fraction of the disk material getting launched into the wind, thereby driving disk evolution through angular momentum removal. Such steady-state solutions, while important for illuminating the physics of wind-launching and for making connection with analytic work, are not guaranteed in nature. There is no *apriori* reason why

the Lundquist number $S \equiv \eta/(hv_A)$ should be spatially constant or of order unity, especially in the inner disks where the electron number density varies rapidly with radius (caused by collisional ionization of the alkali metals and/or thermionic emission from dust grains; Umebayashi & Nakano 1981; Desch & Turner 2015). We have shown that, in the simplest illustrative case of a constant resistivity, a steady-state is not reached in general.

Stepanovs & Fendt (2016) have shown that winds can be launched for disks with plasma-β from $10^{0.7}$ to $10^{3.5}$. They have also confirmed that there is a critical magnetization below which the launching mechanism transitions from the classical magneto-centrifugal mechanism of Blandford & Payne (1982) to the magnetic tower mechanism driven by the toroidal magnetic pressure gradient (Lynden-Bell 1996). This transition occurs near $\beta \approx 30$. Our simulations typically have $\beta \approx 10^3$ (specifically in Zone II of the reference simulation, $\beta = 10^{2.36}$ at $r = 0.3$ au after $t = 1800t_0$), so our finding that the wind is in the magnetic tower regime (see Section 2.3.3.1) is consistent with previous work. This is also consistent with the 1D analytic model of Bai et al. (2016), who found that the disk wind tends to be driven by a magnetic pressure gradient unless the Alfvén speed near the disk surface is much larger than the local Keplerian speed. Given the small magnetic lever arm in this regime, the mass loading rate is high and the wind speed remains low in the steady part of the wind.

2.5.1.2 Rings and gaps

In the era of ALMA, rings and gaps are being observed in an increasing number of disks, including, e.g., HL Tau (ALMA Partnership et al. 2015), TW Hya (Andrews et al. 2016), and HD 163269 (Isella et al. 2016). The most commonly invoked explanations for such features are that they are cleared by planets (Dong et al. 2015) or

are the result of the condensation of abundant volatile compounds (i.e., snowlines; Zhang et al. 2016). In almost all of the disks simulated in this work, gaps are opened with surface density contrast ratios of at least one order of magnitude. The fact that gaps can be created purely through MHD processes is interesting in its simplicity. The mechanism requires only a magnetized disk with an accretion rate that varies as a function of radius. In our simulations, one way to achieve this variation is through an MHD disk wind that carries away differing amounts of angular momentum from different radial locations in the disk. The magnetic torque acting on the surface of the disk then results in a mass accretion rate of $\dot{M}_{\rm acc}(R) \approx RB_\theta B_\phi/\Omega_K$ (Bai et al. 2016, see their equation 19). Therefore, a magnetic disk wind can open a gap (or create a ring) so long as $B_\theta B_\phi$ reaches a local maximum (or minimum) somewhere in the disk. In our particular problem setup, the rings and gaps are formed within a few au of the central mass because only such inner regions have short enough orbital periods to evolve through multiple orbits in the duration of the simulation. However, this mechanism should operate at larger disk radii as long as the magnetic disk wind is able to redistribute angular momentum on these scales as well (Bjerkeli et al. 2016).

Several other MHD mechanisms have been proposed for the creation of radial surface density maxima in disks. For example, the simulations of Flock et al. (2015) and Ruge et al. (2016) have shown that a surface density bump is formed inside the MRI dead zone of a disk, while a gap is opened up outside the dead zone due to MRI-driven mass accretion. The authors find an anti-correlation between the magnetic field and surface density (similar to that shown in Fig. 2.7) as the magnetic field accumulates in the MRI-active gap outside the dead zone. A related phenomenon are the so-called 'zonal flows' (Johansen et al. 2009). Zonal flows occur when a radial pressure gradient is balanced by the Coriolis force, leading to alternating radial bands

of sub and super-Keplerian flows (see Armitage 2015 for a recent review). These flows develop in MRI disk simulations from large-scale variations in the Maxwell stress ($B_r B_\phi$) and result in an anti-correlation between the magnetic pressure and the mass density (Johansen et al. 2009; Kunz & Lesur 2013; Bai & Stone 2014). In global disk simulations, zonal flows and zonal (magnetic) fields can be generated by the Hall effect because the additional Hall term in the induction equation can act to radially confine the vertical magnetic flux (Béthune et al. 2017, 2016). The rings and gaps that form in our simulations share some characteristics with the zonal flows (e.g., both show an anti-correlation between surface density and magnetic pressure), but their formation mechanisms are quite distinct.

In addition to variable magnetic winds, our simulations show that rings can also form directly out of rapidly accreting streams. This ring formation mechanism is observed most clearly in the simulation with a larger initial disk thickness (or temperature; model t4, Section 2.4.3), and to a lesser extent in the reference simulation (Zone III; Section 2.3.3.2). The streams most likely play a role in forming the rings and gaps observed in several other simulations as well, especially in the lower resistivity (D_4) and stronger field (beta_3) cases, where the disk evolution is dominated by a stream-induced envelope. The concept of avalanche accretion streams itself is not new; Kudoh et al. (1998) found such streams in their 2D simulations of thick AGN accretion disks (where the streams were termed 'accretion avalanches'; see also Stone & Norman 1994; Matsumoto et al. 1996; Beckwith et al. 2009). What we have shown here is that such avalanche streams tend to develop in regions of low dimensionless magnetic diffusivity D_m (or high Lundquist number $S = 1/D_m$) and that they can deposit material at fixed locations quickly enough to form rings in some cases or generate enough spatial variation in mass accretion to produce multiple rings and gaps

in others.

2.5.2 Magnetic diffusion and wind-dominated vs. stream-dominated accretion

We found two distinct modes of accretion in coupled disk-wind systems initially threaded by a relatively weak, ordered poloidal magnetic field. They are controlled by the dimensionless magnetic diffusivity parameter D_m (or the Lundquist number $S = 1/D_m$). Low values of D_m promote the formation of avalanche accretion streams, leading to a 'stream-dominated' mode of accretion. Higher values of D_m suppress stream formation, leading to a more steady wind that drives accretion in a more laminar disk, i.e., a 'wind-dominated' mode of accretion. If D_m becomes too large, the strong wind dies out quickly as the wind-launching magnetic field weakens due to diffusion.

The zero diffusivity limit has recently been explored in the 3D ideal MHD simulations of Zhu & Stone (2018) that came to our attention near the conclusion of this investigation. Their study has several aspects in common with the work presented here; for example, both concentrate on relatively thin disks (disk thickness $5 - 10$ per cent of the radius), both adopt a large-scale poloidal magnetic field initially corresponding to a typical plasma-β of 10^3 on the disk midplane, and both employ a spherical-polar coordinate system. The main differences are that (1) their simulations are fully 3D, whereas ours are 2D axisymmetric, and (2) their simulations are formally ideal MHD, whereas we included explicit resistivity. Despite these differences, there is qualitative agreement regarding some key features of the simulations. One of the most intriguing features of our 2D simulations is the development of fast accreting avalanche streams near the disk surface. Zhu & Stone (2018) also observes

the simultaneous fast accretion at high altitudes and slow expansion on the mid-plane, where the fast accretion occurs in a thick layer above the disk extending up to $\sim 1-1.5$ times the local radius (which they term 'disk corona'). We believe that their disk corona is physically equivalent to the thick envelope found in our low diffusivity ($D_{m,0}$) cases. In our case, the thick envelope is produced by the repeated formation and disruption of multiple avalanche accretion streams, as can be seen in Fig. 2.8 (also see movies in the online journal). Although it is not discussed explicitly in their work, we suspect that a similar mechanism is responsible for forming the corona in their simulations as well, although it may be harder to identify rapidly infalling streams in 3D simulations than in 2D ones. The avalanche streams tend to drag the field lines into a radial configuration, which are then wound up by differential rotation. This naturally produces the $r-\phi$ magnetic stress that is found by Zhu & Stone (2018) to dominate the coronal accretion. In any case, our simulations add weight to the emerging picture that a chaotic, fast accreting 'corona' or envelope plays a crucial role in shaping the structure and evolution of thin disks threaded by relatively weak ($\beta \sim 10^3$), open magnetic field lines, especially when the magnetic diffusivity is low.

In more magnetically diffusive disks with larger values of D_m, the situation can be quite different. On one hand, the explicit diffusivity can enable outward field diffusion by itself, allowing for the possibility of a steady-state balance between the outward diffusion and the inward advection of field lines by mass accretion. On the other hand, it can suppress the MRI in the disk and thus remove the turbulent diffusivity that could also enable such a state. This field advection-diffusion balance is illustrated in Zone II of the reference run (Fig. 2.5), where the disk connects smoothly to the wind. One might be tempted to identify the subsonic region at the base of the wind as the 'corona', which has a similar height ($z \sim R$) in the simulations of Zhu & Stone

(2018). However, this subsonic wind base is expanding slowly, and the fast accretion (with an effective α parameter of ~ 2) is limited to the high density disk proper (see Fig. 2.5(c)). Most of the accretion in the more diffusive cases is through the disk and is driven by the magnetic torque from the wind; this is in contrast to the ideal MHD simulations of Zhu & Stone (2018), where the wind plays only a minor role in driving the accretion. Wind-driven accretion appears to hold for other 2D non-ideal MHD simulations of coupled disk-wind systems that include either resistivity (e.g., Stepanovs & Fendt (2016)) or ambipolar diffusion and the Hall effect (Bai & Stone 2017). Whether it stays true in 3D or not remains to be determined. In any case, our results, together with those of Zhu & Stone (2018) and others, suggest that explicit magnetic diffusion from non-ideal MHD effects plays a key role in determining the extent to which the accretion is dominated by a wind or by a thick 'corona'/stream-induced envelope.

We speculate that the two modes of accretion may be unified in the following sense. For a thin disk magnetized with a relatively weak poloidal magnetic field, a toroidal magnetic field is quickly generated. This would naturally 'puff up' the disk in the vertical direction, creating a thick envelope that is supported by the magnetic pressure gradient vertically (see also Hirose & Turner 2011) and by rotation in the cylindrical R-direction. This rotationally supported envelope can become unstable to the MRI, just as the disk, especially when the dimensionless magnetic diffusivity D_m is low. Indeed, its larger vertical extent makes the envelope more prone to the MRI than the thin disk itself. When the diffusivity D_m is high, the MRI is suppressed in the envelope, which allows the magnetic pressure gradient-driven expansion that produced the envelope to continue smoothly to larger distances, forming a slow wind.

2.5.3 Implications of ring and gap formation on dust dynamics and planet formation

It is well-understood that an outward radial pressure gradient in a disk causes the gas to rotate at a sub-Keplerian velocity. Consequently, grains that orbit at the Keplerian speed would experience a headwind, lose angular momentum, and migrate inward (Weidenschilling 1977a). If, however, the radial pressure gradient is reversed due to a 'bump' in the disk surface density, this local maximum is able to halt the inward radial drift of particles and trap them there. In 3D, these radial bumps in the disk surface density can lead to the growth of the Rossby wave instability (RWI), whereby a high pressure nonaxisymmetric vortex grows exponentially, creating an azimuthal dust trap (Lovelace et al. 1999). Azimuthally asymmetric features are observed in disks and can be explained by azimuthal variations in the gas-to-dust ratio and grain size segregation (Casassus et al. 2013). The formation of radial and azimuthal pressure traps are critical for stopping solid particles from spiraling into the star on rapid timescales, thereby allowing the onset of grain growth and the eventual formation of planetesimals.

The emergence of multiple radial density maxima in the simulations presented here shows the potential importance that MHD disk winds and avalanche streams can have on growing the seeds of planet formation. This is especially true in the inner ($\lesssim 1$ au) regions of the disks, where jets and winds of young stellar objects are most likely launched and where the most common type of planets (super-Earths/mini-Neptunes) are located. Indeed, Sun-like stars have a 50 per cent chance of having a compact system of small (non-giant) planets within 1 au (Winn & Fabrycky 2015). While the importance of migration for this population of planets is still unknown, it seems plausible that many of these planets may have formed at their current loca-

tions. If this is the case, an efficient mechanism is needed for trapping dust grains on sub-au scales, especially during the relatively early phases of star formation when most of the mass is processed through the inner disk. Rings and gaps produced by variable magnetic winds and avalanche streams that drive rapid accretion potentially provide an opportunity for grains to accumulate and grow early in the disk's life. This mechanism will likely not be as efficient at later times when YSO jets and winds are observed to be less powerful and the accretion rate is lower. More work is needed to quantify the effects that the disk structures created by magnetically driven winds and avalanche streams have on the dynamics and growth of dust grains.

2.5.4 Future directions

The initial set of idealized simulations presented in this work is aimed at illustrating the basic processes through which rings and gaps are produced by variable winds and avalanche accretion streams. In future refinements we will extend the simulations to a less restrictive geometry. Preliminary 2D (axisymmetric) simulations with two hemispheres show qualitatively similar results to those presented here. Full 3D simulations, such as those of Zhu & Stone (2018) but with non-ideal MHD effects, will be needed to determine whether the formation of rings and gaps is artificially enhanced by the axisymmetric geometry and whether the rings formed in 2D simulations are unstable to the Rossby wave instability. Just as important, there is a need to include a detailed calculation of the ionization structure of the disk and the non-ideal MHD effects. Post-processing the simulations through radiative transfer calculations is needed to make predictions for observable quantities (e.g., variability in near infrared emission and profiles of optical forbidden lines) that can be compared directly with observations (e.g., Cody et al. 2014; Simon et al. 2016). The long term

goal is to include a self-consistent treatment of dust grains in the full 3D non-ideal MHD coupled disk-wind simulations. This would allow us to quantify the effects that wind and stream-induced disk structures have on grain trapping and growth, as well as any potential back-reaction that the grains might have on the gas dynamics of disk accretion, stream formation, and wind launching. The rings and gaps found in our starting simulations provide added impetus to explore the interplay between dust dynamics and winds and streams in greater depth.

2.6 Conclusions

We have presented the results of 2D (axisymmetric) resistive MHD simulations of coupled disk-wind systems with a range of disk parameters (resistivity, magnetic field strength, and temperature), focusing on geometrically thin disks. We find that the structure and dynamics of the disk-wind system strongly depend on the dimensionless magnetic diffusivity parameter $D_m \equiv \eta/(hv_A)$ and that interesting disk features, including rings and gaps, are naturally produced. Specifically, we find that:

1. There are two distinct modes of accretion depending on the dimensionless parameter D_m. Disks with low values of D_m, from either a small resistivity or high field strength, tend to develop fast 'avalanche accretion streams'. The rapid formation and disruption of such streams often leads to a clumpy, thick envelope above the disk that dominates the dynamics of the system (e.g., models beta_3 and D_4; see Fig. 2.8), although a highly variable wind is still launched above the envelope. This envelope appears equivalent to the thick disk 'corona' found independently by Zhu & Stone (2018) in their 3D ideal MHD simulations. In both cases, the disk below the corona/envelope is often expanding radially outward. The streams (and the thick clumpy envelope they produce) are suppressed

in simulations with larger values of D_m (from either a large resistivity or low field strength, e.g., models beta3 and D4). In these more diffusive (larger D_m) simulations, most of the accretion occurs through a laminar thin disk rather than the thick clumpy envelope, and the disk accretion is driven mainly by a magnetic wind.

2. Both wind-dominated and stream-dominated accretion create prominent features in the surface density distribution, especially rings and gaps. The wind-driven ring and gap formation is illustrated most clearly in the innermost region (Zone I) of the reference simulation, where there is substantial redistribution of magnetic flux relative to the mass in the disk that is enabled by the resistivity (Fig. 2.7). Regions with lower mass-to-flux ratios tend to drive stronger winds and accrete faster, producing gaps; those with higher mass-to-flux ratios tend to accrete more slowly, allowing matter to accumulate and form dense rings. Another clear illustration of wind-driven gap formation can be found in models D4 and beta3, where a strong wind is driven from the outer part of the disk but not from the more magnetically diffusive inner part, creating a deep gap between them (Fig. 2.10(e) and (f)). The stream-driven ring formation is illustrated most clearly in the thicker disk model (t4), where a stream feeds a prominent ring at a roughly constant radius (Fig. 2.8, right column). Rings formed this way also have high mass-to-flux ratios. Multiple rings and gaps are formed in other, more complicated cases, especially those with stream-induced envelopes (model D_4 and beta_3). It is likely that both magnetic winds and avalanche accretion streams play a role in their formation, although the relative importance of the two mechanisms is hard to quantify due to the complexity of the flow pattern inside and above the disk.

3. Powerful winds are launched despite the fact that the magnetic field in the disk is rather weak initially (corresponding to a typical plasma-$\beta \sim 10^3$). In the reference simulation where the wind is analyzed in detail, we find that the bulk of the wind is heavily mass-loaded and accelerated by the magnetic pressure gradient to relatively low speeds (a few $\times 10$ km s^{-1}). There are, however, lightly mass-loaded regions that are accelerated magnetocentrifugally to speeds exceeding 100 km s^{-1}, comparable to the jet speeds observed in young stellar objects. The magnetic wind can remove angular momentum from the disk efficiently, leading to disk accretion with an effective α parameter up to order unity. Our simulations add weight to the notion of wind-driven disk evolution, especially in the presence of a suitable level of magnetic diffusivity.

Rings and gaps produced in circumstellar disks by magnetic winds and avalanche accretion streams have important implications on the dynamics and growth of dust grains and ultimately planet formation. The local pressure maxima associated with the rings would act to stop the radial drift of solid particles, possibly trapping them long enough to enable enhanced grain growth that facilitates planetesimal formation. This may be especially important in the inner (i.e., few tenths of an au) disk regions where the largest population of planets reside, as seen by *Kepler*. The simulations presented in this work lay the foundation for future explorations of these and other aspects of the coupled disk-wind systems.

Chapter 3

Ambipolar diffusion and reconnection

This Chapter is adapted from Suriano et al. 2018, MNRAS, 477, 1239, with minimal modifications.

Abstract

Radial substructures in circumstellar disks are now routinely observed by ALMA. There is also growing evidence that disk winds drive accretion in such disks. We show through 2D (axisymmetric) simulations that rings and gaps develop naturally in magnetically coupled disk-wind systems on the scale of tens of au, where ambipolar diffusion (AD) is the dominant non-ideal MHD effect. In simulations where the magnetic field and matter are moderately coupled, the disk remains relatively laminar with the radial electric current steepened by AD into a thin layer near the midplane. The toroidal magnetic field sharply reverses polarity in this layer, generating a large magnetic torque that drives fast accretion, which drags the poloidal field into a highly

pinched radial configuration. The reconnection of this pinched field creates magnetic loops where the net poloidal magnetic flux (and thus the accretion rate) is reduced, yielding dense rings. Neighbouring regions with stronger poloidal magnetic fields accrete faster, forming gaps. In better magnetically coupled simulations, the so-called 'avalanche accretion streams' develop continuously near the disk surface, rendering the disk-wind system more chaotic. Nevertheless, prominent rings and gaps are still produced, at least in part, by reconnection, which again enables the segregation of the poloidal field and the disk material similar to the more diffusive disks. However, the reconnection is now driven by the non-linear growth of MRI channel flows. The formation of rings and gaps in rapidly accreting yet laminar disks has interesting implications for dust settling and trapping, grain growth, and planet formation.

3.1 Introduction

Observations with the Atacama Large Millimeter/submillimeter Array (ALMA) have revealed that many circumstellar disks contain intricate radial substructures (ALMA Partnership et al. 2015; Andrews et al. 2016; Zhang et al. 2016; Nomura et al. 2016; Pérez et al. 2016; Isella et al. 2016; Cieza et al. 2016; van der Plas et al. 2017; Fedele et al. 2017), opening the door for previously inaccessible studies of the physical nature of disks. A number of physical processes have been proposed to explain the formation of rings and gaps in disks, including gap clearing by planets (Dong et al. 2015; Dipierro et al. 2015; Dong et al. 2017; Bae et al. 2017), rapid pebble growth at the condensation fronts of abundant volatile species (Zhang et al. 2015), the pileup of volatile ices in sintering zones just outside snow lines (Okuzumi et al. 2016), sharp changes in the disk viscosity at the boundaries of non-turbulent 'dead zones' (Flock et al. 2015; Ruge et al. 2016), magnetic self-organization through zonal flows (Béthune et al. 2017), and

the secular gravitational instability (Takahashi & Inutsuka 2014).

We presented, in Suriano et al. (2017), a novel mechanism for forming rings and gaps in magnetically coupled disk-wind systems in the presence of Ohmic resistivity, which is the dominant non-ideal magnetohydrodynamic (MHD) effect in the inner (sub-au) part of the disk (Wardle 2007; Turner et al. 2014b). It relies on a magnetically driven disk wind (Blandford & Payne 1982) to remove angular momentum from the disk at a rate that varies strongly with radius, leading to a large spatial variation in accretion rate and thus the disk surface density. Observationally, there is now growing evidence for rotating winds removing angular momentum from disks (Simon et al. 2016; Hirota et al. 2017; Tabone et al. 2017; Lee et al. 2018). Theoretically, a picture of wind-driven disk evolution is also beginning to emerge, with non-ideal MHD effects (Ohmic resistivity, ambipolar diffusion, and the Hall effect) suppressing MHD turbulence from the magnetorotational instability (MRI; Balbus & Hawley 1991) over a wide range of radii, which leaves MHD disk winds as the primary driver of disk accretion in these regions (Fleming et al. 2000; Fleming & Stone 2003; Bai & Stone 2011, 2013; Kunz & Lesur 2013; Gressel et al. 2015).

In this follow-up work, we focus on the intermediate radii of young star disks (a few to tens of au) where ambipolar diffusion (AD) starts to become the most important non-ideal MHD effect, especially in the upper layers of the disk (Wardle 2007; Turner et al. 2014b). We find that rings and gaps are naturally produced in the presence of a significant poloidal magnetic field, just as in the resistive case studied in Suriano et al. (2017). We show that a relatively laminar disk-wind system develops in the presence of a relatively strong ambipolar diffusion, which makes it easier to analyse the simulation results and identify a new mechanism for ring and gap formation. The mechanism is driven by reconnection of the highly pinched poloidal magnetic field in

a midplane current sheet steepened by ambipolar diffusion (Brandenburg & Zweibel 1994), in a manner that is reminiscent of the tearing mode (Furth et al. 1963) or the pinch-tearing mode (Latter et al. 2009). We show that the reconnection leads to weakening of the poloidal field in some regions, which accrete more slowly and form rings, and field concentration in others, where accretion is more efficient creating gaps.

The rest of the Chapter is organized as follows. In Section 3.2 we describe the simulation setup, including the equations solved, the initial disk model, and the boundary conditions. Section 3.3 analyses the results of a reference simulation in detail and explains how rings and gaps are formed in the coupled disk-wind system in the presence of relatively strong ambipolar diffusion. In Section 3.4 we explore how changes in the magnetic field and ambipolar diffusion strength modify the picture of the reference run. In Section 3.5 we compare to other similar works in the field and discuss the implications of our work on dust settling, growth, and trapping that are important to the formation of planetesimals and planets. Finally, Section 3.6 concludes with the main results of this study.

3.2 Problem setup

3.2.1 MHD equations

We use the ZeusTW code (Krasnopolsky et al. 2010) to solve the time-dependent magnetohydrodynamic (MHD) equations in axisymmetric spherical coordinates (r, θ, ϕ). The ZeusTW code is based on the ideal MHD code, ZEUS-3D (version 3.4; Clarke 1996, 2010), which is itself developed from ZEUS-2D (Stone & Norman 1992a,b). In the ZeusTW code, Ohmic resistivity is treated using the algorithm described in

Fleming et al. (2000) and AD is implemented using the fully explicit method of Mac Low et al. (1995) (see also Li et al. 2011). The equations solved are

$$\frac{\partial \rho}{\partial t} + \nabla \cdot (\rho \boldsymbol{v}) = 0, \tag{3.1}$$

$$\rho \frac{\partial \boldsymbol{v}}{\partial t} + \rho \left(\boldsymbol{v} \cdot \nabla \right) \boldsymbol{v} = -\nabla P + \boldsymbol{J} \times \boldsymbol{B}/c - \rho \nabla \Phi_g, \tag{3.2}$$

$$\frac{\partial \boldsymbol{B}}{\partial t} = \nabla \times (\boldsymbol{v} \times \boldsymbol{B}) - \frac{4\pi}{c} \nabla \times \left(\eta_O \boldsymbol{J} + \eta_A \boldsymbol{J}_\perp \right), \tag{3.3}$$

$$\frac{\partial e}{\partial t} + \nabla \cdot (e \boldsymbol{v}) = -P \nabla \cdot \boldsymbol{v}, \tag{3.4}$$

where the internal energy is $e = P/(\Gamma - 1)$ and Γ is the adiabatic index. The current density is $\boldsymbol{J} = (c/4\pi) \nabla \times \boldsymbol{B}$ and the current density perpendicular to the magnetic field is $\boldsymbol{J}_\perp = -(\boldsymbol{J} \times \boldsymbol{B}) \times \boldsymbol{B}/B^2$. The Ohmic resistivity is η_O and the effective ambipolar diffusivity η_A is defined as

$$\eta_A = \frac{B^2}{4\pi \gamma \rho \rho_i}, \tag{3.5}$$

where ρ_i is the ion density and $\gamma = \langle \sigma v \rangle_i / (m + m_i)$ is the frictional drag coefficient with units of cm^3 g^{-1} s^{-1}. The remaining parameters have their usual definitions. When referring to cylindrical coordinates, we will use the notation (R, ϕ, z) such that $R = r \sin\theta$ and $z = r \cos\theta$.

3.2.2 Initial conditions

The initial conditions are similar to those in Suriano et al. (2017). We describe them here in detail for completeness. Specifically, the simulation domain is separated into two regions: a thin, cold, rotating disk orbiting a 1 $M_\odot$ central source at the grid origin

and an initially non-rotating, hot corona above the disk that is quickly replaced by a magnetic wind driven from the disk. We choose the adiabatic index to be $\Gamma = 1.01$ so that the material in the simulation domain is locally isothermal in the sense that any parcel of disk material nearly retains its initial temperature no matter where it moves. The initial temperature distribution is assumed to decrease with radius as a power-law $T \propto r^{-1}$, so that the sound speed is proportional to the local Keplerian speed.

3.2.2.1 Disk

The geometrically thin disk is characterized by the dimensionless parameter $\epsilon = h/r = c_s/v_K \ll 1$, where h is the disk scale height, c_s is the isothermal sound speed, and v_K is the Keplerian speed. The initial value of ϵ is set to 0.05 for all simulations in this work. The disk is limited to the equatorial region where the polar angle $\theta \in [\pi/2 - \theta_0, \pi/2 + \theta_0]$, with disk (half) opening angle set to $\theta_0 = \arctan(2\epsilon)$, i.e., the initial disk half-thickness is set to twice the scale height. This choice is somewhat arbitrary, but a more elaborate treatment of the initial disk surface is not warranted because the structure of the disk surface is quickly modified by a magnetic wind. The disk density takes the form of a radial power law multiplied by a Gaussian function of $z/r = \cos\theta$,

$$\rho_d(r,\theta) = \rho_0 \left(\frac{r}{r_0}\right)^{-\alpha} \exp\left(-\frac{\cos^2\theta}{2\epsilon^2}\right), \tag{3.6}$$

as determined by hydrostatic balance. The subscript '0' refers to values on the disk midplane at the inner radial boundary. For all simulations shown in this paper, we use $\alpha = 3/2$. The disk pressure is set as

$$P_d(r,\theta) = \rho_d c_s^2, \tag{3.7}$$

with $c_s = \epsilon v_K$. The radial pressure gradient causes the equilibrium rotational velocity v_ϕ to be slightly sub-Keplerian,

$$v_\phi = v_K \sqrt{1 - (1+\alpha)\epsilon^2}. \tag{3.8}$$

3.2.2.2 Corona

We require that the hydrostatic corona is initially in pressure balance with the disk surface. This constraint sets the density drop from the disk surface to the corona by $1/[(1+\alpha)\epsilon^2] = 160$, and a corresponding increase in temperature from the disk surface to the corona by the same factor. Therefore, the coronal density and pressure are

$$\rho_c(r) = \rho_0 \epsilon^2 (1+\alpha) \exp\left[-\frac{\cos^2\theta_0}{2\epsilon^2}\right] \left(\frac{r}{r_0}\right)^{-\alpha} \equiv \rho_{c,0} \left(\frac{r}{r_0}\right)^{-\alpha}, \tag{3.9}$$

$$P_c(r) = \rho_c v_K^2/(1+\alpha). \tag{3.10}$$

It is, however, important to note that the initial hot coronal material is quickly replaced by the colder disk material that remains nearly isothermal as it is launched from the disk surface into a wind.

3.2.2.3 Magnetic field

To ensure that the magnetic field is divergence-free initially, we set the magnetic field components using the magnetic flux function Ψ as in Zanni et al. (2007),

$$\Psi(r,\theta) = \frac{4}{3} r_0^2 B_{\rm p,0} \left(\frac{r\sin\theta}{r_0}\right)^{3/4} \frac{m^{5/4}}{\left(m^2 + \cot^2\theta\right)^{5/8}}, \tag{3.11}$$

where $B_{\rm p,0}$ sets the scale for the poloidal field strength and the parameter m controls the bending of the field. The value of $B_{\rm p,0}$ is set by the initial plasma-β, the ratio of

the thermal to magnetic pressure, on the disk midplane, which is approximately 10^3 (0.922×10^3 to be more exact) for most of the simulations. Since varying m from 0.1 to 1 has little effect on the long-term disk or wind magnetic field structure (Stepanovs & Fendt 2014), we use $m = 0.5$ for all simulations presented in this work. The initial magnetic field components are then calculated as

$$B_r = \frac{1}{r^2 \sin\theta} \frac{\partial \Psi}{\partial \theta}, \tag{3.12}$$

$$B_\theta = -\frac{1}{r \sin\theta} \frac{\partial \Psi}{\partial r}. \tag{3.13}$$

3.2.3 Ambipolar diffusion

The magnetic diffusivities associated with non-ideal MHD effects, including ambipolar diffusion, depend on the densities of charged particles, which can in principle be computed through detailed chemical networks (e.g., Bai & Goodman 2009). Here, as a first step toward a comprehensive model, we will simply parametrize the density of ions as

$$\rho_i = \rho_{i,0} f(\theta) \left(\frac{\rho}{\rho_0} \right)^{\alpha_{AD}}, \tag{3.14}$$

where

$$f(\theta) = \begin{cases} \exp\left(\frac{\cos^2(\theta+\theta_0)}{2\epsilon^2}\right) & \theta < \pi/2 - \theta_0 \\ 1 & \pi/2 - \theta_0 \leq \theta \leq \pi/2 + \theta_0 \\ \exp\left(\frac{\cos^2(\theta-\theta_0)}{2\epsilon^2}\right) & \theta > \pi/2 + \theta_0. \end{cases} \tag{3.15}$$

The angular dependence $f(\theta)$ is chosen such that, at a given radius, the ion density increases rapidly in the tenuous disk atmosphere, to mimic the ionization by high energy photons (UV and X-rays) from the central young star in addition to cosmic rays (e.g., Umebayashi & Nakano 1981; Perez-Becker & Chiang 2011a; Glassgold et al.

2017). In the simulations presented in this work, we take $\alpha_{AD} = 0.5$. This power-law dependence for the ion density is roughly what is expected when the volumetric cosmic ray ionization rate is balanced by the recombination rate of ions and electrons, under the constraint of charge neutrality (i.e., $\zeta n \propto n_e n_i \propto n_i^2$, where ζ is the cosmic ray ionization rate per hydrogen nucleus; see page 362 of Shu 1992).

The magnitude of the ion density, and therefore the ion-neutral drag force, $\boldsymbol{F_d} = \gamma\rho\rho_i(\boldsymbol{v_i} - \boldsymbol{v})$, is sometimes quantified through the dimensionless ambipolar Elsasser number (Chiang & Murray-Clay 2007; Perez-Becker & Chiang 2011b; Bai & Stone 2011),

$$\Lambda = \frac{\gamma\rho_i}{\Omega} = \frac{v_A^2}{\eta_A\Omega}, \tag{3.16}$$

where γ is the frictional drag coefficient. Physically, the Elsasser number is the collision frequency of a neutral particle in a sea of ions of density ρ_i, normalized to the Keplerian orbital frequency. For example, the Elsasser number will be unity when the neutral particle collides 2π times in one orbital period. As the neutral-ion collision frequency increases to infinity, so does the Elsasser number, and the bulk neutral medium becomes perfectly coupled to the ions/magnetic field (i.e., the ideal MHD limit). Similarly, as the Elsasser number drops to zero, the neutrals and ions no longer collide; the neutrals are entirely decoupled from the magnetic field. For our reference simulation, we choose the Elsasser number to be $\Lambda_0 = 0.25$ at the inner boundary on the disk midplane, but will vary this parameter to gauge its effects on the coupled disk-wind system. The choice of $\alpha_{AD} = 0.5$, assuming that the drag coefficient γ is constant, implies that the Elsasser number is proportional to $r^{3/4}$, thus larger radii are better coupled than smaller radii in the reference simulation.

In some cases, we have considered an explicit Ohmic resistivity η_O in addition to ambipolar diffusion. In these cases, it is useful to compute the effective ambipolar

diffusivity η_A according to equation (3.5), to facilitate the comparison of the two effects.

3.2.4 Grid

The equations are solved for $r \in [1, 100]$ au and $\theta \in [0, \pi]$. The radial grid limits are chosen such that they encompass the anticipated disk region where ambipolar diffusion is the most important non-ideal effect, especially in the upper layers of the disk (Turner et al. 2014b). A 'ratioed' grid is used in the radial direction such that $dr_{i+1}/dr_i = 1.012$ is constant and $r_{i+1} = r_i + dr_i$. The grid spacing at the inner edge is set as $dr_0 = 2.3 r_0 d\theta$. The grid is uniform in θ with a resolution of $n_r \times n_\theta = 400 \times 720$. This results in 24 grid cells from the disk midplane to surface (at two disk scale heights) in the reference run.

3.2.5 Boundary conditions

Both the inner and outer radial boundaries use the standard outflow condition in Zeus codes, where the flow quantities in the first active zone are copied into the ghost zones except for the radial component of the velocity, v_r, which is set to zero in the ghost zones if it points into the computation domain in the first active zone (i.e., if $v_r > 0$ in the first active zone at the inner radial boundary or $v_r < 0$ in the first active zone at outer radial boundary). The standard axial reflection boundary condition is used on the polar axis ($\theta = 0$ and π), where the density and radial components of the velocity and magnetic field (v_r and B_r) in the ghost zones take their values in the corresponding active zones while the polar and azimuthal components (v_θ, B_θ, and v_ϕ) take the negative of their values in the corresponding active zones. We set B_ϕ to vanish on the polar axis and on the inner radial boundary, since it is taken to be

non-rotating.

3.3 Reference model and the formation of rings and gaps through reconnection

We will first discuss in detail a reference simulation to which other simulations with different parameters can be compared. The parameters used in all simulations are listed in Table 3.1. The initial density at r_0 on the disk midplane is $\rho_0 = 1.3 \times 10^{-10}$ g cm^{-3}. Of the parameters to be changed in later simulations, this 'reference' simulation uses $\beta_0 \sim 10^3$ and $\Lambda_0 = 0.25$. Note that the radial power-law dependence of the ambipolar Elsasser number is $\Lambda \propto r^{3/4}$, whereas the initial distribution of plasma-β is constant with radius.

3.3.1 Global picture

The overall global evolution of the disk is seen in Fig. 3.1. The frames show the simulation at times of 0, 200, 1000, and $2500t_0$ (left to right), where $t_0 = 1$ yr is the orbital period at the inner edge of the simulation domain ($r_0 = 1$ au). The disk wind launching proceeds in an inside-out fashion, i.e, the wind is launched from larger disk radii as the simulation progresses. By $1000t_0$ (one orbit at the outer radius $r = 100$ au), the simulation appears to have no memory of the initial simulation setup and the magnetic field geometry is conducive to launching an MHD disk wind at all radii. From initial inspection, the disk wind that is launched is very steady in time (see the supplementary material of Suriano et al. 2018 online for an animated version of Fig. 3.1). The magnetic flux is also very much fixed in time following an initial adjustment period of approximately $t/t_0 = 100$. From this point on, the poloidal

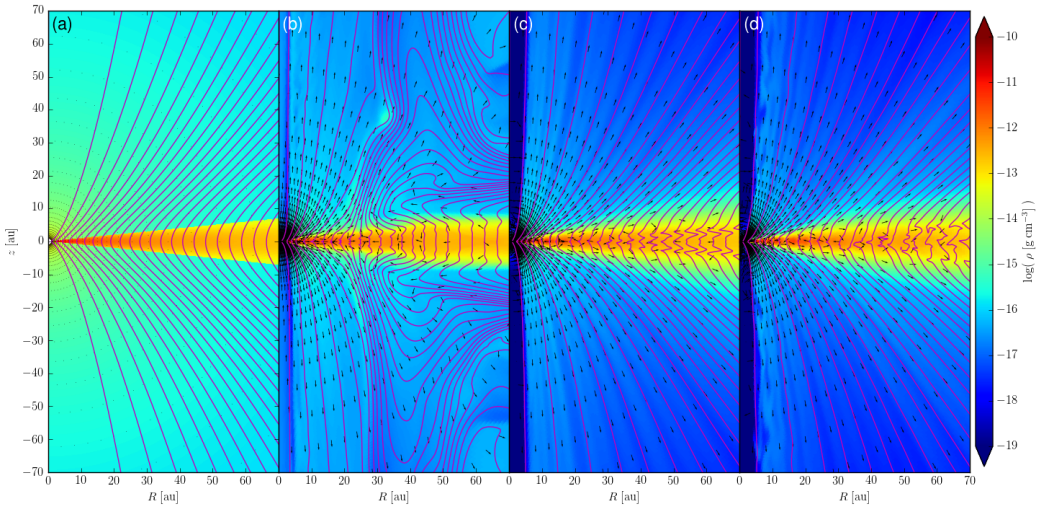

Fig. 3.1.— A representative ('reference') axisymmetric simulation. Shown is the mass volume density (logarithmically spaced colour contours in units of g cm^{-3}), the poloidal magnetic field lines (magenta), and the poloidal velocity unit vectors (black). Panels (a)-(d) corresponding to simulation times of 0, 200, 1000, and 2500 inner orbital periods, respectively. (See the supplementary material of Suriano et al. 2018 in the online journal for an animated version of this figure.)

magnetic field lines stay in close proximity to their equilibrium footpoint in the disk (magenta lines in Fig. 3.1). However, there is persistent laminar accretion radially inward through the disk and across magnetic field lines.

A relatively massive and steady wind is launched from the disk surface for almost the entire simulation. Figure 3.2 plots the mass outflow rate for the wind through a sphere of radius $r = 10$ au, excluding the disk region ($|\pi/2 - \theta| < 2\epsilon$; black line). The mass outflow rate slowly decreases for times $t/t_0 \gtrsim 300$ from a value of $\dot{M}_{\rm w} \approx 7 \times 10^{-7}$ M$_\odot$ yr^{-1} down to approximately 3×10^{-7} M$_\odot$ yr^{-1} by $t/t_0 = 5000$. Most of the mass lost in the wind moves rather slowly, with a radial expansion speed less than the local Keplerian rotation speed at $r = 10$ au for a one solar-mass star ($v_r < 10$ km s^{-1}; blue line). This picture is reminiscent of Suriano et al. (2017), where a weak initial magnetic field (again, $\beta \sim 10^3$) is able to drive slow and massive outflow. There is, however, a substantial mass loss from a relatively fast outflow ($v_r > 10$ km s^{-1}) as well (red line). Note that the mass infall rate in the low-density polar region is of the order 10^{-13} M$_\odot$ yr^{-1}, which is much smaller than the total mass outflow rate. The mass accretion rate through the disk at this same radius ($r = 10$ au) is of the same order as the total outflow rate (green line). It stays relatively constant at $\dot{M}_{\rm acc} \approx 8 \times 10^{-7}$ M$_\odot$ yr^{-1}, even as the outflow rate decreases slowly at later times.

3.3.2 Disk-wind connection

Figure 3.3 plots various physical quantities of the reference simulation at $t/t_0 = 2500$ up to a radius of $r = 20$ au. Panel (a) shows the poloidal velocity as the accreting disk material is peeled off the disk surface and launched in a wind. The velocity of the disk accretion is of the order 1 m s^{-1}, while in the wind, material is accelerated up to velocities of $v_{\rm p} \gtrsim 10$ km s^{-1}. The disk and wind regions are easily distinguishable

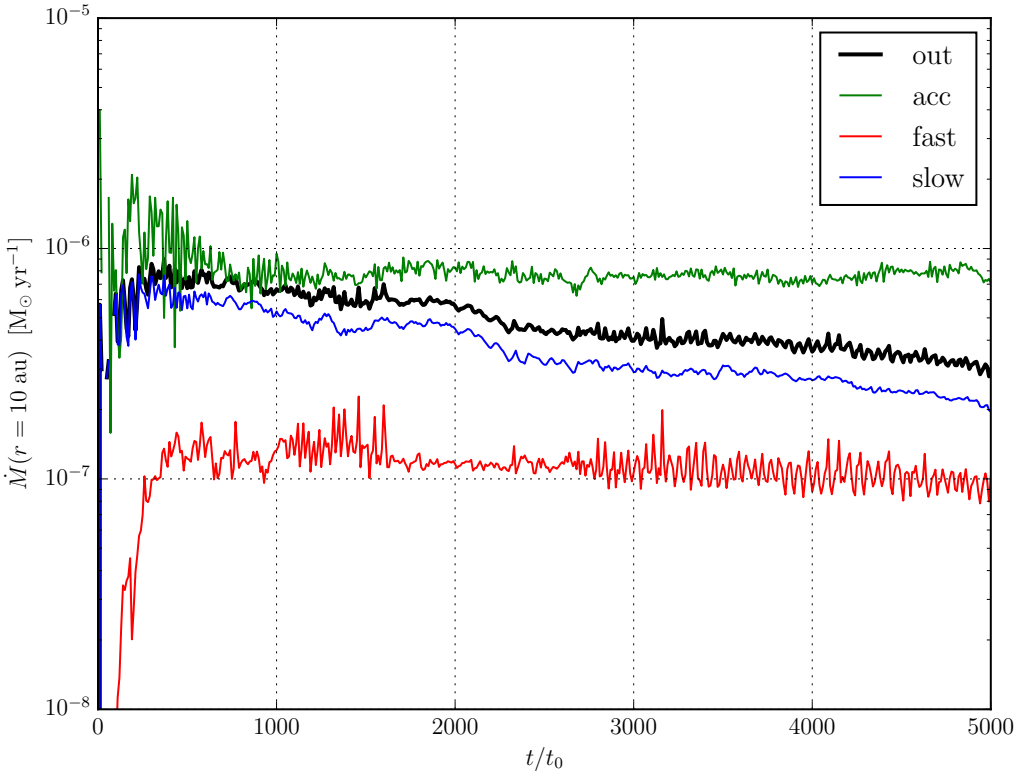

Fig. 3.2.— The mass outflow rates ($\mathrm{M}_\odot$ yr^{-1}) as a function of time in the reference simulation through a sphere of radius $r = 10$ au. The total mass outflow rate both above and below the disk ($|\pi/2 - \theta| > 2\epsilon$) is shown in black. It is separated into two velocity components, with the fast component ($v_r > 10$ km s^{-1}) shown in red and the slow component ($v_r \leq 10$ km s^{-1}) in blue. The green line shows the mass accretion rate through the disk ($|\pi/2 - \theta| < 2\epsilon$).

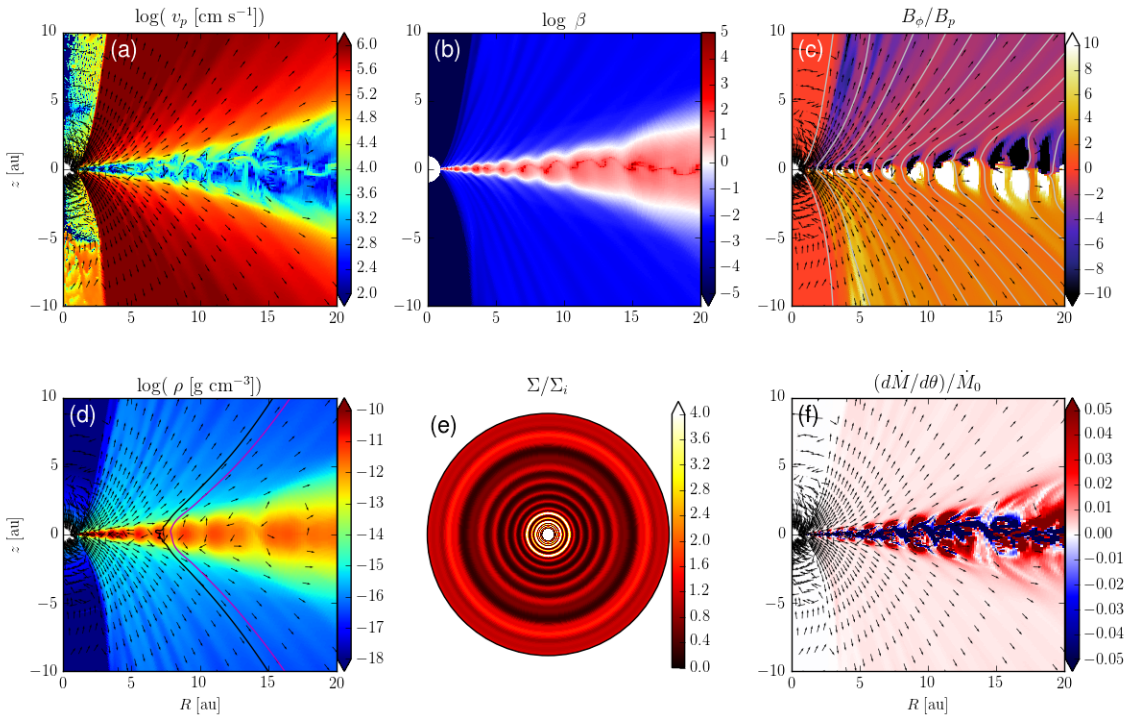

Fig. 3.3.— The reference simulation at time $t/t_0 = 2500$. The colour contours show (a) the logarithm of poloidal velocity (cm s^{-1}), (b) the logarithm of plasma-β, (c) the ratio of the toroidal to the poloidal magnetic field components, B_ϕ/B_p, (d) the logarithm of density (g cm^{-3}), (e) an axisymmetric, face-on view of the disk surface density distribution normalized to the initial power-law distribution, $\Sigma_i = \Sigma_0(r/r_0)^{-1/2}$, and (f) the mass flux per unit polar angle, $d\dot{M}/d\theta = 2\pi r^2 \rho v_r \sin\theta$, normalized to $\dot{M}_0 = r_0^2 \rho_0 c_{s,0}$. Poloidal magnetic field lines (i.e., magnetic flux contours) are shown in grey in panel (c). Panel (d) shows two specific poloidal magnetic field lines with midplane footpoints at $r = 8$ au (magneta; see Fig. 3.4) and $r = 7$ au (black; see Fig. 3.5). Poloidal velocity unit vectors are plotted in black in panels (a), (c), (d), and (f). (See the supplementary material of Suriano et al. 2018 in the online journal for an animated version of this figure.)

in this plot. They are also quite distinct in panel (b), where the ratio of the thermal pressure to the magnetic pressure, i.e., plasma-β, is plotted. The initial β at the disk midplane is $\sim 10^3$ and it is constant as a function of radius. At the time shown, the thermal and magnetic pressures become approximately equal at the base of the wind ($\beta \sim 1$), while β decreases to 10^{-2} or less in the wind zone. The bulk of the disk has plasma-β of approximately 10, although there remains a thin layer where the plasma-β peaks at a value slightly larger than the initial β_0. This thin layer is where the toroidal magnetic field goes to zero as it reverses direction; it is therefore a current layer (see also the simulations of Bai & Stone 2013; Bai 2013; Gressel et al. 2015; Bai & Stone 2017; Béthune et al. 2017; Bai 2017). This can be seen in panel (c), which plots the ratio of the toroidal magnetic field to the poloidal magnetic field, B_ϕ/B_p. The white regions are where $B_\phi > 0$ in the disk and the black regions have $B_\phi < 0$. The poloidal magnetic field lines (i.e., constant magnetic flux contours) are shown in grey. Note that the toroidal field greatly dominates the poloidal field in distinct radial locations, while the poloidal field is stronger (with a smaller $|B_\phi/B_\mathrm{p}|$) in adjacent regions. These regions with less twisted field lines correspond to regions with lower densities in the disk, as shown in panel (d). They will be referred to as 'gaps.' The neighbouring regions, where the field lines are more twisted, have higher densities; they will be referred to as 'rings.' The rings and gaps are shown more clearly in the face-on view of the disk in panel (e), where the distribution of the surface density (normalized to the initial distribution) is plotted. How such rings and gaps form will be discussed in detail in Section 3.3.3. Here, we would like to point out that there is vigorous accretion (and some expansion) in both types of regions, as shown in panel (f), which plots the spatial distribution of the radial mass flux per unit polar angle, $d\dot{M}/d\theta = 2\pi r^2 \rho v_r \sin\theta$. The blue cells show negative mass flux or

inward accretion and the red cells represent positive mass flux or outward expansion. We see that most of the accretion in the disk occurs along the thin current sheet previously mentioned. In disk regions above and below this layer, there is a strong variation in mass flux, with larger outward mass flux from rings compared to those from the adjacent gaps, although this strong variation does not appear to extend into the (faster) wind zone.

To understand the connection between the disk region and wind region more quantitatively, we plot various physical quantities along two representative field lines. In Fig. 3.4, we show plots along a magnetic field line that passes through a gap at a radius of 8 au on the midplane (see the magenta magnetic field line plotted in Fig. 3.3d). Panel (a) of Fig. 3.4 shows that the density peaks near the midplane, at a value of approximately 10^{-12} g cm^{-3}. It drops off quick inside the disk (the vertical dashed lines mark the initial disk surface at two scale heights). Beyond the sonic point (marked by a yellow circle on the curve), the decrease in density becomes less steep, transitioning from an exponential drop-off to a power-law decline, as expected as the approximately hydrostatic disk transitions to a supersonic wind. Even in this low density gap region, the disk is still dominated by the thermal pressure, with a plasma-β of order 10 near the midplane (panel b). The plasma-β decreases rapidly away from the midplane, reaching a value of order 0.1 at the sonic point; beyond the sonic point, the supersonic wind is completely magnetically dominated. This magnetic field, specifically its pressure gradient, is responsible for accelerating the outermost layer of the disk through the sonic point to produce the wind. The wind acceleration along this particular field line is illustrated in panel (c), which shows clearly the transition from slow inward motion near the disk midplane ($v_r < 0$, i.e., accretion) to fast outflow through the sonic point at approximately three disk scale heights.

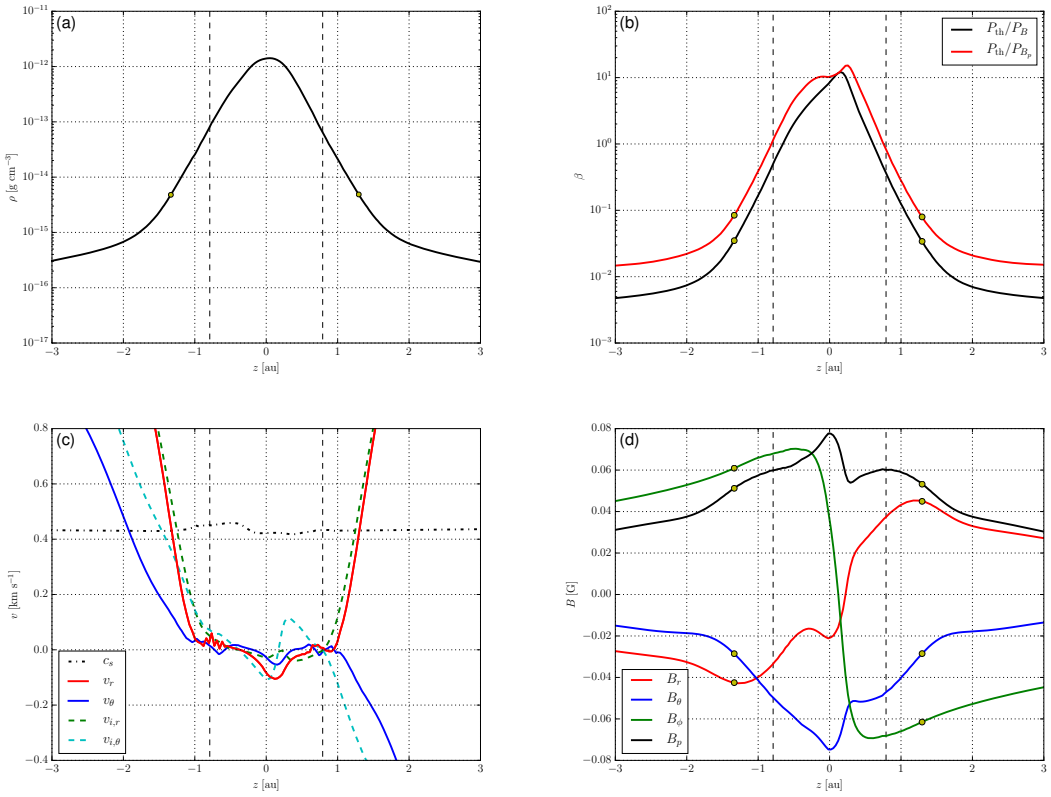

Fig. 3.4.— Physical quantities plotted along a poloidal magnetic field line as a function of the vertical height z. This representative field line passes through a low-density gap at $r = 8$ au. The panels show (a) the density distribution, (b) plasma-β for the total magnetic field strength (black) and for the poloidal magnetic field strength (red), (c) the poloidal components of the neutral (solid lines) and ion velocities (dashed lines), and the adiabatic sound speed (dash-dotted line), and (d) the magnetic field components. The yellow circles show the sonic point (where the poloidal velocity is equal to the adiabatic sound speed) and the vertical dashed lines show the initial disk height of $z = \pm 2h_0$.

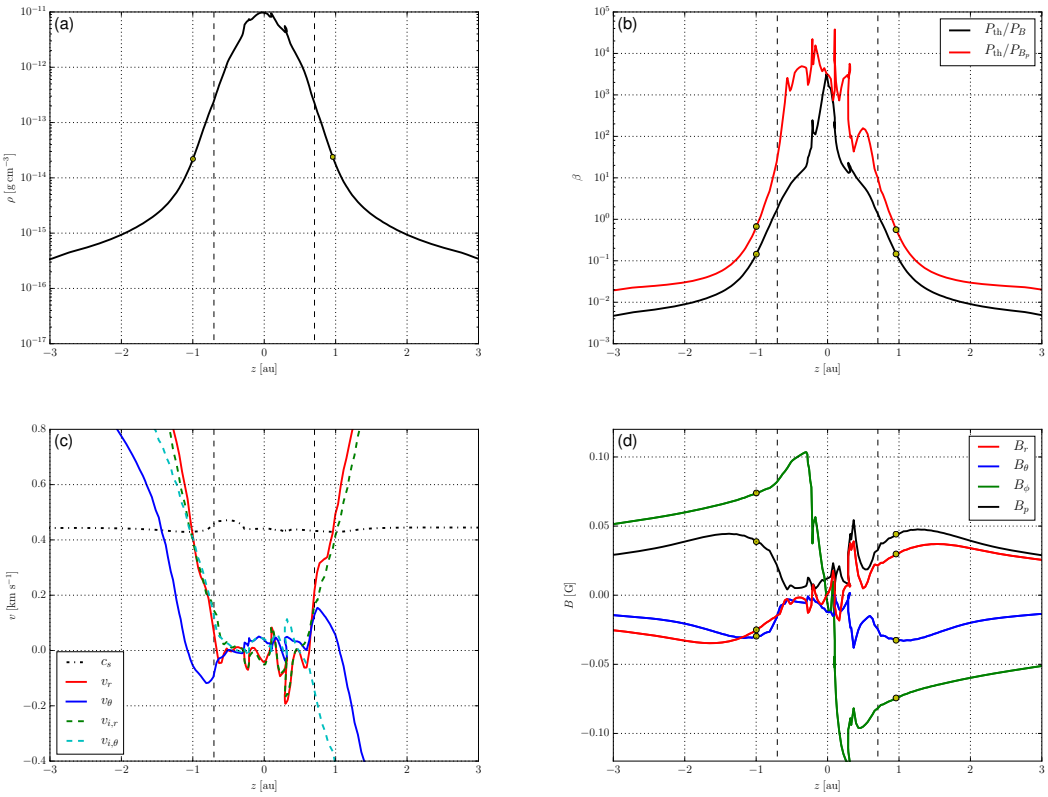

Fig. 3.5.— Physical quantities plotted along a poloidal magnetic field line as a function of the vertical height z. This representative field line passes through a dense ring at $r = 7$ au. The panels show (a) the density distribution, (b) plasma-β for the total magnetic field strength (black) and for the poloidal magnetic field strength (red), (c) the poloidal components of the neutral (solid lines) and ion velocities (dashed lines), and the adiabatic sound speed (dash-dotted line), and (d) the magnetic field components. The yellow circles show the sonic point (where the poloidal velocity is equal to the adiabatic sound speed) and the vertical dashed lines show the initial disk height of $z = \pm 2h_0$.

The sound speed remains nearly constant along the field line, which is indicative of a 'cold' wind with a temperature comparable to that of the disk. Note that the outflow acceleration beyond the sonic point is rather gradual, with the velocity increasing over many disk scale heights. This is consistent with magnetically driven winds with heavy mass loading (Anderson et al. 2005).

In panel (c), we have plotted ion speeds together with the speeds for the bulk neutral material. The largest difference is between the velocity component v_θ and $v_{i,\theta}$, especially in the wind zone. In particular, $v_{i,\theta}$ is more positive than v_θ below the disk (negative z), indicating that the ions are moving faster than the neutrals *away from* the disk. There must be a magnetic force pointing away from the disk which drives the ion-neutral drift through ambipolar diffusion; it is the same force that accelerates the wind in the first place. The situation is similar above the disk as the magnetic force that drives the wind also moves the ions away from the disk faster than the neutrals in the negative θ direction. This force comes mostly from the toroidal component of the magnetic field, which dominates the poloidal component in the wind zone, as shown in panel (d). The gradual decrease of the toroidal component, evident in panel (d), yields a magnetic pressure gradient along the poloidal field line that lifts up the material near the disk surface against gravity and slowly accelerates it to produce a wind. Closer to the midplane, the poloidal field component (particularly B_θ) becomes more dominant, indicating that the field line passes through the gap region of the disk with relatively little bending in the r direction or twisting in the ϕ direction.

The situation is quite different along the field line that passes through a dense ring at a radius of 7 au (Fig. 3.5). Here, the density at the midplane is an order of magnitude higher than that of the neighbouring gap (see Fig. 3.4a). It decreases

rapidly away from the midplane and the decrease becomes slower beyond the sonic point, signalling the transition from the disk to a wind. The plasma-β through the ring is more than 10^3 near the disk midplane, more than two orders of magnitude larger than that in the gap. In other words, as measured by β, the ring is much less magnetized than the gap. The difference is even larger when only the poloidal field component is considered. From the red curve in Fig. 3.5(b), which plots the ratio of the thermal pressure to the magnetic pressure due to the poloidal field only, it is clear that the poloidal field in the ring is not only weak (and much weaker than the toroidal component) but also highly variable as a function of z. Nevertheless, the basic disk-wind structure is preserved, as shown in panel (c), where the poloidal components of the ion and neutral velocities are plotted. Again, the transition from a slowly moving disk (in the poloidal plane) to a faster expanding supersonic wind is evident. Compared to the relatively smooth accretion in the gap, which has a single negative peak in $v_r(z)$ (see red line in Fig. 3.4c), the radial flow in the ring is much more complex: it has six negative peaks and at least three positive peaks, indicating the coexistence of multiple channels of accretion and expansion in the ring. These channels are reflected in the magnetic structure (panel d), particularly in the vertical distribution of the radial component, $B_r(z)$, which has several sign reversals consistent with channel flows in the weakly magnetized ring. As alluded to earlier, the most striking difference in the magnetic field between the ring and the gap is the strength of the poloidal magnetic field, especially the polar component, B_θ, which is much lower in the ring than in the gap (compare Fig. 3.4d and 3.5d). In the ring, the magnetic field is completely dominated by the toroidal component, except near the midplane where B_ϕ changes direction.

3.3.3 Formation of rings and gaps

In this subsection, we will demonstrate that the formation of rings and gaps in the reference simulation is closely related to the magnetic structure that develops in the disk, particularly the sharp pinching of the poloidal field line near the midplane that leads to magnetic reconnection. This field pinching is caused by the development of a current sheet near the midplane, as we show next.

3.3.3.1 Midplane current sheet

We start by reminding the reader of the simulation setup, where the disk is rotating slightly sub-Keplerian for $|\pi/2 - \theta| < 2\epsilon$, the coronal regions above and below the disk are not rotating, and the magnetic field has no ϕ component initially. As the simulation begins to run, a toroidal magnetic field is quickly generated near the boundary between the rotating disk and the stationary corona due to differential rotation. This can been seen in the left panel of Fig. 3.6, which plots the toroidal component of the magnetic field as a function of θ at a representative disk radius $r = 20$ au. At $t/t_0 = 10$, the solid black line shows that a toroidal magnetic field has already been generated near the disk surface, but has yet to penetrate into the bulk of the disk. Associated with the variation of B_ϕ with polar angle θ is a radial current,

$$J_r = \frac{c}{4\pi} \frac{1}{r \sin\theta} \frac{\partial (B_\phi \sin\theta)}{\partial \theta} \approx \frac{c}{4\pi} \frac{dB_\phi}{r d\theta}, \tag{3.17}$$

where $\sin\theta \approx 1$ in the thin disk. This current is plotted in the right panel of Fig. 3.6, which shows two positive peaks near 5° above and below the disk midplane at time $t/t_0 = 10$, corresponding to the sharp drop of $|B_\phi|$ going from the corona into the disk. At later times, the region of high toroidal field, $|B_\phi|$, above and below the

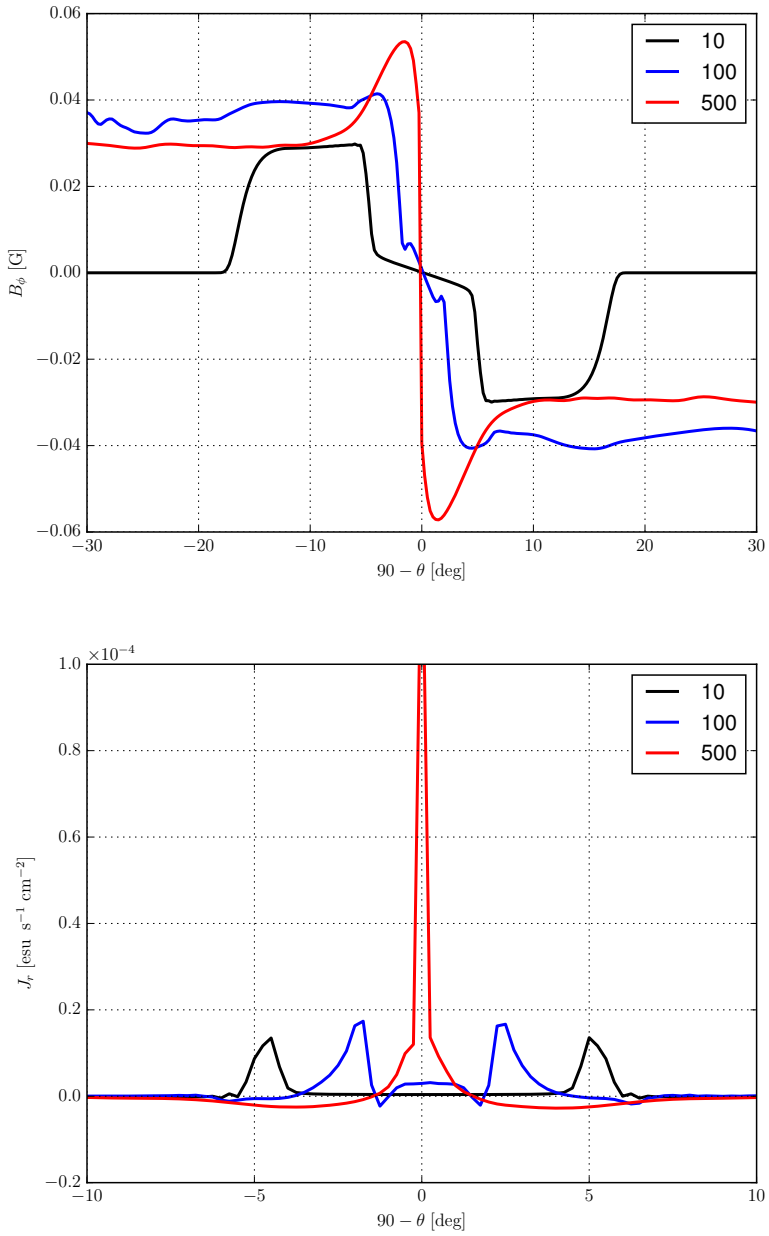

Fig. 3.6.— The toroidal magnetic field B_ϕ (left) and the radial current density J_r (right) plotted versus $90° - \theta$ (zero at the midplane and negative below it) at radius $r = 20$ au. The legend labels are the simulation time in units of the inner orbital period t_0.

midplane expands both outward into the corona and, more importantly, toward the disk midplane. The latter drives the two current layers (one on each side of the midplane) towards the midplane, until they merge together into a single, thin, current sheet, as shown in Fig. 3.6 (right).

Ambipolar diffusion plays a key role producing the thin midplane current sheet. First, were it not for the presence of AD (or some other magnetic diffusivity, such as resistivity), prominent avalanche streams would have developed near the disk surface, which would drive the entire disk and its envelope into an unsteady state and make the formation of a laminar midplane current sheet impossible (see Suriano et al. 2017 and Section 3.4.1 below)[1]. Second, as first stressed by Brandenburg & Zweibel (1994), AD tends to steepen the magnetic gradient near a magnetic null, i.e., where the magnetic field changes polarity. The reason is that the Lorentz force associated with the magnetic pressure gradient drives the ions (relative to the neutrals) toward the null from both sides. Since the field lines (of opposite polarity across the null) are tied to the ions, they are dragged towards the null as well, leading to a steepening of the magnetic gradient, which in turn yields a stronger magnetic force that drives the ions and the field lines even closer to the null. Since the ambipolar magnetic diffusivity, η_A, is proportional to the field strength (see equation 3.5) and thus vanishes at the null, this steepening would result in an infinitely thin, singular, current sheet in principle. In practice, the thickness of the current sheet is limited by the grid resolution.

Sharp magnetic field reversals that give rise to thin current sheets are prone to reconnection. However, this is not the case for the midplane current sheet shown in Fig. 3.6, because it is produced by the reversal of the toroidal field component B_ϕ and it is impossible to reconnect oppositely directing toroidal fields under the

[1]In this reference run, AD does not appear to suppress the development of the MRI completely. Channel-like features are evident at large radii where the disk is better coupled to the magnetic field as measured by the Elsasser number (see Fig. 3.1c).

adopted axisymmetry[2]. Nevertheless, this primary current sheet leads to another current component that does allow for reconnection.

3.3.3.2 Reconnection of pinched radial magnetic field

The secondary component of the midplane current sheet develops as a result of mass accretion in the disk, which is concentrated in the primary radial current (J_r) sheet near the midplane (see Fig. 3.6). The mass accretion is driven by the removal of angular momentum due to the Lorentz force ($\propto J_r B_\theta$) in the azimuthal direction, which peaks in the radial current sheet where the toroidal magnetic field changes sign. Pictorially, as the ϕ component of the magnetic field changes from the $+\phi$ direction below the disk to the $-\phi$ direction above the disk in a thin midplane layer, the magnetic field lines become severely kinked in the azimuthal direction. The sharp field kink generates a magnetic tension force in the $-\phi$ direction that exerts a braking torque and drives the disk accretion in the current sheet.

The accretion through the midplane current sheet now drags the poloidal magnetic field lines inward with the flow. This results in a pronounced radial pinch of the poloidal magnetic field, which transports the poloidal magnetic flux inward and yields another current component in the azimuthal direction, J_ϕ. Eventually, the radial pinch becomes so severe that the magnetic field reconnects, forming poloidal magnetic field loops that are reminiscent of the tearing mode instability (Furth et al. 1963; see also Zweibel & Yamada 2009). An example of the reconnection process is shown in Fig. 3.7, which plots lines of constant poloidal magnetic flux, i.e. poloidal magnetic field lines, along with the ratio of the toroidal to poloidal magnetic field, B_ϕ/B_p (colour contours), at a radius centred on $r = 6.5$ au from time $t/t_0 = 200$ to 230. At

[2]Reconnection of the highly pinched toroidal field is expected in 3D, and will be explored in a future investigation.

the first frame shown, the poloidal magnetic field highlighted in bold already has a kink across the midplane. The pinch grows with time until the field line is stretched almost parallel to the midplane over approximately four radial grid cells at $t/t_0 = 210$. By the next frame shown at $t/t_0 = 220$, the field has reconnected, forming a loop near $r = 6.4$ au. In the last frame the loop has disappeared, however, the process of its formation has left a lasting mark on the magnetic field structure. The region now has a much larger toroidal magnetic field component compared to its poloidal component. The now weaker poloidal field strength can be seen clearly in the last panel from the lack of field lines in the post-reconnection region.

3.3.3.3 Reconnection-driven ring and gap formation

The general picture for the reconnection-driven ring and gap formation is as follows. A poloidal magnetic field line that initially threads the disk rather smoothly is dragged by preferential accretion near the midplane into a highly pinched radial configuration (see upper-right panel of Fig. 3.7 for an illustration). Reconnection of the highly pinched field line produces a poloidal magnetic loop next to a poloidal field line that still threads the disk more smoothly (see lower-left panel of Fig. 3.7). After reconnection, the material trapped on the magnetic loop is detached from the original (pre-reconnection) poloidal field line, which results in the separation of matter and (poloidal) magnetic flux. Specifically, there is no net poloidal magnetic flux passing through the matter on the loop and there is less matter remaining on the original poloidal field line (since some of the matter on the original field line is now on the detached magnetic loop). The net effect is a redistribution of the poloidal magnetic flux away from the loop-forming region into an adjacent region where the poloidal flux accumulates. Since mass accretion tends to be faster in regions with stronger

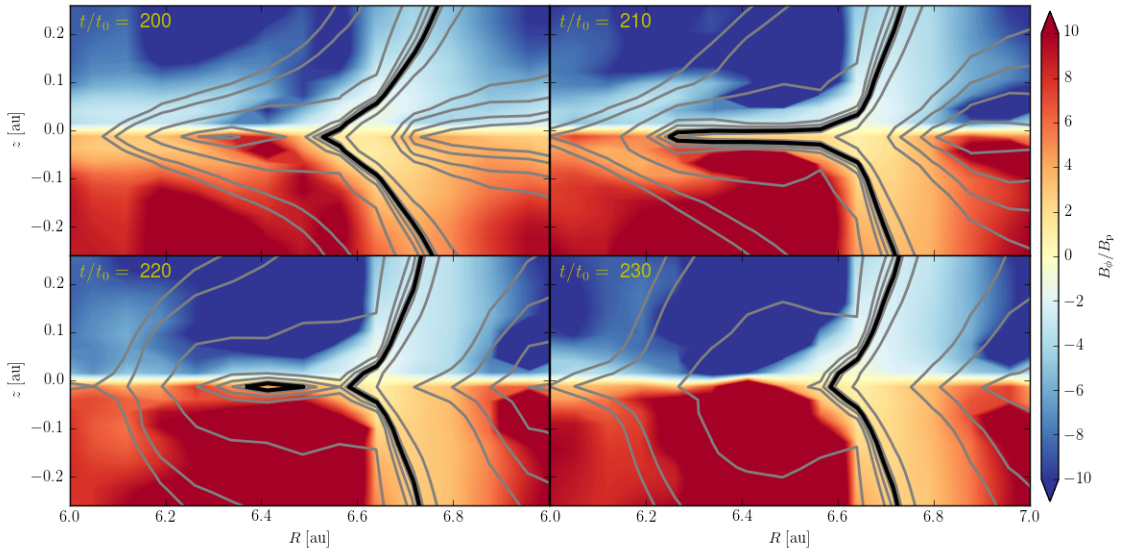

Fig. 3.7.— Poloidal magnetic field lines at four different times are shown in grey, with a reconnecting field line highlighted in black. The colours show the ratio of the toroidal to poloidal magnetic field, B_ϕ/B_p.

poloidal magnetic fields, it is not surprising that the reconnection-induced variation of the poloidal field strength with radius would lead to a spatial variation in the mass accretion rate that would in turn lead to spatial variation in the mass (surface) density, i.e., the formation of rings and gaps. [3]

The preferential concentration of poloidal field lines inside the low-density gaps of the disk is illustrated pictorially in Fig. 3.8(a), which is a snapshot of the inner part of the reference simulation (up to 15 au) at a representative time when the simulation has reached a quasi-steady state, $t/t_0 = 2500$. The field concentration is quantified in panel (b), which plots the vertical component of the magnetic field (B_z, in red) at the midplane and surface density of the disk (in black), both relative to their initial values at $t = 0$. Two features stand out: (1) there is a strong anti-correlation between the surface density and vertical field strength, as expected in the reconnection-induced scenario of ring and gap formation, and (2) the poloidal magnetic field is typically much weaker in the high-density ring regions (where B_z is close to zero) than in the low-density gap regions (where B_z is increased over its initial value by a factor of $2 - 4$). This drastic segregation of poloidal magnetic flux relative to matter appears to be quite stable with time (persisting for thousands of inner orbits), despite the fact that there is continued mass accretion through both the rings and gaps.

For our reference run, we believe that the key to maintaining the concentration of poloidal magnetic flux in the gap regions is ambipolar diffusion: it allows the bulk neutral material to accrete radially inward through the gaps without dragging the ions (and the magnetic field lines tied to them) with it. This is illustrated in panel (c) of Fig. 3.8, which plots the radial component of the ion (red line) and neutral (black line) velocity at the midplane. As expected, the neutrals accrete faster in the

[3]The stronger poloidal field in a gap can also lead to a faster depletion of the local disk material via a stronger magnetically driven wind (e.g., Casse & Ferreira 2000). However, this effect is less important compared to the faster accretion in the gap in general.

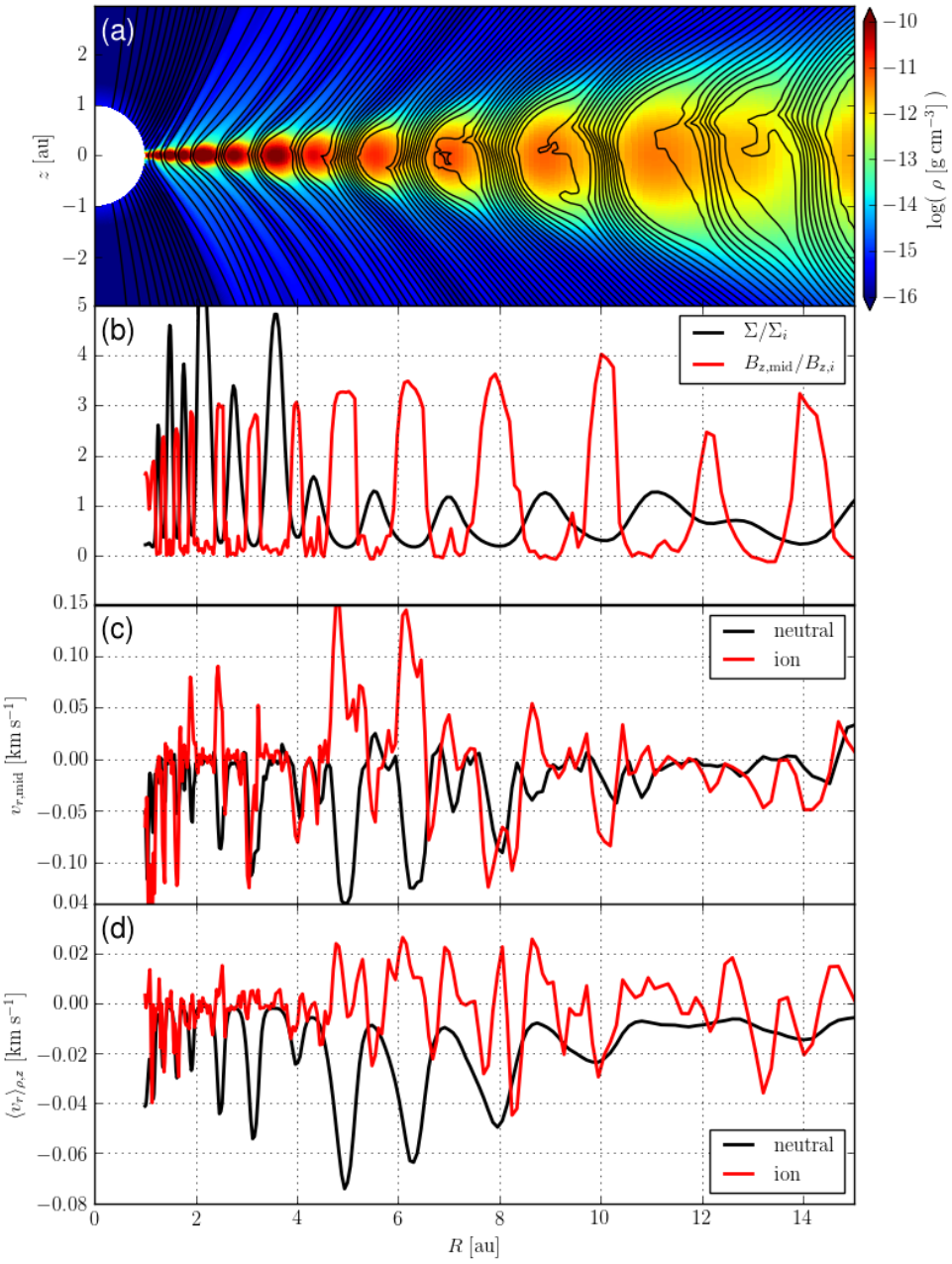

Fig. 3.8.— The density, magnetic field strength, and velocities plotted up to $r = 15$ au at $t/t_0 = 2500$. The panels show (a) the logarithm of the density (g cm^{-3}) in colour and the poloidal magnetic field lines (i.e., magnetic flux contours) in black, (b) the surface density normalized to the initial radial distribution, $\Sigma_i \propto r^{-1/2}$, and the vertical magnetic field strength at the midplane normalized to its initial distribution, $B_{z,i} \propto r^{-5/4}$, (c) the radial velocity (km s^{-1}) of neutrals (black) and ions (red) at the midplane, and (d) the density-weighted vertical average of the radial velocity (km s^{-1}) of neutrals (black) and ions (red) over $z = \pm 2h$. (See the supplementary material of Suriano et al. 2018 in the online journal for an animated version of this figure.)

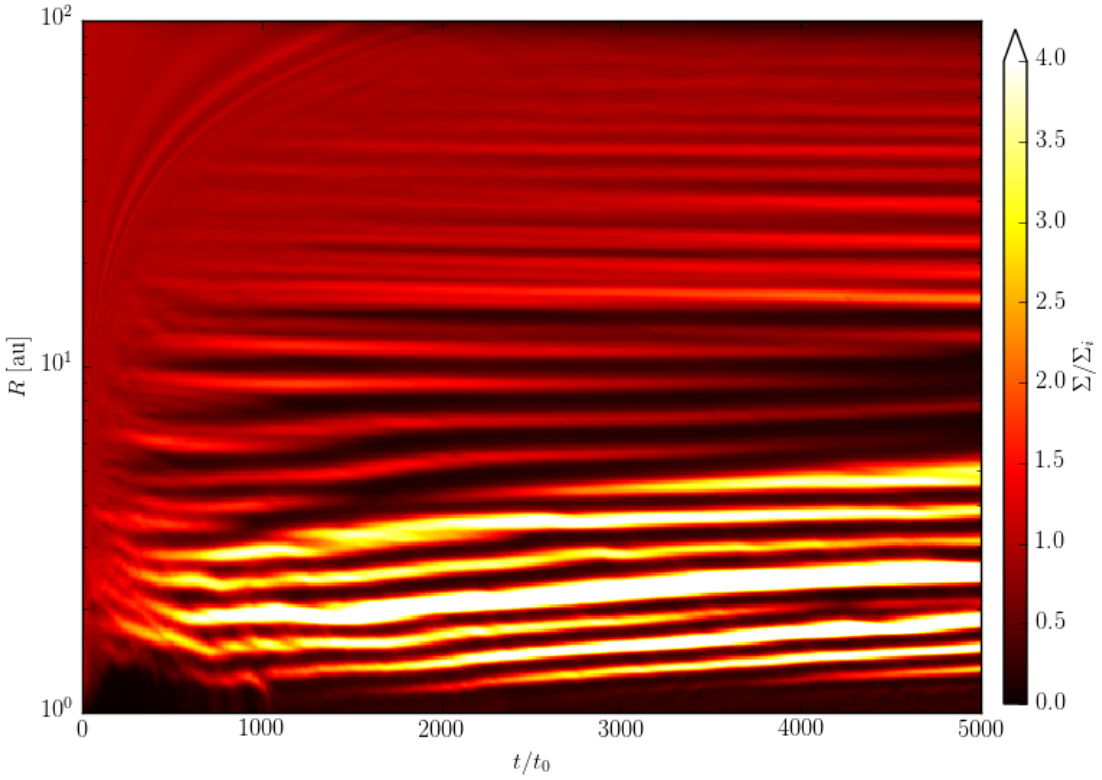

Fig. 3.9.— The surface density of the disk (normalized to its initial radial distribution) as a function of radius and time, showing that most of rings and gaps created in the reference run remain stable for thousands of inner orbital periods.

low-density gaps than in the high-density rings. One may naively expect the same trend for the ions but, in the presence of significant ambipolar diffusion, this is not necessarily the case. Indeed, at the time shown in Fig. 3.8, the ions are moving *outward* in several of the gaps, especially the two near $r = 5$ and 6.5 au. The ions are forced to expand against the infalling neutrals by an outward Lorentz force due to either a temporary poloidal flux concentration near the inner edge of the gap (in a manner that is reminiscent of the forced ion-neutral separation in the AD-shock in magnetized accretion onto low-mass protostars first described in Li & McKee 1996) or an outward magnetic pressure gradient from the toroidal field component. In any case, the radially outward Lorentz force in the gap appears strong enough to keep the ions (and the poloidal field lines) in a state of dynamic equilibrium against the rapid infall of neutrals, at least under the assumption of (2D) axisymmetry. The dynamic equilibrium of the ions (and the field lines attached to them) is shown more clearly in Fig. 3.8(d), which plots the vertically averaged radial velocity weighted by density. The average ion speed fluctuates around zero as the neutrals accrete inward, especially in the gap regions. Whether this remains true in full 3D simulations is unclear and will be explored in future investigations.

The rings and gaps, once fully developed, remain remarkably stable over time. This is illustrated in Fig. 3.9, where the surface density (relative to its initial distribution) is plotted at each radius as a function of time, as done in Béthune et al. (2017) for plasma-β (see their Fig. 30). Note that most of the rings and gaps are stable for at least 4000 inner orbital periods. There are a few exceptions. For example, the two rings near 10 au appear to merge together around $t/t_0 = 5000$, whereas the ring at 6 au starts to fade away at later times. It would be interesting to determine whether these rings and gaps remain stable for long periods of time in full 3D simulations.

3.4 Effects of magnetic coupling and field strength on ring and gap formation

The most important features in the reference simulation are the rings and gaps that develop spontaneously in the disk. In this section, we will explore how their formation is affected by how well the ions (and therefore the magnetic field) are coupled to the bulk neutral fluid. The magnetic field coupling is changed by varying the AD Elsasser number at r_0 and $\theta = \pi/2$, Λ_0, which sets the scale for the Elsasser number everywhere; the ion density profile is unchanged. The AD Elsasser number controls the coupling between the ions and the bulk neutral fluid, as $\Lambda \propto \gamma\rho_i$, where $\gamma\rho_i$ is the collision frequency between the neutrals and ions. When Λ is small, so is the collision frequency, and, therefore, the ions/magnetic field are poorly coupled to the neutral fluid. As Λ increases, the magnetic field becomes increasingly coupled to the motions of the bulk neutral fluid. The ideal MHD limit is reached as the AD Elsasser number approaches infinity, $\Lambda \to \infty$. In Table 3.1, we list the simulation runs performed to examine the effect that the magnetic coupling strength has on the ring and gap formation mechanism described in the previous section. First, we will present the results of the simulations as the Elsasser number increases from 0.01 to 2 (in the simulations named ad-els0.01, ad-els0.05, ad-els0.1, ad-els0.5, ad-els1.0, and ad-els2.0), as well as the ideal MHD case (Section 3.4.1). Next, we show the effects of introducing an explicit Ohmic resistivity into the reference simulation, where the Ohmic resistivity, η_O, is constant everywhere and is equal to 0.26, 2.6, and 26 times the initial effective ambipolar resistivity, $\eta_{A,0}$, at r_0 on the disk midplane ($\theta = \pi/2$). These simulations are named oh0.26, oh2.6, and oh26 respectively. They are discussed in Section 3.4.2 together with simulations that have different initial

magnetic field strengths, with the midplane plasma-β approximately ten times higher (model beta1e4) and lower (beta1e2) than that of the reference run. We conclude this section with an analysis of the magnetic stresses in the disk (Section 3.4.3).

3.4.1 AD Elsasser number

Before describing the results of the simulations, we will briefly describe our expectations as the AD Elsasser number is varied in the disk. In the reference run, we see a rather steady disk wind launched as disk material concentrates into rings and poloidal magnetic flux concentrates into gaps. The region demagnetized of poloidal field (where the density will grow to form a ring) develops as the radial magnetic field is stretched towards the $-r$ direction due to rapid accretion in the primary midplane current layer (J_r). As discussed in Section 3.3.3.1, the development of a strong midplane current layer where $B_\phi = 0$ is a direct result of ambipolar diffusion because it is formed as the ions and toroidal magnetic field lines drift towards the magnetic null ($B_\phi = 0$) relative to the bulk neutral material. In the limiting case that the Elsasser number goes to infinity, i.e., the ideal MHD case, the AD-enabled midplane current layer is not expected to develop and this ring and gap formation mechanism would be turned off. Instead, the so-called 'avalanche' accretion streams are expected to develop near the disk surface, which may form rings and gaps through another mechanism (see Suriano et al. 2017). In the other limiting case where the Elsasser number approaches zero, the ions have no knowledge of the bulk fluid and the magnetic field will straighten out vertically without any effect on the disk at all. In particular, the field will neither launch a disk wind nor create any disk substructure. Therefore, there must be a minimum Elsasser number below which the formation of rings and gaps is expected to be suppressed.

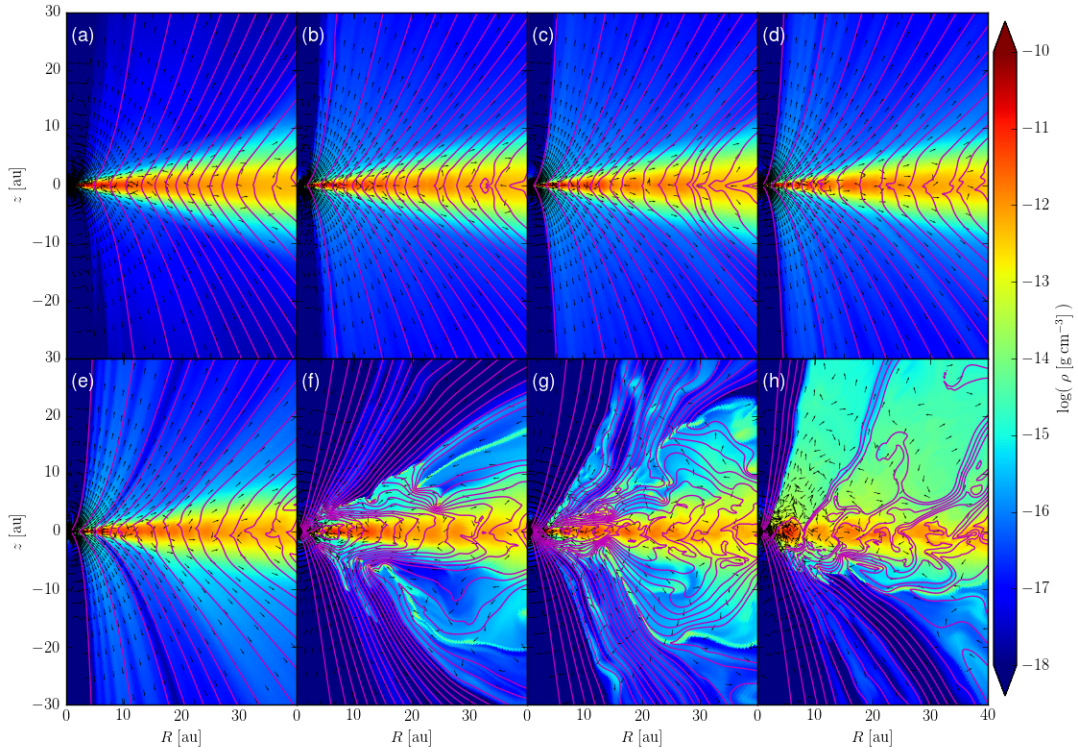

Fig. 3.10.— Snapshots at $t/t_0 = 2000$ of the eight simulations where the AD Elsasser number is varied. Shown is the mass volume density (logarithmically spaced colour contours in units of g cm^{-3}), the poloidal magnetic field lines (magenta), and the poloidal velocity unit vectors (black). The AD Elsasser number increases sequentially from panels (a)-(h). The reference simulation (ad-els0.25) is shown in panel (d). The simulation panels in alphabetical order are: (a) ad-els0.01; (b) ad-els0.05; (c) ad-els0.1; (d) ad-els0.25; (e) ad-els0.5; (f) ad-els1.0; (g) ad-els2.0; (h) ideal. See Table 3.1 for details. (See the supplementary material of Suriano et al. 2018 in the online journal for an animated version of this figure.)

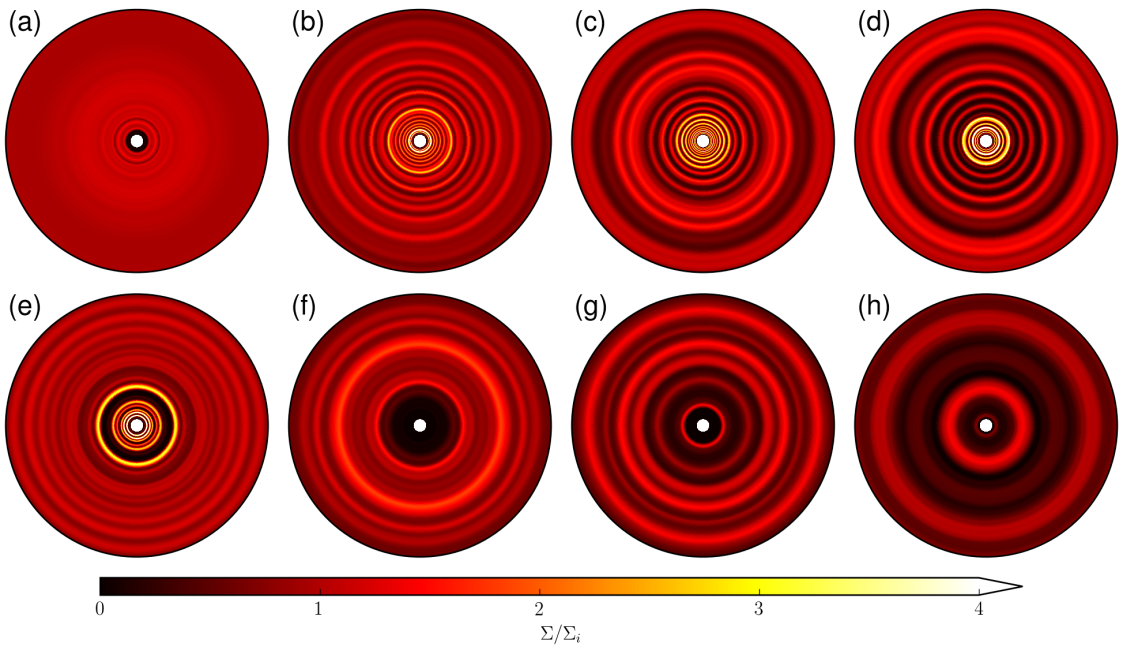

Fig. 3.11.— Face-on surface density profiles (up to a radius of 20 au) of the eight simulations where the AD Elsasser number is varied at $t/t_0 = 2000$. The AD Elsasser number increases sequentially from panels (a)-(h). The reference simulation (ad-els0.25) is shown in panel (d). The simulation panels in alphabetical order are: (a) ad-els0.01; (b) ad-els0.05; (c) ad-els0.1; (d) ad-els0.25; (e) ad-els0.5; (f) ad-els1.0; (g) ad-els2.0; (h) ideal. See Table 3.1 for details. (See the supplementary material of Suriano et al. 2018 in the online journal for an animated version of this figure.)

Table 3.1: Model parameters for all simulation runs.

	$\beta/10^3$	$\gamma/10^{-3}$ [cm^3 g^{-1} s^{-1}]	$\Lambda_0 = \gamma\rho_{i,0}/\Omega_0$	$\eta_{A,0}/10^{14}$ [cm^2 s^{-1}]	$\eta_O/10^{14}$ [cm^2 s^{-1}]
ad-els0.01	0.922	0.1763	0.01	243	–
ad-els0.05	0.922	0.8816	0.05	48.6	–
ad-els0.1	0.922	1.763	0.1	24.3	–
ad-els0.25 (ref)	0.922	4.408	0.25	9.71	–
ad-els0.5	0.922	8.816	0.5	4.86	–
ad-els1.0	0.922	17.63	1.0	2.43	–
ad-els2.0	0.922	35.26	2.0	1.21	–
ideal	0.922	–	–	–	–
oh0.26	0.922	4.408	0.25	9.71	2.5
oh2.6	0.922	4.408	0.25	9.71	25
oh26	0.922	4.408	0.25	9.71	250
beta1e2	0.0922	4.408	0.25	97.1	–
beta1e4	9.22	4.408	0.25	0.971	–

These expectations are borne out by the simulations. Figures 3.10 and 3.11 show, respectively, the edge-on and face-on view of simulations at a common time $t/t_0 = 2000$ with increasing AD Elsasser numbers from panel (a) to (h). In the most magnetically diffusive case ($\Lambda_0 = 0.01$), a wind is launched steadily from the disk, removes angular momentum from the disk and drives disk accretion that is rather laminar (Fig. 3.10a), but there is little evidence for the development of rings and gaps (Fig. 3.11a). Specifically, there is little evidence for the sharp radial pinching of poloidal magnetic field lines near the midplane that is conducive to reconnection, which is the driver of the redistribution of the poloidal magnetic flux relative to matter and is crucial to the ring and gap formation in the scenario discussed in Section 3.3.3. The lack of sharp radial pinching is to be expected, because it would be smoothed out quickly by the large magnetic diffusivity. As the diffusivity decreases (i.e., the magnetic field becomes better coupled to the bulk disk material), it becomes easier for the midplane mass accretion to drag the poloidal field lines into a radially pinched configuration that is prone to reconnection. Indeed, this occurs over at least one decade in the AD Elsasser number, from $\Lambda_0 = 0.05$ to 0.5, where the disk wind remains rather steady (see Fig. 3.10b-e), but repeated field pinching and reconnection have created multiple rings and gaps in the disk (Fig. 3.11b-e).

In the intermediate parameter regime between AD Elsasser number $\Lambda_0 = 0.05$ and 0.5, rings and gaps are more prominent in the inner part of the disk than in the outer part. This is quantified in Fig. 3.12, where the surface density of the disk (normalized to its initial value) is plotted as a function of radius. It is clear from panels (b)-(e) that most of the rings and gaps of high contrast are confined to a radius of order 10 au. One reason may be that the inner part of the disk has had more time (relative to its orbital period) for the substructures to develop. Another is that mass accretion,

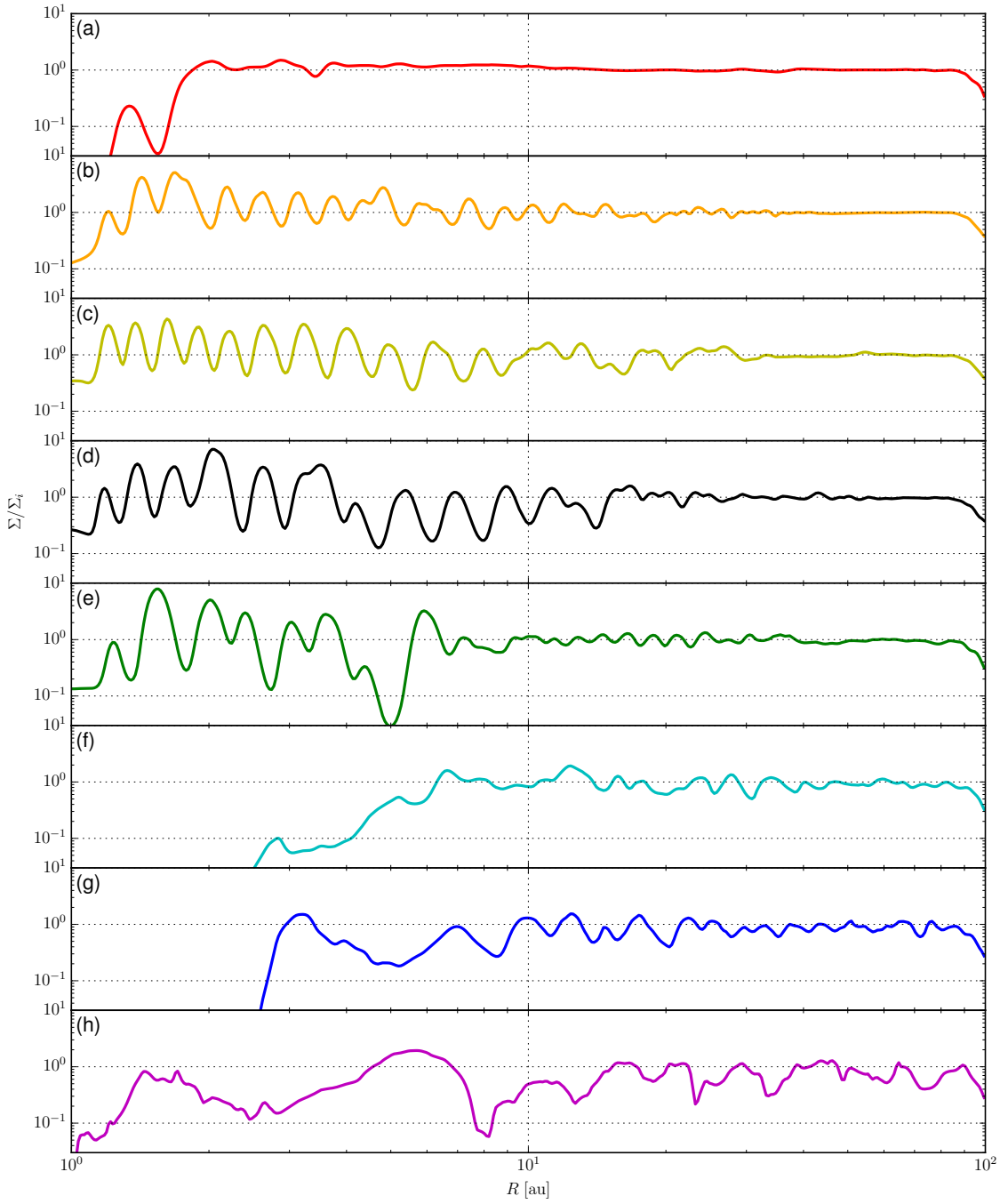

Fig. 3.12.— Surface density profiles at time $t/t_0 = 2000$ for simulations with different AD Elsasser numbers. The surface density profiles are normalized to the initial surface density distribution, $\Sigma_i = \Sigma_0(r/r_0)^{-1/2}$. The AD Elsasser number increases sequentially from the top panel to the bottom panel: (a) ad-els0.01; (b) ad-els0.05; (c) ad-els0.1; (d) ad-els0.25 (ref); (e) ad-els0.5; (f) ad-els1.0; (g) ad-els2.0; (h) ideal.

especially during the initial adjustment before a quasi-steady state is reached, may have redistributed some poloidal magnetic flux from the outer part of the disk to the inner part, making it easier to form rings and gaps there (the effects of magnetic field strength will be discussed in the next subsection). As the disk becomes better magnetically coupled (going from panel b to e), the number of rings and gaps in the inner 10 au region appears to decrease somewhat and the contrast between adjacent rings and gaps tends to increase on average. The higher contrast may be related to the fact that a better magnetic coupling would allow more poloidal magnetic flux to be trapped in the inner disk region.

As the AD Elsasser number increases further (to $\Lambda_0 = 1.0$ and larger), another feature starts to become important. It is the development of the classical 'channel flows' of the magnetorotational instability. The channels flows are already present in the intermediate regime for Λ_0, especially in the outer part of the disk (see panels c and d of Fig. 3.1 for the reference run), where the magnetic field is better coupled to the disk compared to the inner part as measured by the Elsasser number, which scales with radius as $\Lambda \propto r^{3/4}$. Their growth was kept in check by ambipolar diffusion in relatively diffusive models with Λ_0 up to 0.5 (panel e in Fig. 3.10, 3.11, and 3.12). For better magnetically coupled disks, these channel flows run away, especially near the disk surface, forming the so-called avalanche accretion streams (see Matsumoto et al. 1996; Kudoh et al. 1998 and Suriano et al. 2017). When fully developed, they dominate the dynamics of both the disk and the wind, driving both to an unsteady state (see panels f-h of Fig. 3.10).

Despite the transition to a more chaotic dynamical state, prominent rings and gaps are still formed, especially in the outer part of the disk (see panels f-h of Fig. 3.11). Part of the reason is that the strong variability of the clumpy wind is able to create

variation in the disk surface density. Another, perhaps more important, reason is that the distribution of the poloidal magnetic flux is highly inhomogeneous in the disk and regions with concentrated magnetic flux tend to accrete faster leading to lower surface densities (i.e., gaps), similar to the more magnetically diffusive cases (e.g., the reference run and Fig. 3.8). Since the poloidal field bunching is present even in the ideal MHD case,[4] its formation does not require ambipolar diffusion, which is formally different from the more diffusive reference case[5] (see discussion in Section 3.3.3.3). Nevertheless, there is widespread reconnection in these better coupled cases as well (this is best seen in the movie version of Fig. 3.10 available online). The reconnection is still driven by sharp radial pinching of the poloidal field lines. The difference is that here the pinching is caused by the non-linear development of unstable channel flows (Bai & Stone 2014) rather than the AD-driven midplane current sheet. As a result, the reconnection occurs more sporadically and is less confined to the midplane. The net result is the same: a redistribution of poloidal magnetic flux relative to the matter, creating regions of stronger (poloidal) magnetization that tend to form gaps and regions of weaker (poloidal) magnetization that tend to form rings. These considerations strengthen the case for reconnection as a key to ring and gap formation in a coupled, magnetized disk-wind system, either through an AD-driven midplane

[4]In the ideal MHD case, the wind is significantly stronger in the upper hemisphere than in the lower hemisphere (see Fig. 3.10h). Such an asymmetry has been observed in the non-ideal shearing box simulations of Lesur et al. (2014) and Bai (2015), and in the global non-ideal MHD simulations of Béthune et al. (2017). The fact that it shows up in global ideal MHD simulations as well indicates that it may be a general feature of magnetically coupled disk-wind systems that should be examined more closely.

[5]Poloidal field bunching in the ideal MHD limit has been observed in the shearing box simulations of Moll (2012) in the case of strong disk magnetization corresponding to plasma-β of order unity, however, artificial injection of matter onto the field lines (to prevent rapid depletion of disk material) complicates the interpretation of the result. Current global 3D ideal MHD simulations of weak field cases of $\beta \sim 10^3$ or larger (e.g., Zhu & Stone 2018) do not appear to show as prominent poloidal field bunching as our 2D (axisymmetric) case. Whether this difference is due to the difference in dimensionality of the simulations or some other aspects (e.g., initial and boundary conditions) remains to be determined.

current sheet in relatively diffusive disks, the non-linear development of MRI channel flows in better coupled disks, or some other means.

3.4.2 Explicit resistivity and magnetic field strength

The introduction of explicit Ohmic resistivity into the reference simulation can give us some important insights on the ring and gap formation mechanism. We add an Ohmic resistivity, η_O, that is constant in both space and time (as in Suriano et al. 2017). Specifically, three values of η_0 are considered corresponding to 0.26, 2.6, and 26 times the effective ambipolar resistivity at the inner edge of the disk at the midplane, $\eta_{A,0} = 9.71 \times 10^{14}$ cm^{2}s^{-1}; they are named oh0.26, oh2.6, and oh26, respectively. These simulations are plotted in panels (a)-(c) of Fig. 3.13 and 3.14. In the most diffusive case with $\eta_O = 26\ \eta_{A,0}$, there is some concentration of mass at small radii, indicating that there is still mass accretion. However, there is little evidence for rings and gaps with the formation mechanism apparently turned off by the addition of a large resistivity. This strengthens the case for reconnection-driven ring and gap formation, because the large resistivity erases the sharp magnetic field geometries needed for reconnection. As the resistivity decreases, rings and gaps start to appear. In particular, when the resistivity η_O drops below the characteristic AD resistivity $\eta_{A,0}$ (model oh0.26), the simulation looks very similar to the reference run that does not have any explicit resistivity. Their similarity, particularly in the location and structure of the rings and gaps, is quantified in Fig. 3.15(a).

Besides magnetic diffusivity, the magnetic field strength also strongly affects the ring and gap formation. The second column of Fig. 3.13 and 3.14 (panels d-f) shows the effects of varying the initial magnetic field strength, as characterized by the midplane plasma-β, keeping everything else the same as in the reference run (panel e).

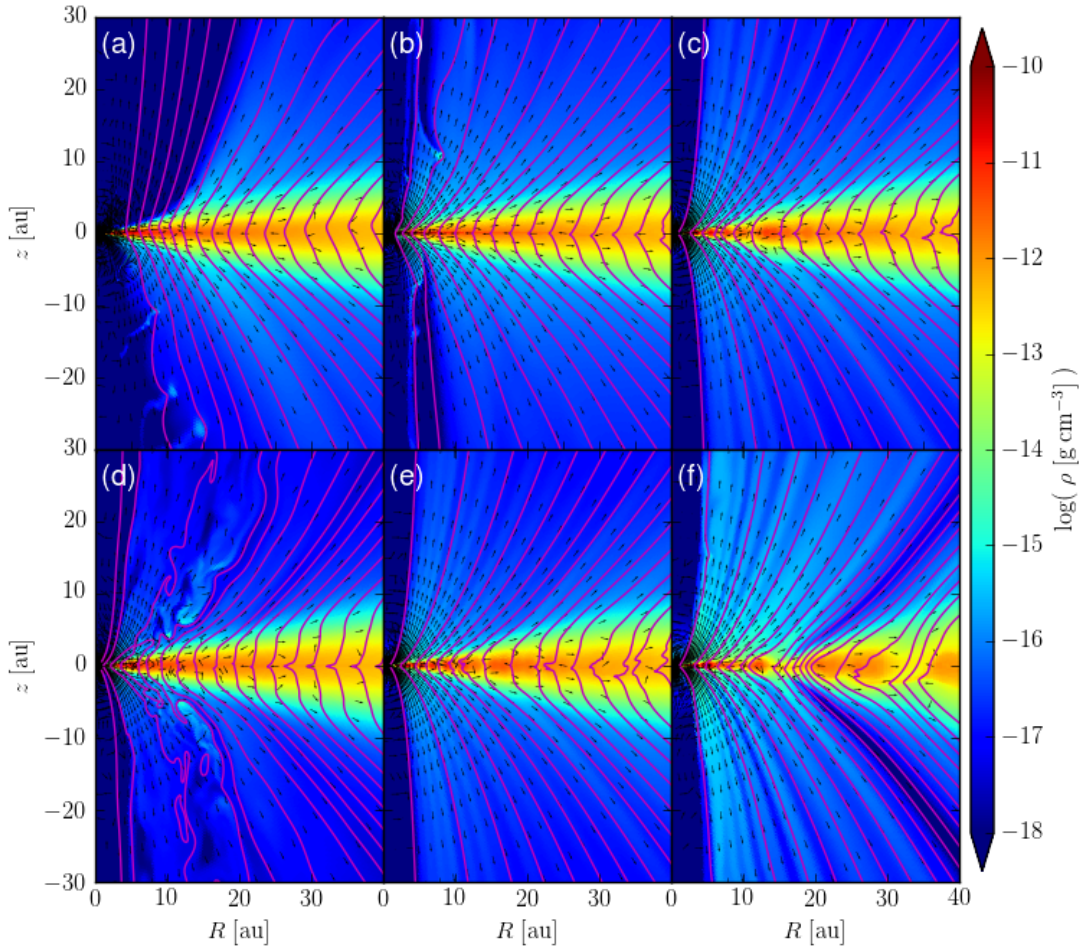

Fig. 3.13.— Snapshots of simulations where the explicit Ohmic resistivity and plasma-β are varied at $t/t_0 = 2000$. Shown is the mass volume density (logarithmically spaced colour contours in units of g cm^{-3}), the poloidal magnetic field lines (magenta), and the poloidal velocity unit vectors (black). In the top row, the explicit resistivity is decreased from panels (a)-(c). Plasma-β varies from high to low across the bottom row in panels (d)-(f). The reference simulation (ad-els0.25) is shown in panel (e). The simulation panels in alphabetical order are: (a) oh26; (b) oh2.6; (c) oh0.26; (d) beta1e4; (e) ad-els0.25; (f) beta1e2. See Table 3.1 for details. (See the supplementary material of Suriano et al. 2018 in the online journal for an animated version of this figure.)

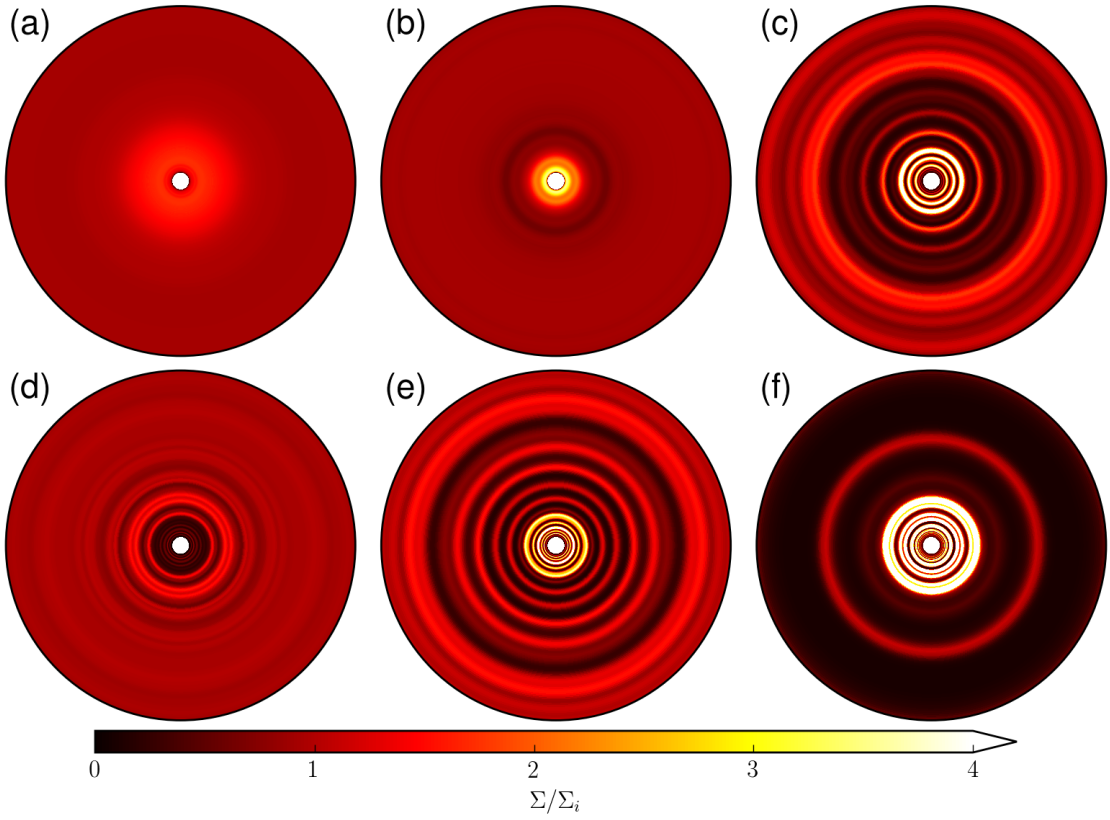

Fig. 3.14.— Face-on surface density profiles (up to a radius of 20 au) of the simulations where the explicit Ohmic resistivity and plasma-β are varied at $t/t_0 = 2000$. In the top row, the explicit resistivity is decreased from panels (a)-(c). Plasma-β varies from high to low across the bottom row in panels (d)-(f). The reference simulation (ad-els0.25) is shown in panel (e). The simulation panels in alphabetical order are: (a) oh26; (b) oh2.6; (c) oh0.26; (d) beta1e4; (e) ad-els0.25; (f) beta1e2. (See the supplementary material of Suriano et al. 2018 in the online journal for an animated version of this figure.)

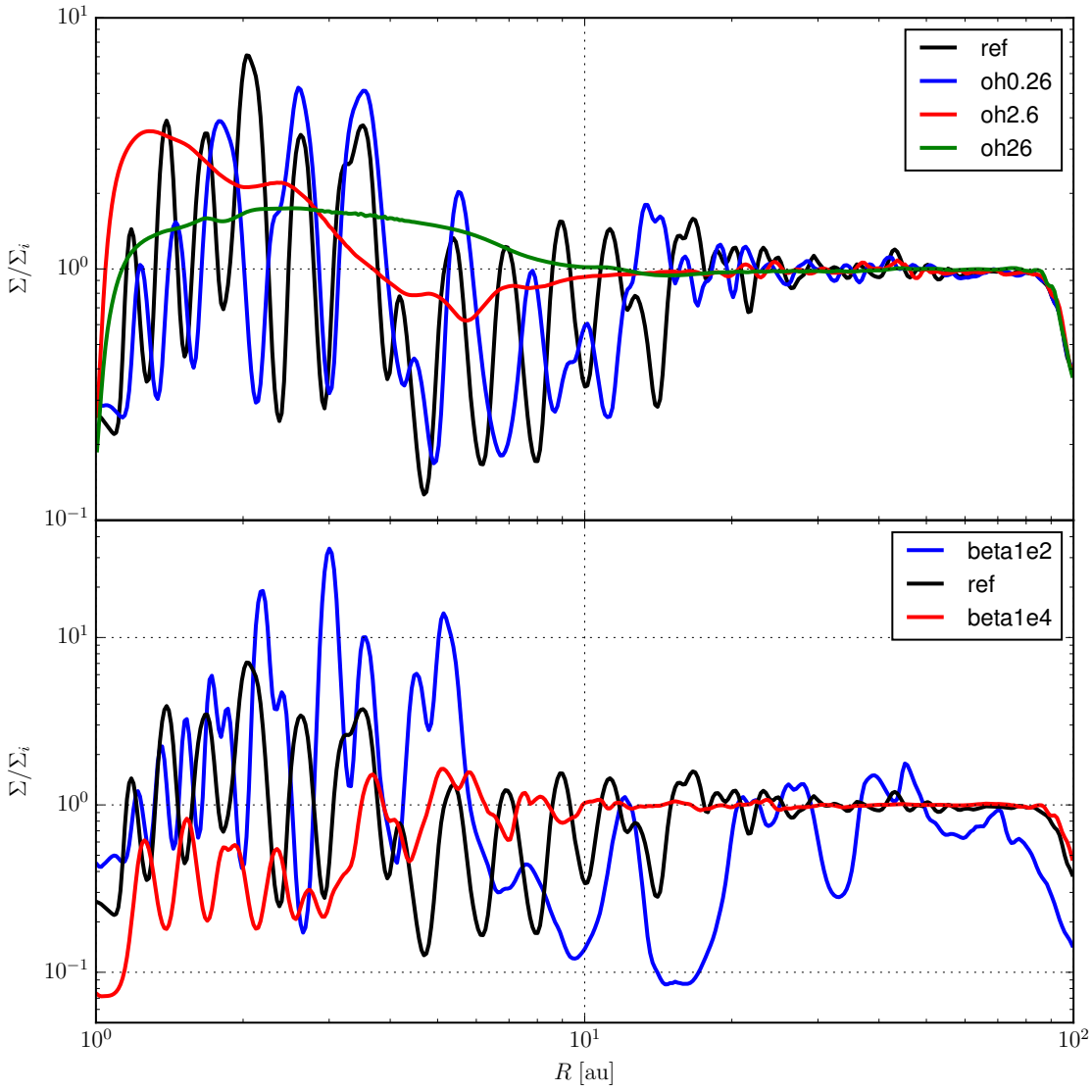

Fig. 3.15.— Surface density profiles at time $t/t_0 = 2000$ for simulations with different explicit Ohmic resistivities (top) and initial magnetic field strengths, i.e., β_0 (bottom). The surface density profiles are normalized to the initial surface density distribution, $\Sigma_i = \Sigma_0 (r/r_0)^{-1/2}$.

These simulations are quantitatively similar, in that a wind is launched from the disk and rings and gaps are formed in all three cases. However, it takes longer for the weaker magnetic field case to produce a well-developed wind. Specifically, in the most weakly magnetized case (model beta1e4), it takes approximately 700 inner orbital periods for the disk wind from the inner part of the disk to become fully developed. This is because it takes longer to generate a strong enough toroidal field out of the weaker initial poloidal field to push the outer layers of the disk to large distances. The weakest field case should be the most prone to the MRI, however, there is no evidence for accretion streams developing near the disk surface.

As in the reference run, the ambipolar diffusion is able to concentrate the radial current (J_r) into a thin sheet near the midplane, where preferential accretion leads to severe radial pinching of the poloidal field, eventually leading to reconnection-driven ring and gap formation. The rings and gaps formed in this simulation have a relatively low contrast, however. This is because, with a weak initial field, there is less poloidal magnetic flux concentrated in the gaps after reconnection making the accretion of disk material from the gaps into the neighbouring rings less efficient.

In the stronger magnetic field case (model beta1e2), a quasi-steady wind is quickly established (see panel f of Fig. 3.13). It drives fast disk accretion, especially near the midplane, where reconnection of the sharply pinched poloidal field leads to demagnetization in some regions (creating rings) and bunching of poloidal field lines in others (creating gaps). The stronger poloidal field drives a more complete depletion of disk material, creating wider gaps with lower column densities, as illustrated in Fig. 3.14(f) and quantified in Fig. 3.15(b). In addition, the stronger overall field allows more material to be moved from the outer part of the disk to smaller disk radii, where several rings have much higher surface densities than their counterparts in the

weaker field cases. The most massive inner ring at $r = 3$ au has a contrast ratio of $\sim 10^2$. In any case, in the presence of the reference level of ambipolar diffusion, the same reconnection-driven ring and gap formation mechanism appears to operate over a range of disk plasma-β with more strongly magnetized disks forming rings and gaps with higher surface density contrast.

3.4.3 Magnetic stresses and two modes of accretion

We have shown in Section 3.4.1 and 3.4.2 that the level of magnetic diffusivity, particularly ambipolar diffusion, plays a key role in determining the structure of the magnetically coupled disk-wind system. Specifically, more magnetically diffusive systems tend to be more laminar, with a well-developed wind that is expected to play a dominant role in driving disk accretion. Better magnetically coupled systems are more prone to MRI channel flows, which drive the system to a chaotic state. Although a wind is still developed, it may not play as important a role in disk accretion. In this subsection, we will try to quantify this expectation.

We do this through the dimensionless α parameters (Shakura & Sunyaev 1973), corresponding to the $r\phi$ and $z\phi$ components of the Maxwell stress, $T_{r\phi} = -\frac{B_r B_\phi}{4\pi}$ and $T_{\theta\phi} = -\frac{B_\theta B_\phi}{4\pi}$, respectively, defined as:

$$\alpha_{r\phi} \equiv \frac{\int T_{r\phi} dz}{\int P dz}, \tag{3.18}$$

$$\alpha_{\theta\phi} \equiv \frac{T_{\theta\phi}\Big|_{\pi/2-\theta_0}^{\pi/2+\theta_0}}{P_{\rm mid}}, \tag{3.19}$$

where P is the thermal pressure and $P_{\rm mid}$ is the pressure on the disk midplane. In the first term, the integration is between the lower and upper surfaces of the initial

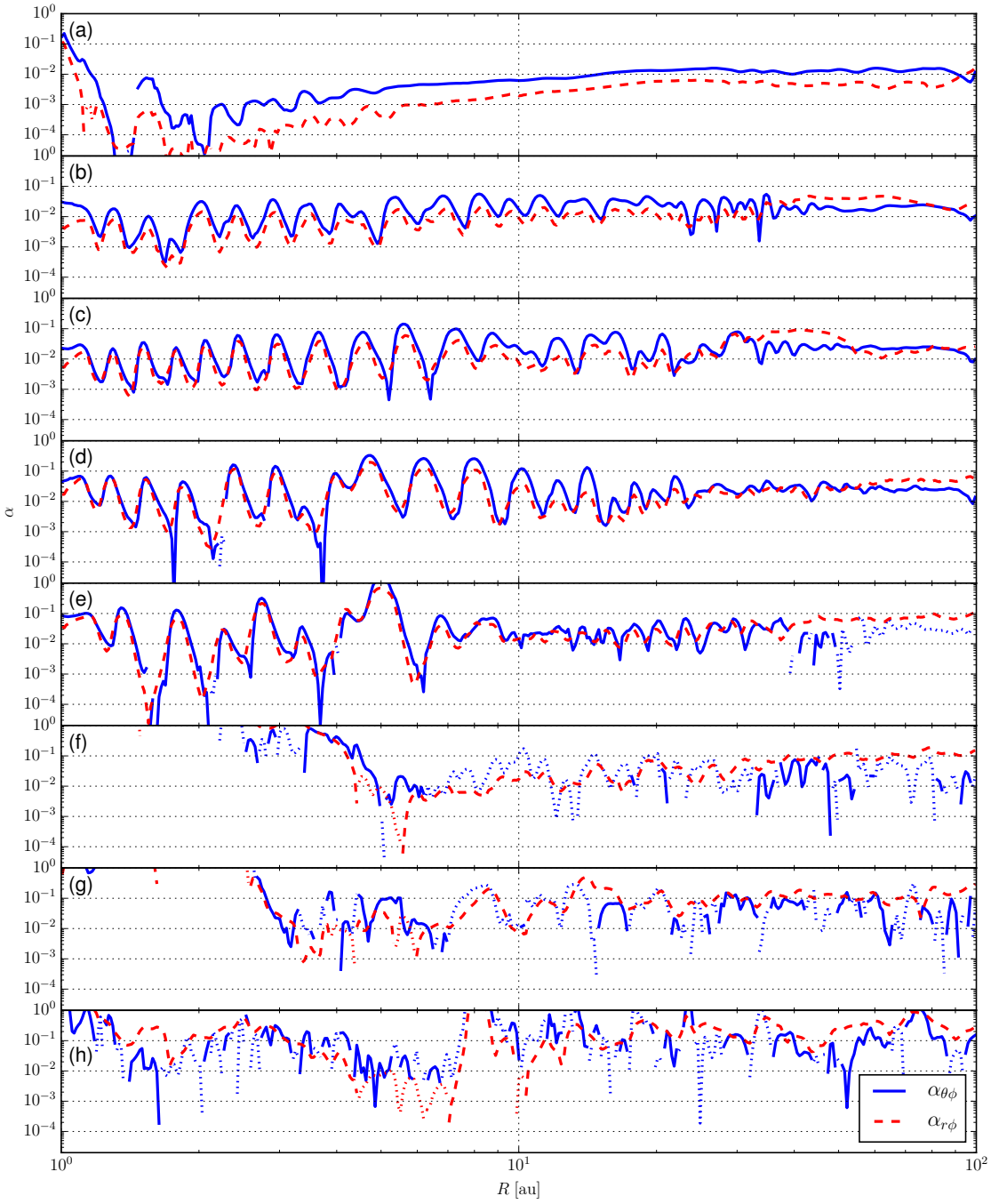

Fig. 3.16.— The α parameter from the vertical wind stress, $\alpha_{\theta\phi}$ (see equation 3.18; solid blue line), and the radial shear stress, $\alpha_{r\phi}$ (see equation 3.19; dashed red line). The vertical wind stress is calculated at the surface $\theta = \pi/2 \pm 2\epsilon$ and the radial shear stress is integrated between these surfaces. The dotted lines show where the effective α is negative. The AD Elsasser number increases sequentially from the top panel to the bottom panel: (a) ad-els0.01; (b) ad-els0.05; (c) ad-els0.1; (d) ad-els0.25 (ref); (e) ad-els0.5; (f) ad-els1.0; (g) ad-els2.0; (h) ideal.

disk, $\theta = \pi/2 \pm \theta_0$. The second term is evaluated at these surfaces. Since the polar shear stress $T_{\theta\phi}$ is the magnetic stress that moves angular momentum across the disk surface (at a constant polar angle θ), we will refer it to as the 'wind stress.' The other component, $T_{r\phi}$, will be referred to as the 'radial shear stress.'

Figure 3.16 compares these two α parameters for the set of simulations where the AD Elsasser number is varied. In the least coupled simulation, the wind stress is larger than the radial shear stress by a factor of a few. As the Elsasser number increases, the radial shear stress begins to grow until it is approximately equal to the wind stress by the simulation where the AD Elsasser number is $\Lambda_0 = 0.5$ (see Fig. 3.16e). In the intermediate parameter regime (Λ_0 between 0.05 and 0.5), where the wind remains relatively laminar and the rings and gaps are rather steady, the two stresses are strongly correlated with both peaking in low-density gaps where the poloidal magnetic field lines are concentrated (compare, for example, panel d of Fig. 3.16 to panel d of Fig. 3.12, which shows that both stresses peak in the low-density gaps for the reference run). As the Elsasser number increases further, the avalanche accretion streams become prevalent, driving the atmosphere of disk and the base of the wind to be chaotic. This transition to a more chaotic disk-wind system is already present in the outer part of the disk in the $\Lambda_0 = 0.5$ case beyond ~ 50 au (see panel e), where the avalanche accretion flows have reversed the direction of the polar shear stress $T_{\theta\phi}$ at the initial surface of the disk ($\theta = \pi/2 \pm \theta_0$). For the cases with higher $\Lambda_0 = 1.0,\ 2.0,$ and ∞ (ideal MHD), the effective α parameter for $T_{\theta\phi}$ becomes highly variable in both space and time and is often negative. However, $T_{r\phi}$ stays mostly positive, indicating that angular momentum in the disk is more persistently transported radially outward by avalanche accretion streams rather than vertically across the initial disk surface.

3.5 Discussion

3.5.1 Comparison to other works

This work examines how radial substructure can be created in a circumstellar disk in the presence of ambipolar diffusion on the scale of a few to tens of au, as part of a magnetically coupled disk-wind system. In Suriano et al. (2017), a similar phenomenon was observed to operate near the innermost disk radii ($\sim$ 0.1 au), where Ohmic resistivity dominates. As in Suriano et al. (2017), we again find that rings and gaps are formed solely from MHD processes. Here, the effects of AD have a clear and physically motivated interpretation as to how radial substructure is formed in simulations where the ions and neutrals are moderately coupled. The mechanism, described in Section 3.3.3, relies on mass accretion through an AD-induced, midplane (J_r) current layer, where the poloidal magnetic field is dragged radially inward until it reconnects. The reconnection creates regions with magnetic loops where the net poloidal flux is decreased and mass accretion is less efficient, allowing matter to pile up into rings. It also enables the post-reconnection poloidal field to bunch up in localized regions, where mass accretion is more efficient, creating gaps.

The formation of radial disk substructures in MHD simulations (besides those formed by planets) has been seen at the boundaries of dead zones (Dzyurkevich et al. 2010; Flock et al. 2015; Ruge et al. 2016) and in the context of zonal flows (Johansen et al. 2009; Kunz & Lesur 2013; Dittrich et al. 2013; Simon & Armitage 2014; Bai & Stone 2014; Bai 2015; Béthune et al. 2016, 2017). The concentration of poloidal magnetic field lines specifically in the presence of AD was observed in the disk simulations of Bai & Stone (2014) and Béthune et al. (2017). This has been

interpreted through the following form of the induction equation:

$$\frac{d\Phi_B(R,z)}{dt} = -2\pi R\mathcal{E}_\phi, \tag{3.20}$$

where Φ_B is the vertical magnetic flux, and $\mathcal{E}_\phi$ is the ϕ component of the electromotive force (EMF; equation 8 of Bai & Stone 2017; see also equation 23 of Béthune et al. 2017). The EMF induced by AD is equal to $\boldsymbol{\mathcal{E}}_A = \eta_A \boldsymbol{J}_\perp$, where $\boldsymbol{J}_\perp$ is the component of the current perpendicular to the magnetic field (as defined in equation 3.3). When the azimuthal component of this perpendicular current, $J_{\perp,\phi}$, has a sign opposite to that of J_ϕ, the AD EMF becomes anti-diffusive in nature, which would lead to the concentration of poloidal magnetic field lines. We have examined $J_{\perp,\phi}$ and J_ϕ in our reference run (where there is large spatial variation of the poloidal magnetic field strength, see Fig. 3.8b), and found that they have opposite signs in some regions but the same sign in others, which makes it hard to establish unambiguously the extent to which this mechanism may be operating in our simulations. In any case, we find that our results can be explained by a more pictorial mechanism: reconnection of sharply pinched poloidal field lines (e.g., Fig. 3.7) that drives the segregation of poloidal magnetic flux relative to matter, which in turn leads to the formation of radial substructure. We note that Bai & Stone (2014) also considered the possibility of reconnection playing a role in concentrating magnetic flux in the zonal flows found in their shearing box simulations (see their Fig. 9 for a cartoon illustrating the possibility). The relatively laminar nature of the disk accretion in the presence of a moderately strong ambipolar diffusion allowed us to isolate the reconnection events more clearly in our (2D) global simulations (see Fig. 3.7). Whether it has a deeper physical connection with the mechanism that relies on $J_{\perp,\phi}$ and J_ϕ having opposite signs remains to be ascertained.

Although rings and gaps are prominent in most of our simulations, they are not a common feature of previous simulations. For example, the recent global accretion disk simulations of Bai & Stone (2017) and Bai (2017) do not seem to show such radial substructure. This is likely due to the fact that a weaker initial poloidal field strength is used (however, see the shearing box simulations of Bai 2015 where zonal flows develop with $\beta = 10^5$). Specifically, in the simulations of Bai (2017) the initial magnetic field in the disk is characterized by $\beta = 10^5$, which is higher than the largest initial value of plasma-β used in our simulations. In our $\beta \sim 10^4$ simulation, rings and gaps are still present. However, the surface density contrast is reduced compared to the reference run of $\beta \sim 10^3$ (see Fig. 3.15). Although the same magnetic field variations and midplane pinching still occur in the weaker magnetic field simulation of $\beta \sim 10^4$ (see Fig. 3.13c), the magnetic field is less able to move matter around to form rings and gaps and the timescale for the magnetic field to dynamically influence the matter will be longer compared to the stronger field case. As such, we expect the formation of rings and gaps to become increasingly less efficient as the magnetic field strength is reduced towards the purely hydrodynamic limit.

The initial field strengths in the ideal simulations of Zhu & Stone (2018) are similar to those adopted here ($\beta_0 \sim 10^3$). They show that most of the accretion occurs in a vertically extended disk 'envelope,' with radial (as opposed to vertical) transport of angular momentum playing a dominant role in driving disk accretion. As discussed extensively in Suriano et al. (2017), this is consistent with the development of avalanche accretions streams as the Ohmic resistivity is reduced. It is also in agreement with the simulations in this work as we move towards the ideal MHD regime of large Elsasser numbers (see Fig. 3.16). This agreement strengthens the case for the transition from a laminar disk-wind system to a more chaotic system

dominated by the rapid formation and break up of accretion streams as the magnetic diffusivity (either Ohmic or ambipolar) is reduced.

3.5.2 Dust dynamics and grain growth

Wind-driven laminar disk accretion is an important feature of the moderately well magnetically coupled disks studied both in this paper (from AD) and in Suriano et al. (2017) (due to Ohmic dissipation). There is some evidence that such a laminar accretion may be required for the HL Tau disk. As stressed by Pinte et al. (2016), there is tension between the small scale height of (sub)millimeter-emitting dust grains (inferred from the lack of azimuthal variation in the gap widths for the inclined HL disk, indicating strong dust settling) and the substantial ongoing mass accretion observed in the system, which, if driven by turbulence, would require a turbulence too strong to allow for the inferred degree of dust settling. This tension can be removed if the accretion is driven by ordered magnetic stresses rather than MRI-induced turbulence (Hasegawa et al. 2017), as in our simulations with high to moderate levels of AD (such as the reference run), since dust grains can still settle to the midplane even with strong accretion. Furthermore, rings and gaps are naturally produced in these laminarly accreting disk-wind systems through the AD-aided magnetic reconnection; this mechanism can in principle produce the rings and gaps observed in the HL Tau disk. In practice, our model parameters are chosen for the purposes of illustrating the basic principles of ring and gap formation in the presence of ambipolar diffusion rather than for comparison with any specific object. Taken at the face value, the typical mass accretion rate of 10^{-6} $M_\odot$ yr^{-1} found in the reference simulation is at least an order of magnitude larger than that inferred for classical T Tauri stars (Hartmann et al. 2016). However, it is more consistent with the accretion rates inferred

for younger protostellar disks (e.g., Yen et al. 2017), although, it is possible to reduce the mass accretion rates in these simulations through rescaling (e.g., by adopting a lower initial disk density, ρ_0; see Appendix of Stepanovs & Fendt 2014).

The formation of rings and gaps in a relatively laminar disk has important implications for the dynamics of dust grains. Pressure maxima, such as those formed from dense gas rings, are known sites of dust trapping (Whipple 1972; Chiang & Youdin 2010). Without such traps, large millimeter-sized grains would migrate inward quickly as they lose angular momentum to the more slowly rotating gas that is partially supported by the radial pressure gradient (Weidenschilling 1977a). This rapid radial drift is particularly problematic for low-mass disks around brown dwarfs (Pinilla et al. 2013). For example, in the case of 2M0444, Ricci et al. (2017) has shown explicitly that, without any dust trap, millimeter-sized grains would be quickly depleted from the outer part of this disk (on the scale of tens to a hundred au; see the upper-left panel of their Fig. 3), in direct contradiction to observations. They also demonstrated that this fundamental problem can be resolved if there are multiple pressure peaks in the outer disk (see the lower-right panel of their Fig. 3). Such pressure peaks are naturally produced in our simulations (see, e.g., Fig. 3.8 of the reference run).

Our mechanism of producing rings has two strengths. First, it takes into account ambipolar diffusion, which is the dominant non-ideal MHD effect in the outer disk where dust trapping is needed to be consistent with dust continuum observations. Second, it can in principle operate not only in relatively evolved protoplanetary disks but also younger protostellar disks as long as such disks are significantly magnetized with a poloidal field. Indeed, our mechanism is likely to work more efficiently in the earlier phases of disk evolution where the disk is expected to be threaded by a

strong poloidal magnetic field, perhaps inherited from the collapse of dense cores, which are known to be magnetized with rather ordered magnetic fields (e.g., Troland & Crutcher 2008; Li et al. 2014a,b). Such ordered poloidal fields can drive fast disk accretion expected in the early phases without generating a high level of turbulence in the outer (AD-dominated) region, which should make it easier for the dust to settle vertically and grow near the midplane, even during the early, perhaps Class 0, phase of star formation. In other words, strong accretion does not necessarily mean strong turbulence. Even in the earliest, Class 0 phase of star formation, large grains (if they are present) can be trapped in principle by the pressure bumps that naturally develop in the magnetically coupled disk-wind systems. Observationally, whether rings and gaps are prevalent in Class 0 disks is unknown at the present time, because they are more difficult to observe in the presence of a massive protostellar envelope, however, there is some evidence that rings and gaps are already present in at least the Class I phase (see observations of IRS 63 in ρ Oph by Segura-Cox et al., *in prep.*).

Lastly, we note that the laminar disk wind in our reference and related simulations can preferentially remove gas from the disk, if the dust has settled to the midplane (or perhaps been trapped near the rings). As discussed by Suzuki et al. (2010), this could lead to an increase in the dust-to-gas mass ratio (see also Gorti et al. 2015; Bai et al. 2016), conducive to the development of the streaming instability (Youdin & Goodman 2005; Squire & Hopkins 2018), which may facilitate the formation of planetesimals and eventually planets (e.g., Chiang & Youdin 2010). This process of grain settling, growth, and trapping may be as efficient, in not more, in the early, protostellar phase of star formation compared to the later, protoplanetary phase. We will postpone a quantitative exploration of this interesting topic to a future investigation.

3.6 Conclusion

We have carried out 2D (axisymmetric) simulations of magnetically coupled disk-wind systems in the presence of a poloidal magnetic field and ambipolar diffusion (AD). The field strength is characterized by the plasma-β and AD by the dimensionless Elsasser number Λ_0. We focused on $\beta \sim 10^3$ and explored a wide range of values for Λ_0, from 0.01 to ∞ (ideal MHD). Our main conclusions are as follows:

1. In moderately well coupled systems with Λ_0 between 0.05 and 0.5, including the reference simulation (ad-els0.25), we find that prominent rings and gaps are formed in the disk through a novel mechanism, AD-assisted reconnection. This mechanism starts with the twisting of the initial poloidal magnetic field into a toroidal field that reverses polarity across the disk midplane. Ambipolar diffusion enables the Lorentz force from the toroidal field pressure gradient to drive the ions (and the toroidal field lines tied to them) towards the magnetic null near the midplane, which steepens the radial (J_r) current sheet in a run-away process first described in Brandenburg & Zweibel (1994). The field kink generates a toroidal Lorentz force that removes angular momentum from the thin radial current sheet, forcing it to accrete preferentially relative to the rest of the disk. The preferential midplane accretion drags the poloidal field lines into a sharply pinched configuration, where the radial component of the magnetic field reverses polarity over a thin, secondary azimuthal (J_ϕ) current sheet. Reconnection of the radial pinch produces two types of regions with distinct poloidal field topologies: one occupied by magnetic loops and another that remains threaded by ordered poloidal fields. The weakening of the net poloidal field in the former makes angular momentum removal less efficient, allowing disk material to accumulate to form dense rings. Conversely, those regions that gained poloidal

flux after reconnection are magnetically braked more strongly, with a faster draining of disk material that leads to gap formation. In addition, AD allows for a quasi-steady state of the ring and gap structure, where the field lines can stay more or less fixed in place despite rapid mass accretion in gaps because of the ion-neutral drift. We find little evidence for the formation of prominent rings and gaps in the case of the highest ambipolar diffusion considered in this work ($\Lambda = 0.01$) and cases with large, additional Ohmic diffusivities. This finding is consistent with the above scenario because the radial pinching of the poloidal field is smoothed out by the excessive magnetic diffusivity, suppressing the reconnection that lies at the heart of the mechanism.

2. In better magnetically coupled disk-wind systems with larger Λ_0, as well as the ideal MHD limit, we find that avalanche accretion streams develop spontaneously near the disk surface. The accretion streams lead to unsteady/chaotic disk accretion and outflow, as found previously in Suriano et al. (2017) for cases of low or zero Ohmic resistivities (see also Zhu & Stone 2018). Prominent rings and gaps are still formed in the disk. Part of the reason is the large temporal and spatial variations induced by the constant formation and destruction of the streams will inevitably produce spatial variation in the mass accretion rate and thus the surface density. Perhaps more importantly, the poloidal field lines are concentrated in some regions and excluded from others, with the more strongly magnetized regions producing gaps and the less magnetized regions forming rings, just as in the more magnetically diffusive reference case. We suggest that this segregation of poloidal magnetic flux and matter is also due to reconnection of highly pinched poloidal fields. In this case, the pinching is caused by the avalanche accretion streams (a form of MRI channel flows) rather

than the midplane current sheet steepened by AD. The fact that rings and gaps are formed in both laminar and chaotic disk-wind systems over a wide range of magnetic diffusivities suggests that they are a robust feature of such systems, at least when the initial poloidal magnetic field is relatively strong. For more weakly magnetized systems, reconnection may still occur but the resulting redistribution of poloidal magnetic flux would have less of a dynamical effect on the gas, making ring and gap formation less efficient.

3. If young star disks are threaded by a significant poloidal magnetic field, especially during the early phases of star formation, it may drive rapid disk accretion through a magnetic wind without necessarily generating strong turbulence in the disk, particularly in the outer parts of the disk that are only moderately well coupled to the magnetic field. The lack of a strong turbulence despite rapid accretion may allow dust to settle early in the process of star formation, facilitating early grain growth. Large grains may be trapped in the rings that are naturally produced in the system, which may promote the formation of planetesimals and eventually planets.

Chapter 4

The formation of rings and gaps in three dimensions

This Chapter is based on ongoing work to be submitted to MNRAS for publication (Suriano et al. 2018, in preparation).

Abstract

Previous 2D (axisymmetric) investigations have shown that rings and gaps develop naturally in magnetically coupled disk-wind systems in the presence of Ohmic dissipation and especially ambipolar diffusion (AD). Here we extend the 2D simulations with AD to fully three dimensions (3D). We find that rings and gaps develop naturally in 3D as well, from the same basic mechanism that was identified for the 2D simulations, namely, redistribution of the poloidal magnetic flux relative to the disk material resulted from reconnection of a sharp pinching of the magnetic field lines, with the gaps typically more strongly magnetized poloidally than the (denser) rings. The rings and gaps start out rather smoothly in our 3D simulations that have ax-

isymmetric initial conditions. Non-axisymmetric variations arise spontaneously at later times, but they do not grow to such an extent as to disrupt the rings and gaps. These disk substructures persist to the end of the simulations, lasting up to 3000 times the orbital period at the inner edge of the simulated disk. The longevity of the perturbed but still coherent rings make them attractive sites for trapping large grains that would otherwise be lost to rapid radial migration due to gas drag. We find that rings and gaps are formed for a range of ambipolar diffusivities and magnetic field strengths. They are more prominent in disks that are better coupled to the magnetic field and are more strongly magnetized for the parameter range explored.

4.1 Introduction

We are now entering an era where state-of-the-art observational facilities are providing increasingly stringent constraints on the physical properties of circumstellar disks. Specifically, the Atacama Large Millimeter/submillimeter Array (ALMA) has shown that a large number of circumstellar disks have detailed radial and azimuthal substructures (ALMA Partnership et al. 2015; Andrews et al. 2016; Zhang et al. 2016; Nomura et al. 2016; Pérez et al. 2016; Isella et al. 2016; Cieza et al. 2016; van der Plas et al. 2017; Fedele et al. 2017, 2018; Dipierro et al. 2018). How the various observed structures form remains undetermined, though a number of promising physical mechanisms have been proposed, including planet-disk interactions (Dong et al. 2017; Bae et al. 2017), rapid pebble growth at the condensation fronts of abundant volatile species (Zhang et al. 2015), the pileup of volatile ices in sintering zones just outside snow lines (Okuzumi et al. 2016), sharp changes in the disk viscosity at the boundaries of non-turbulent 'dead zones' (Flock et al. 2015; Ruge et al. 2016), magnetic self-organization through zonal flows (Béthune et al. 2017), and variable

magnetic disk winds (Suriano et al. 2017, 2018). Disk substructures (i.e., rings and gaps, spirals, vortices) have an undoubtedly important influence on the concentration and growth of dust grains in the disks around young stars. They could, for example, prevent fast radial migration of large grains through disks by trapping the grains in the pressure maxima they create possibly even early in the disk lifetime.

So far, the formation of radial substructures via MHD disk winds have only been explored in two dimensions (2D), which necessitates that the structures be axisymmetric (Suriano et al. 2017, 2018). In 2D, the formation of rings and gaps on observable scales ($r \sim 10$ au or larger) results from the effects of ambipolar diffusion (AD; Suriano et al. 2018), where AD is the most important non-ideal MHD effect. Suriano et al. (2018) finds that rings and gaps are naturally produced in the presence of a significant poloidal magnetic field and a relatively strong ambipolar diffusion, from which a relatively laminar disk-wind system develops. The mechanism is driven by reconnection of the highly pinched poloidal magnetic field in a thin midplane current sheet where the reconnection leads to the weakening of the poloidal field in some regions, which accrete more slowly and form rings, and field concentration in others, which accrete efficiently and open up gaps.

This work explores the formation of rings and gaps in circumstellar disks by magnetic disk winds in the presence of ambipolar diffusion in three dimensions (3D), a logical next step to fully determine whether, and if so, how substructures develop in magnetically coupled disk-wind systems. We find that prominent rings and gaps are still formed in 3D, and that the same mechanism of a thin midplane current sheet leading to reconnection and, therefore, the redistribution of the poloidal magnetic flux relative to disk matter, seems to be at work. In addition, we find interesting non-axisymmetric structures that are absent from the previous 2D (axisymmetric)

simulations.

The rest of the Chapter is organized as follows. In Section 4.2, we describe the simulation setup, including the initial and boundary conditions. The results of the simulations are presented in Section 4.3, with a focus on a reference simulation where the AD Elsasser number at the inner edge of the disk is $\Lambda_0 = 0.25$ (see Section 4.2.3 for the description of this quantity). Other simulations with different AD Elsasser numbers, magnetic field strengths, and numerical resolution are discussed in Section 4.4. Finally, in Section 4.5 we summarize the main results and make concluding remarks.

4.2 Simulation setup

4.2.1 MHD equations

We use the ZeusTW code (Krasnopolsky et al. 2010) to solve the time-dependent magnetohydrodynamic (MHD) equations in spherical polar coordinates (r, θ, ϕ). The equations solved are

$$\frac{\partial \rho}{\partial t} + \nabla \cdot (\rho \boldsymbol{v}) = 0, \tag{4.1}$$

$$\rho \frac{\partial \boldsymbol{v}}{\partial t} + \rho \left(\boldsymbol{v} \cdot \nabla \right) \boldsymbol{v} = -\nabla P + \boldsymbol{J} \times \boldsymbol{B}/c - \rho \nabla \Phi_g, \tag{4.2}$$

$$\frac{\partial \boldsymbol{B}}{\partial t} = \nabla \times (\boldsymbol{v} \times \boldsymbol{B}) - \frac{4\pi}{c} \nabla \times \left(\eta_O \boldsymbol{J} + \eta_A \boldsymbol{J}_\perp \right), \tag{4.3}$$

$$\frac{\partial e}{\partial t} + \nabla \cdot (e \boldsymbol{v}) = -P \nabla \cdot \boldsymbol{v}, \tag{4.4}$$

where the internal energy is $e = P/(\Gamma - 1)$ and Γ is the adiabatic index. The current density is $\boldsymbol{J} = (c/4\pi) \nabla \times \boldsymbol{B}$ and the current density perpendicular to the magnetic field is $\boldsymbol{J}_\perp = -\boldsymbol{J} \times \boldsymbol{B} \times \boldsymbol{B}/B^2$. The Ohmic resistivity is η_O and the effective ambipolar

diffusivity η_A is defined as

$$\eta_A = \frac{B^2}{4\pi\gamma\rho\rho_i}, \tag{4.5}$$

where ρ_i is the ion density and $\gamma = \langle\sigma v\rangle_i/(m + m_i)$ is the frictional drag coefficient with units of cm^3 g^{-1} s^{-1}. The remaining parameters have their usual definitions. When referring to cylindrical coordinates, we will use the notation (R, ϕ, z) such that $R = r\sin\theta$ and $z = r\cos\theta$.

4.2.2 Initial conditions

The initial conditions are similar to those in Suriano et al. (2018). We describe them here in detail for completeness. Specifically, the simulation domain is separated into two regions: a thin, cold, rotating disk orbiting a 1 M$_\odot$ central source at the grid origin and an initially non-rotating, hot corona above the disk that is quickly replaced by a magnetic wind driven from the disk. We choose the adiabatic index to be $\Gamma = 1.01$ so that each parcel of material remains nearly isothermal as it moves around in the computation domain. All simulations are initialized to be axisymmetric, although non-axisymetric structures develop naturally at later times.

4.2.2.1 Disk

The geometrically thin disk is characterized by the dimensionless parameter $\epsilon = h/r = c_s/v_K \ll 1$, where h is the disk scale height, c_s is the isothermal sound speed, and v_K is the Keplerian speed. The disk is limited to the equatorial region where the polar angle $\theta \in [\pi/2 - \theta_0, \pi/2 + \theta_0]$, with disk (half) opening angle set to $\theta_0 = \arctan(2\epsilon)$. The disk density takes the form of a radial power law multiplied by a Gaussian function of $z/r = \cos\theta$,

$$\rho_d(r, \theta, \phi) = \rho_0 \left(\frac{r}{r_0}\right)^{-\alpha} \exp\left(-\frac{\cos^2\theta}{2\epsilon^2}\right), \tag{4.6}$$

as determined by hydrostatic balance. The subscript '0' refers to values on the disk midplane at the inner radial boundary. For all simulations shown in this Chapter, we use $\alpha = 3/2$. The disk pressure is set as

$$P_d(r, \theta, \phi) = \rho_d c_s^2, \tag{4.7}$$

with $c_s = \epsilon v_K$. The radial pressure gradient causes the equilibrium rotational velocity v_ϕ to be slightly sub-Keplerian,

$$v_\phi = v_K \sqrt{1 - (1+\alpha)\epsilon^2}. \tag{4.8}$$

4.2.2.2 Corona

We require that the hydrostatic corona is initially in pressure balance with the disk surface. This constraint sets the density drop from the disk surface to the corona as $(1+\alpha)\epsilon^2$. Therefore, the coronal density and pressure are

$$\rho_c(r) = \rho_0 \epsilon^2 (1+\alpha) \exp\left[-\frac{\cos^2\theta_0}{2\epsilon^2}\right] \left(\frac{r}{r_0}\right)^{-\alpha} \equiv \rho_{c,0} \left(\frac{r}{r_0}\right)^{-\alpha}, \tag{4.9}$$

$$P_c(r) = \rho_c v_K^2/(1+\alpha). \tag{4.10}$$

4.2.2.3 Magnetic field

To ensure that the magnetic field is divergence-free initially, we set the magnetic field components using the magnetic flux function Ψ as in Zanni et al. (2007),

$$\Psi(r, \theta) = \frac{4}{3} r_0^2 B_{\mathrm{p},0} \left(\frac{r \sin\theta}{r_0}\right)^{3/4} \frac{m^{5/4}}{\left(m^2 + \cot^2\theta\right)^{5/8}}, \tag{4.11}$$

where $B_{\rm p,0}$ sets the scale for the poloidal field strength and the parameter m controls the bending of the field. The value of $B_{\rm p,0}$ is set by the initial plasma-β, the ratio of the thermal to magnetic pressure, on the disk midplane, which is 10^3 for most of the simulations. Since varying m from 0.1 to 1 has little effect on the long-term disk or wind magnetic field structure (Stepanovs & Fendt 2014), we use $m = 0.5$ for all simulations presented in this work. The initial magnetic field components are then calculated as

$$B_r = \frac{1}{r^2 \sin\theta} \frac{\partial \Psi}{\partial \theta}, \tag{4.12}$$

$$B_\theta = -\frac{1}{r \sin\theta} \frac{\partial \Psi}{\partial r}. \tag{4.13}$$

4.2.3 Ambipolar diffusion

The magnetic diffusivities associated with non-ideal MHD effects, including ambipolar diffusion, depend on the densities of charged particles, which can in principle be computed through detailed chemical networks (e.g., Bai & Goodman 2009). Here, as a first step toward a comprehensive model, we will simply parametrize the density of ions as

$$\rho_i = \rho_{i,0} f(\theta) \left(\frac{\rho}{\rho_0} \right)^{\alpha_{AD}}, \tag{4.14}$$

where

$$f(\theta) = \begin{cases} \exp\left(\frac{\cos^2(\theta+\theta_0)}{2\epsilon^2}\right) & \theta < \pi/2 - \theta_0 \\ 1 & \pi/2 - \theta_0 \leq \theta \leq \pi/2 + \theta_0 \\ \exp\left(\frac{\cos^2(\theta-\theta_0)}{2\epsilon^2}\right) & \theta > \pi/2 + \theta_0. \end{cases} \tag{4.15}$$

The angular dependence $f(\theta)$ is chosen such that, at a given radius, the ion density increases rapidly in the tenuous disk atmosphere, to mimic the ionization by high energy photons (UV and X-rays) from the central young star in addition to cosmic

rays (e.g., Umebayashi & Nakano 1981; Perez-Becker & Chiang 2011a; Glassgold et al. 2017). In the simulations presented in this work, we take $\alpha_{AD} = 0.5$. This power-law dependence for the ion density is roughly what is expected when the volumetric cosmic ray ionization rate is balanced by the recombination rate of ions and electrons, under the constraint of charge neutrality (i.e., $\zeta n \propto n_e n_i \propto n_i^2$, where ζ is the cosmic ray ionization rate per hydrogen nucleus; see page 362 of Shu 1992).

The magnitude of the ion density, and therefore the ion-neutral drag force, $\boldsymbol{F_d} = \gamma \rho \rho_i (\boldsymbol{v_i} - \boldsymbol{v})$, is sometimes quantified through the dimensionless ambipolar Elsasser number,

$$\Lambda = \frac{\gamma \rho_i}{\Omega} = \frac{v_A^2}{\eta_A \Omega}, \tag{4.16}$$

where γ is the frictional drag coefficient. Physically, the Elsasser number is the collision frequency of a neutral particle in a sea of ions of density ρ_i, normalized to the Keplerian orbital frequency. The Elsasser number will be unity when the neutral particle collides 2π times with ions in one orbital period. As the neutral-ion collision frequency increases to infinity, so does the Elsasser number, and the bulk neutral medium becomes perfectly coupled to the ions/magnetic field (i.e., the ideal MHD limit). Similarly, as the Elsasser number drops to zero, the neutrals and ions no longer collide; the neutrals are entirely decoupled from the magnetic field. For our reference simulation, we choose the Elsasser number to be $\Lambda_0 = 0.25$ at the inner boundary on the disk midplane, but will vary this parameter to gauge its effects on the coupled disk-wind system. The choice of $\alpha_{AD} = 0.5$, assuming that the drag coefficient γ is constant, implies that the Elsasser number is proportional to $r^{3/4}$, thus larger radii are better coupled than smaller radii when measured by this parameter in the reference simulation.

4.2.4 Grid

The equations are solved for $r \in [1, 100]$ au, $\theta \in [0, \pi]$, and $\phi \in [0, 2\pi]$ with a resolution of $n_r \times n_\theta \times n_\phi = 200 \times 180 \times 180$ typically (although a higher resolution simulation is also performed for a shorter time). A 'ratioed' grid is used in the radial direction such that dr_{i+1}/dr_i is constant and $r_{i+1} = r_i + dr_i$. The grid spacing at the inner edge is set as $dr_0 = 2.3 r_0 d\theta_{\rm mid}$. The θ grid is separated into three 60° blocks, the middle of which, from $\theta = 60°$ to 120°, is uniform with 120 cells for a resolution of 0.5° per cell or 12 cells from the disk midplane to the initial disk surface at two scale heights. The first and last θ grid blocks are ratioed grids with the cell size matched to the resolution of the middle block at their boundary and increasing towards the poles where the width of the cells at the poles reaches 5.1°. The ϕ grid is uniform with 180 cells. This results in the cells at the inner boundary on the midplane being a box with dimensions of approximately 2:1:4 in the $r : \theta : \phi$ directions.

4.2.5 Boundary conditions

Both the inner and outer radial boundaries use the standard outflow condition, as usual in Zeus codes. The reflection boundary condition is used on the polar axis ($\theta = 0$ and π). The ϕ component of the magnetic field is set to zero on the polar axis. We also set B_ϕ to vanish on the inner radial boundary since it is taken to be non-rotating.

4.3 Reference Simulation

We run a small suite of simulations to examine the formation of substructure in disks that are threaded by an ordered poloidal magnetic field. The simulations differ in

either the Elsasser number (i.e., the degree of magnetic coupling), the magnetic field strength, or the grid resolution (see Table 4.1 for a list of models). We run all of the simulations, except for the high resolution simulation, for at least 2000 times the inner orbital period t_0, or $t/t_0 = 2000$. This section will focus on a reference run where the Elsasser number at the inner edge of the disk is $\Lambda_0 = 0.25$ and the midplane plasma-β is 10^3.

Table 4.1: Model Parameters

	β	Λ_0	Resolution
ad-els0.05	10^3	0.05	200×180×180
reference	10^3	0.25	200×180×180
ad-els1.25	10^3	1.25	200×180×180
beta1e4	10^4	0.25	200×180×180
ref-hires	10^3	0.25	300×270×270

4.3.1 Global view

Fig. 4.1 gives a global perspective on the reference simulation. This figure shows azimuthally averaged snapshots of the density (colour map), poloidal magnetic flux contours [1] (white), and poloidal velocity unit vectors (black) out to $R = 70$ au at four times ($t/t_0 = 0, 500, 1000, 2500$). Upon first inspection, the magnetic field in the disk has two distinct modes of evolution separated at about $r \sim 30$ au in the second frame shown in Fig. 4.1 (at $t/t_0 = 500$). Within this radius (except for the inner most region that is threaded by a dipole-like field), the magnetic field is dragged

[1] At any given point in a meridian plane (such as that shown in Fig. 4.1), the poloidal magnetic flux $\Psi_{\rm pol}$ is defined as the total magnetic flux enclosed by a circle centered on the axis that passes through that point. The contours of constant $\Psi_{\rm pol}$ in a meridian plane (shown as white lines in the figure) are 'effective' poloidal magnetic field lines. It can be shown that the effective poloidal field lines defined in this way for 3D simulations have the same mathematical properties as the actual poloidal field lines in 2D (axisymmetric) simulations. In particular, if we replace the magnetic flux function Ψ in equations (4.12) and (4.13) for the 2D systems by $\Psi_{\rm pol}/(2\pi)$, we obtain the radial and polar components of the 'effective' poloidal magnetic field plotted in Fig. 4.1. Each of the 'effective' field lines is unique and does not begin or end inside the simulation domain, just as in the 2D case.

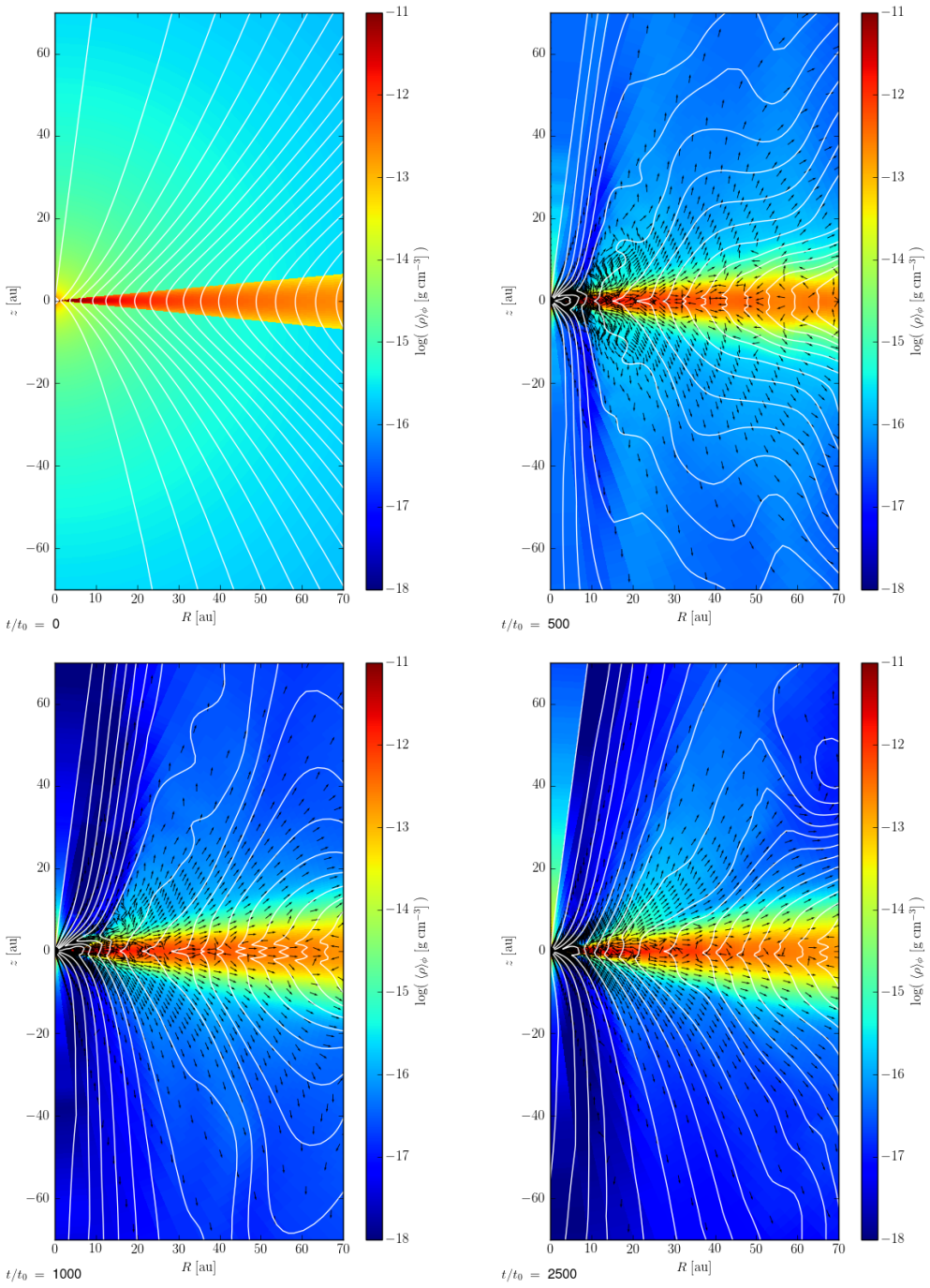

Fig. 4.1.— A representative ('reference') 3D simulation of ϕ-averaged quantities. Shown is the mass volume density (logarithmically spaced colour contours in units of g cm^{-3}), the 'effective' poloidal magnetic field lines (white), and the poloidal velocity unit vectors (black). Panels (a)-(d) corresponding to simulation times of 0, 500, 1000, and 2500 inner orbital periods, respectively.

radially inward through the midplane leading to a sharp radial pinch. This is caused by the vertical steepening of a midplane current sheet due to AD as described in detail in Suriano et al. (2018) (see their Section 3.3.1). The current peaks where the toroidal magnetic field changes sign from positive below the disk to negative above the disk and the effects of AD further steepen the magnetic gradient near a magnetic null (Brandenburg & Zweibel 1994). This is the same phenomenon that leads to the magnetic reconnection of the poloidal magnetic field in 2D. Outside of $r \sim 30$ au, 'channel-flow like' structures are evident. This is because the disk material at a larger radius is better coupled to the magnetic field than at a smaller radius, since the radial dependence of the Elsasser number goes as $\Lambda \propto r^{3/4}$. The demarcation radius between these two types of disk accretion moves outward with time, because it takes time for the current layers created at the disk surfaces to migrate towards and converge at the disk midplane as the induced toroidal magnetic pressure gradient from the winding of the initially poloidal field grows. By the last frame shown in Fig. 4.1 at $t/t_0 = 2500$, the magnetic field lines are radially pinched from the midplane accretion layer out to approximately 50 au.

Fig. 4.1 shows clearly that a wind is launched over most of the disk surface, except close to the inner edge where the field configuration is affected by the boundary condition. Figure 4.2 shows both the mass accretion through the disk at a representative radius $r = 20$ au ($|\pi/2 - \theta| < \theta_d$; black line) and the mass outflow rate through a sphere of the same radius excluding the disk region (green line). The mass accretion rate is approximately 10^{-6} $M_\odot$ yr^{-1}, while the mass outflow rate is approximately 3×10^{-7} $M_\odot$ yr^{-1}. Therefore, more mass is accreted inward through the disk than is ejected away in the wind at this radius.

To further illustrate the overall evolution of the disk, Fig. 4.3 shows several ϕ-

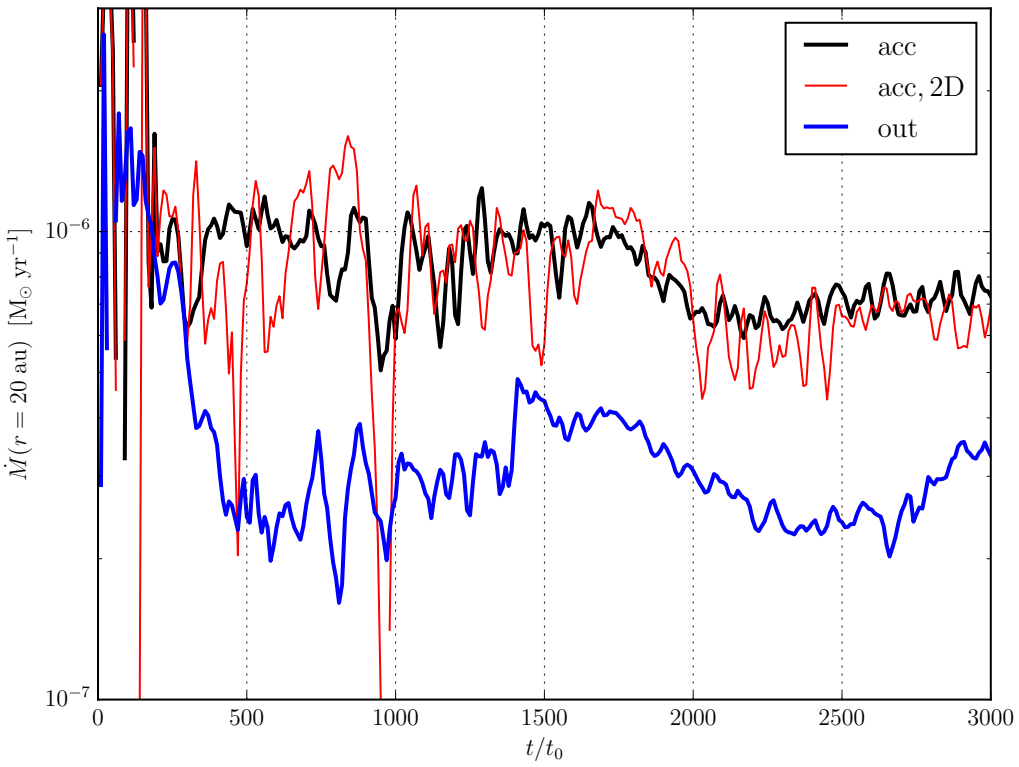

Fig. 4.2.— The mass accretion and outflow rates ($\mathrm{M}_\odot\ \mathrm{yr}^{-1}$) as a function of time in the 3D reference simulation through a sphere of radius $r = 20$ au. The mass accretion rate through the disk ($|\pi/2 - \theta| < 2\epsilon$) is shown in black and that for the corresponding 2D simulation is shown in red for comparison. The total mass outflow rate both above and below the disk ($|\pi/2 - \theta| > 2\epsilon$) is shown in blue.

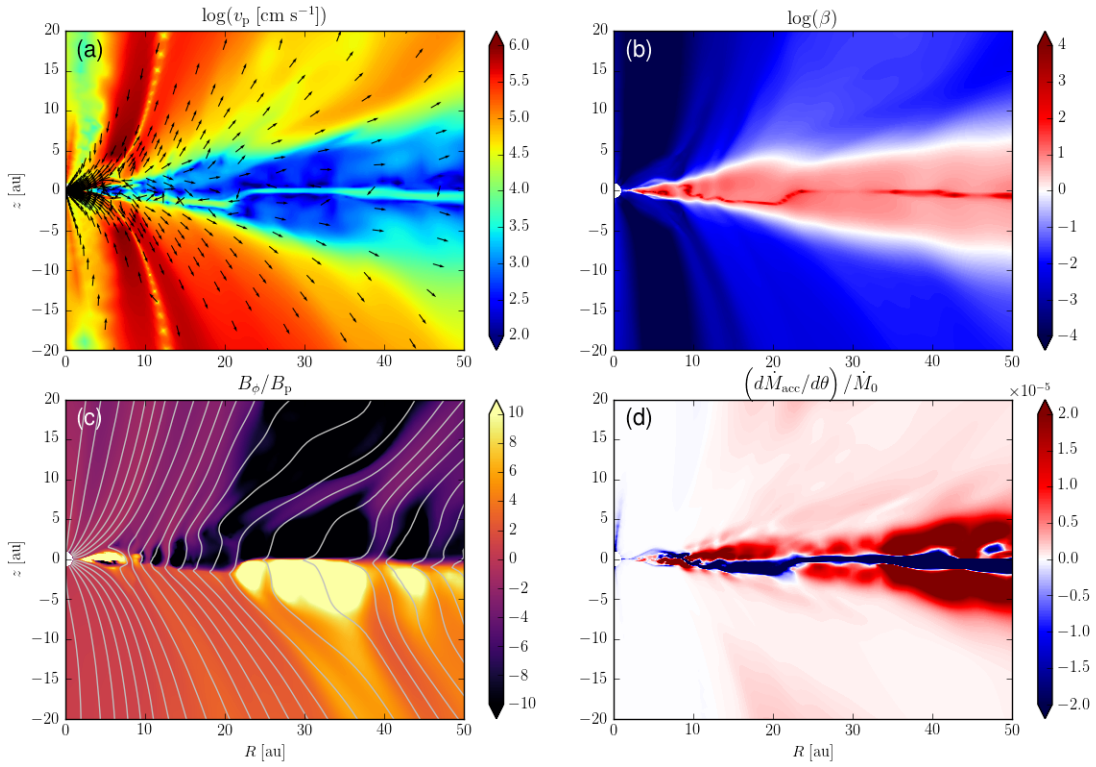

Fig. 4.3.— The reference simulation at a representative time $t/t_0 = 2500$. The panels show the following ϕ-averaged quantities: (a) the logarithm of the poloidal speed (cm s^{-1}) with poloidal velocity unit vectors; (b) the logarithm of plasma-β; (c) the ratio of the toroidal to the poloidal magnetic field strength with magnetic flux contours (gray lines); (d) the differential mass accretion rate integrated over ϕ, i.e., $d\dot{M}_{\rm acc}/d\theta = \int_0^{2\pi} \rho v_r r^2 \sin\theta d\phi$, normalized to $\dot{M}_0 = r_0^2 \rho_0 c_{s,0}$.

averaged disk quantities. Panel (a) shows the distribution of poloidal speed where the fastest accretion through the disk is limited to a thin current layer near the midplane with accretion speeds on the order of 10 m s^{-1}. Above and below this accretion layer, the poloidal velocity is directed outward and the speed is approximately one order of magnitude less than in the accretion layer. Also in the thin accretion layer, the value of plasma-β peaks at values approaching 10^4 (panel b). Similarly, the mass accretion rate is largest in this thin layer as shown in Fig. 4.3(d), which plots the ϕ-integrated radial mass accretion rate per unit polar angle, $d\dot{M}_{\rm acc}/d\theta = \int_0^{2\pi} \rho v_r r^2 \sin\theta d\phi$. Again, the disk mass moves outward above the midplane accretion layer and further extends to a tenuous disk wind beyond the disk surfaces. Despite the disk excretion above the midplane layer, there is still a large net mass accretion rate when averaged over the disk (see Fig. 4.2). The accretion takes place through a strong current layer, which is where the ϕ component of the magnetic field changes sign. The field reversal leads to a low value of B_ϕ in the accretion layer, which is the reason why its plasma-β is high. It can also be seen in panel (c) of Fig. 4.3, which plots the ratio of the toroidal to the poloidal magnetic field. We see that the magnetic field is pinched radially inward where the toroidal magnetic field changes sign from positive below the disk to negative above the disk. Also, we see a variation in $B_\phi/B_{\rm p}$ as a function of radius, where poloidal magnetic field lines concentrate in some regions while the toroidal magnetic field dominates in other, the cause of which will be discussed in the next section.

4.3.2 The formation of rings and gaps

As previously mentioned, the accretion layer is also the location of a thin current sheet. The creation of the current sheet starts at the disk surfaces as the differential

rotation between the disk and the initially static disk corona rapidly induces a toroidal magnetic field outside of the disk. The toroidal magnetic field is responsible for driving an outward radial current $J_r \approx \frac{c}{4\pi}\frac{dB_\phi}{rd\theta}$ since B_ϕ changes from positive below the disk to negative above. As the magnetic field is continually wound up, a large toroidal magnetic gradient is generated outside of the disk, with a corresponding Lorentz force pushing the ions (and the toroidal magnetic field lines tied to the ions) towards the midplane, thus moving the surface current layers closer together until they combine at the disk midplane to form a single current sheet where B_ϕ reverses polarity. The magnetic pressure gradient is further steepened at the magnetic null due to the effects of AD (Brandenburg & Zweibel 1994), creating a thin midplane current layer. Finally, the Lorentz force exerted due to the radial current ($F_{L,\phi} \propto J_r B_z$) is in the $-\phi$ direction, draining angular momentum in the current layer leading to strong accretion and the inward pinch of the poloidal magnetic field there. The eventual reconnection of the radial magnetic field as it is dragged inward leads to the creation of a poloidal magnetic field loop, thereby leaving the region that it encloses devoid of vertical (or poloidal) magnetic flux. In neighboring regions, however, the poloidal magnetic field concentrates. The disk mass then grows in the regions where the vertical magnetic flux is lowest (rings) and the neighboring regions with larger poloidal magnetic flux can drive faster accretion though them. This phenomenon is essence of the reconnection-driven ring and gap formation mechanism described in Section 3.3 of Suriano et al. (2018) (see their figures 6 and 7). Again, Fig. 4.3(c) shows the eventual magnetic field configuration of alternating bands of toroidal and poloidal magnetic field concentrations and the radial pinch in the magnetic flux contours at the current layer where $B_\phi = 0$.

As described in Suriano et al. (2018) and above, the end result of the ring and

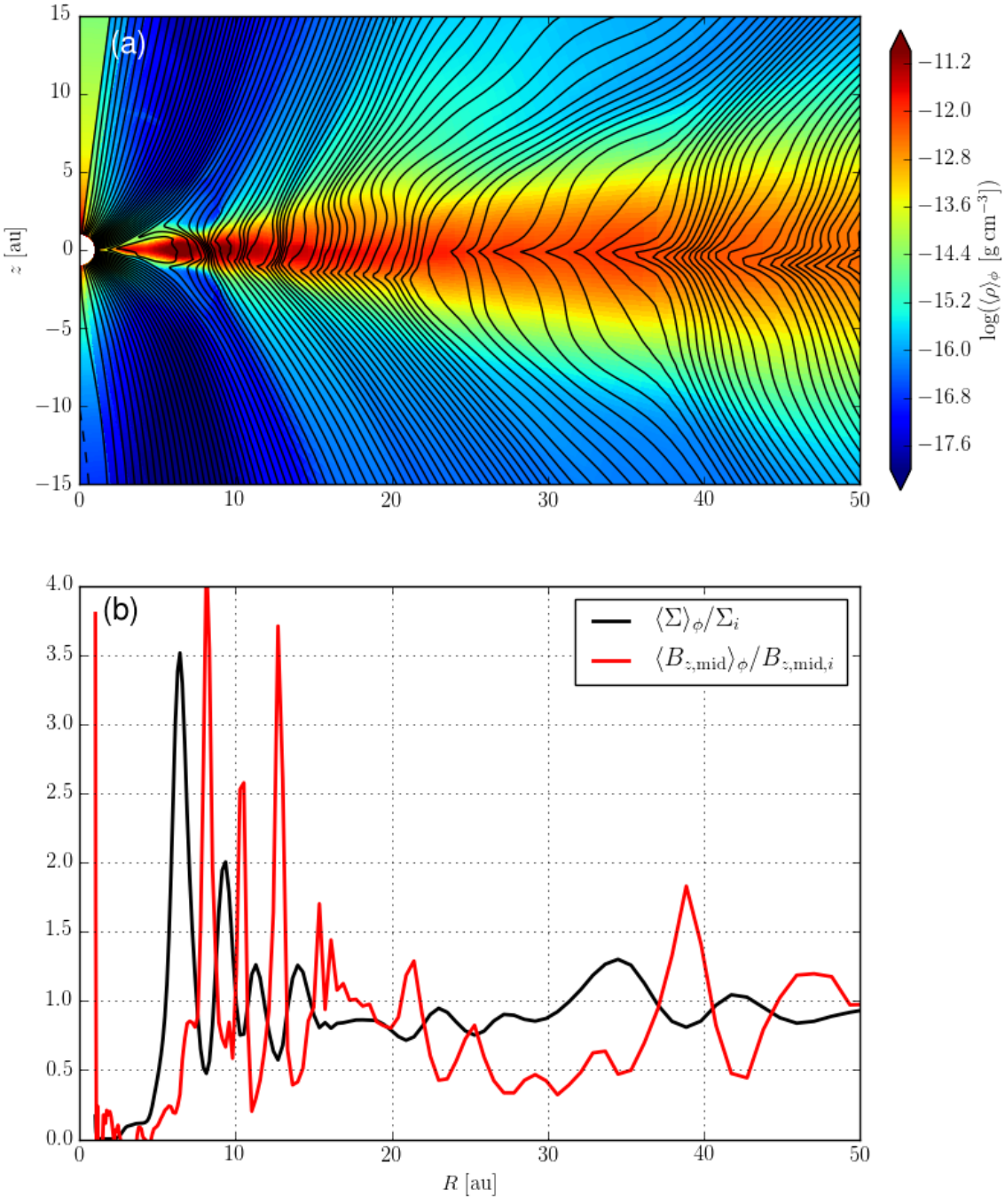

Fig. 4.4.— The reference simulation at a representative time $t/t_0 = 2500$. The top panel plots the logarithm of the density (colour map) and the ϕ integrated magnetic flux contours (or effective poloidal field lines, black lines). The bottom panel shows the ϕ averaged surface density (black) and vertical magnetic field at the disk midplane (red) normalized respectively by their initial distribution.

gap formation through the reconnection of a radial magnetic field is the redistribution of the poloidal magnetic flux relative to the disk material, as illustrated in Figure 4.4. The top panel shows the ϕ-averaged density distribution (colour map) and the effective poloidal field lines (black lines). It is clear that the poloidal field lines are distributed very unevenly, especially inside the disk. Specifically, the field lines bunch up in some regions but spread out in others. The corresponding strong variation of the vertical magnetic field strength at the disk midplane is quantified in the panel (b) (red line). For comparison, the surface density distribution is also plotted in the same panel (black line). It is clear that the surface density is strongly anti-correlated with the vertical field strength, especially in the region around 10 au, where the contrast between the dense, weakly magnetized rings and the more diffuse but more strongly magnetized gaps is the largest. This anti-correlation starts at early times when the rings and gaps are still nearly axisymmetric, so it is likely created by the same mechanism as in the 2D (axisymmetric) simulations, namely, the redistribution of poloidal magnetic flux relative to disk material through reconnection. The anti-correlation persists to later times (such as that shown in Fig. 4.4) when the rings and gaps become more non-axisymmetric (see the next subsection). As this 3D simulation is approximately half of the resolution of the similar 2D simulations in Suriano et al. (2018), and the effective poloidal magnetic field lines are drawn by integrating over the azimuthal angle, it is more difficult to observe the field lines in the act of reconnecting (as in figure 7 of Suriano et al. 2018). Nonetheless, the close similarity between the 2D and 3D simulations, especially in the severe radial pinching of the poloidal magnetic field in a thin fast-accreting layer and the anti-correlation between the disk surface density and poloidal field strength, leaves little doubt that the same mechanism is at work in both 2D and 3D. It strengthens the case that the mecha-

nism, first identified in more restrictive but conceptually simpler 2D (axisymmetric) systems, is robust in full three dimensions.

As mentioned in Suriano et al. (2018), a major concern as to whether the ring and gap formation mechanism found in 2D could still work in 3D is that, in 3D, the highly azimuthally pinched toroidal magnetic field across the midplane current sheet (where B_ϕ reverses direction sharply) can also, in principle, reconnect. If this happens, it may weaken the magnetic torque that drives the accretion through the midplane current layer, which may, in turn, weaken the radial pinching of the poloidal field that lies at the heart of the mechanism: the reconnection-enabled redistribution of matter relative to the poloidal magnetic flux. Although it is difficult to directly prove or disprove the occurrence of reconnection of oppositely directing B_ϕ in the 3D reference simulation, there are indications that, if it does occur, its dynamical effects are relatively modest. First, it has a relatively moderate effect on the disk mass accretion rate, as illustrated in Fig. 4.2, which shows the time averaged accretion rate at a representative radius as a function of time for both the 3D and a corresponding 2D simulation. If reconnection of the azimuthal field component in 3D had erased the sharp field pinch in the azimuthal direction, it would have greatly reduced the magnetic braking torque and thus the accretion rate compared to the 2D simulation, which is not the case. In fact, the accretion rate at the representative radius of 20 au is somewhat higher in 3D than in 2D over the last 1000 t_0. The similarity in disk mass accretion rate is not limited to that radius. Fig. 4.5 shows that the time-averaged mass accretion rates over the last 1000 t_0 are comparable at most radii for the 3D and corresponding 2D simulations. Even more directly, we have examined the vertical distribution of B_ϕ in both 2D and 3D simulations, and found that the sharp transition from a positive to a negative B_ϕ going vertically up through the disk

remains ubiquitous in 3D, with gradients comparable to those in 2D (see Fig. 4.6 for an example).

It is not clear why there is no widespread field reconnection in the azimuthal direction that drastically reduces the concentrated mass accretion in the J_r current layer and weakens the ring and gap formation mechanism. One possibility is that differential rotation in the disk would rapidly regenerate the azimuthal field pinch out of the global, ordered poloidal field that threads the disk, even if the pinch is smoothed out sporadically by reconnection. This is different from the field pinch in the radial direction, which is created by differential radial accretion on a longer time scale and thus harder to regenerate once smoothed out by reconnection. We believe that the fact that the rotational speed v_ϕ is much higher than the radial accretion speed v_r is ultimately responsible for the different behavior in the field pinch and reconnection in the azimuthal and radial direction. In any case, the 2D and 3D simulations appear fundamentally similar, especially at early times when the rings and gaps in the 3D simulations remain nearly axisymmetric, however, there are some differences between them. The most important is the azimuthal variation of the disk substructures that can only be studied in 3D.

4.3.3 Azimuthal variations

The disk quantity that has the most prominent radial substructure is the vertical magnetic field strength at the midplane, $B_{z,\mathrm{mid}}$, as illustrated in Fig. 4.4(b). Substantial substructure in $B_{z,\mathrm{mid}}$ develops in the azimuthal direction as well, as shown in Fig. 4.7. As an example, we will focus on the prominent peak in the normalized vertical field strength around $r = 40$ au. This peak starts to stand out from the background around $t/t_0 = 1000$, as shown in the first panel (a). At this time, the

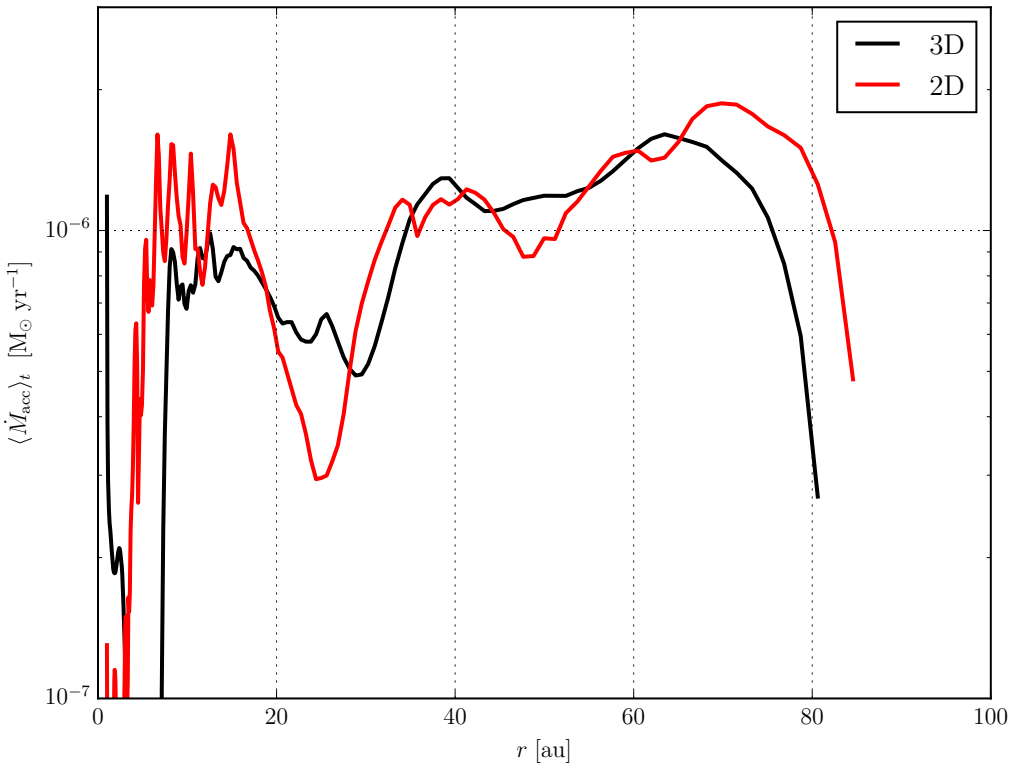

Fig. 4.5.— The time averaged mass accretion rate from $t/t_0 = 2000$ to 3000 as a function of disk radius for both the reference 3D simulation and its 2D counterpart. The broad similarity between the two means that the pinching of the magnetic field lines in the azimuthal direction that drives the mass accretion is not significantly reduced, if at all, by reconnection.

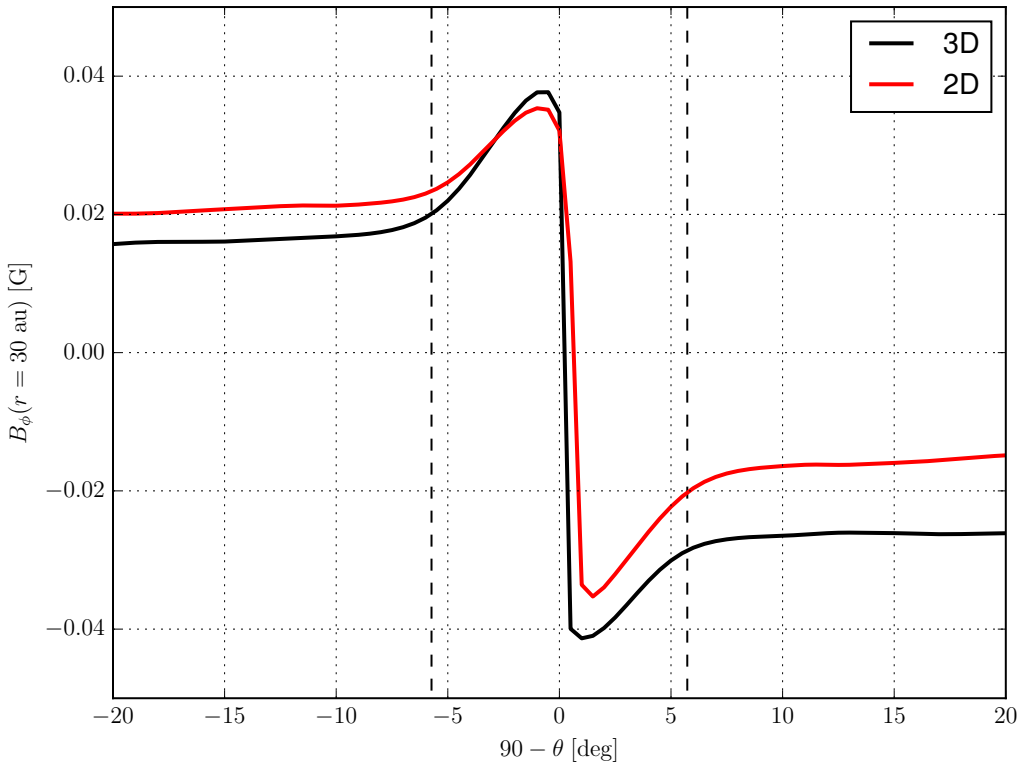

Fig. 4.6.— The variation of the toroidal component of the magnetic field B_ϕ as a function of $90 - \theta$ (degrees; negative is below the midplane and positive is above the midplane) at a representative radius $r = 30$ au in the reference 3D simulation (ϕ-averaged) and the corresponding 2D simulation at $t/t_0 = 2500$. The two dashed vertical lines mark the disk surfaces at $\theta = 90° \pm 2\epsilon$.

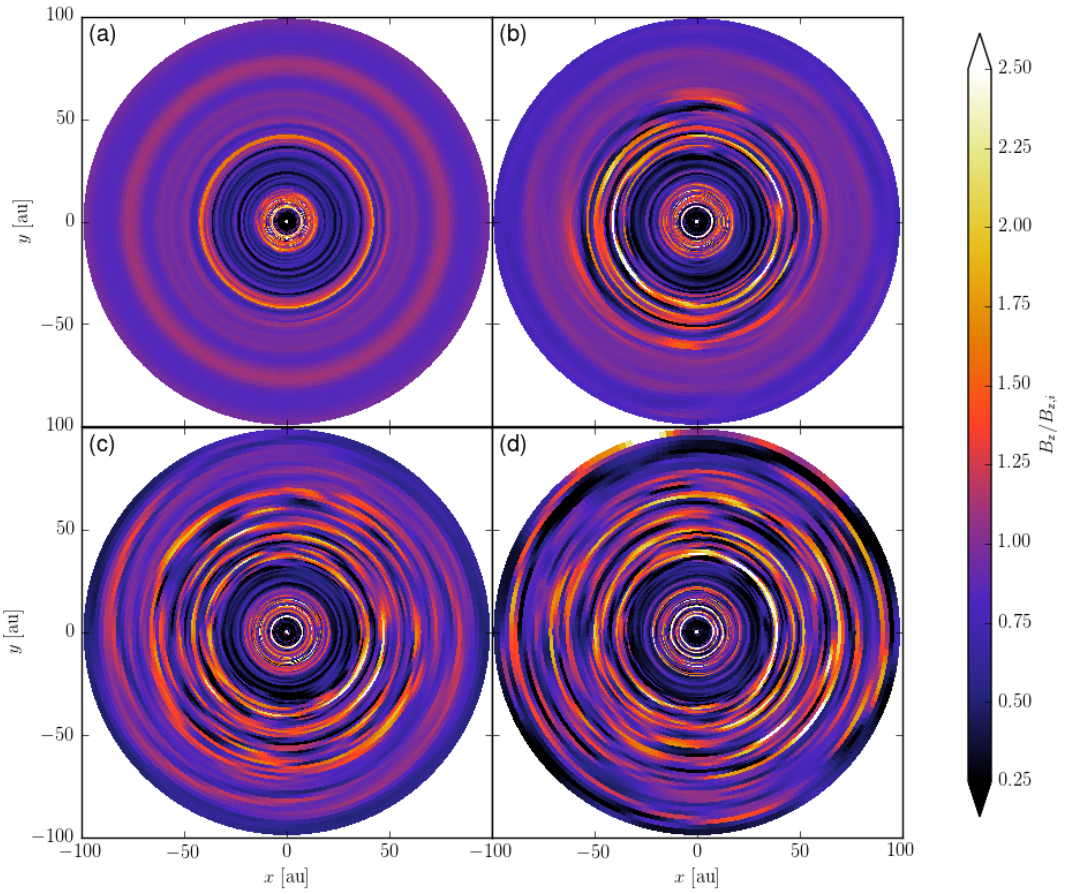

Fig. 4.7.— Spatial variation of the vertical magnetic field strength at the midplane normalized to its initial value for the reference simulation at four representative times: (a) $t/t_0 = 1000$, (b) 1500, (c) 2000, and (d) 3000. They show clearly that the initially axisymmetric rings of enhanced vertical field are perturbed but not disrupted in 3D.

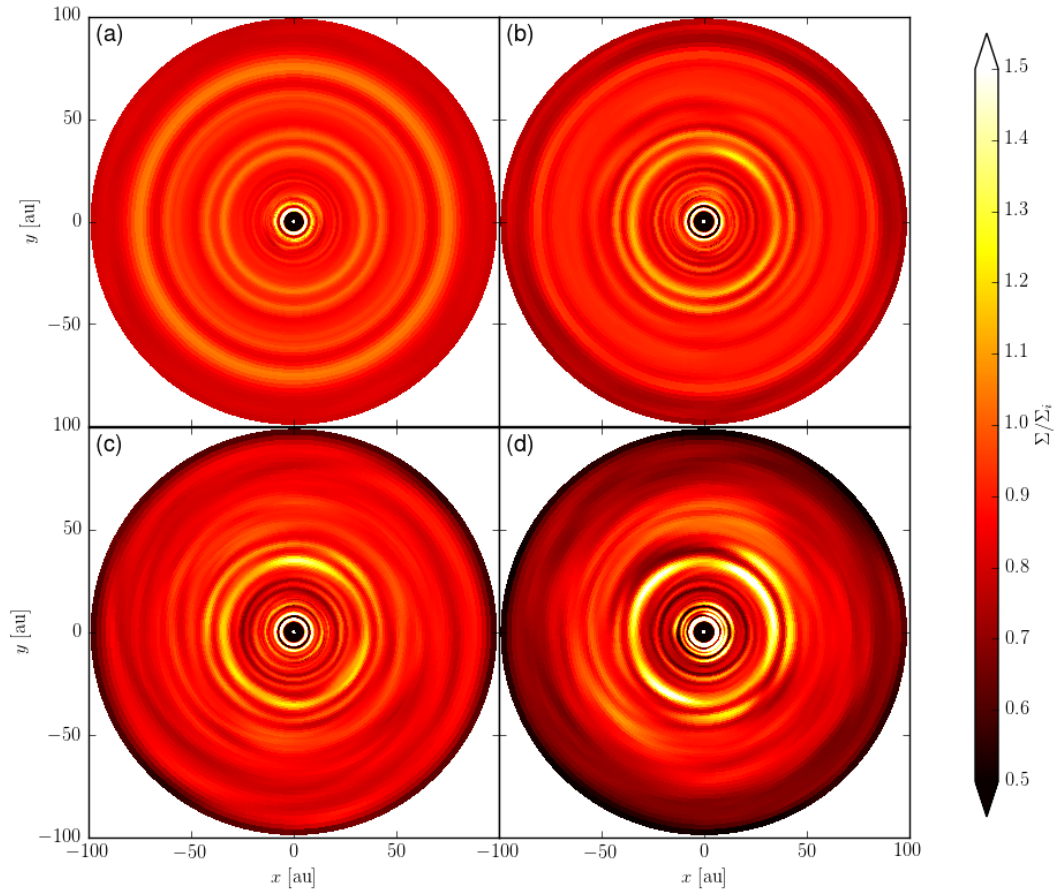

Fig. 4.8.— Spatial variation of the disk surface density normalized to its initial value for the reference simulation at 4 representative times: (a) $t/t_0 = 1000$, (b) 1500, (c) 2000, and (d) 3000. They show clearly that the initially axisymmetric rings of enhanced surface density are perturbed but not disrupted in 3D.

structure remains highly axisymmetric. The lack of significant azimuthal variation up to this time means that this structure must be formed from the initially axisymmetric conditions in the same way as the structures in $B_{z,\mathrm{mid}}$ formed in the corresponding 2D (axisymmetric) simulation. Significant azimuthal variations start to develop around $t/t_0 = 1500$, with some azimuthal regions having significantly stronger vertical fields than others. Presumably the variation develops from the numerical noise associated with the finite simulation grid since the initial conditions are axisymmetric and there is no explicit perturbation added. It may be amplified by potential instabilities in the system, both inside the disk (such as the MRI) and in the wind, which is dominated by a toroidal magnetic field that is prone to kink instabilities (e.g., Anderson et al. 2006). It could also be driven by sporadic reconnection of the highly pinched field lines in the azimuthal direction, but it is hard to find direct evidence of this process, as mentioned earlier. Although exactly how and why the azimuthal variations develop is unclear, they do not grow to such an extent as to disrupt the ring-like structure completely. This is illustrated in panels (c) and (d) of the Fig. 4.7, which show the spatial distributions of the normalized $B_{z,\mathrm{mid}}$ at $t/t_0 = 2000$ and 3000, respectively. Around $t/t_0 = 2000$, the ring-like structure becomes rather clumpy. It consists of several distinct strands of partial ringlets. Importantly, these strands do not evolve separately, which would have led to the disintegration of the ring-like structure. Rather, they stay close together and sometimes merge into structures that are even more axisymmetric at later times, as seen in panel (d). This apparent stability is not unique to the ring formed originally near $r = 40$ au. It appears to be a general property of the ring-like features in the vertical magnetic field distribution.

Azimuthal variation develops in the surface density distribution as well, although it is less prominent than that in the vertical field strength, as illustrated in Fig. 4.8.

As before, we again focus on the outer disk region near $r \sim 40$ au. At the time $t/t_0 = 1000$, when a prominent axisymmetric ring develops in the vertical field at ~ 40 au (panel a of Fig. 4.7), an axisymmetric (dark) gap with a depressed surface density (Fig. 4.8a) is present at the same location, sandwiched by two (bright) rings of enhanced surface densities. As the system evolves further, mild inhomogeneities start to develop along the rings, as shown in panel (b), when $t/t_0 = 1500$. This is particularly clear for the interior of the two aforementioned rings, where a bright arc forms near $\phi = 60°$, the angle corresponding to 1 o'clock. A local depression of the vertical field strength occurs at this same location along the high surface density ring (see panel b of Fig. 4.7). Conversely, the depressions near the two ends of this bright surface density arc correspond to two local enhancements in $B_{z,\mathrm{mid}}$. Nevertheless, the surface density varies azimuthally less than the vertical magnetic field. This is perhaps to be expected, because the magnetic energy density is much less than the thermal energy density, especially in the rings. Another interesting feature that is obvious from comparing panel (b) of Fig. 4.7 and 4.8 is that there are more fine radial structures for the vertical field strength than for the surface density. In particular, the second outermost low-surface density gap contains at least two rings of enhanced $B_{z,\mathrm{mid}}$. The bright clump near 2 o'clock at $t/t_0 = 1500$ gradually spreads out along the ring (presumably from the shearing in the disk) and becomes less prominent (although does not disappear completely) over the next one or two (local) orbits. By the time $t/t_0 = 2000$ shown in panel (c), it was superseded by another bright clump (around 12 o'clock) that grew out of a fainter arc along the ring. Although exactly why that particular arc grows to be become more prominent in time is unclear, it could be related to the Rossby wave instability (e.g., Lovelace et al. 1999; Armitage 2015). In any case, despite the formation and growth of the azimuthal inhomogeneities, they

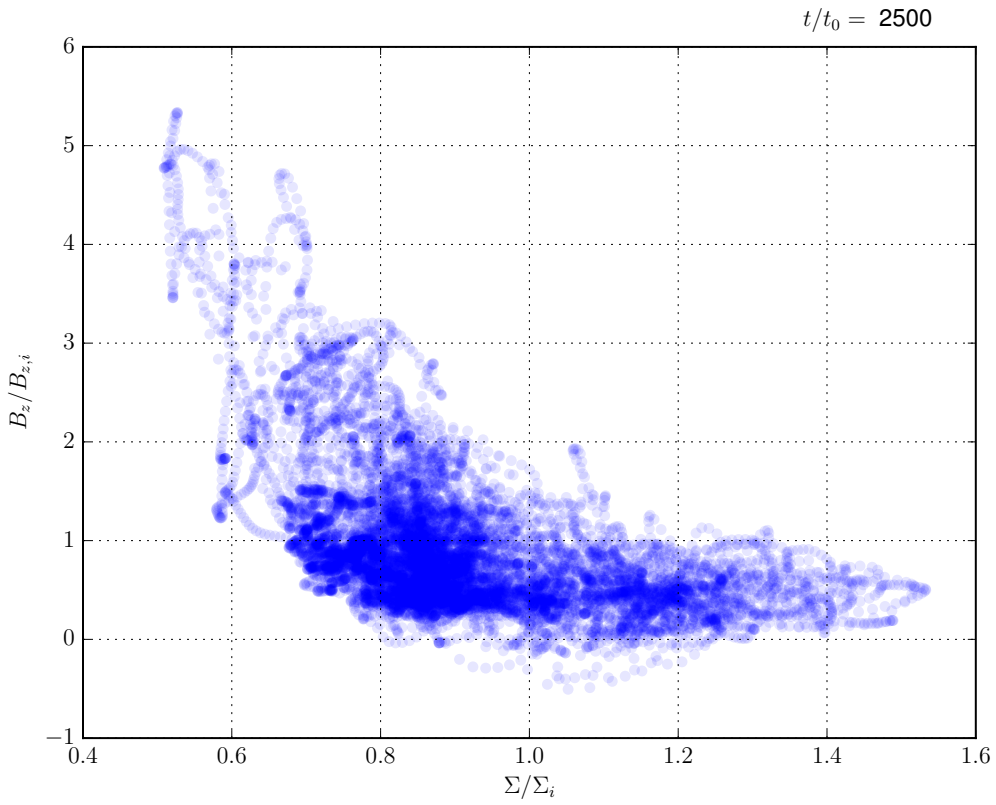

Fig. 4.9.— Scatter diagram showing the anti-correlation between the normalized surface density and vertical field strength within $\pm 2\epsilon$ of the disk midplane ($\phi = \pi/2$) for a range of radius between 10 and 50 au at $t/t_0 = 2500$.

appear to become saturated at a relatively low amplitude and do not disrupt the rings completely. Indeed, by the end of the simulation ($t/t_0 = 3000$, panel d), the 12 o'clock bright arc is still there, but there are two other bright arcs that have since grown, giving the ring a fragmented appearance. The ring just to larger radii is fainter and part of it (near 11 o'clock) is missing; the missing part corresponds to a region where the vertical magnetic field is enhanced (see panel d of Fig. 4.7). The general anti-correlation between the surface density and the vertical field strength is shown in Fig. 4.9, which plots the two quantities against each other between $r = 10$ and 50 au in the disk (one pair for each cell within $\pm 2\epsilon$ of the midplane) at the representative time $t/t_0 = 2500$.

Our discussion so far has been focused on the outer region of the disk where the rings and gaps are less crowded. The general behavior is similar in the inner disk, where the substructures have a longer time to grow and saturate relative to the local orbital period. One difference is that some of the narrow, faint rings in the $B_{z,\mathrm{mid}}$ map which formed early in the simulation appear to merge together to form thicker and brighter rings at later times. By the end of the simulation at $t/t_0 = 3000$, high-contrast rings and gaps are established in the inner disk for both the vertical magnetic field (panel d of Fig. 4.7) and the surface density (panel d of Fig. 4.8). The fact that they last for hundreds of local orbital periods is strong evidence for the stability of such substructures in 3D.

4.4 Parameter survey

We have carried out four simulations in addition to the reference run (Table 4.1). Model ad-els0.05 is 5 times more diffusive than the reference run (with a characteristic AD Elsasser number $\Lambda_0 = 0.05$ instead of 0.25) and Model ad-els1.25 is 5 times less

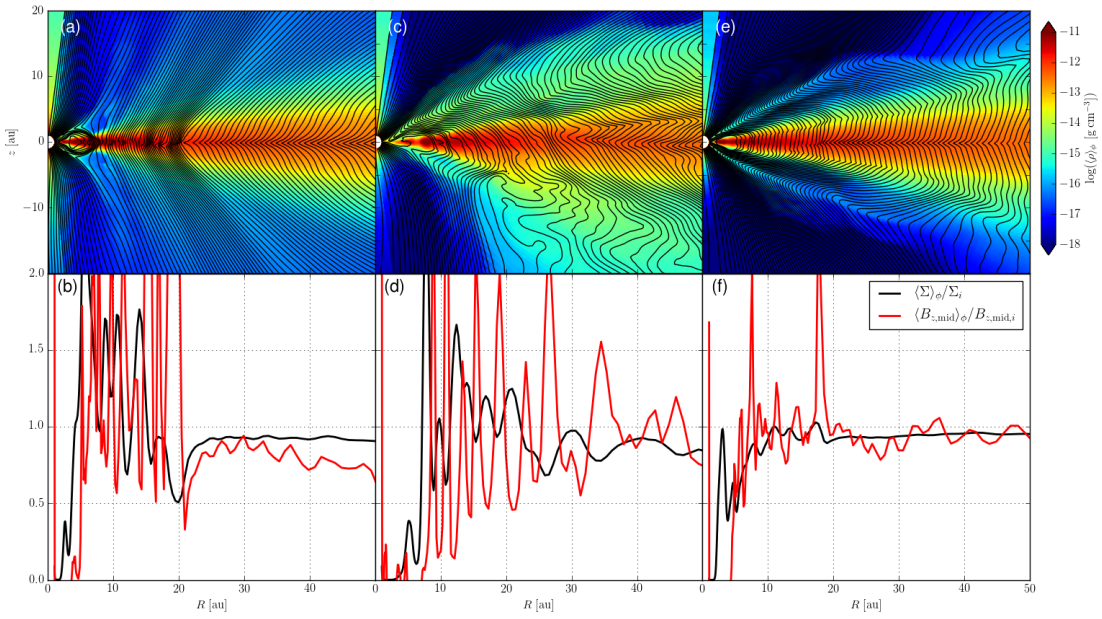

Fig. 4.10.— The simulations ad-els0.05 (left) and ad-els1.25 (middle) at time $t/t_0 = 2500$ and beta1e4 (right) at $t/t_0 = 2350$. The top panel plots the logarithm of the density (colour map) and the ϕ integrated magnetic flux contours (or effective poloidal field lines, black lines). The bottom panel shows the ϕ averaged surface density (black) and vertical magnetic field at the disk midplane (red) normalized respectively by their initial distribution.

diffusive (or better magnetically coupled) than the reference run. Model beta1e4 has a weaker initial magnetic field than the reference run, with a plasma-β of 10^4 rather than 10^3. These three models are shown in Fig. 4.10 through Fig. 4.13, and discussed one by one in Section 4.4.1 below. Model ref-hires is a higher resolution version of the reference run, with the number of cells increased by 50 per cent in each of the three dimensions (though the resolution of the non-uniform θ grid at the disk is doubled). It is discussed separately in Section 4.4.2.

4.4.1 Ambipolar diffusion and field strength

In Fig. 4.10, we compare the azimuthally averaged density distribution (colour map) and effective poloidal magnetic field lines (black lines) in the top panels and the azimuthally averaged distributions of the normalized surface density and vertical field strength at the midplane in the bottom panels for the three variants of the reference simulation. These panels are to be compared with Fig. 4.4 for the reference run. A general trend is that the disk atmosphere and wind are more laminar in the more magnetically diffusive case, with the sharply pinched poloidal field lines confined closer to the disk midplane (Fig. 4.10a). As the magnetic field becomes better coupled to the disk material, the so-called 'avalanche' accretion streams start to develop near the disk surface, driving the atmosphere and wind to be more chaotic (Fig. 4.10c), consistent with the 2D simulations of Suriano et al. (2018). Despite a factor of 25 difference between the most diffusive and the least diffusive models, prominent rings and gaps with strong radial variation in surface density develop in all three $\beta = 10^3$ cases. In the more weakly magnetized case of $\beta = 10^4$, rings and gaps are still formed, but they are less prominent with lower amplitudes of radial variation in both the surface density and the vertical field strength compared to the more strongly

magnetized reference simulation. Nevertheless, in all three variants of the reference simulation, the gaps tend to have a stronger vertical field than the rings, just as in the reference case. This broad similarity indicates that the same mechanism is at work in creating disk substructures over a range of conditions.

The ambipolar diffusivity has a strong effect on the degree of azimuthal variation in the rings and gaps. The effect is particularly striking on the vertical field strength $B_{\rm z,mid}$ at the midplane. In the most diffusive model (ad-els0.05), rings of enhanced $B_{\rm z,mid}$ start out as axisymmetric structures (see panel a of Fig. 4.11), as in the reference case. They stay largely axisymmetric at later times. In contrast, in the least diffusive model (ad-els1.25), the rings develop large azimuthal variations and become rather clumpy in appearance. The variations do not disrupt the rings completely, however. Why the azimuthal variation of $B_{\rm z,mid}$ is so strongly affected by the ambipolar diffusivity is uncertain. One possibility is that the better coupled case is more unstable to MRI, especially the surface 'avalanche' accretion streams, which are intrinsically non-axisymmetric. Such (non-axisymmetric) instabilities are weakened or even suppressed if the ambipolar diffusivity is large enough. Another possibility is that the poloidal magnetic field lines are expected to be wrapped more strongly by the vertical differential rotation in a better coupled disk, creating a more severe pinching of the field lines in the azimuthal direction that is more prone to reconnection. Reconnection of a sharply reversed ϕ component of the magnetic field will necessarily introduce an azimuthal variation to the vertical field strength.

The difference in the azimuthal variation of $B_{\rm z,mid}$ shows up in the surface density as well. A comparison of panels (e)-(h) of Fig. 4.11 to those of Fig. 4.12 shows that rings of enhanced surface density are much more perturbed in the least diffusive model than in the most diffusive model. In addition, the disk material at large radii

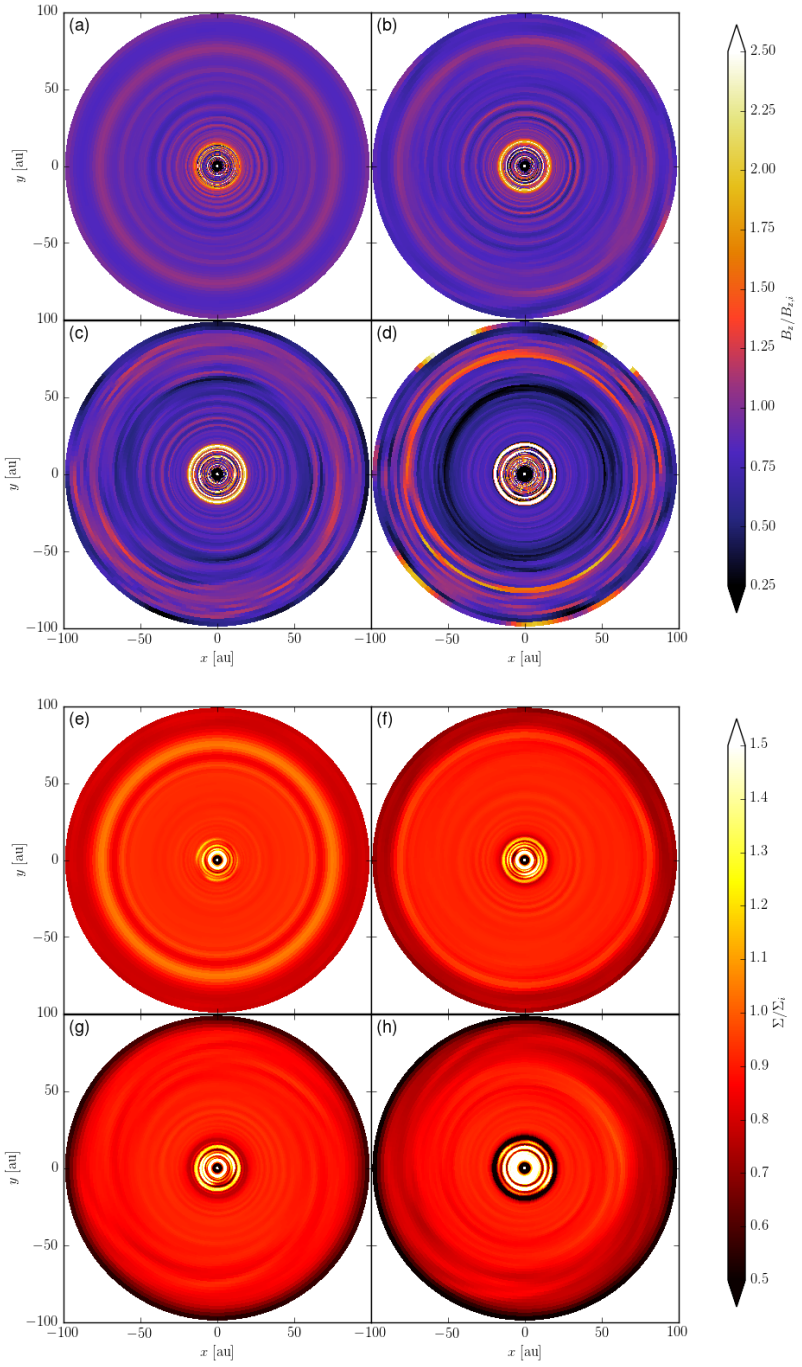

Fig. 4.11.— Spatial variation of the vertical magnetic field strength at the midplane (top) and the disk surface density (bottom) normalized to their initial values for the most diffusive simulation with $\Lambda_0 = 0.05$ (model ad-els0.05) at four representative times: (a/e) $t/t_0 = 1000$, (b/f) 1500, (c/g) 2000, and (d/h) 3000. They show clearly that the initially axisymmetric rings of enhanced surface density remain more or less axisymmetric in 3D.

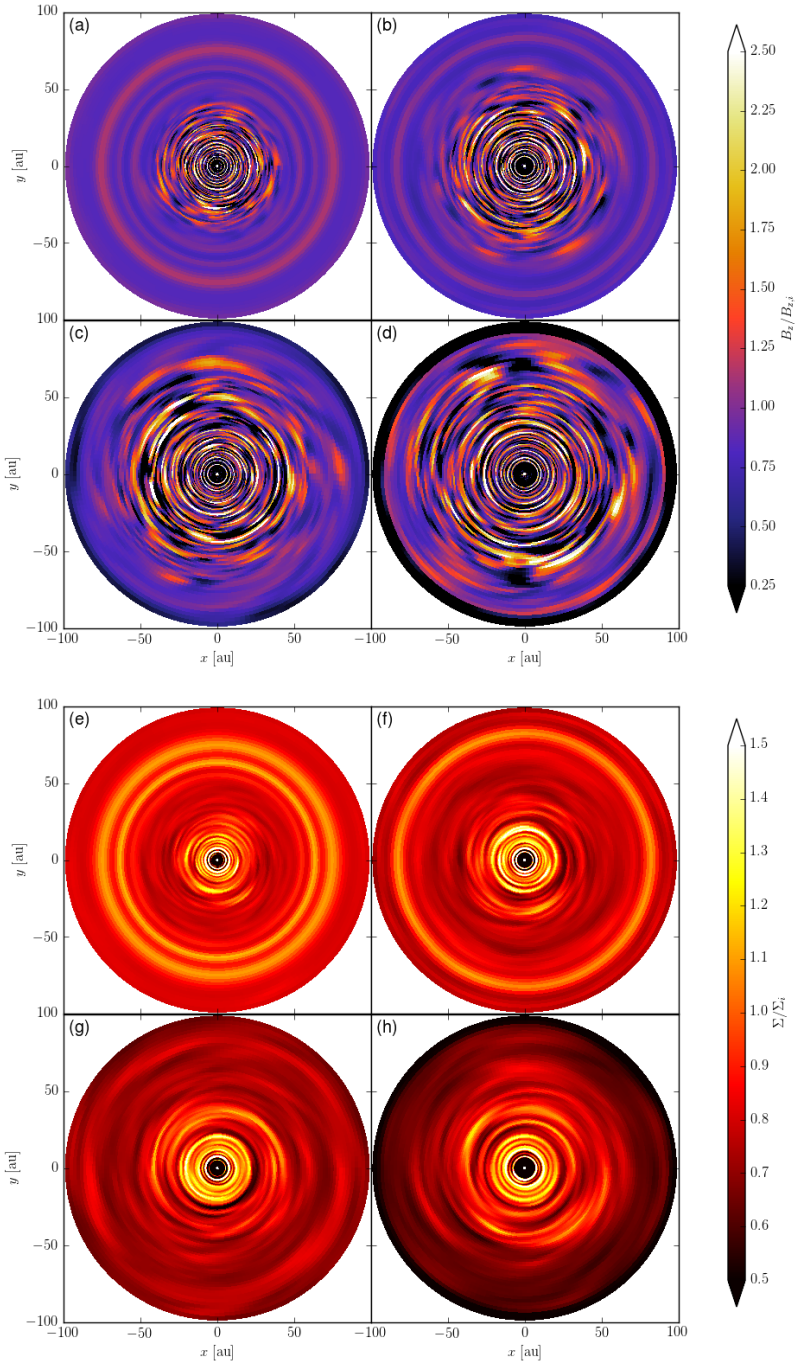

Fig. 4.12.— Spatial variation of the vertical magnetic field strength at the midplane (top) and the disk surface density (bottom) normalized to their initial values for the least diffusive simulation with $\Lambda_0 = 1.25$ (model ad-els1.25) at four representative times: (a/e) $t/t_0 = 1000$, (b/f) 1500, (c/g) 2000, and (d/h) 2500. They show clearly that the initially axisymmetric rings of enhanced surface density are strongly perturbed but not disrupted in 3D.

(beyond ~ 40 au) is more depleted in the former than in the later, especially at late times. Apparently, the better magnetic coupling has allowed more efficient angular momentum transport in the outer part of the disk.

When the initial magnetic field strength is reduced by a factor of $\sqrt{10}$ compared to the reference simulation (model beta1e4), rings and gaps are still formed, but they are much less prominent than those formed in the more strongly magnetized reference case (see Fig. 4.13), in both vertical field strength and surface density. The former is likely because the field is too weak to drive a fast enough midplane accretion to pinch the poloidal field lines radially enough for frequent reconnection. The latter comes about because it is harder for a weaker field to move the gas around to form prominent substructures.

4.4.2 Spatial resolution

Because of computational constraints, we are able to run just one higher resolution simulation and only for a much shorter time. The simulation (model ref-hires in Table 4.1) has parameters identical to the reference run, except that the number of cells is increased by a factor of 1.5 in each of the three directions. The same type of non-uniform θ grid is used as in the previous simulations. Although the total θ resolution is increased by 1.5, the middle θ grid block has twice the number of cells compared to the other simulations, thus doubling the vertical disk resolution. The results are shown in Fig. 4.14 and 4.15 for a representative time $t/t_0 = 1200$. The top panel of Fig. 4.14 shows clearly the localized bunching of the effective poloidal magnetic field lines, which is quantified in the bottom panel. Also evident in the bottom panel is the characteristic anti-correlation between the distributions of the vertical field strength and the surface density. The increase in spatial resolution does

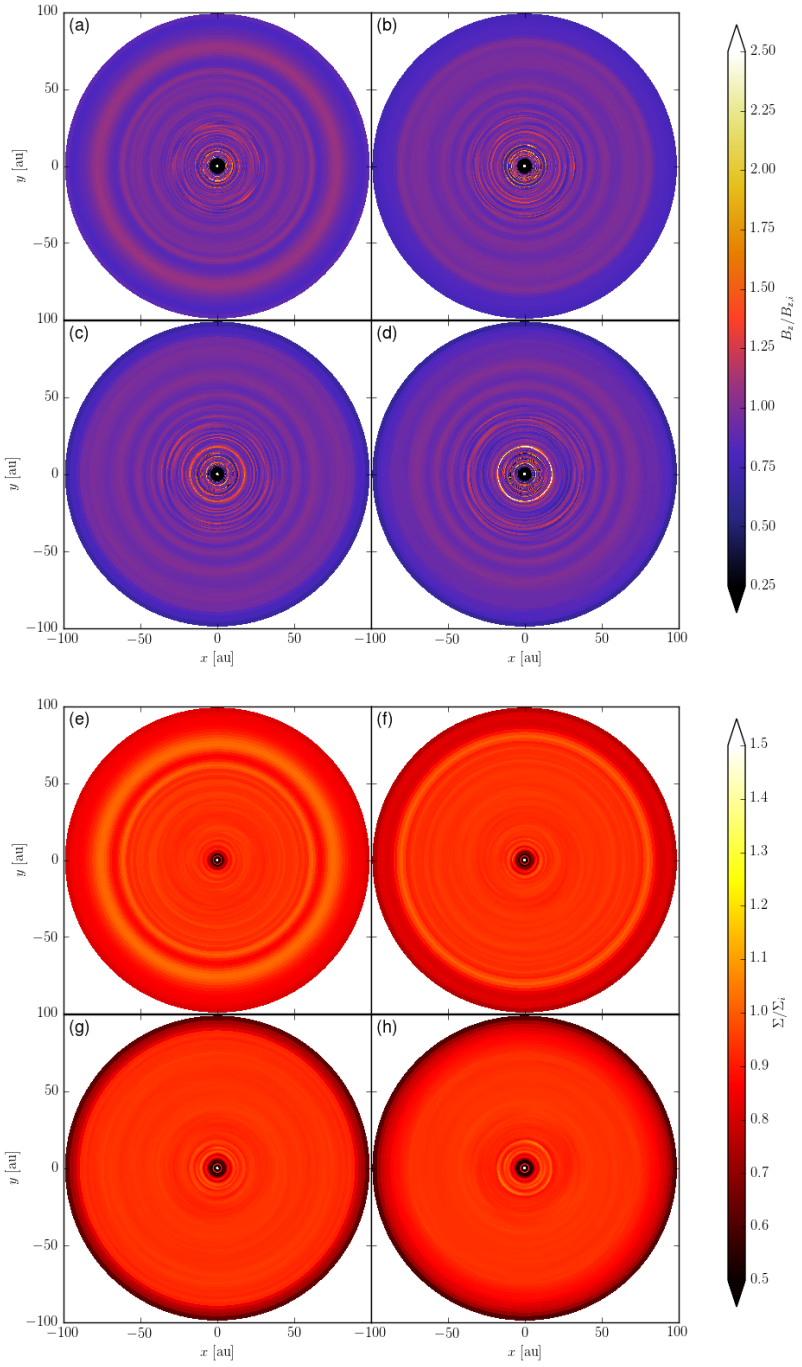

Fig. 4.13.— Spatial variation of the vertical magnetic field strength at the midplane (top) and the disk surface density (bottom) normalized to their initial values for the most weakly magnetized simulation with $\beta = 10^4$ (model beta1e4) at four representative times: (a/e) $t/t_0 = 1000$, (b/f) 1500, (c/g) 2000, and (d/h) 2350. Although rings and gaps are still formed, they are much less prominent than those created in the more strongly magnetized reference case.

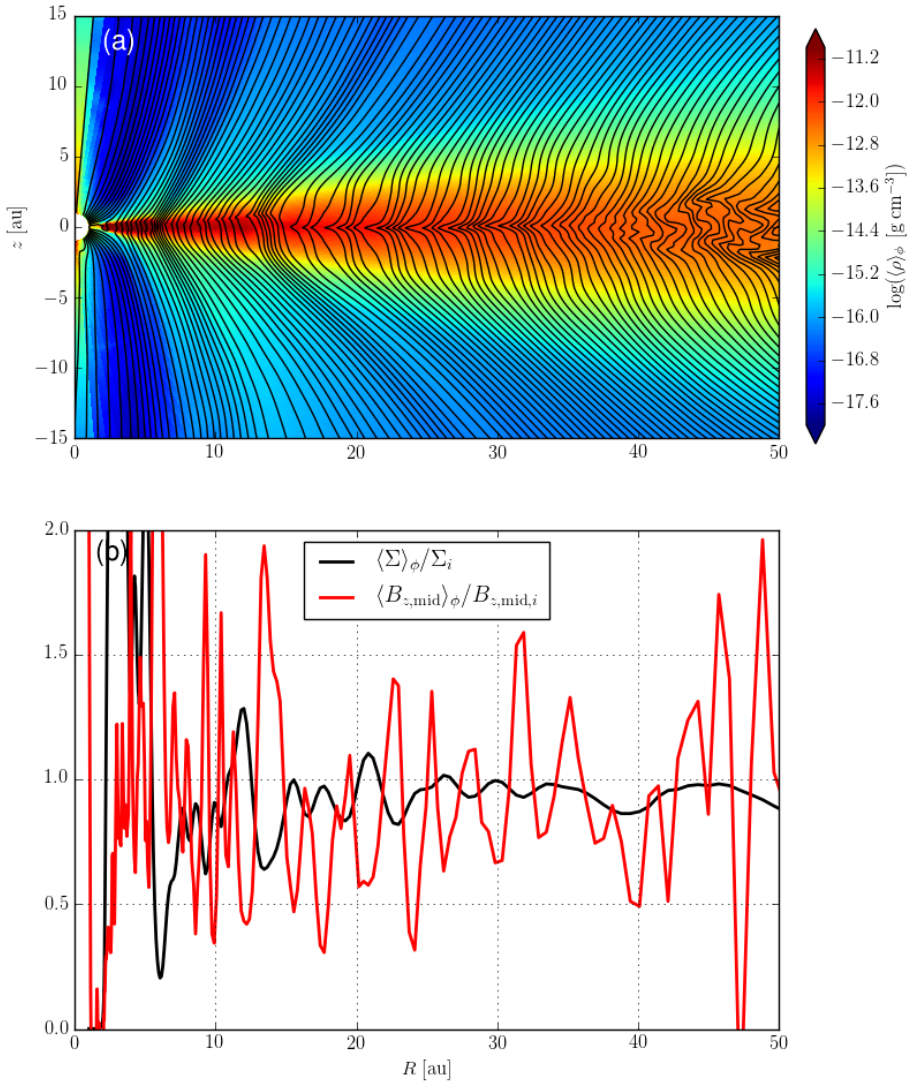

Fig. 4.14.— The high resolution simulation (model ref-hires) at a representative time $t/t_0 = 1200$. The top panel plots the logarithm of the density (colour map) and the ϕ integrated magnetic flux contours (or effective poloidal field lines, black lines). The bottom panel shows the ϕ averaged surface density (black) and vertical magnetic field at the disk midplane (red) normalized respectively by their initial distribution.

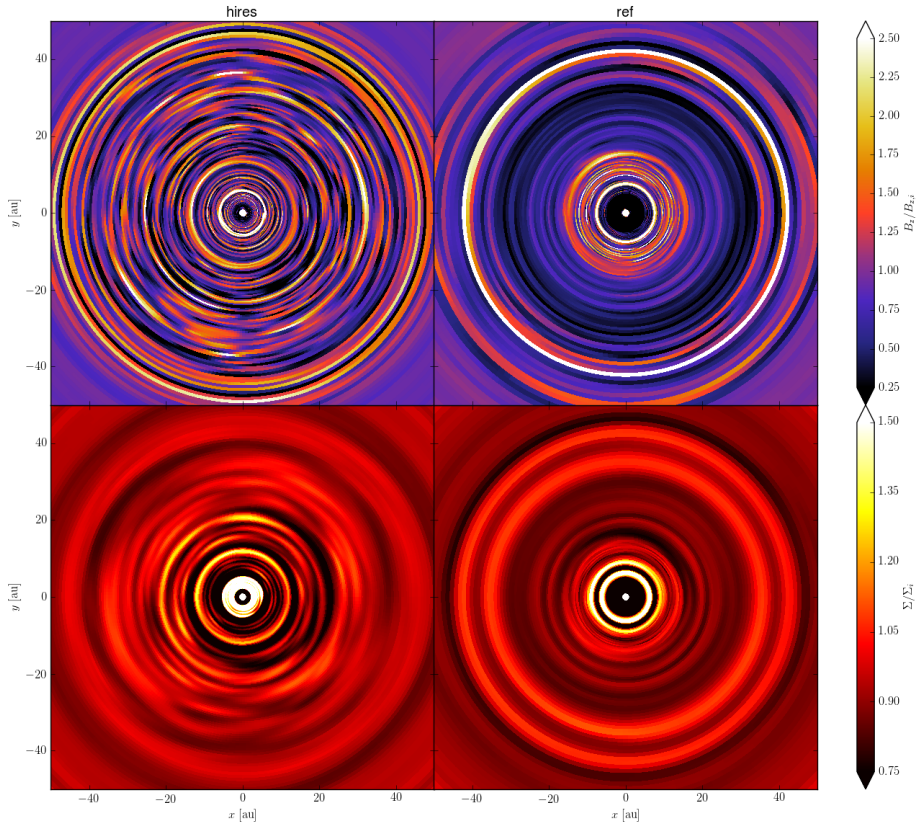

Fig. 4.15.— Spatial variation of the vertical magnetic field strength at the midplane (top row) and the disk surface density (bottom row) normalized to their respective initial distribution for the high resolution simulation (left column) and the reference simulation (right column) at a representative time $t/t_0 = 1200$. The disk substructures are just as prominent, if not more so, as in the reference simulation.

not weaken the disk substructures. In fact, there are more rings and gaps in both the vertical field strength and the surface density, and such radial substructures are more prominent in the higher resolution simulation compared to the reference simulation, especially in the outer regions of the disk. The substructures can be seen more clearly in Fig. 4.14, which shows the face-on view of the vertical magnetic field distribution and the surface density distribution for the high resolution simulation (left column) compared to the reference simulation (right column). We are confident that the prominent disk substructures are not an artifact of the relatively low resolution of the reference simulation, although their detailed properties could be resolution-dependent.

4.5 Conclusion

We have carried out a set of 3D simulations of magnetically coupled disk-wind systems including ambipolar diffusion for different values of the ambipolar diffusivity and the magnetic field strength, as well as two different spatial resolutions. Our main conclusions are as follows.

1. Prominent rings and gaps are formed in the disk in 3D simulations, as in previous 2D (axisymmetric) simulations. They are formed through the same mechanism identified previously in the 2D case, the redistribution of the poloidal magnetic flux relative to the disk material via the reconnection of highly pinched poloidal field lines in the radial direction. The redistribution is shown clearly in the anti-correlation of the distributions of the disk surface density and the vertical magnetic field strength at the midplane, with rings of enhanced surface density less strongly magnetized compared to the gaps.

2. The rings and gaps that develop from the axisymmetric initial conditions adopted in the 3D simulations are relatively axisymmetric at early times. They are distorted by azimuthal variations at later times. The variations do not grow to such an extent as to disrupt the rings and gaps completely. The mostly axisymmetric rings of enhanced surface density persist to the end of the simulation in all cases, which lasts up to 3000 orbits at the inner disk edge.

3. The rings and gaps are more prominent when the magnetic field is better coupled to the bulk disk material and when the (poloidal) magnetic field is stronger. Better magnetically coupled disks tend to have stronger azimuthal variations in the disk substructures.

4. Disk substructures are just as prominent, if not more so, in the higher resolution simulation compared to the lower resolution simulations.

Chapter 5

Conclusion

5.1 Summary

This thesis has explored the formation of radial substructure in magnetized protoplanetary disks (PPDs) using the ZeusTW MHD code. The work is motivated by (1) the need to understand non-ideal MHD effects on the connection of magnetized disk winds to the global evolution of PPDs, and (2) the rings and gaps detected in an increasing number of disks through millimeter and near infrared (NIR) scattered light observations. In Chapter 2, we have found that in 2D-axisymmetric MHD simulations that include Ohmic resistivity, rings and gaps can be formed in disks through purely MHD processes in one of two ways. First, from the removal of angular momentum via a disk wind if the wind torque (and, therefore, the wind driven mass accretion rate) varies as a function of disk radius. Second, via the transport of mass through the so-called "avalanche accretion streams," which are a manifestation of the magnetorotational instability (MRI) channel flows in two dimensions. These two mechanisms operate at two different regimes determined by the Lundquist number, $S \equiv hv_A/\eta$, where h is the disk scale height, v_A the Alfvén velocity, and η the Ohmic resistivity.

When S is large, the avalanche accretion streams dominate the disk dynamics and the accretion rate is set by a vertically-extended envelope ($z \sim R$) produced from the repeated formation and disruption of the streams. However, if S becomes small enough to suppress the streams, the accretion is laminar through the disk midplane and the formation of rings and gaps is driven by the disk wind. The ability of a laminar (non-turbulent) disk to spontaneously form rings and gaps via an MHD disk wind is important because it allows dust to settle in an actively accreting disk, which appears to be the case for HL Tau (Hasegawa et al. 2017).

Chapter 3 focuses on the ambipolar diffusion-dominated outer regions of protoplanetary disks ($r = 1 - 100$ au). Again, we found that a nearly steady disk wind is driven from the disk surface mainly by the magnetic pressure gradient from the toroidal field, while the bulk of the accretion is concentrated in a thin current layer near the midplane (where the toroidal magnetic field changes sign). We outline a mechanism where the reconnection of the highly pinched radial magnetic field in the midplane current layer creates a strong variation in the vertical magnetic flux through the disk as a function of radius. Prominent rings and gaps form in the disk as a result of this mechanism with the surface density correlating inversely with magnetic flux (as in Chapter 2). In the gaps, the relatively large poloidal magnetic field leads to the rapid accretion of the bulk (neutral) material as angular momentum is removed by the disk wind. Ions and magnetic field lines that are tied to them are not accreted rapidly, however, because the strong field drives a large ion-neutral drift velocity. Inside dense rings, the poloidal field is much weaker and is dominated by a strong toroidal component. The overall ring/gap pattern is considerably more stable than the case with Ohmic resistivity. It not only provides a plausible explanation for the rings and gaps observed on the tens of au scale (where AD is important) in several

disks, but can also potentially prevent large grains from migrating too quickly from the outer disk (where they are often observed) through rapid radial drift.

Finally, Chapter 4 extends the 2D simulations with AD performed in Chapter 3 to three dimensions. Rings and gaps are still formed, just as the 2D case. In particular, there is still a clear anti-correlation between the mass surface density and the vertical magnetic flux through the disk midplane. The same mechanism of the AD-assisted reconnection of a pinched radial magnetic field creating a radial variation of the vertical magnetic flux is likely still at work, especially given that the rings and gaps are axisymmetric at early simulation times. The reconnection of the magnetic field at the midplane current layer is not restricted to the poloidal plane in 3D; reconnection in the azimuthal direction could seed the non-axisymmetric disk substructure, which is most noticeable in the vertical magnetic field strength than in the surface density. Less diffusive (better magnetically coupled) disks develop more prominent and smaller scale non-axisymmetric structures, while weaker magnetic field strengths lead to smaller contrast ratios in the surface density rings and gaps. A higher resolution simulation confirms that the existence of rings and gaps does not depend on the resolution, but their detailed properties could be resolution-dependent.

In what follows, we will provide a more detailed (and more technical) summary of the thesis, based on the summaries at the end of Chapters $2-4$. This is followed by an outlook on future directions in Section 5.2.

5.1.1 Resistive axisymmetric simulations

Chapter 2 presents the results of 2D (axisymmetric) resistive MHD simulations of coupled disk-wind systems with a range of disk parameters (resistivity, magnetic field strength, and temperature), focusing on geometrically thin disks. We find that the

structure and dynamics of the disk-wind system strongly depend on the dimensionless magnetic diffusivity parameter $D_m \equiv \eta/(hv_A)$ and that interesting disk features, including rings and gaps, are naturally produced. Specifically, we find that:

1. There are two distinct modes of accretion depending on the dimensionless parameter D_m. Disks with low values of D_m, from either a small resistivity or high field strength, tend to develop fast 'avalanche accretion streams'. The rapid formation and disruption of such streams often leads to a clumpy, thick envelope above the disk that dominates the dynamics of the system, although a highly variable wind is still launched above the envelope. The streams (and the thick clumpy envelope they produce) are suppressed in simulations with larger values of D_m (from either a large resistivity or low field strength, e.g., models beta3 and D4). In these more diffusive (larger D_m) simulations, most of the accretion occurs through a laminar thin disk rather than the thick clumpy envelope, and the disk accretion is driven mainly by a magnetic wind.

2. Both wind-dominated and stream-dominated accretion create prominent features in the surface density distribution, especially rings and gaps. The wind-driven ring and gap formation is illustrated most clearly in the innermost region (Zone I) of the reference simulation, where there is substantial redistribution of magnetic flux relative to the mass in the disk that is enabled by the resistivity. Regions with lower mass-to-flux ratios tend to drive stronger winds and accrete faster, producing gaps; those with higher mass-to-flux ratios tend to accrete more slowly, allowing matter to accumulate and form dense rings. Another stream-driven ring formation mechanism is illustrated most clearly in the thicker disk model (t4), where a stream feeds a prominent ring at a roughly constant radius. Multiple rings and gaps are formed in other, more complicated

cases, especially those with stream-induced envelopes (model D_4 and beta_3). It is likely that both magnetic winds and avalanche accretion streams play a role in the formation of rings and gaps, although the relative importance of the two mechanisms is hard to quantify due to the complexity of the flow pattern inside and above the disk.

3. Powerful winds are launched despite the fact that the magnetic field in the disk is rather weak initially (corresponding to a typical plasma-$\beta \sim 10^3$). In the reference simulation where the wind is analyzed in detail, we find that the bulk of the wind is heavily mass-loaded and accelerated by the magnetic pressure gradient to relatively low speeds (a few $\times 10$ km s^{-1}). There are, however, lightly mass-loaded regions that are accelerated magnetocentrifugally to speeds exceeding 100 km s^{-1}, comparable to the jet speeds observed in young stellar objects. The magnetic wind can remove angular momentum from the disk efficiently, leading to disk accretion with an effective α parameter up to order unity. Our simulations add weight to the notion of wind-driven disk evolution, especially in the presence of a suitable level of magnetic diffusivity.

4. Rings and gaps produced in circumstellar disks by magnetic winds and avalanche accretion streams have important implications on the dynamics and growth of dust grains and ultimately planet formation. The local pressure maxima associated with the rings would act to stop the radial drift of solid particles, possibly trapping them long enough to enable enhanced grain growth that facilitates planetesimal formation. This may be especially important in the inner (i.e., few tenths of an au) disk regions where the largest population of planets reside, as seen by *Kepler*.

5.1.2 Ambipolar diffusion and reconnection

In Chapter 3, we have carried out 2D (axisymmetric) simulations of magnetically coupled disk-wind systems in the presence of a poloidal magnetic field and ambipolar diffusion (AD). The field strength is characterized by the plasma-β and AD by the dimensionless Elsasser number Λ_0. We focused on $\beta \sim 10^3$ and explored a wide range of values for Λ_0, from 0.01 to ∞ (ideal MHD). Our main conclusions from Chapter 3 are as follows:

1. In moderately well coupled systems with Λ_0 between 0.05 and 0.5, including the reference simulation (ad-els0.25), we find that prominent rings and gaps are formed in the disk through a novel mechanism, AD-assisted reconnection. This mechanism starts with the twisting of the initial poloidal magnetic field into a toroidal field that reverses polarity across the disk midplane. Ambipolar diffusion enables the Lorentz force from the toroidal field pressure gradient to drive the ions (and the toroidal field lines tied to them) towards the magnetic null near the midplane, which steepens the radial (J_r) current sheet in a run-away process first described in Brandenburg & Zweibel (1994). The field kink generates a toroidal Lorentz force that removes angular momentum from the thin radial current sheet, forcing it to accrete preferentially relative to the rest of the disk. The preferential midplane accretion drags the poloidal field lines into a sharply pinched configuration, where the radial component of the magnetic field reverses polarity over a thin, secondary azimuthal (J_ϕ) current sheet. Reconnection of the radial pinch produces two types of regions with distinct poloidal field topologies: one occupied by magnetic loops and another that remains threaded by ordered poloidal fields. The weakening of the net poloidal field in the former makes angular momentum removal less efficient, allowing

disk material to accumulate to form dense rings. Conversely, those regions that gained poloidal flux after reconnection are magnetically braked more strongly, with a faster draining of disk material that leads to gap formation. In addition, AD allows for a quasi-steady state of the ring and gap structure, where the field lines can stay more or less fixed in place despite rapid mass accretion in gaps because of the ion-neutral drift.

2. In better magnetically coupled disk-wind systems with larger Λ_0, as well as the ideal MHD limit, we find that avalanche accretion streams develop spontaneously near the disk surface. The accretion streams lead to unsteady/chaotic disk accretion and outflow, as found previously in Chapter 2 for cases of low or zero Ohmic resistivities (see also Zhu & Stone 2018). Prominent rings and gaps are still formed in the disk; the poloidal field lines are concentrated in some regions and excluded from others, with the more strongly magnetized regions producing gaps and the less magnetized regions forming rings, just as in the more magnetically diffusive reference case. We suggest that this segregation of poloidal magnetic flux and matter is also due to reconnection of highly pinched poloidal fields. In this case, the pinching is caused by the avalanche accretion streams (a form of MRI channel flows) rather than the midplane current sheet steepened by AD. The fact that rings and gaps are formed in both laminar and chaotic disk-wind systems over a wide range of magnetic diffusivities suggests that they are a robust feature of such systems, at least when the initial poloidal magnetic field is relatively strong. For more weakly magnetized systems, reconnection may still occur but the resulting redistribution of poloidal magnetic flux would have less of a dynamical effect on the gas, making ring and gap formation less efficient.

3. If young star disks are threaded by a significant poloidal magnetic field, especially during the early phases of star formation, it may drive rapid disk accretion through a magnetic wind without necessarily generating strong turbulence in the disk, particularly in the outer parts of the disk that are only moderately well coupled to the magnetic field. The lack of a strong turbulence despite rapid accretion may allow dust to settle early in the process of star formation, facilitating early grain growth. Large grains may be trapped in the rings that are naturally produced in the system, which may promote the formation of planetesimals and eventually planets.

5.1.3 Three-dimensional simulations

In Chapter 4, we carried out a set of 3D simulations of magnetically coupled disk-wind systems including ambipolar diffusion for different values of the ambipolar diffusivity and the magnetic field strength and two different spatial resolutions. The main conclusions are as follows.

1. Rings and gaps are formed in disks in 3D simulations, as in previous 2D (axisymmetric) simulations. They are formed through the same mechanism identified previously in the 2D case, the redistribution of the poloidal magnetic flux relative to the disk material via the reconnection of highly pinched poloidal field lines in the radial direction. This redistribution is seen clearly in the anti-correlation of the distributions of the disk surface density and the vertical magnetic field strength at the midplane, with rings of enhanced surface density less strongly magnetized compared to the gaps.

2. The rings and gaps that develop from the axisymmetric initial conditions adopted in the 3D simulations are relatively axisymmetric at early times. They are dis-

torted by azimuthal variations at later times. The variations do not grow to such an extent as to disrupt the rings and gaps completely. The mostly axisymmetric rings of enhanced surface density persist to the end of the simulation in all cases (up to 3000 orbits at the inner disk edge).

3. The rings and gaps are more prominent when the magnetic field is better coupled to the bulk disk material and when the (poloidal) magnetic field is stronger. Better magnetically coupled disks tend to have stronger azimuthal variations in the disk substructure.

4. Disk substructures are just as prominent (more so in the outer disk), for a higher resolution simulation compared to the lower resolution simulations.

5.2 Future Outlook

5.2.1 The Hall effect

The simulations discussed in this thesis explored the impact of two non-ideal MHD effects, Ohmic resistivity and ambipolar diffusion, on the formation of disk substructure. The logical next step would be to include the third non-ideal effect, the Hall effect (HE), first in axisymmetric 2D simulations, and then in global 3D simulations as in Chapter 4. The HE is known to be important in controlling the dynamics of magnetized protoplanetary disks (e.g., Kunz & Lesur 2013; Bai 2014, 2015; Béthune et al. 2016; Bai & Stone 2017; Bai 2017), especially at disk radii from $1-10$ au where it is likely the dominant non-ideal MHD effect (see Turner et al. 2014b; Armitage 2015 for review).

A unique feature of the HE is that it depends on the polarity of the magnetic

field, unlikely the other two non-ideal MHD effects. This can be seen from the fact that the Hall diffusivity depends linearly on the magnetic field (i.e., $\eta_H \propto B$), and thus changes sign when the field polarity is reversed. This dependence is illustrated, for example, by Bai & Stone (2017), who demonstrated that the magnetic flux is transported through the disk differently in the presence of the HE when the magnetic field direction is aligned or anti-aligned with the angular velocity. When the magnetic field is aligned with the disk rotation, the vertical gradient of the toroidal magnetic field generates an outward-directing radial current density, which leads to an inward radial drift of the electrons (and the magnetic field lines tied to them) relative to the ions (and the bulk neutral material to which the ions are tied collisionally), since such a drift is required to generate the outward-directing electric current. In contrast, when the magnetic field flips its polarity so that it is anti-aligned with the disk rotation, the same vertical gradient of the toroidal magnetic field generates an inward- rather than outward-directing radial current density, which drives the electrons (and the magnetic field lines tied to them) to drift outward, instead of inward, relative to the ions (and neutrals). This same line of reasoning could be important for solving the so-called "magnetic braking catastrophe," (see Li et al. 2014b) in which rotationally supported disks are difficult to form without the removal of a significant amount of magnetic flux; the flux removal will depend on the orientation of the magnetic field relative to the rotation axis where the Hall effect is important.

5.2.2 Disk chemistry and ionization

Whether non-ideal MHD effects are important to the disk dynamics or not depends critically on the disk ionization. As a first step, we have adopted in this thesis a simple, parametrized approach to treat the coefficients for the non-ideal MHD

effects. Specifically, the resistivity is taken to be constant throughout the simulations in Chapter 2 and a simple power-law dependence of the ion density on the bulk neutral density is adopted to treat the ambipolar diffusion inside the disk in Chapter 3 & 4; above the disk, the ionization is assumed to increase rapidly so that the ambipolar diffusion quickly becomes inefficient above two disk scale heights. In a more complete model, there is obviously a strong need to compute the disk ionization and thus non-ideal MHD coefficients self-consistently.

Protoplanetary disks have several sources of ionization with their relative importance depending on the location in the disk. The sources of disk ionization include:

1. Thermal ionization of alkali metals (i.e., potassium with $\chi = 4.34$ eV) in warm inner disk regions
2. Cosmic rays with a canonical ionization rate of $\zeta_{\rm CR} = 10^{-17}$ s^{-1}
3. Ultraviolet photons from the central star or cluster environment
4. Stellar X-ray photons
5. Decay of radionuclides (i.e., ^{26}Al)

Ideally, these ionization sources should be included to compute the disk ionization self-consistently everywhere in the disk at all simulation times. This requires the implementation of a chemical network as formulated, e.g., by Umebayashi & Nakano (1990) (see also Ilgner & Nelson 2006; Bai & Goodman 2009; Padovani et al. 2014). These simplified equilibrium chemical networks contain $\sim$10 chemical species, including free electrons and protons, the neutral hydrogen molecule H_2, the hydrogen ion H_3^+, a neutral and $+1e$-charged heavy molecule species, a heavy metal atom and its $+1e$-charged ion, and neutral or singly ($\pm 1e$) charged dust grains with various sizes

according to the MRN size distribution (Mathis et al. 1977). This has already been implemented into the ZeusTW code (Zhao et al. 2016) and was used in the context of disk formation from prestellar cores. We plan to extend this capability to our protoplanetary disk simulations in the future.

5.2.3 Dust grain dynamics

So far, our simulations included gas only. An important next step is to treat dust grain dynamics, through either post-processing or direct inclusion of the grains into the MHD simulations. This step is crucial for at least two reasons: (1) it allows for the direct comparison between simulations and observations of disk substructures, which are usually traced observationally through either direct dust emission at (sub)mm-wavelengths by relatively large grains or scattered light at NIR by relatively small grains; (2) provide insights into how the disk dynamics (such as the level of turbulence, which may be low for the wind-driven disk accretion) and radial structures (such as rings and gaps) affect the grain growth, vertical settling, and radial drift, all of which are currently uncertain but crucial to the formation of planetesimals and, eventually, planets.

The dynamics of dust particles relative to the gas in protoplanetary disks is most often characterized by the stopping time of a dust particle (Whipple 1972; Weidenschilling 1977a),

$$t_s = \frac{m\Delta v}{F_{\rm drag}}, \tag{5.1}$$

where m is the mass of the particle, Δv is the velocity difference between the particle and the gas $\Delta v = v_{\rm dust} - v_{\rm gas}$, and $F_{\rm drag}$ is the drag force acting on the particle. In the well-known Epstein regime that is generally applicable in disks for millimeter- or centimeter-sized grains that are directly accessible to radio observations, i.e., where

the particle size is small compared to the mean free path of the gas and the gas particles hit the dust particle individually rather than acting on it as a fluid, the stopping time can be written independent of Δv as (assuming the gas thermal velocity is roughly the same as the gas sound speed)

$$t_s = \frac{\bar{\rho}_{\rm solid} a}{\rho_{\rm gas} c_s}. \tag{5.2}$$

where $\bar{\rho}_{\rm solid}$ is solid density of the particle (approximately 3 g cm^{-3}) and a is the radius of the particle. The dimensionless stopping time, or the Stokes number, is then defined as

$$\mathrm{St} \equiv t_s \Omega_K. \tag{5.3}$$

Particles with a Stokes number of order unity are special in the disk in that they are expected to drift radially inward the fastest. This is because smaller particles with a Stokes number much less than unity are well coupled to the gas, which orbits the central star at a sub-Keplerian speed because of the partial support provided to the gas by the pressure gradient in a (smooth) disk. The tight coupling of the small particles to the gas means that they must orbit the central star at roughly the same sub-Keplerian speed as well. Since these sub-Keplerian particles do not experience the gas pressure gradient directly, they would be pulled inward by the unbalanced gravitational force (i.e., excess over the centrifugal force from the sub-Keplerian rotation), until a terminal infall (or inward drift) speed is reached where the unbalanced gravitational pull is balanced by the outward drag force on the particles from their inward drift through the gas. Since smaller particles have a larger surface area relative to their mass, they are better coupled to the gas through collisions, with a smaller drift speed needed to generate the same amount of drag force per unit mass

to balance the excess gravitational acceleration due to sub-Keplerian rotation. This is the reason why, in the limit of $\mathrm{St} \ll 1$, smaller particles tend to drift slower radially, with the drift speed increasing with the particle size.

In the opposite limit of $\mathrm{St} \gg 1$, the trend is reversed. This is because large particles in this regime are poorly coupled to the gas through collisions. They orbit the central star at an essentially Keplerian speed, and experience a "head wind" from the more slowly rotating (sub-Keplerian) gas that reduces their orbital energy (and angular momentum). The reduction forces the particles to drift radially inward, with smaller particles drifting inward more quickly because they are better coupled to the gas and thus experience an effectively stronger "head wind" (relative to their mass) that reduces their orbital energy (and angular momentum) more efficiently. The end result is that the drift speed peaks for particles with $\mathrm{St} \sim 1$.

One consequence of the above result is the well-known "meter size barrier" in planetesimal formation. Objects of approximately $a \sim 1$ m have a Stokes number of order unity at $r \sim 1$ au in the MMSN[1] and are expected to drift rapidly inward on a timescale of less than 100 yr, much shorter than the expected lifetime of protoplanetary disks, thus limiting the maximum size to which dust grains could grow. In the simulations presented in this thesis, the particle size which yields a Stokes number of unity at a radius of 10 au is around $a = 10$ cm.

Despite this theoretical meter size barrier, we know that grains must be able to overcome the barrier and grow to bigger sizes in order to form kilometer-sized

[1]The minimum mass solar nebula (MMSN; Weidenschilling 1977b; Hayashi 1981) is the minimum amount of mass required to form the planets in the solar system *in situ*. The radial mass distribution of the MMSN is found by spreading the mass of each planet in the solar system over an annulus centered on their orbital radii and adding back the appropriate amount of gas that would have been present in the young disk. The resulting mass surface density distribution is found to be $\Sigma \simeq 1700 \text{ g cm}^{-2} \ (R/\text{au})^{-3/2}$ with a total disk mass of the order 10^{-2} $\mathrm{M}_\odot$. Similarly, one can construct the MMEN (where the "E" is for extrasolar) from all known exoplanets to a similar mass surface density distribution but with the scaling increased by a factor of five (Chiang & Laughlin 2013).

planetesimals and eventually planets on appropriate timescales in disks. One possible way to circumvent this problem is that the inward migration of large solid particles is halted by pressure maxima in disks. Particles drift through the disk in the direction of the positive radial pressure gradient, i.e., towards pressure maxima. For this reason, pressure maxima in disks are often referred to as dust traps as they will attract solids particles from both sides of a pressure maximum. At the peak of the pressure distribution, where $dP/dr = 0$, the gas will orbit at the Keplerian speed; there will be no difference in orbital speed between the gas and the dust and, therefore, no drag force acting on the dust to force it to migrate inward. Such pressure bumps are needed to stop the fast migration of large grains through the disk; they are potential sites of rapid grain growth.

The simulations presented in thesis provided a natural mechanism for the formation of such sites in magnetized accretion disks. Such dust traps would be especially important in low-mass disks around brown dwarfs where millimeter-sized grains are inferred on the 100 au scale from observations, especially with ALMA (Pinilla et al. 2013). Dust grains are well-coupled to the gas for relatively massive disks with mass greater than the MMSN (10^{-2} $M_{\odot}$); for example, they have a Stokes number $\mathrm{St} \sim 0.03 \ll 1$ at 100 au of our reference models (that are not far from MMSN). Since the Stokes number for grains of a given size is inversely proportional to the surface density of the gas, lowering the surface density by a factor of 10, for example, would increase the Stokes number of those grains by a corresponding factor from 0.03 to 0.3 (i.e., much closer to the $\mathrm{St} \sim 1$ regime where the grains drift radially inward the fastest). Indeed, in the specific case of the young brown dwarf 2M0444, Ricci et al. (2017) showed that the observationally inferred millimeter-sized grains in the outer part of the disk would disappear quickly through radial migration if they were not

trapped. They showed further that the observations could be explained by having multiple pressure peaks in the outer disk, like those that form in our simulations. The potential for disk substructures to slow down the rapid radial migration of large particles and facilitate the formation of planetesimals and planets provides a strong motivation for future investigations of their effects on grain dynamics and growth.

In addition, the ability of a laminar disk to spontaneously form rings and gaps via an MHD disk wind is important because it allows dust to settle vertically in an actively accreting disk, which appears to be the case for HL Tau (Pinte et al. 2016; Hasegawa et al. 2017). From the simulation results in Chapter 3, we speculated that the AD-enhanced midplane accretion could account for such large accretion rates despite a high degree of dust settling, and, therefore, a lack of disk turbulence. This idea has since been corroborated by the simulations of Riols & Lesur (2018), which included dust grains in (shearing-box) MHD simulations of protoplanetary disks. Furthermore, small grains, depending on how well coupled they are to the gas flow, may be swept up in disk winds or vertically suspended in the disk atmosphere (Turner et al. 2014a; Miyake et al. 2016). This could potentially be responsible for the IR variability observed in many young stars. If gas is removed preferentially by the disk winds relative to dust grains (especially large grains that are not well coupled to the gas), the local dust-to-gas ratio in the wind-launching region of the disk is expected to increase with time, with interesting implications for the grain dynamics and growth that are important for planet formation (Suzuki et al. 2010; Gorti et al. 2015; Bai et al. 2016).

For these reasons, it is important and compelling to continue the investigation of the formation of substructures in magnetized protoplanetary disk simulations by including more detailed microscopic physics and the dynamics of dust grains, which

are more directly tied to observations and planet formation.

References

Adams, F. C., Lada, C. J., & Shu, F. H. 1987, ApJ, 312, 788

Alcalá, J. M., Natta, A., Manara, C. F., Spezzi, L., Stelzer, B., Frasca, A., Biazzo, K., Covino, E., Randich, S., Rigliaco, E., Testi, L., Comerón, F., Cupani, G., & D'Elia, V. 2014, A&A, 561, A2

Alexander, R., Pascucci, I., Andrews, S., Armitage, P., & Cieza, L. 2014, Protostars and Planets VI, 475

ALMA Partnership, Brogan, C. L., Pérez, L. M., Hunter, T. R., Dent, W. R. F., Hales, A. S., Hills, R. E., Corder, S., Fomalont, E. B., Vlahakis, C., Asaki, Y., Barkats, D., Hirota, A., Hodge, J. A., Impellizzeri, C. M. V., Kneissl, R., Liuzzo, E., Lucas, R., Marcelino, N., Matsushita, S., Nakanishi, K., Phillips, N., Richards, A. M. S., Toledo, I., Aladro, R., Broguiere, D., Cortes, J. R., Cortes, P. C., Espada, D., Galarza, F., Garcia-Appadoo, D., Guzman-Ramirez, L., Humphreys, E. M., Jung, T., Kameno, S., Laing, R. A., Leon, S., Marconi, G., Mignano, A., Nikolic, B., Nyman, L.-A., Radiszcz, M., Remijan, A., Rodón, J. A., Sawada, T., Takahashi, S., Tilanus, R. P. J., Vila Vilaro, B., Watson, L. C., Wiklind, T., Akiyama, E., Chapillon, E., de Gregorio-Monsalvo, I., Di Francesco, J., Gueth, F., Kawamura, A., Lee, C.-F., Nguyen Luong, Q., Mangum, J., Pietu, V., Sanhueza, P., Saigo, K., Takakuwa, S., Ubach, C., van Kempen, T., Wootten, A., Castro-Carrizo, A.,

Francke, H., Gallardo, J., Garcia, J., Gonzalez, S., Hill, T., Kaminski, T., Kurono, Y., Liu, H.-Y., Lopez, C., Morales, F., Plarre, K., Schieven, G., Testi, L., Videla, L., Villard, E., Andreani, P., Hibbard, J. E., & Tatematsu, K. 2015, ApJ, 808, L3

Anderson, J. M., Li, Z.-Y., Krasnopolsky, R., & Blandford, R. D. 2003, ApJ, 590, L107

—. 2005, ApJ, 630, 945

—. 2006, ApJ, 653, L33

Andrews, S. M., Wilner, D. J., Hughes, A. M., Qi, C., & Dullemond, C. P. 2010, ApJ, 723, 1241

Andrews, S. M., Wilner, D. J., Zhu, Z., Birnstiel, T., Carpenter, J. M., Pérez, L. M., Bai, X.-N., Öberg, K. I., Hughes, A. M., Isella, A., & Ricci, L. 2016, ApJ, 820, L40

Armitage, P. J. 2015, ArXiv e-prints

Avenhaus, H., Quanz, S. P., Garufi, A., Perez, S., Casassus, S., Pinte, C., Bertrang, G. H.-M., Caceres, C., Benisty, M., & Dominik, C. 2018, ArXiv e-prints

Bacciotti, F., Mundt, R., Ray, T. P., Eislöffel, J., Solf, J., & Camezind, M. 2000, ApJ, 537, L49

Bae, J., Zhu, Z., & Hartmann, L. 2017, ApJ, 850, 201

Bai, X.-N. 2013, ApJ, 772, 96

—. 2014, ApJ, 791, 137

—. 2015, ApJ, 798, 84

—. 2016, ApJ, 821, 80

—. 2017, ApJ, 845, 75

Bai, X.-N. & Goodman, J. 2009, ApJ, 701, 737

Bai, X.-N. & Stone, J. M. 2011, ApJ, 736, 144

—. 2013, ApJ, 769, 76

—. 2014, ApJ, 796, 31

—. 2017, ApJ, 836, 46

Bai, X.-N., Ye, J., Goodman, J., & Yuan, F. 2016, ApJ, 818, 152

Balbus, S. A. & Hawley, J. F. 1991, ApJ, 376, 214

—. 1998, Reviews of Modern Physics, 70, 1

Bally, J., Reipurth, B., & Davis, C. J. 2007, Protostars and Planets V, 215

Banzatti, A. & Pontoppidan, K. M. 2015, ApJ, 809, 167

Beckwith, K., Hawley, J. F., & Krolik, J. H. 2009, ApJ, 707, 428

Benisty, M., Stolker, T., Pohl, A., de Boer, J., Lesur, G., Dominik, C., Dullemond, C. P., Langlois, M., Min, M., Wagner, K., Henning, T., Juhasz, A., Pinilla, P., Facchini, S., Apai, D., van Boekel, R., Garufi, A., Ginski, C., Ménard, F., Pinte, C., Quanz, S. P., Zurlo, A., Boccaletti, A., Bonnefoy, M., Beuzit, J. L., Chauvin, G., Cudel, M., Desidera, S., Feldt, M., Fontanive, C., Gratton, R., Kasper, M., Lagrange, A.-M., LeCoroller, H., Mouillet, D., Mesa, D., Sissa, E., Vigan, A.,

Antichi, J., Buey, T., Fusco, T., Gisler, D., Llored, M., Magnard, Y., Moeller-Nilsson, O., Pragt, J., Roelfsema, R., Sauvage, J.-F., & Wildi, F. 2017, A&A, 597, A42

Béthune, W., Lesur, G., & Ferreira, J. 2016, A&A, 589, A87

—. 2017, A&A, 600, A75

Bjerkeli, P., van der Wiel, M. H. D., Harsono, D., Ramsey, J. P., & Jørgensen, J. K. 2016, Nature, 540, 406

Blaes, O. M. & Balbus, S. A. 1994, ApJ, 421, 163

Blandford, R. D. & Payne, D. G. 1982, MNRAS, 199, 883

Brandenburg, A. & Zweibel, E. G. 1994, ApJ, 427, L91

Burrows, C. J., Stapelfeldt, K. R., Watson, A. M., Krist, J. E., Ballester, G. E., Clarke, J. T., Crisp, D., Gallagher, III, J. S., Griffiths, R. E., Hester, J. J., Hoessel, J. G., Holtzman, J. A., Mould, J. R., Scowen, P. A., Trauger, J. T., & Westphal, J. A. 1996, ApJ, 473, 437

Casassus, S., van der Plas, G., M, S. P., Dent, W. R. F., Fomalont, E., Hagelberg, J., Hales, A., Jordán, A., Mawet, D., Ménard, F., Wootten, A., Wilner, D., Hughes, A. M., Schreiber, M. R., Girard, J. H., Ercolano, B., Canovas, H., Román, P. E., & Salinas, V. 2013, Nature, 493, 191

Casse, F. & Ferreira, J. 2000, A&A, 353, 1115

Casse, F. & Keppens, R. 2002, ApJ, 581, 988

—. 2004, ApJ, 601, 90

Chandrasekhar, S. 1960, Proceedings of the National Academy of Science, 46, 253

—. 1961, Hydrodynamic and hydromagnetic stability

Chiang, E. & Laughlin, G. 2013, MNRAS, 431, 3444

Chiang, E. & Murray-Clay, R. 2007, Nature Physics, 3, 604

Chiang, E. & Youdin, A. N. 2010, Annual Review of Earth and Planetary Sciences, 38, 493

Cieza, L. A., Casassus, S., Tobin, J., Bos, S. P., Williams, J. P., Perez, S., Zhu, Z., Caceres, C., Canovas, H., Dunham, M. M., Hales, A., Prieto, J. L., Principe, D. A., Schreiber, M. R., Ruiz-Rodriguez, D., & Zurlo, A. 2016, Nature, 535, 258

Clarke, D. A. 1996, ApJ, 457, 291

—. 2010, ApJS, 187, 119

Cody, A. M., Stauffer, J., Baglin, A., Micela, G., Rebull, L. M., Flaccomio, E., Morales-Calderón, M., Aigrain, S., Bouvier, J., Hillenbrand, L. A., Gutermuth, R., Song, I., Turner, N., Alencar, S. H. P., Zwintz, K., Plavchan, P., Carpenter, J., Findeisen, K., Carey, S., Terebey, S., Hartmann, L., Calvet, N., Teixeira, P., Vrba, F. J., Wolk, S., Covey, K., Poppenhaeger, K., Günther, H. M., Forbrich, J., Whitney, B., Affer, L., Herbst, W., Hora, J., Barrado, D., Holtzman, J., Marchis, F., Wood, K., Medeiros Guimarães, M., Lillo Box, J., Gillen, E., McQuillan, A., Espaillat, C., Allen, L., D'Alessio, P., & Favata, F. 2014, AJ, 147, 82

Combet, C. & Ferreira, J. 2008, A&A, 479, 481

Desch, S. J. & Turner, N. J. 2015, ApJ, 811, 156

Dipierro, G., Price, D., Laibe, G., Hirsh, K., Cerioli, A., & Lodato, G. 2015, MNRAS, 453, L73

Dipierro, G., Ricci, L., Pérez, L., Lodato, G., Alexander, R. D., Laibe, G., Andrews, S., Carpenter, J. M., Chandler, C. J., Greaves, J. A., Hall, C., Henning, T., Kwon, W., Linz, H., Mundy, L., Sargent, A., Tazzari, M., Testi, L., & Wilner, D. 2018, MNRAS, 475, 5296

Dittrich, K., Klahr, H., & Johansen, A. 2013, ApJ, 763, 117

Dong, R., Li, S., Chiang, E., & Li, H. 2017, ApJ, 843, 127

Dong, R., Zhu, Z., & Whitney, B. 2015, ApJ, 809, 93

Dzyurkevich, N., Flock, M., Turner, N. J., Klahr, H., & Henning, T. 2010, A&A, 515, A70

Evans, C. R. & Hawley, J. F. 1988, ApJ, 332, 659

Fedele, D., Carney, M., Hogerheijde, M. R., Walsh, C., Miotello, A., Klaassen, P., Bruderer, S., Henning, T., & van Dishoeck, E. F. 2017, A&A, 600, A72

Fedele, D., Tazzari, M., Booth, R., Testi, L., Clarke, C. J., Pascucci, I., Kospal, A., Semenov, D., Bruderer, S., Henning, T., & Teague, R. 2018, A&A, 610, A24

Ferreira, J. 1997, A&A, 319, 340

Flaherty, K. M., Hughes, A. M., Rose, S. C., Simon, J. B., Qi, C., Andrews, S. M., Kóspál, Á., Wilner, D. J., Chiang, E., Armitage, P. J., & Bai, X.-n. 2017, ApJ, 843, 150

Fleming, T. & Stone, J. M. 2003, ApJ, 585, 908

Fleming, T. P., Stone, J. M., & Hawley, J. F. 2000, ApJ, 530, 464

Flock, M., Ruge, J. P., Dzyurkevich, N., Henning, T., Klahr, H., & Wolf, S. 2015, A&A, 574, A68

Frank, A., Ray, T. P., Cabrit, S., Hartigan, P., Arce, H. G., Bacciotti, F., Bally, J., Benisty, M., Eislöffel, J., Güdel, M., Lebedev, S., Nisini, B., & Raga, A. 2014, Protostars and Planets VI, 451

Furth, H. P., Killeen, J., & Rosenbluth, M. N. 1963, Physics of Fluids, 6, 459

Ginski, C., Stolker, T., Pinilla, P., Dominik, C., Boccaletti, A., de Boer, J., Benisty, M., Biller, B., Feldt, M., Garufi, A., Keller, C. U., Kenworthy, M., Maire, A. L., Ménard, F., Mesa, D., Milli, J., Min, M., Pinte, C., Quanz, S. P., van Boekel, R., Bonnefoy, M., Chauvin, G., Desidera, S., Gratton, R., Girard, J. H. V., Keppler, M., Kopytova, T., Lagrange, A.-M., Langlois, M., Rouan, D., & Vigan, A. 2016, A&A, 595, A112

Glassgold, A. E., Lizano, S., & Galli, D. 2017, MNRAS, 472, 2447

Goldreich, P. & Tremaine, S. 1980, ApJ, 241, 425

Goodman, J. & Xu, G. 1994, ApJ, 432, 213

Gorti, U., Hollenbach, D., & Dullemond, C. P. 2015, ApJ, 804, 29

Greene, T. P., Wilking, B. A., Andre, P., Young, E. T., & Lada, C. J. 1994, ApJ, 434, 614

Greenhill, L. J., Goddi, C., Chandler, C. J., Matthews, L. D., & Humphreys, E. M. L. 2013, ApJ, 770, L32

Gressel, O., Turner, N. J., Nelson, R. P., & McNally, C. P. 2015, ApJ, 801, 84

Gullbring, E., Hartmann, L., Briceño, C., & Calvet, N. 1998, ApJ, 492, 323

Haro, G. 1952, ApJ, 115, 572

—. 1953, ApJ, 117, 73

Hartmann, L. 1998, Accretion Processes in Star Formation

Hartmann, L., Calvet, N., Gullbring, E., & D'Alessio, P. 1998, ApJ, 495, 385

Hartmann, L., Herczeg, G., & Calvet, N. 2016, ARA&A, 54, 135

Hartmann, L., Hewett, R., & Calvet, N. 1994, ApJ, 426, 669

Hasegawa, Y., Okuzumi, S., Flock, M., & Turner, N. J. 2017, ApJ, 845, 31

Hawley, J. F., Fendt, C., Hardcastle, M., Nokhrina, E., & Tchekhovskoy, A. 2015, Space Sci. Rev., 191, 441

Hayashi, C. 1981, Progress of Theoretical Physics Supplement, 70, 35

Herbig, G. H. 1951, ApJ, 113, 697

Heyvaerts, J. & Norman, C. 1989, ApJ, 347, 1055

Hirose, S. & Turner, N. J. 2011, ApJ, 732, L30

Hirota, T., Machida, M. N., Matsushita, Y., Motogi, K., Matsumoto, N., Kim, M. K., Burns, R. A., & Honma, M. 2017, Nature Astronomy, 1, 0146

Hughes, A. M., Wilner, D. J., Andrews, S. M., Qi, C., & Hogerheijde, M. R. 2011, ApJ, 727, 85

Ilgner, M. & Nelson, R. P. 2006, A&A, 445, 205

Isella, A., Guidi, G., Testi, L., Liu, S., Li, H., Li, S., Weaver, E., Boehler, Y., Carperter, J. M., De Gregorio-Monsalvo, I., Manara, C. F., Natta, A., Pérez, L. M., Ricci, L., Sargent, A., Tazzari, M., & Turner, N. 2016, Physical Review Letters, 117, 251101

Johansen, A., Youdin, A., & Klahr, H. 2009, ApJ, 697, 1269

Kato, S. X., Kudoh, T., & Shibata, K. 2002, ApJ, 565, 1035

Kley, W. & Nelson, R. P. 2012, ARA&A, 50, 211

Koenigl, A. 1991, ApJ, 370, L39

Konigl, A. & Pudritz, R. E. 2000, Protostars and Planets IV, 759

Königl, A., Salmeron, R., & Wardle, M. 2010, MNRAS, 401, 479

Krasnopolsky, R., Li, Z.-Y., & Blandford, R. 1999, ApJ, 526, 631

Krasnopolsky, R., Li, Z.-Y., & Shang, H. 2010, ApJ, 716, 1541

—. 2011, ApJ, 733, 54

Kudoh, T., Matsumoto, R., & Shibata, K. 1998, ApJ, 508, 186

—. 2002, PASJ, 54, 121

Kunz, M. W. & Lesur, G. 2013, MNRAS, 434, 2295

Lada, C. J. 1987, in IAU Symposium, Vol. 115, Star Forming Regions, ed. M. Peimbert & J. Jugaku, 1–17

Latter, H. N., Lesaffre, P., & Balbus, S. A. 2009, MNRAS, 394, 715

Launhardt, R., Pavlyuchenkov, Y., Gueth, F., Chen, X., Dutrey, A., Guilloteau, S., Henning, T., Piétu, V., Schreyer, K., & Semenov, D. 2009, A&A, 494, 147

Lee, C.-F., Li, Z.-Y., Codella, C., Ho, P. T. P., Podio, L., Hirano, N., Shang, H., Turner, N. J., & Zhang, Q. 2018, ApJ, 856, 14

Lee, C.-F., Li, Z.-Y., Ho, P. T. P., Hirano, N., Zhang, Q., & Shang, H. 2017, Science Advances, 3, e1602935

Lesur, G., Kunz, M. W., & Fromang, S. 2014, A&A, 566, A56

Li, H.-B., Goodman, A., Sridharan, T. K., Houde, M., Li, Z.-Y., Novak, G., & Tang, K. S. 2014a, Protostars and Planets VI, 101

Li, Z.-Y. 1995, ApJ, 444, 848

Li, Z.-Y., Banerjee, R., Pudritz, R. E., Jørgensen, J. K., Shang, H., Krasnopolsky, R., & Maury, A. 2014b, Protostars and Planets VI, 173

Li, Z.-Y., Krasnopolsky, R., & Shang, H. 2011, ApJ, 738, 180

Li, Z.-Y. & McKee, C. F. 1996, ApJ, 464, 373

Lii, P., Romanova, M., & Lovelace, R. 2012, MNRAS, 420, 2020

Lin, D. N. C. & Papaloizou, J. 1986, ApJ, 307, 395

Loomis, R. A., Öberg, K. I., Andrews, S. M., & MacGregor, M. A. 2017, ApJ, 840, 23

Lovelace, R. V. E., Li, H., Colgate, S. A., & Nelson, A. F. 1999, ApJ, 513, 805

Lynden-Bell, D. 1996, MNRAS, 279, 389

—. 2003, MNRAS, 341, 1360

Lynden-Bell, D. & Pringle, J. E. 1974, MNRAS, 168, 603

Mac Low, M.-M., Norman, M. L., Konigl, A., & Wardle, M. 1995, ApJ, 442, 726

Mathis, J. S., Rumpl, W., & Nordsieck, K. H. 1977, ApJ, 217, 425

Matsumoto, R., Uchida, Y., Hirose, S., Shibata, K., Hayashi, M. R., Ferrari, A., Bodo, G., & Norman, C. 1996, ApJ, 461, 115

Matt, S. & Pudritz, R. E. 2008, ApJ, 678, 1109

Matthews, L. D., Greenhill, L. J., Goddi, C., Chandler, C. J., Humphreys, E. M. L., & Kunz, M. W. 2010, ApJ, 708, 80

McCaughrean, M. J. & O'dell, C. R. 1996, AJ, 111, 1977

Melia, F. 2009, High-Energy Astrophysics

Miyake, T., Suzuki, T. K., & Inutsuka, S.-i. 2016, ApJ, 821, 3

Moll, R. 2012, A&A, 548, A76

Momose, M., Morita, A., Fukagawa, M., Muto, T., Takeuchi, T., Hashimoto, J., Honda, M., Kudo, T., Okamoto, Y. K., Kanagawa, K. D., Tanaka, H., Grady, C. A., Sitko, M. L., Akiyama, E., Currie, T., Follette, K. B., Mayama, S., Kusakabe, N., Abe, L., Brandner, W., Brandt, T. D., Carson, J. C., Egner, S., Feldt, M., Goto, M., Guyon, O., Hayano, Y., Hayashi, M., Hayashi, S. S., Henning, T., Hodapp, K. W., Ishii, M., Iye, M., Janson, M., Kandori, R., Knapp, G. R., Kuzuhara, M., Kwon, J., Matsuo, T., McElwain, M. W., Miyama, S., Morino, J.-I., Moro-Martin, A., Nishimura, T., Pyo, T.-S., Serabyn, E., Suenaga, T., Suto, H., Suzuki, R.,

Takahashi, Y. H., Takami, M., Takato, N., Terada, H., Thalmann, C., Tomono, D., Turner, E. L., Watanabe, M., Wisniewski, J., Yamada, T., Takami, H., Usuda, T., & Tamura, M. 2015, PASJ, 67, 83

Monnier, J. D., Harries, T. J., Aarnio, A., Adams, F. C., Andrews, S., Calvet, N., Espaillat, C., Hartmann, L., Hinkley, S., Kraus, S., McClure, M., Oppenheimer, R., Perrin, M., & Wilner, D. 2017, ApJ, 838, 20

Murphy, G. C., Ferreira, J., & Zanni, C. 2010, A&A, 512, A82

Nomura, H., Tsukagoshi, T., Kawabe, R., Ishimoto, D., Okuzumi, S., Muto, T., Kanagawa, K. D., Ida, S., Walsh, C., Millar, T. J., & Bai, X.-N. 2016, ApJ, 819, L7

O'dell, C. R. 1998, AJ, 115, 263

O'dell, C. R. & Wen, Z. 1994, ApJ, 436, 194

O'dell, C. R., Wen, Z., & Hu, X. 1993, ApJ, 410, 696

Okuzumi, S., Momose, M., Sirono, S.-i., Kobayashi, H., & Tanaka, H. 2016, ApJ, 821, 82

Padovani, M., Galli, D., Hennebelle, P., Commerçon, B., & Joos, M. 2014, A&A, 571, A33

Pérez, L. M., Carpenter, J. M., Andrews, S. M., Ricci, L., Isella, A., Linz, H., Sargent, A. I., Wilner, D. J., Henning, T., Deller, A. T., Chandler, C. J., Dullemond, C. P., Lazio, J., Menten, K. M., Corder, S. A., Storm, S., Testi, L., Tazzari, M., Kwon, W., Calvet, N., Greaves, J. S., Harris, R. J., & Mundy, L. G. 2016, Science, 353, 1519

Perez-Becker, D. & Chiang, E. 2011a, ApJ, 735, 8

—. 2011b, ApJ, 727, 2

Pinilla, P., Birnstiel, T., Benisty, M., Ricci, L., Natta, A., Dullemond, C. P., Dominik, C., & Testi, L. 2013, A&A, 554, A95

Pinte, C., Dent, W. R. F., Ménard, F., Hales, A., Hill, T., Cortes, P., & de Gregorio-Monsalvo, I. 2016, ApJ, 816, 25

Pohl, A., Benisty, M., Pinilla, P., Ginski, C., de Boer, J., Avenhaus, H., Henning, T., Zurlo, A., Boccaletti, A., Augereau, J.-C., Birnstiel, T., Dominik, C., Facchini, S., Fedele, D., Janson, M., Keppler, M., Kral, Q., Langlois, M., Ligi, R., Maire, A.-L., Ménard, F., Meyer, M., Pinte, C., Quanz, S. P., Sauvage, J.-F., Sezestre, É., Stolker, T., Szulágyi, J., van Boekel, R., van der Plas, G., Villenave, M., Baruffolo, A., Baudoz, P., Le Mignant, D., Maurel, D., Ramos, J., & Weber, L. 2017, ApJ, 850, 52

Pontoppidan, K. M., Blake, G. A., & Smette, A. 2011, ApJ, 733, 84

Pringle, J. E. 1981, ARA&A, 19, 137

Pudritz, R. E. & Norman, C. A. 1983, ApJ, 274, 677

Ray, T., Dougados, C., Bacciotti, F., Eislöffel, J., & Chrysostomou, A. 2007, Protostars and Planets V, 231

Reipurth, B., Yu, K. C., Heathcote, S., Bally, J., & Rodríguez, L. F. 2000, AJ, 120, 1449

Ricci, L., Rome, H., Pinilla, P., Facchini, S., Birnstiel, T., & Testi, L. 2017, ApJ, 846, 19

Riols, A. & Lesur, G. 2018, ArXiv e-prints

Ruge, J. P., Flock, M., Wolf, S., Dzyurkevich, N., Fromang, S., Henning, T., Klahr, H., & Meheut, H. 2016, A&A, 590, A17

Salmeron, R., Königl, A., & Wardle, M. 2011, MNRAS, 412, 1162

Shakura, N. I. & Sunyaev, R. A. 1973, A&A, 24, 337

Shang, H., Glassgold, A. E., Shu, F. H., & Lizano, S. 2002, ApJ, 564, 853

Sheehan, P. D. & Eisner, J. A. 2018, ApJ, 857, 18

Sheikhnezami, S., Fendt, C., Porth, O., Vaidya, B., & Ghanbari, J. 2012, ApJ, 757, 65

Shu, F., Najita, J., Ostriker, E., Wilkin, F., Ruden, S., & Lizano, S. 1994, ApJ, 429, 781

Shu, F. H. 1992, Physics of Astrophysics, Vol. II (University Science Books)

Shu, F. H., Najita, J. R., Shang, H., & Li, Z.-Y. 2000, Protostars and Planets IV, 789

Simon, J. B. & Armitage, P. J. 2014, ApJ, 784, 15

Simon, M. N., Pascucci, I., Edwards, S., Feng, W., Gorti, U., Hollenbach, D., Rigliaco, E., & Keane, J. T. 2016, ApJ, 831, 169

Spruit, H. C. 1996, ArXiv Astrophysics e-prints

Spruit, H. C. 2010, in Lecture Notes in Physics, Berlin Springer Verlag, Vol. 794, Lecture Notes in Physics, Berlin Springer Verlag, ed. T. Belloni, 233

Squire, J. & Hopkins, P. F. 2018, MNRAS, 477, 5011

Stapelfeldt, K. R., Krist, J. E., Ménard, F., Bouvier, J., Padgett, D. L., & Burrows, C. J. 1998, ApJ, 502, L65

Stepanovs, D. & Fendt, C. 2014, ApJ, 793, 31

—. 2016, ApJ, 825, 14

Stolker, T., Dominik, C., Avenhaus, H., Min, M., de Boer, J., Ginski, C., Schmid, H. M., Juhasz, A., Bazzon, A., Waters, L. B. F. M., Garufi, A., Augereau, J.-C., Benisty, M., Boccaletti, A., Henning, T., Langlois, M., Maire, A.-L., Ménard, F., Meyer, M. R., Pinte, C., Quanz, S. P., Thalmann, C., Beuzit, J.-L., Carbillet, M., Costille, A., Dohlen, K., Feldt, M., Gisler, D., Mouillet, D., Pavlov, A., Perret, D., Petit, C., Pragt, J., Rochat, S., Roelfsema, R., Salasnich, B., Soenke, C., & Wildi, F. 2016, A&A, 595, A113

Stone, J. M., Mihalas, D., & Norman, M. L. 1992, ApJS, 80, 819

Stone, J. M. & Norman, M. L. 1992a, ApJS, 80, 753

—. 1992b, ApJS, 80, 791

—. 1994, ApJ, 433, 746

Strom, S. E. 1972, PASP, 84, 745

Suriano, S. S., Li, Z.-Y., Krasnopolsky, R., & Shang, H. 2017, MNRAS, 468, 3850

—. 2018, MNRAS, 477, 1239

Suzuki, T. K., Muto, T., & Inutsuka, S.-i. 2010, ApJ, 718, 1289

Suzuki, T. K., Ogihara, M., Morbidelli, A., Crida, A., & Guillot, T. 2016, A&A, 596, A74

Tabone, B., Cabrit, S., Bianchi, E., Ferreira, J., Pineau des Forêts, G., Codella, C., Gusdorf, A., Gueth, F., Podio, L., & Chapillon, E. 2017, A&A, 607, L6

Takahashi, S. Z. & Inutsuka, S.-i. 2014, ApJ, 794, 55

Troland, T. H. & Crutcher, R. M. 2008, ApJ, 680, 457

Turner, N. J., Benisty, M., Dullemond, C. P., & Hirose, S. 2014a, ApJ, 780, 42

Turner, N. J., Fromang, S., Gammie, C., Klahr, H., Lesur, G., Wardle, M., & Bai, X.-N. 2014b, Protostars and Planets VI, 411

Tzeferacos, P., Ferrari, A., Mignone, A., Zanni, C., Bodo, G., & Massaglia, S. 2009, MNRAS, 400, 820

Umebayashi, T. & Nakano, T. 1981, PASJ, 33, 617

—. 1990, MNRAS, 243, 103

Čemeljić, M., Shang, H., & Chiang, T.-Y. 2013, ApJ, 768, 5

van Boekel, R., Henning, T., Menu, J., de Boer, J., Langlois, M., Müller, A., Avenhaus, H., Boccaletti, A., Schmid, H. M., Thalmann, C., Benisty, M., Dominik, C., Ginski, C., Girard, J. H., Gisler, D., Lobo Gomes, A., Menard, F., Min, M., Pavlov, A., Pohl, A., Quanz, S. P., Rabou, P., Roelfsema, R., Sauvage, J.-F., Teague, R., Wildi, F., & Zurlo, A. 2017, ApJ, 837, 132

van der Plas, G., Wright, C. M., Ménard, F., Casassus, S., Canovas, H., Pinte, C., Maddison, S. T., Maaskant, K., Avenhaus, H., Cieza, L., Perez, S., & Ubach, C. 2017, A&A, 597, A32

Velikhov, E. 1959, J. Expt. Theor. Phys. (USSR), 36, 1398

Wardle, M. 2007, Ap&SS, 311, 35

Wardle, M. & Koenigl, A. 1993, ApJ, 410, 218

Weidenschilling, S. J. 1977a, MNRAS, 180, 57

—. 1977b, Ap&SS, 51, 153

Whipple, F. L. 1972, in From Plasma to Planet, ed. A. Elvius, 211

Wilking, B. A. & Lada, C. J. 1983, ApJ, 274, 698

Williams, J. P. & Cieza, L. A. 2011, ARA&A, 49, 67

Winn, J. N. & Fabrycky, D. C. 2015, ARA&A, 53, 409

Yen, H.-W., Koch, P. M., Takakuwa, S., Krasnopolsky, R., Ohashi, N., & Aso, Y. 2017, ApJ, 834, 178

Youdin, A. N. & Goodman, J. 2005, ApJ, 620, 459

Zanni, C., Ferrari, A., Rosner, R., Bodo, G., & Massaglia, S. 2007, A&A, 469, 811

Zhang, K., Bergin, E. A., Blake, G. A., Cleeves, L. I., Hogerheijde, M., Salinas, V., & Schwarz, K. R. 2016, ApJ, 818, L16

Zhang, K., Blake, G. A., & Bergin, E. A. 2015, ApJ, 806, L7

Zhao, B., Caselli, P., & Li, Z.-Y. 2018, MNRAS

Zhao, B., Caselli, P., Li, Z.-Y., Krasnopolsky, R., Shang, H., & Nakamura, F. 2016, MNRAS, 460, 2050

Zhu, Z. & Stone, J. M. 2018, ApJ, 857, 34

Zweibel, E. G. & Yamada, M. 2009, ARA&A, 47, 291